BULK PROPERTIES AND PHYSICAL CHARACTERISTICS OF STRIPPED-ENVELOPE SUPERNOVAE

Simon John Prentice

A thesis submitted in partial fulfilment of the requirements of

Liverpool John Moores University

for the degree of

Doctor of Philosophy.

February 2018

Declaration

The work presented in this thesis was carried out at the Astrophysics Research Institute, Liverpool John Moores University. Unless otherwise stated, it is the original work of the author.

While registered as a candidate for the degree of Doctor of Philosophy, for which submission is now made, the author has not been registered as a candidate for any other award. This thesis has not been submitted in whole, or in part, for any other degree.

Simon John Prentice
Astrophysics Research Institute
Liverpool John Moores University
IC2, Liverpool Science Park
146 Brownlow Hill
Liverpool
L3 5RF
UK

MAY 29, 2018

Abstract

Stripped-envelope supernovae (SE-SNe) are a subset of core-collapse supernovae; the explosive death of a massive star. Their defining characteristic is the lack of prominent He and/or H envelope suggesting significant mass loss prior to explosion. Their progenitors may be high mass single stars (> 30 $M_{\odot}$) or lower mass stars that are stripped via binary interaction. Since their discovery as a separate population in 1983, and until recently, the data on these objects steadily increased. SN discoveries have increased year on year since the early 2000s with the advent of targeted and untargeted surveys looking at the skies for transient objects. As a result, some of these surveys have amassed photometric and spectroscopic data on a large number of SE-SNe. The last few years has seen this data made available, dramatically increasing the number of objects with data. I present an investigation into the bulk properties of SE-SNe, using a large database accumulated from public sources, the Palomar Transient Factory, the Public ESO Spectroscopic Survey of Transient Objects, and my own observations.

I begin the investigation by constructing and analysing the largest set of bolometric light curves of SE-SNe to date – 85 objects. The light curves are analysed to derive temporal characteristics and peak luminosity $L_{\rm p}$, enabling the construction of a luminosity function. Subsequently, the mass of ^{56}Ni synthesized in the explosion, along with the ratio of ejecta mass to ejecta kinetic energy, are calculated. It is found that broad-lined SNe Ic (SNe Ic-BL) and gamma-ray burst SNe are the most luminous subtypes with a combined median $L_{\rm p}$, in erg s^{-1}, of $\log_{10}(L_{\rm p}) = 43.00$ compared to 42.51 for SNe Ic, 42.50 for SNe Ib, and 42.36 for SNe IIb. It is also found that SNe Ic-BL synthesize approximately twice the amount of ^{56}Ni compared with SNe Ic, Ib, and IIb,

with median $M_{\rm Ni}$ = 0.34, 0.16, 0.14, and 0.11 $M_{\odot}$, respectively. SNe Ic-BL, and to a lesser extent SNe Ic, typically rise quicker than SNe Ib/IIb; consequently, their light curves are not as broad.

Next I examine the spectroscopic properties of these SNe using analytical methods. For He-rich SNe, the presence of H becomes the focus. The strength, velocity, and ratio between absorption and emission of H are measured, along with additional analysis of He I lines, in order to categorize the SNe. The He-poor SNe are ordered according to the number of absorption features N present in the spectra, which is a measure of the degree of line blending. The kinetic energy per unit mass Ek/Mej is strongly affected by mass at high velocity, and such situations principally occur when the outer density profile of the ejecta is shallow, leading to the blending of lines. Using the results, the existing SE-SN taxonomic scheme is adapted

I then present the data and analysis of 19 SE-SNe observed since 2012. These SNe are analysed within the context of the earlier findings in this work, as well as examining the ejecta mass distributions as derived from an analytical light curve model. The results support the assertion that SE-SNe reside in a parameter space which is still under-sampled as approximately 20 – 25 percent of these objects have properties that deviate significantly from that of the bulk population. The statistics of the ejecta mass distributions also provide evidence that these SNe arise from relatively low mass progenitors (< 25 $M_{\odot}$) as the mean ejecta mass for all SN types is 2 – 4 $M_{\odot}$. Furthermore, distribution of ejecta mass appears unimodal, which suggests that SE-SNe are preferentially arising from one channel; stars that undergo binary interaction.

Understanding SE-SNe is important as their stripped pre-explosion progenitor stars are hot, making them sources of ionizing radiation. Their explosions influence their local environment by injecting energy, both radiative and kinetic, and seeding the ISM with the ashes of nucleosynthesis. Finally, they are a source of neutron stars and stellar mass black holes in the universe, which gives rise to other astrophysical events such as X-ray binaries, pulsars, and strong gravitational wave events.

Publications

Prentice, S. J. et al., “”SN 2016coi/ASASSN-16fp: An example of residual helium in a type Ic supernova?”, 2018, MNRAS

Prentice, S. J. and Mazzali, P. A., “A physically motivated classification of stripped-envelope supernovae”, 2017, MNRAS, 469, 2672-2694.

Prentice, S. J. et al., “The bolometric light curves and physical parameters of stripped-envelope supernovae”, 2016, MNRAS, 458, 2973-3002.

Kuncarayakti, H. and Maeda, K. and Ashall, C. J. and **Prentice, S. J.**, et al., “SN 2017dio: a type-Ic supernova exploding in a hydrogen-rich circumstellar medium”, 2018, ApJ letters, 854, L14

Tartaglia, L. et al., including **Prentice, S. J**, “The early detection and follow-up of the highly obscured Type II supernova 2016ija/DLT16am”, 2018, ApJ, 853, 62

Smartt, S. J. et al., including **Prentice, S. J**, “A kilonova as the electromagnetic counterpart to a gravitational-wave source”, 2017, Nature

Abbott, B. P. et al., including **Prentice, S. J**, “Multi-messenger Observations of a Bi-

nary Neutron Star Merger", 2017, ApJ Letters

Shivvers, I. et al., including **Prentice, S.**, "The nearby Type Ibn supernova 2015G: signatures of asymmetry and progenitor constraints", 2017, MNRAS, 471, 4381-4397

Mazzali, P. A. and Sauer, D. N. and Pian, E. and Deng, J. and **Prentice, S.** et al., "Modelling the Type Ic SN 2004aw: a moderately energetic explosion of a massive C+O star without a GRB", 2017, MNRAS, 469, 2498-2508

De Cia, A. et al., including **Prentice, S.** , "Light curves of hydrogen-poor Superluminous Supernovae from the Palomar Transient Factory", 2017, ArXiv e-prints, 1708.01623

Bose, S. et al., including **Prentice, S.** , "Gaia17biu/SN 2017egm in NGC 3191: the closest hydrogen-poor superluminous supernova to date is in a "normal", massive, metal-rich spiral galaxy", 2018, ApJ, 853, 57

Cartier, R. et al., including **Prentice, S.** , "Early observations of the nearby Type Ia supernova SN 2015F", 2017, MNRAS, 464, 4476-4494

Ashall, C. and Pian, E. and Mazzali, P. A. and Palazzi, E. and **Prentice, S. J.** et al. , "GRB 161219B-SN 2016jca: a powerful stellar collapse", 2017, ArXiv e-prints, 1702.04339

Leloudas, G. et al., including **Prentice, S.** , "The superluminous transient ASASSN-15lh as a tidal disruption event from a Kerr black hole", 2016, Nature Astronomy, 1, 0002

Ashall, C. and Mazzali, P. and Sasdelli, M. and **Prentice, S. J.** , "Luminosity distributions of Type Ia supernovae", 2016, MNRAS, 460, 3529-3544

Sasdelli, M. and Ishida, E. E. O. and Hillebrandt, W. and Ashall, C. and Mazzali, P. A. and **Prentice, S. J.**, "Breaking the colour-reddening degeneracy in Type Ia supernovae", 2016, MNRAS, 460, 373-382

Greiner, J. and Mazzali, P. A. and Kann, D. A. and Krühler, T. and Pian, E. and **Prentice, S.** et al., "A very luminous magnetar-powered supernova associated with an ultra-long γ-ray burst" , 2015, Nature, 523, 189-192

Acknowledgements

I would like to thank my supervisor, Paolo Mazzali, for his all-round insightfulness and for guiding me on this journey. The ARI staff who have assisted me; David Bersier, Matt Darnley, Phil James. The support, emotional and otherwise, provided by my fellow ARI PhD students; Gavin Lamb, Chris Ashall, Emma Beasor, Lawrence Short. Also Yjan Gordon at the University of Hull. A very special mention to The League for absolutely everything they do. Toby and Keira Prentice for being distractions throughout and for being very good reasons to do this. Raffaela Baechler for support, inspiration, and everything else. Finally my parents, without whom I wouldn't be who I am.

SIMON JOHN PRENTICE MAY 29, 2018

"It was a dark and stormy night..."

- Edward Bulwer-Lytton

Contents

List of Tables

List of Figures

Chapter 1

Introduction

Supernovae (SNe) are amongst the most energetic events in the universe with a typical integrated radiative emission of $\sim 10^{49}$ erg, kinetic energy $\sim 10^{51}$ erg, and, if the explosion mechanism involves the catastrophic collapse of the iron core of a massive star, $\sim 10^{53}$ erg emitted in the form of neutrinos (Janka, 2017).

Historically SNe were classified according to the presence/absence of hydrogen in their spectra. Type I SNe had no spectral evidence for H and the light curves reached a single peak before decaying. Type II SNe showed strong H P-Cygni features in their spectra and were defined by a light curve that rose to a peak after a few days before settling on to a "plateau" phase where the luminosity remained almost constant for some period of weeks/months before decreasing dramatically on to a linear decay. It was identified that the type II SNe contained spectroscopic features of elements that were readily available in stars; H, He, Na, Ca, O, Fe, whereas SNe I consisted of alpha chain elements, the result of explosive silicon burning. Thus, it was theorised that Type I SNe were the result of the thermonuclear explosion of a white dwarf while type II SNe are the result of the collapse of the iron core in a massive star; core-collapse supernovae (CC-SNe). The plateau phase in the type II light curve occurs as a recombination wave passes through the H envelope of the exploded star, as this occurs at approximately constant temperature and radius so the luminosity remains the same.

A subset of CC-SNe show light curves more akin to Type I SNe but with the signs of

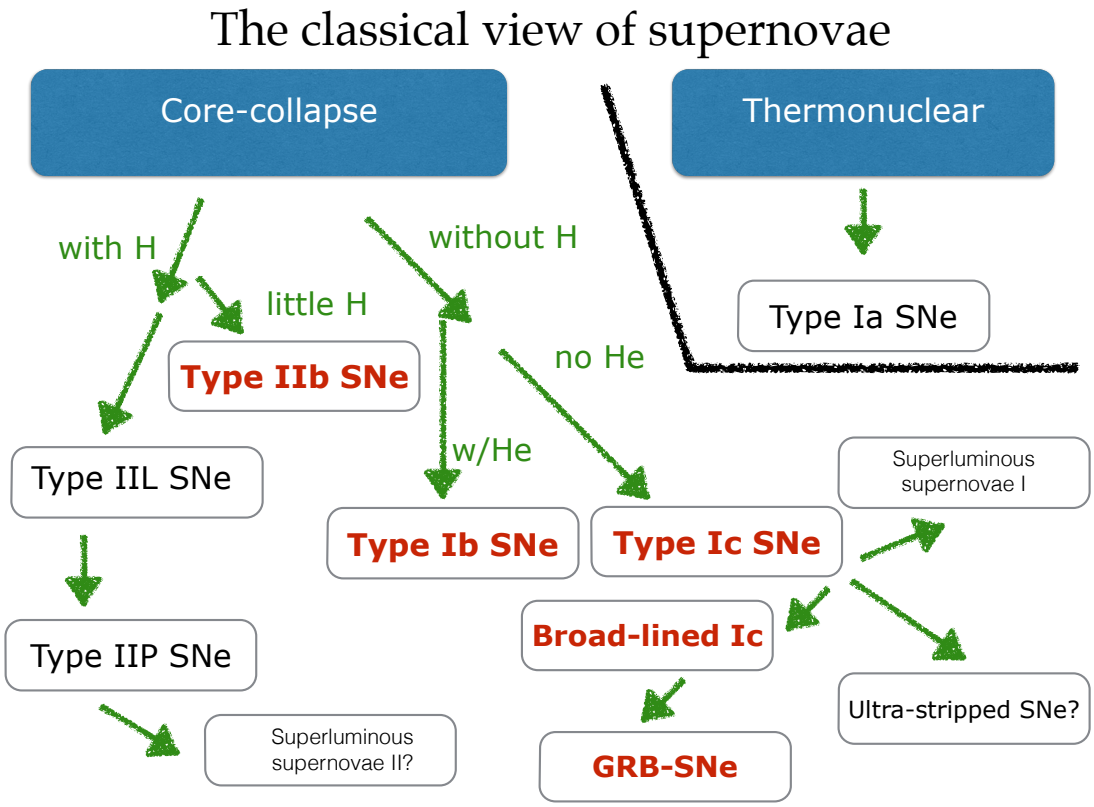

Figure 1.1: The traditional view of SN classification. The "stripped-envelope SNe" sub-types, and the focus of this thesis, are in bold red text.

stellar material in the ejecta. The key difference between these SNe and the canonical type II SNe is the lack of strong H lines in the spectra. Thus the light curves are explained by the absence of the recombination phase revealing that these SNe have been stripped almost entirely of their outer H envelope; these are "stripped-envelope supernovae" (SE-SNe, SNe Ibc). The volume-limited rates of CC-SNe in the local universe were presented in Shivvers et al. (2017). Here it was found that SNe II account for ~ 70 percent of all CC events while SE-SNe are the remaining 30 percent.

1.1 The classical view of SE-SN classification

As previously described, supernovae are traditionally classified along a single axes; the spectroscopic presence or absence of hydrogen. Stripped envelope supernovae straddle the two groups in classification with the traditional classification scheme (see

Figure 1.1), from least stripped to most stripped, named as IIb, Ib, Ic. If a SN Ic shows broad spectral lines then it can be labelled as "broad lined" leading to the addition of "BL" to the classification; Ic-BL. These highly blended lines are not restricted to SNe Ic, for example the case of broad lined SN IIb 2003dh (Hunter et al., 2009; Mazzali et al., 2009) which had very broad lines in its early spectra before displaying a strong Hα signature and narrower lines closer to maximum light.

An important note – technically superluminous supernovae of type I (Gal-Yam, 2012) are SE-SNe, as these show spectral similarity to some SNe Ic after maximum light indicating severe stripping. They are omitted from these studies into SNe Ibc, and throughout this thesis, because their photometric and spectroscopic appearance, and physical properties are differentiated enough from traditional SNe Ibc (e.g., Nicholl et al., 2015) to justify a different classification. It is only in the nebular phase that these objects begin to look similar (they show the emission lines common to H-poor core-collapse events). Furthermore, their ejecta and especially their luminosity ($E_{\rm rad} \sim 10^{52}$ erg) is likely powered differently to traditional SE-SNe; rotational energy from a compact object rather than radioactive decay (Inserra et al., 2013).

In this section I give a brief overview of the SE-SN sub-groups and identify key features.

1.1.1 SNe IIb

The defining characteristic of SNe IIb is that they show prominent H P-Cygni lines in their spectra. The strength of the Hα emission is significantly less than that of SNe IIP however, and their light curves are more similar to SNe Ia in terms of the main peak luminosity being powered by the decay chain of ^{56}Ni.

Some SNe IIb show an initial peak and declining phase (see Section 1.2). This early peak is attributed to the shock cooling tail of the stellar envelope following shock-breakout (SBO). If there is an SBO cooling tail then the spectra of SNe IIb approximately a day after explosion can be defined by a featureless blackbody ($T \sim 150,000$

K at peak), that over the course of a few days, cools and gives way to strong H lines.

He P-Cygni features become apparent after some amount of time, this is dependent upon the SN and the amount of H in the outer shell. This can range from shortly after explosion to a few days after maximum, as was the case of SN 1993J where the He-lines did not appear until 18 – 20 days after explosion (Matheson et al., 2000b).

SNe IIb account for ~ 34 percent of SE-SNe (Shivvers et al., 2017).

1.1.2 SNe Ib

Removal of the H envelope to the level where H no longer leaves a spectroscopic signature, leaves a He-star. The explosion of a star in this phase results in spectra that display strong He I $\lambda\lambda$ 4472, 5876, 6678 lines for several weeks, although these eventually fade as the photosphere disappears. This supernova is that of type Ib, and they account for ~ 36 percent of SE-SNe (Shivvers et al., 2017).

1.1.3 SNe Ic

The loss of both the H and He envelope prior to explosions leads to a type Ic SN. Spectroscopically they show lines associated with elements found within massive stars, e.g., Fe II, Si II, Na I, O I, Ca II, Mg II. The diversity in line profiles and line velocities is a defining feature of this SN subgroup. SNe Ic spectral line profiles can range from narrow, low velocity lines (e.g., SN 2007gr Hunter et al., 2009) to broad, highly blended, high velocity lines (e.g. SN 1997ef; Iwamoto et al., 2000; Mazzali et al., 2000). The kinetic energy $E_{\rm k}$ of these objects can also span more than an order of magnitude; from 10^{51} erg to a few 10^{52} erg ("hypernovae"; Iwamoto et al., 1998). That $E_{\rm k}$ encompasses such a large range of energies suggests different explosion mechanisms exist to power these SNe as the hypernovae require a large energy reservoir that efficiently transfers energy to the ejecta (Woosley et al., 1994; Mazzali et al., 2014). Note, that the term "hypernova" was originally used to describe type Ibc SNe that showed broad lines in their spectra (e.g., GRB-SN 1998bw, SN 200ap, SN 1997ef) which is commensurate

with a high specific kinetic energy. However, since the discovery of superluminous supernovae in 2005 (SN 2005ap; Quimby et al., 2007), which may also have $E_{\rm k} \sim 10^{52}$ erg but with a specific kinetic energy of ~ 1 [10^{51} erg]/$M_{\odot}$, the term "hypernova" has fallen out of use.

Shivvers et al. (2017) determined that "normal" SNe Ic are ~ 22 percent of all SE-SNe while those with broad lines are ~ 4 percent.

1.1.4 Gamma-ray burst supernovae

The most energetic SE-SNe are those associated with gamma-ray bursts (GRBs). These events are rare and seen to large redshifts due to the energetic and beamed high energy transient that signals the beginning of core collapse. There are 16 spectroscopically confirmed GRB-SNe, two XRF-SNe, and at least 13 GRB-SNe assumed from GRB afterglow light curve bumps.

The closest GRB-SN observed was also the first; SN 1998bw/GRB 980425 at a redshift of $z = 0.0085$ (Galama et al., 1998). It was noted for its unusually broad lines, an indication of very high velocity ejecta, large ejecta mass $M_{\rm ej} \sim 10\ {\rm M}_{\odot}$, and high kinetic energy $\sim 40 \times 10^{52}$ erg (Iwamoto et al., 1998). Its peak absolute B-band magnitude of $M_B = -18.88 \pm 0.05$ mag made it the most luminous SE-SN known at the time, and comparable with luminosities of SNe Ia, as can be seen when considering M_B averages of -18.28 mag (SNe Ia), -16.68 mag (SN Ibc), and -15.69 mag (SNe II) (Galama et al., 1998). The next closest GRB-SN was SN 2017iuk associated with GRB 171205A at $z = 0.037$. With a median redshift of $z = 0.49$, and only two with $z < 0.1$, it is clear that collecting data of these SNe is difficult. K-corrections are non-negligible, leading to the flux peak occurring at redder wavelengths and if these SNe are dim, they may also be obscured by the GRB afterglow.

As of yet, GRBs have only been associated with broad lined type Ic SNe.

1.2 SE-SN Light curves

Almost all SE-SN light curves are in the same category as type I SNe, that is, they rise over the course of a few weeks to a peak luminosity before decaying onto a somewhat linear slope. The energy to power the light curves comes from the decay chain of ^{56}Ni $>$ ^{56}Co $>$ ^{56}Fe, with the time to peak determined by the distribution of ^{56}Ni in the ejecta and the diffusion time scale/opacity of the ejecta.

As previously mentioned in the context of SNe IIb, if the progenitor star is sufficiently extended then it may be possible to observe the cooling of the ejecta following shock-breakout (SBO) at early times. This is rare however and is assumed to occur in stars that have extended envelopes prior to explosion (for example Arcavi et al., 2011; Soderberg et al., 2012; Piro and Nakar, 2013; Piro, 2015). As the shock from core-collapse traverses the envelope of the exploding star it preferentially deposits energy in the outer layers. The luminosity of the initial event, and the duration of cooling are directly related to the size of the emitting region and the diffusion time of photons through unshocked material, and thus, the size of the progenitor star at CC and the mass loss rate of the star immediately prior to CC (Ensman and Burrows, 1992; Matzner and McKee, 1999; Svirski and Nakar, 2014b; Ohtani et al., 2018). It has also given rise to discussion on compact and extended progenitor stars for SNe IIb (Chevalier and Soderberg, 2010). These are normally the most H-rich SNe IIb, e.g. SN 1993J (Nomoto et al., 1993), SN 2011fu (Morales-Garoffolo et al., 2014a), SN 2013df (Morales-Garoffolo et al., 2014b), and SN 2016gkg (Tartaglia et al., 2017), other SNe IIb that are caught early, for example SN 1996cb (Qiu et al., 1999), SN 2011dh (Arcavi et al., 2011), and SN 2011ei (Milisavljevic et al., 2013b) do not have a shock-cooling tail.

Two SNe Ib have shown early peaks in their light curves; SN 1999ex, where an early peak was seen in the U-band (Stritzinger et al., 2002), and peculiar SN 2008D which was observed serendipitously at explosion by the Swift telescope as it observed SN 2007uy (Malesani et al., 2009). In the case of SN 2008D, the initial peak has been attributed to the failed break-out of a relativistic jet (Mazzali et al., 2008) or SBO

cooling within an optically thick wind (Chevalier and Fransson, 2008; Modjaz et al., 2009; Balberg and Loeb, 2011; Svirski and Nakar, 2014a).

Another notable example is seen with GRB-SNe, where the afterglow from the GRB (Galama et al., 1997; Bloom et al., 1998; Lipkin et al., 2004) masks the SN light at early times. This effect can be weak, as in the case of SN 1998bw/GRB 980425 (Galama et al., 1998) or strong (e.g., SN 2003dh/GRB 030329 Mazzali et al., 2003; Matheson et al., 2003).

Taddia et al. (2016) reported a double peaked light curve associated with the type Ic iPTF15dtg which they attribute to SBO cooling from low mass (< 0.045 $M_{\odot}$) material surrounding the progenitor out to ~ 500 $R_{\odot}$. They ruled out interaction with a companion, shock-breakout from the progenitor surface, or magnetar powered shock breakout.

There are two examples of highly unusual double-peaked light curves for which the first peak is not explained by SBO as their time-scales are considerably longer but the luminosity relatively low; SN 2005bf (Tominaga et al., 2005; Maeda et al., 2007; Tanaka et al., 2009b) and PTF11mnb (Taddia et al., 2018a). In these SNe the first peak is attributed to a normal SN-like explosion which is powered by radioactivity, while the later peak is powered by a magnetar which is spun up by some accreted material. Magnetars as a source of radiative energy have been invoked for superluminous supernovae (e.g., Dessart et al., 2012; Kasen et al., 2016; Moriya et al., 2017; Nicholl et al., 2017; Wang et al., 2017) and the luminous GRB-SN 2011kl supernova (Greiner et al., 2015).

1.3 Spectra - The photospheric and nebular epochs

SE-SNe have two clearly defined spectroscopic phases; photospheric and nebular, see Figure 1.2. These are based upon the physical processes that form the spectra.

The photospheric phase lasts from explosion to around a few weeks past maximum

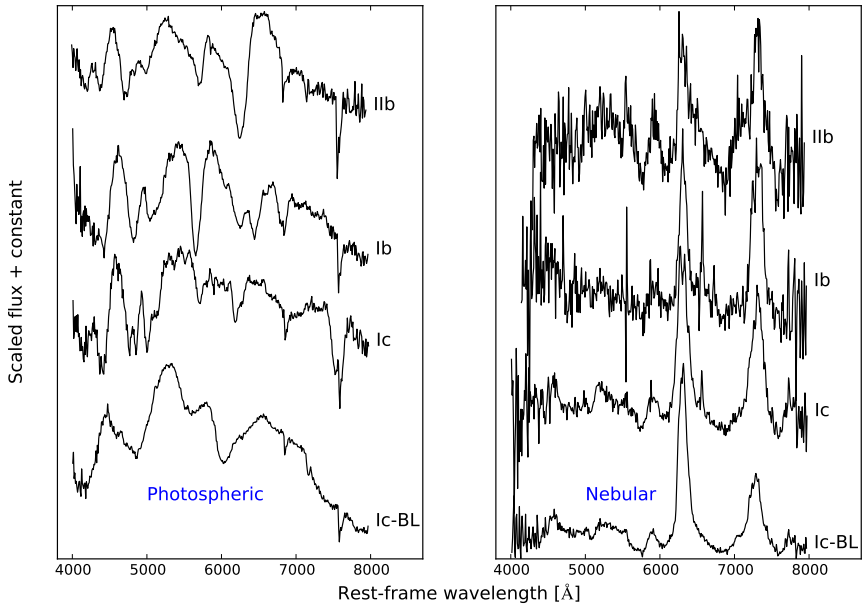

Figure 1.2: Example Liverpool Telescope/SPRAT spectra of SE-SNe in the photospheric and nebular phases. The important feature at nebular times is the [O I] $\lambda\lambda$6300, 6363 line, and note the absence of non-host Hα emission even in the SN IIb.

light for a typical SE-SN. During this time the spectra are characterised by an underlying black body that shows absorption and emission lines corresponding to the composition and velocity of the ejecta above the photosphere. Photons emitted from the photosphere undergo a series of scattering and absorption/re-emission events (e.g., Mazzali and Lucy, 1993; Mazzali et al., 2000). This process leads to a redistribution of flux from shorter wavelengths to longer wavelengths. Spectra at these epochs probe the outer layers of the ejecta and provide information about the state of the star pre-explosion. With a good time-series of early spectra, spectroscopic modelling can be used to determine the proportion and mass of elements in the ejecta as a function of velocity. This method of "abundance tomography" (Sauer et al., 2006; Ashall et al., 2014; Mazzali et al., 2017) is particularly useful for SE-SNe, where the type of progenitor star is often unknown. Also, the spectra in this phase can be used to map the density profile of the SN ejecta in the line-of-sight and so early data provide the best estimate of the kinetic energy because it is contained in the highest velocity material. The left panel of Figure 1.2 shows photospheric phase spectra for a few different types of SE-SNe.

The nebular phase (right panel, Figure 1.2) can begin from $40+$ days with the emergence of the Na I D and Ca II NIR emission lines, but is fully seen around $\sim$ 100 d when the [O I] $\lambda\lambda$6300, 6363 dominates the spectrum. During this time the ejecta becomes diffuse and increasingly transparent to the decay products of ^{56}Co (gamma rays and positrons) except for electrons, which can be scattered to high kinetic energies by interaction with the gamma-rays and positrons. Positrons become the primary source of energy in the ejecta as time progresses because their velocity is significantly less than the speed of light so they diffuse slower. These non-thermal electrons then excite the surrounding gas into meta-stable states, and the eventual de-excitation of these states leads to emission lines. That meta-stable states, which lead to the emission of photon energies corresponding to forbidden and semi-forbidden lines, are able to exist demonstrates the low-density nature of the ejecta at this time. The most prominent nebular phase emission lines are associated with elements found in massive stars; O, Ca, Mg, Na, Fe, Si. The strongest of these are [O I] $\lambda\lambda$6300, 6363, Ca II] $\lambda\lambda$7291, 7324, Ca II near infra-red triplet, and O I λ7773 (e.g., Filippenko et al., 1993; Mazzali et al., 2010). Because the He and/or H shells have largely been stripped away in a SE-SN event, oxygen makes up a significant fraction of the mass of the ejecta. Hence the luminosity of the [O I] line can be used as a diagnostic for ejecta mass (see, for example, Uomoto and Kirshner, 1986; Chugai, 1994; Elmhamdi et al., 2003). This method depends upon various assumptions with regards to the excitation efficiency of the non-thermal electrons, the O temperature, and the fractional mass of O excited by the electrons. This method was used by Valenti et al. (2012) to demonstrate that SN 2011bm, with its unusually broad light curve, contained $5 - 10$ M$_\odot$ of O, out of a total ejecta mass of $7 - 17$ M$_\odot$, making it the most massive SE-SN ever observed.

1.4 Explosion mechanisms

Exploding a star was thought to be relatively straight forward; the collapse of the Fe core releases $\sim$ 10^{53} erg of gravitational potential energy, which is more than enough to account for the $\sim 10^{51}$ in kinetic energy required to unbind the envelope. In

the standard core-collapse model (e.g., Colgate and White, 1966; Bethe and Wilson, 1985), at ~ 1.4 $M_\odot$ the electron-degenerate Fe core collapses under the pressure of the overlaying material. The Fe nuclei and e^- within the core undergo electron capture, $p + e^- \rightarrow n + \nu_e$, which further removes the electron degeneracy pressure and rapidly compresses the innermost part of the core down to nuclear densities, leading to a proto-neutron star (PNS). At about $M_{\rm PNS} \sim 0.5$ $M_\odot$ the equation of state stiffens and the PNS "bounces"; it passes maximum compressibility and then rebounds to a slightly larger radius. This bounce sends a shock through the in-falling material above and instantly dissociates it into protons and neutrons. In the "prompt mechanism" this shock then continues and unbinds the star, however, explosion modelling has been unable to explode a star in this method (see Buras et al., 2006; Janka et al., 2007). The dissociation of nuclei is endothermic and robs the shock of energy, leading it to stall against the ram-pressure of the in-falling material at the shock radius $R_{\rm s} \sim 100 - 200$ km above the surface of the PNS. However, the cross-section of these newly-dissociated protons and neutrons to neutrinos is relatively large, and with the high neutrino flux emitted from the cooling of the PNS, and large densities in this region there is heating by neutrinos in the "gain" layer between below $R_{\rm s}$. After a few hundred ms the heating can provide enough energy to reinvigorate the shock and explode the star; this is the "delayed neutrino-heating mechanism" (Janka et al., 2006; Janka, 2012), see Figure 1.3. The kinetic energy imparted via this method is somewhat self-regulating and limited to a few 10^{51} erg because the expansion of the ejecta reduces the reaction rate of the neutrinos and nucleons. 1D explosion models still fail to explode the model stars in many cases. More success can be obtained with 2D models (Janka et al., 2016) and in 3D models (e.g., Takiwaki et al., 2012; Müller and Janka, 2015; Roberts et al., 2016). Multi-D models have also shown the importance of asymmetries in the material above $R_{\rm s}$, which leads to low pressure regions at the Si/Si-O interface, and allows the shocked material to push through and unbind the star. This is important for fast-rotating models where neutrino luminosities are lower (Summa et al., 2018).

The dissociated material behind the shock is the source of radioactive ^{56}Ni, as these protons and neutrons rapidly burn up the alpha chain to iron group elements; primarily

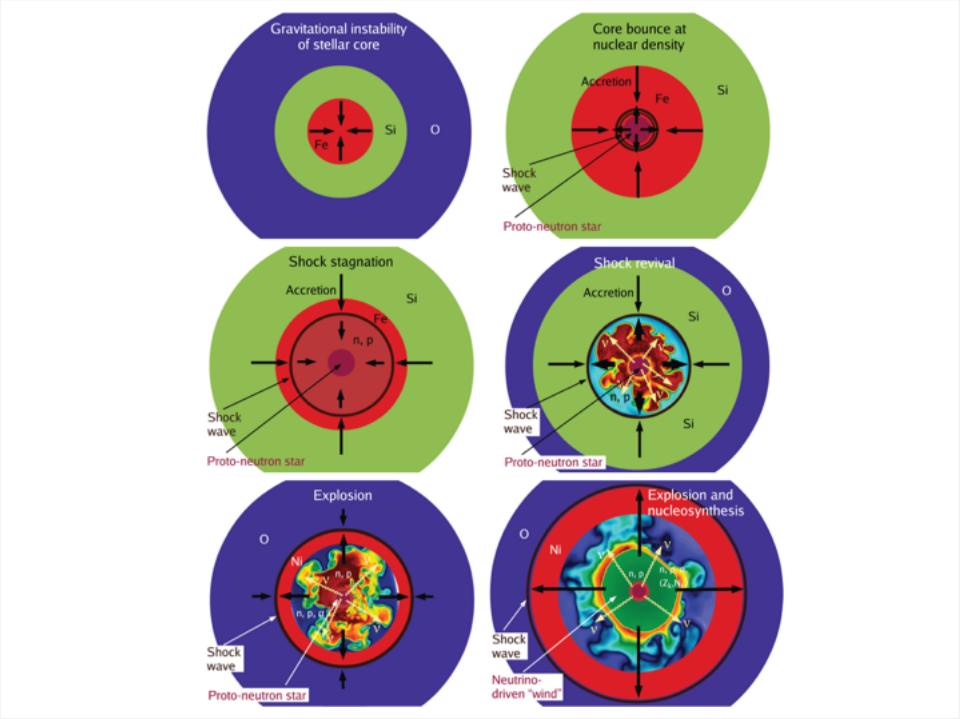

Figure 1.3: Panels describing the moment of core-collapse and explosions of a star (Janka, 2012)

^{56}Ni.

Alternate explosion methods have been suggested to explain extreme events. Woosley (1993) introduced the "collapsar" model to explain GRBs, and this has been extended to explain GRB-SNe (Dessart et al., 2017). In this model explosive silicon burning can occur in the accretion disk around a newly-formed black hole or at the edges of the jet launched by this object (see Barnes et al., 2017). High velocity ^{56}Ni has been required in the models of GRB-SNe (e.g. SN 2016jca/GRB 161219A; Ashall et al., 2017), confirming that the latter is a possibility.

Rapidly rotating compact objects contain a large amount of rotational energy. For a 1.4 $M_\odot$ neutron star (NS) with a rotation period of $\sim$ 1 ms (close to the break-up limit) this can be at least 2.5×10^{52} erg (Mazzali et al., 2014) or an order of magnitude higher if the NS is more massive (Metzger et al., 2015). These objects contain enough energy to explain the kinetic energies of GRB-SNe, $\sim 10^{52}$ erg, and with a sufficiently high magnetic field (10^{15} G; magnetars) can transfer this energy in just a few seconds. The magnetar must promptly collapse to a black hole (and presumably launch a GRB) in

order to avoid influencing the light curve of the SN (as happens with superluminous supernovae; Inserra et al., 2013; Nicholl et al., 2017). It should be noted that millisecond magnetars are seen in the Galaxy (e.g, Olausen and Kaspi, 2014), but these are spun down slowly over thousands of years rather than in a quick burst as is required here.

Finally, the ability to explode a star is also connected to the core mass at the time of core collapse. It has been seen in explosion simulations that stars of masses greater than $M_{\rm ZAMS}\sim 30$ M$_\odot$ are difficult to explode as they do not form a PNS and instead collapse directly to a black hole (Woosley and Heger, 2007; Janka, 2012; Sukhbold et al., 2016). In this regard, O'Connor and Ott (2011) find that the black hole formation time $t_{\rm BH}$ is proportional to the post-bounce compactness $\xi_{2.5}^{-3/2}$, which is a measure of the density of the innermost 2.5 M$_\odot$. If a black hole forms within ~ 0.5 s then the SN fails because the shock cannot be re-energised. This leads to "islands of explodability", between 20 and 60 M$_\odot$, where some mass ranges (e.g., 25 – 32 M$_\odot$ and 50 – 55 M$_\odot$) are more likely to explode than others.

1.4.1 Asphericity

Modelling of explosions suggests that asphericity is important for re-invigorating the shock and exploding the star. This can translate into global asymmetries in the explosion. To investigate asymmetry in explosions there are two methods. The first is by measuring polarisation, because emission from a spherically symmetric surface has no overall polarisation then a polarised signal indicates that the emitting region is not spherically symmetric. Spectropolarimetry provides more information as to polarisation across different wavelengths. As the spectra are formed by photon interaction with material in the ejecta, the distribution of this material can be revealed through spectropolarimetry. This method has been used to investigate the SN Ic 2007gr (Tanaka et al., 2008) peculiar SN Ib 2005bf (Tanaka et al., 2009a), SN IIb 2008aq (Stevance et al., 2016), SN IIb 2008ax (Chornock et al., 2011), SN IIb 2011dh (Mauerhan et al., 2015), and peculiar SN Ic-BL 2014ad (Stevance et al., 2017). In each case a significant

degree of polarisation was detected revealing that the explosions were asymmetric to some degree.

The next method is by examining the line profile of the [O I] $\lambda\lambda$ 6300,6363 emission line as this is sensitive to the velocity and physical distribution of O in the ejecta (see Figure 1.4). A spherically symmetric shell of emitting material produces a "flat-top" line profile to a distant observer. In aspherical explosions, particularly those associated with jets, the bulk of the high velocity material exits at the poles, while low velocity material (primarily O) is found in an equatorial torus, rather than a shell, having been disrupted along the jet axis. If the SN is viewed down this axis, then the distribution of the O-rich material is somewhat planar with little material moving in the direction of the observer. The absence of this material removes the outer wings of the [O I] line, transforming the box like profile into a sharp single peak. However, viewed equatorially, the effect is to remove the bulk of the material moving tangentially to the observer. Thus, if one imagines the "flat-top" profile but removes some amount of flux at the rest wavelength of the line then the result is a double peaked emission. The widths of the peaks are dependent on the velocity differential δv of the material moving directly towards and away from the observer (Mazzali et al., 2005; Maeda et al., 2008; Tanaka et al., 2009c) but see Milisavljevic et al. (2010) as double peaked emission can also arise from the doublet nature of the [O I] line. In this case the peaks are relatively close together with an equivalent $\delta v \sim 3000$ km s^{-1}.

Asphericity will affect the observables of the SN. Light curve rise times and peak luminosities can be changed depending upon the position of the observer with respect to the explosion as different angles can have different distributions of material, leading to different photon diffusion times and ^{56}Ni distributions. Differences in line-of-sight velocity will affect the spectra through differences in line blending and measured line velocity, and material distributions are reflected in line strength (Tanaka et al., 2007; Barnes et al., 2017). Physical characteristics (e.g., ejecta mass, kinetic energy) derived from modelling of light curves and spectra are also subject to change if spherical symmetry is assumed in the model.

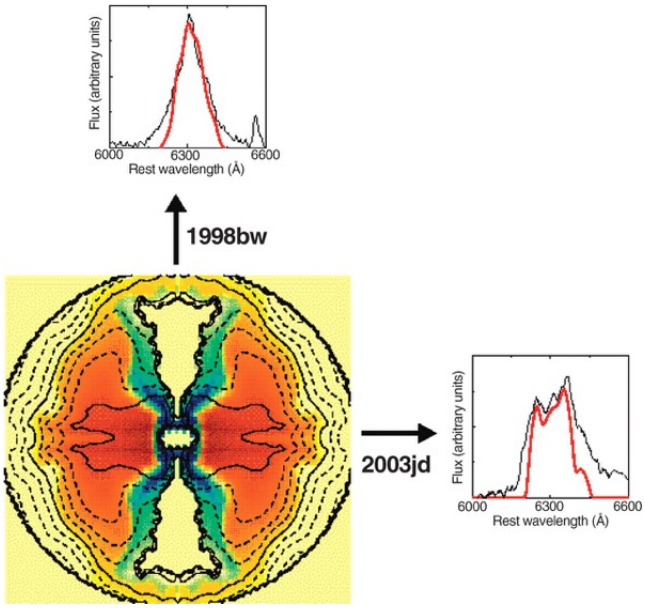

Figure 1.4: Figure from Mazzali et al. (2005) showing how the [O I] $\lambda\lambda$6363, 6300 line profile changes for an asymmetric explosion depending upon the position of the observer.

1.4.2 Relativistic ejecta

Radio observations of non-GRB related SE-SNe have revealed detections and non-detections (Chevalier and Fransson, 2006; Soderberg et al., 2006). Non-detections place limits on the density of material surrounding the progenitor star and the maximum velocity of the ejecta. Notable detections are seen with SN 2002ap (Soderberg et al., 2006), SN Ic 2007gr (Paragi et al., 2010) but see Soderberg et al. (2010), SN Ic-BL 2009bb (Pignata et al., 2011), SN Ic PTF11qcj (Corsi et al., 2014), SN Ic PTF12gzk (Horesh et al., 2013) and Ic-BL 2012ap (Margutti et al., 2014b). The presence of bright radio emission (SNe 2009bb and 2012ap) has been interpreted as the deceleration of mildly relativistic ejecta ($0.1 - 0.6c$) as it sweeps up material around the explosion site. This relativistic ejecta is energised by a short-lived "central engine", either a black hole or neutron star. Figure 1.5 shows how $E_{\rm k}$ derived from the optical emission compares with $E_{\rm k}$ from the radio, in relation to purely hydrodynamic explosion models (Tan et al., 2001) and those with extended energy injection (Lazzati et al., 2012). The presence of mildly relativistic ejecta may suggest a failed GRB, with the jet failing to escape the envelope of the star (Margutti et al., 2014b).

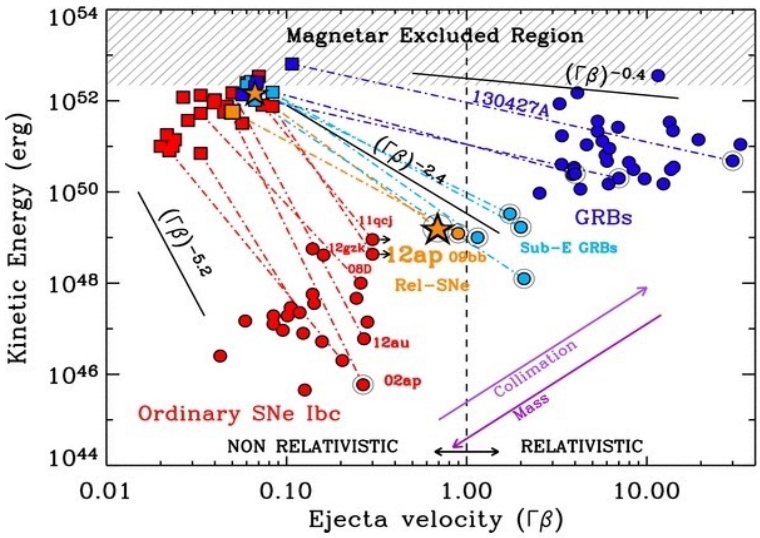

Figure 1.5: Kinetic of SE-SNe energy of in optical (square) and radio emission (circles) as a function of ejecta velocity (given by $\Gamma\beta$ where Γ is the shock Lorentz factor and β is the shock velocity; (Tan et al., 2001)). Optical to radio slopes are shown for purely hydrodynamical models, short-lived central engines, and long-lived central engines ($E_{\rm k}\propto (\Gamma\beta)^{-5.2}, (\Gamma\beta)^{-2.4}, (\Gamma\beta)^{-0.4}$ respectively). Radio detections in some non-GRB SE-SNe indicate mildly relativistic outflow consistent with the short-lived central engine model.

1.5 Progenitors

The progenitor stars of SE-SNe are largely unknown, because the type of progenitor depends on the $M_{\rm ZAMS}$ of the star that gives rise to a Ibc event, which depends upon how the mass is lost. Solar metallicity single stars of $M_{\rm ZAMS} > 25$ M$_\odot$ can lose sufficient mass to explode as Ibc events and will be > 10 M$_\odot$ at the time of explosion. If a neutron star (1.4 M$_\odot$) is left as a remnant then the ejecta masses of the resulting SN will also be > 10 M$_\odot$. Comparatively, stars of lower mass (12 – 25 M$_\odot$) can also explode as SE-SNe if they are stripped of their outer envelope by binary interaction. These stars will have a final mass of 2 – 8 M$_\odot$, which will lead to SNe with ejecta masses $\sim 1 - 7$ M$_\odot$. Given that 70% of massive stars in the Milky Way are estimated to be close enough to undergo mass transfer (Sana et al., 2012), the latter method has the potential to be the dominant pathway to SNe Ibc.

Here, I outline several ways of estimating the the final and $M_{\rm ZAMS}$ masses of SNe Ibc progenitor stars and highlight the tension between different methods.

1.5.1 Direct detection

There have been a few direct detections of the progenitors of SE-SNe, and for these the majority are H/He-rich SNe IIb. Typically such a detection requires identification of a progenitor candidate in pre-explosion imaging (see Kilpatrick et al., 2017) or waiting until the SN has faded and comparing the colour excess between pre-explosions and post explosion images in order to determine colour of the progenitor star. The colour or spectral energy distribution (SED) of the star allows it to be placed within a Hertzsprung-Russell (HR) diagram. Then, from the possible evolutionary tracks that can lead to that position, estimates on the $M_{\rm ZAMS}$ of the star can be made. This method carries considerable uncertainties, as the final position of the star in the HR diagram is dependent upon the star's metallicity, rotation, and most importantly, method of mass loss. Single stars must be considerably more massive than those stripped by binary interaction to end up in the same position in the HR diagram at the point of explosion (Eldridge et al., 2013).

The pre-explosion star of SN 1993J was a red K-type supergiant with $M_{\rm ZAMS} \sim 17$ $M_\odot$ (Smartt, 2009; Aldering et al., 1994), SN 2008ax a helium star which originally had $M_{\rm ZAMS} = 10$ – 14 $M_\odot$ (Crockett et al., 2008) or a B/A supergiant (Folatelli et al., 2015) (but see Arcavi et al., 2011), SN 2011dh was a yellow supergiant (YSG) at the time of explosion and had $M_{\rm ZAMS}= 13 \pm 3$ $M_\odot$ (Maund et al., 2011), SN 2013df was likewise a YSG with $M_{\rm ZAMS} = 13-17$ $M_\odot$. Most recently, SN 2016gkg was an A-type or F-type star at the time of explosion with $M_{\rm ZAMS}= 15 - 20$ $M_\odot$ (Kilpatrick et al., 2017; Tartaglia et al., 2017)

There has been one detection of the progenitor of a SN Ib to date; this is associated with iPTF13bvn and appears to have been a low mass He-star with $M_{\rm ZAMS}$ $10 - 20$ $M_\odot$ and with evidence for a binary companion (Cao et al., 2013; Eldridge and Maund, 2016; Fremling et al., 2014; Bersten et al., 2014; Eldridge and Maund, 2016) although Groh et al. (2013) suggest that progenitor was a single massive WR star with $M_{\rm ZAMS}$ in the region 31 – 35 $M_\odot$. However their model ejecta masses are of the order of 8 $M_\odot$ which is considerably larger than the 2 – 4 $M_\odot$ suggested by the light curve and

spectra (Fremling et al., 2016; Bersten et al., 2014).

The search for the progenitor of a SN Ic is ongoing, however, if, as expected these stars are in a Wolf-Rayet phase at explosion they may be difficult to see in optical HST data as they primarily emit in the UV. The most recent potential progenitor candidate is for that of Ic-7 SN 2017ein (Van Dyk et al., 2017). It may be some 18 months before the results of work on this is known however as the SN will have to fade substantially before analysis of the pre- and post-explosion regions can be undertaken.

1.5.2 Theoretical stellar evolution: single stars as progenitors of SE-SNe

The theoretical evolution of massive stars can be used to test what kind of progenitors lead to SE-SNe. As long as the pre-explosion star has lost its outer envelope of H/He it can be considered a candidate for a SE-SN event (ignoring whether or not such a star will explode). Mass loss rates of massive stars is dependent upon initial mass, rotation, and metallicity. Mass loss via winds is greater for higher metallicity because winds are driven by radiation pressure on spectral lines, which increases with the proportion of heavy elements (Castor et al., 1975; Vink, 2017). This leads to the expectation that the ratio of SNe II to Ibc, and SNe Ib to Ic, increases as metallicity decreases. The rotating models of Georgy et al. (2009, 2012) (Figure 1.6) show that, for various metallicities, SNe Ic occur in stars with $M_{\rm ZAMS}> 30$ M$_\odot$ while SNe Ib are the result of stars $M_{\rm ZAMS}$ between $20 - 30$ M$_\odot$. Interestingly their models suggest that a NS forms for all stars with $M_{\rm ZAMS}$ between $8 - 120$ M$_\odot$. Their final ejecta masses are significantly greater that that inferred from the light curves and spectra of SE-SNe with $M(Z = 0.004) > 10$ M$_\odot$, $M(Z = 0.008) > 9$ M$_\odot$, $M(Z = 0.02) > 8.5$ M$_\odot$, and $M(Z = 0.04) > 5$M$_\odot$. The lowest ejecta mass from their models is 4.9 M$_\odot$ for a $M_{\rm ZAMS}= 120$ M$_\odot$ star at $Z = 0.04$. Similar results were found by Groh et al. (2013) when considering rotating and non-rotating models at solar metallicity (Figure1.7). The SN types in these works are defined by the mass of H and He left in the evolved star prior to explosion; SNe Ic have no H and He < 0.6 M$_\odot$, SNe Ib have no H and

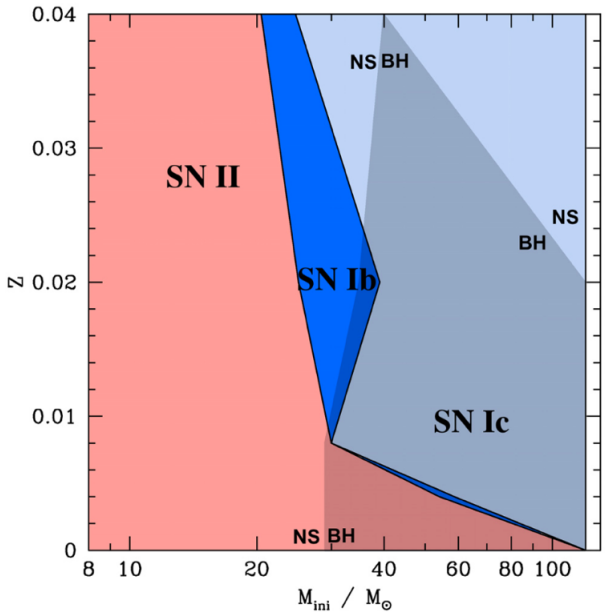

Figure 1.6: Figure from Georgy et al. (2009) showing the type of SN produced for a star of initial mass between 20 – 120 $M_\odot$ as a function of metallicity. Here, SNe Ic arise from stars > 30 $M_\odot$and SNe Ib from stars $20 - 30$ $M_\odot$. At very low metallicities almost all stars retain some amount of H.

He > 0.6 $M_\odot$, SNe IIb have $0 - 2$ $M_\odot$ of H. However, these abundances are greatly in excess of those found by Hachinger et al. (2012), where spectral modelling shows that He and H features appear when more than $0.06 - 0.14$ $M_\odot$ of He and less of H exists in the ejecta.

1.5.3 Theoretical stellar evolution: Binaries

Mass loss from single star evolution would suggest that very massive stars only lead to SE-SNe. Indeed, the rates of SE-SNe are considered inconsistent with that of purely single stars, under the assumption of a Salpeter initial mass function (IMF) (Smith et al., 2011). If mass loss is greater in more massive stars then we should expect to see far fewer SNe Ic compared to SNe IIb than we do. This does assume however that IMFs do not vary with metallicity and in regions of significant star formation. As a contrast, it has been seen in the 30 Doradus star forming region that there is an excess of stars with $M_{\mathrm{ZAMS}} > 30$ $M_\odot$ (Schneider et al., 2018).

Nevertheless, interaction between binary stars allows for mass transfer from one to

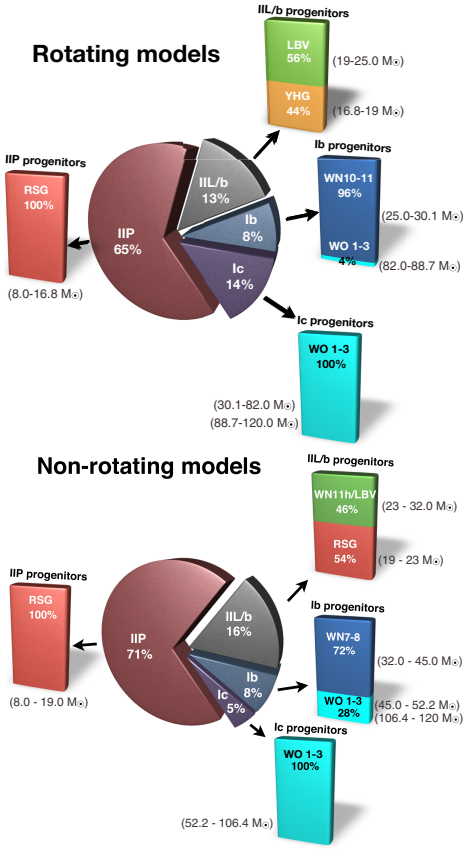

Figure 1.7: SN type as a function of initial mass at solar metallicity for rotating and non-rotating single star models from Groh et al. (2013). SNe Ic occur in stars > 30 $M_{\odot}$.

the other or for mass to be lost from the system during a common envelope phase (Nomoto et al., 1994). This process provides another pathway for a star to be stripped of its outer layers and explode as a type Ibc SN. SNe Ib and IIb were investigated in a grid of binary models with initial mass between 10 –18 $M_{\odot}$ by Yoon et al. (2017), for solar and LMC metallicity. They find that SNe Ib and IIb can be replicated for a variety of orbital periods, see Figure 1.8, and that the final masses of these stars were between 3 and 8 $M_{\odot}$, which is in line with those derived from modelling of the SNe (e.g., Lyman et al., 2016; Taddia et al., 2016). However, they were unable to strip the stars sufficiently of He to produce SNe Ic.

The Binary Population and Spectral Synthesis code (see Eldridge et al., 2008, 2017) has shown that binary interaction plays an important role during the evolution of the progenitors of SE-SNe. Eldridge et al. (2013) provided limiting magnitudes to the progenitors of 12 SE-SNe by examining archival HST and deep ground-based imaging.

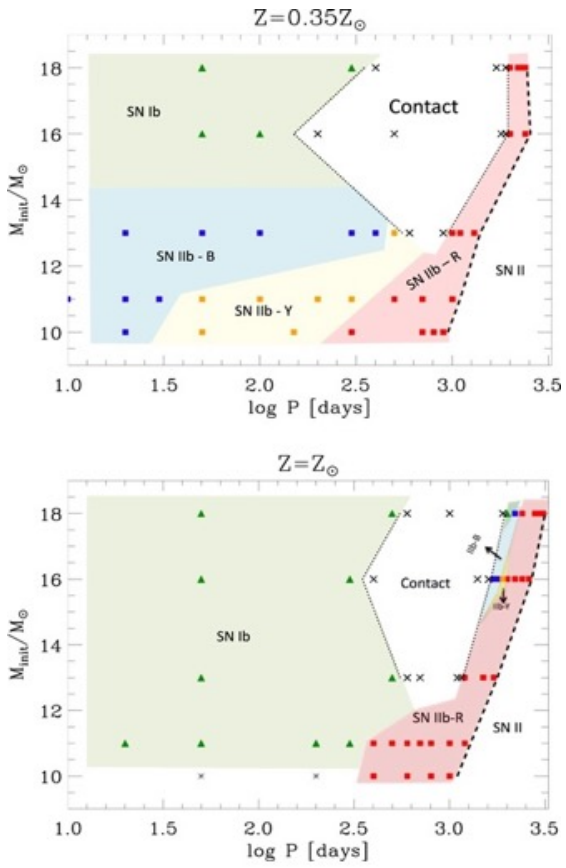

Figure 1.8: From Yoon et al. (2017) from stars in binary systems as a function of initial mass and metallicity of the primary.

Their results suggest that the progenitors stars are not missed by chance, rather they indicate that they are mostly stars of mass < 25 M$_\odot$.

1.5.4 Observational evidence for binary companions

Observational evidence for a significant binary fraction can be found through different analytical routes. The most obvious method is to check the explosion site after the SN has faded. This had led to the discovery of companion stars for three SNe IIb; SNe 1993J, 2011dh, and 2001ig (Maund et al., 2004; Folatelli et al., 2014; Fox et al., 2014; Maund et al., 2015; Ryder et al., 2018), although the extent to which the primary and secondary interact is unknown.

Crockett et al. (2007) performed analysis on HST images of the explosion site of the broad lined SN 2002ap and limited the mass of a potential companion to < 20 M$_\odot$.

Zapartas et al. (2017) used a mix of population synthesis simulations and observations to place an upper limit on a main sequence companion of $8 - 10$ M$_\odot$. They in turn use this to limit the progenitor mass of SN 2002ap to < 23 M$_\odot$, which is consistent with that found by Mazzali et al. (2002). The explosion site of SN 1994I was examined by Van Dyk et al. (2016) using the HST, this allowed them to place upper limits on a companion of ~ 10 M$_\odot$.

By examining explosion sites Kuncarayakti et al. (2017) favour the evolutionary pathway that allows SE-SNe to arise from single and binary stars, but not single stars alone. Graur et al. (2017a) suggest that the relative numbers of SE-SNe to SNe II in different galaxies is a result of a binary, rather than single star, progenitor pathway.

Smith et al. (2018) identified a group of WN3/O3 stars that are isolated and likely the result of mass stripping from binaries, with $M_{\rm ZAMS}$ 10-18 M$_\odot$ and speculated that these are likely progenitors of SNe Ib and Ibn.

The theoretical prediction is that SNe II can occur in stars of solar metallicity and masses < 25 M$_\odot$ (Groh et al., 2013), or ~ 19 M$_\odot$ for SNe IIP (Georgy, 2012), although observational evidence suggests these SNe arise from stars with $M_{\rm ZAMS}$ 12 – 16 M$_\odot$ (Valenti et al., 2016). However, this could be due to an underestimate of the dust in the local environment of the progenitor star, leading to redder colours and an underestimate of the age (Beasor and Davies, 2016).

Eldridge et al. (2013) note that the H-free phase of a star with < 20 M$_\odot$, stripped by binary interaction, is likely $< 10^4$ years, so the stars in the pre-explosion He-star phase are rare and this explains why they are not seen in the Galaxy.

The Cassiopeia A SN remnant (SNR) is the only known remnant of a SE-SNe, in this case a SN IIb that exploded ~ 1680. It provides the best and closest opportunity to examine the local environment of a type Ibc SN. The properties of the remnant are consistent with a 10 – 25 M$_\odot$ progenitor and asymmetries in the remnant distribution may be the result of a common-envelope phase (Krause et al., 2008). However, work by Kochanek (2018) shows that there are no high mass stars in the local vicinity, and that if there was a companion present when the SN exploded it had $M < M_\odot$. Kochanek

(2018) suggest that the system may have been disrupted before the explosion, leading to a runaway star.

1.6 Host galaxies, metallicity, and stellar populations

Observations of the explosion site years after the SN light had faded away allows one to measure the metallicity of the explosion location, look for binary companions, estimate the star formation rate, and estimate the age of the local stellar population.

There have been numerous studies published in the last decade investigating the metallicity of these regions. By linking host metallicity to host mass it is assumed that metallicity is the dominant factor in SE-SN subtypes through metallicity-dependent mass loss. If single massive single stars are the primary progenitor of SNe Ibc then it should be expected that they are found primarily in high metallicity environments.

Modjaz et al. (2008) compared the explosions sites of GRB-SNe and SNe Ic and found that the latter occurred in more metal rich regions. The host galaxies of CC-SNe found by the Palomar Transient Factory (PTF) were investigated by Arcavi et al. (2010). They found that SNe IIb, Ib, and Ic-BL preferentially occur in dwarf galaxies, hence low metallicities, while SNe Ic dominate in high mass galaxies. Graur et al. (2017b) found SNe Ic and Ib were under-represented in low mass galaxies, but that SNe IIb were well represented in both low and high mass galaxies, their findings for SNe Ib and IIb thus being in contrast with Arcavi et al. (2010). Sanders et al. (2012) found that the metallicity at the sites of SNe Ib and Ic could not be differentiated statistically, and that Ic-BL SNe were found in lower metallicity environments with apparently younger stellar ages. Anderson et al. (2012) find that SN Ibc are more often associated with H alpha emission compared with SNe IIP, with the interpretation that the progenitors stars had a higher $M_{\rm ZAMS}$ than Type II SNe because these SNe would come from younger stellar populations. Galbany et al. (2016) examined the hosts of nearby ($0.005< z <0.03$) SNe and found that SNe Ic and II occur in more metal rich galaxies than SNe Ib, IIb, and Ic-BL, even accounting for biases in targeted surveys (which tar-

get more massive and therefore more metal-rich galaxies). They use this information to suggest that SNe Ib are the result of binary interaction and that at least some SNe Ic are the result of single star evolution. Kuncarayakti et al. (2017) performed a similar analysis and found that upper limits on the age of stellar populations also favoured some low mass < 25 $M_{\odot}$ progenitors for SE-SNe, although their results suggested that these stars were typically younger and hence more massive than those associated with type II SNe. The work of Graur et al. (2017a) shows that SE-SNe occur in galaxies of higher mass, lower specific star formation rate, and higher metallicity than SNe II. Maund (2018) concludes that the positions of SNe Ic in the host galaxies supports progenitors $M_{\rm ZAMS} > 30$ $M_{\odot}$, but notes that this is in tension with the much lower ejecta masses found through light curve modelling, see Section 1.7. The PMAS/PPak Integral-field Supernova hosts Compilation (PISCO) (Galbany et al., 2018) again found that SNe Ic are found in environments with higher metallicity than other SN types, and with higher star formation rates (SFR). More of these SNe occur in regions with a stellar age between 0-40 Myrs. Contrastingly, the authors found that SNe IIb had a significant contribution from regions where the populations were assumed to be 40 Myrs old or greater, which they noticed was older than the SN IIP populations. SNe Ib were found to reside in stellar populations of assumed age between those of SNe Ic and SNe IIb.

However, using H II regions to determine stellar population age is not necessarily robust as these regions can survive for a few tens of millions of years, which is enough time for several generations of massive stars and for less massive stars to evolve and explode (Crowther, 2013).

The presence of SNe Ic in regions of high metallicity does tend to support the argument that at least some of these SNe arise from single stars. However, this is countered by the presence of Ic-BL and GRB-SNe in low metallicity environments, both of which are highly stripped and yet the latter of which are known to come from high mass stars (Ashall et al., 2017).

1.6.1 Pre-explosion mass loss, CSM interaction and flash spectroscopy

The rate of mass loss in massive stars, in the final years before core-collapse, is not well understood. Svirski and Nakar (2014b) note that X-ray light curve associated with SN 2008D can be explained by emission through a thick wind, and that the density of this wind at larger radii, given through radio observations, suggests that the mass loss rate of the pre-SN star increased by an order of magnitude ~ 10 days before explosion.

Precursor outbursts have been seen at the locations of stars before they explode (Ofek et al., 2014; Margutti et al., 2014a; Fraser et al., 2013; Arcavi et al., 2017; Benetti et al., 2018). Typically, these outbursts are associated with H-rich SNe, and the subsequent explosions show significant interaction between the SN ejecta and the expelled material (SNe IIn). The exception to this is the tentative pre-cursor eruptions seen with non CSM interacting SN Ic PTF11qcj (Corsi et al., 2014). SN interaction with the circumstellar medium is not uncommon; if the SN is deficient in H and shows signs of interaction with He-rich CSM then narrow lines of He (plus other atomic species, chiefly O and Ca) are produced as kinetic energy from the ejecta is processed into radiative energy. These SNe are labelled "Ibn" to denote that they have narrow emission lines (see, for example Matheson et al., 2001). The interaction with He-rich CSM suggests that the progenitor star was undergoing a period of mass loss shortly before explosion.

The SN Ib 2014C was seen to interact with hydrogen in its vicinity $\sim$ a year after explosion (Milisavljevic et al., 2015a; Margutti et al., 2017). This has been interpreted as material ejected due to binary interaction in the preceding $10^3 - 10^4$ years, with a possible mass loss rate of ~ 1 $M_\odot yr^{-1}$ in short periods (Margutti et al., 2017).

There are very rare examples of He-poor SNe interacting with material in their immediate environment, although the physical processes that lead to the interaction and the actual supernova classifications are not well constrained. SN 2010mb (Ben-Ami et al., 2014) was an unusual He-poor SN, highly luminous with a very slowly evolving light curve. Its spectrum showed strong emission from [O I] λ 5577 compared to [O I] $\lambda\lambda$6300, 6363 which required high densities and was interpreted as interaction

between the SN ejecta and material ejected a few years previously. Ben-Ami et al. (2014) estimate $M_{\rm ej} \sim 13$ M$_\odot$ and suggest that this was a pulsational pair-instability SN (PPISN). The classification of the SN as a type Ic is suspect, as the SN spectrum is not immediately obvious in the superimposed interaction + continuum + supernova spectra. As a candidate for a PPISN, it is unlike canonical SNe Ic which are driven by core collapse and the formation of a compact remnant.

Comparatively, SN 2017dio (Kuncarayakti et al., 2017) was a SN Ic with strong H interaction. The absence of He lines in the spectra from either the SN or the CSM led to the interpretation that the SN ejecta was interacting with the wind from the companion star.

Very early detection of a SN (< 1 day) may allow observation of narrow emission lines resulting from the photo-ionization and recombination of the CSM. This was first noticed for the type IIb SN 2013cu (Gal-Yam et al., 2014), which showed strong but short-lived emission signatures of H, He I, He II, C IV, and N IV in its optical spectra, some 15.5 hours after explosion. From this, Gal-Yam et al. (2014) were able to observe the composition of the CSM around the SN and infer that it showed Wolf-Rayet-like wind signatures, suggesting that the progenitor of the SN was a WN(h) star, a Wolf-Rayet star which shows narrow traces of hydrogen.

1.7 Bulk studies

In recent years the amount of data available on SE-SNe has increased significantly, and with this the studies typically involve larger data sets. Key to this are the release of multi-colour photometry for 25 SE-SNe (Drout et al., 2011), nearly 100 CfA spectra of SE-SNe (Modjaz et al., 2014), the corresponding multi-colour photometry (Bianco et al., 2014), and 20 Sloan Digital Sky Survey Supernovae (Taddia et al., 2015). In total this changed the number of photometrically well-sampled SE-SNe from the 30s to the 80s, and those with both spectra and pre-peak photometry from less than 10 to approximately 20.

Prior to 2014 the largest studies on SE-SNe had been conducted primarily focused on either spectra (Filippenko, 1997; Matheson et al., 2001), or photometry (Clocchiatti and Wheeler, 1997; Drout et al., 2011). The work by Filippenko (1997) and Matheson et al. (2001) characterised the spectra of SE-SNe and became the standard for classification and observable properties. Clocchiatti and Wheeler (1997) investigated the late time decay slope of the bolometric light curves of SE-SNe. This was updated by Wheeler et al. (2015) who demonstrated that SE-SNe show more heterogeneity in their late-time light curves than they do around peak. Drout et al. (2011) took 25 SNe Ibc/II and used multi-band light curves, as well as taking R-band data as a proxy for the bolometric emission, to estimate the characteristics of the SNe.

However, the largest analysis at this time was the analysis of the bolometric light curves of 61 SE-SNe (Cano, 2013), although the sample in this study was weighted towards GRB-SNe (20 out of 61). Their results suggest that for SE-SN subtypes of Ib, Ic, Ic-BL and GRB/XRF SNe, the latter are more massive at $<M_{\rm ej}> \sim 6$ M$_{\odot}$, while the other SNe have a median $M_{\rm ej} \sim 3.5 - 4$ M$_{\odot}$.

Pritchard et al. (2014) used Swift data to analyse the UV emission of 13 SE-SNe (3 GRB/XRF-SNe, 6 Ib, and 4 IIb). They find that SE-SNe are UV-faint, with the exception of SNe that have a shock-cooling tail (some SNe IIb) or a GRB-afterglow.

Lyman et al. (2016) used the bolometric light curves of 38 stripped-envelope supernovae to derive physical parameters (peak luminosity, rise and decay rates) of these objects. They find that SNe Ib and Ic have similar parameters, and infer from that that they have similar progenitors. They also note that SNe IIb are largely homogeneous in their physical characteristics. They use the analytical light curve models of Arnett (1982) to estimate ejecta masses for the objects in their sample and find that the SNe are all similar in ejecta mass, but that those SNe that are associated with GRBs, or show broad-lines, are more energetic and synthesise more ^{56}Ni.

The effectiveness of deriving statistics from the number of objects available is affected by the need to subdivide the total number of SNe into their smaller sub-populations. For example, the work of Pritchard et al. (2014) contained only SNe Ic associated with

GRBs.

Taddia et al. (2015) used data from the Sloan Digital Sky Survey SN survey II (SDSS-II) to build a set of 20 SN Ib/c bolometric light curves and their corresponding properties. Likewise Taddia et al. (2018b) analysed 34 SE-SN light curves of the Carnegie Supernova Project. They suggest a correlation between the late time linear decay (in magnitude units) and the post peak decay rate. The derived ejecta masses of $1.1 - 6.2$ $M_{\odot}$ for the SNe in their sample.

1.8 Thesis outline

In the subsequent chapters I will detail my investigation of stripped-envelope supernovae. This definition excludes SLSNe and interacting SNe; the latter because the interaction power the light curves and prevents properties of the SN being extracted.

I start by analysing of the largest sample of bolometric light curves to date (Chapter 2); this chapter was published as Prentice et al. (2016). In Chapter 3 I examine the spectra of SNe from this database, plus my own observations, and categorise the spectra according to H/He line strength and line broadness. I then use this to show how intrinsic physical characteristics are connected to these properties. This chapter was published in Prentice and Mazzali (2017). In Chapter 4 I present the observations I have undertaken from 2015 – 2018, plus the PESSTO SNe observed during this time, and any further SNe whose data I have been given to analyse, and compare this with properties of SNe updated from the original bolometric light curve database. Finally, a general conclusion and suggestions for future work will be presented in Chapter 5.

Chapter 2

Bolometric light curves

The bolometric light curve of a SN, in a basic sense, is a measure of energy transfer from the interior to the exterior of the ejecta. During the photospheric phase the energy source is assumed to be located deep within the ejecta and must pass through the material above it. Thus, the bolometric light curve of is a function of ejecta mass $M_{\rm ej}$, ^{56}Ni mass $M_{\rm Ni}$, ^{56}Ni distribution, opacity κ, ejecta velocity, and the degree of asphericity.

This chapter, published in Prentice et al. (2016), investigates the bulk properties of the bolometric light curves of SE-SNe during the photospheric phase. Some consideration is also given over the the multi-band colour evolution of the SNe during this phase.

2.1 Database

I compiled a list of data for SE-SNe which are publicly available in the literature. Over 100 were found, typically covering a period of $\sim$ 20 years. In most cases, the data were found in studies involving single objects. However, larger datasets have recently been published. Bianco et al. (2014) presented 64 SNe Ib/c observed by the Harvard-Smithsonian Center for Astrophysics (CfA) SN group in the period 2001 to 2009. 20 SNe Ib/c from the SDSS-II were analysed by Taddia et al. (2015) using data from Sako et al. (2014). Consequently, the number of SNe available more than doubled in less

than a year. In addition to this, I gained access to the Palomar Transient Factory (PTF)[1] (Law et al., 2009) and the intermediate Palomar Transient Factory (iPTF) archives, increasing the number of SNe available. Thus, the total number of SNe in the initial database is as follows:

- Public — single object — ~ 50
- Public — CfA — 64
- Public — SDSS II — 20
- Public — *Swift* — 15
- iPTF/PTF — 128.

2.1.1 Selection criteria

With a large database of SNe, the next step was to consider what was required from the dataset. To build a consistent group of bolometric LCs it was necessary that, as best as possible, the photometry from SN to SN was well sampled over the same rest-frame wavelength range. Ideally, the sample should have shown good coverage in the wavelength range corresponding to the bulk of the SN light (i.e., between the V and R bands), which also corresponds to the turnover in the spectral energy distribution (SED) around bolometric peak. It should also have sufficient coverage in adjacent bands in order to build SEDs across a uniform wavelength range and, as I wanted to derive time-dependent parameters from the SN peak, it was essential that the coverage included this epoch. This led to the following two criteria for inclusion in our sample:

- The peak of the SN must be observed in the B, V, and R bands or equivalents.
- The temporal coverage must have been sufficient that the rise and/or decay time from half-maximum luminosity to maximum luminosity could be derived or the explosion date well constrained.

[1] www.ptf.caltech.edu

These restrictions immediately ruled out more than 70% of the literature SNe, with the majority lacking observations at peak or sufficient coverage in multiple filters. This affected the CfA and *Swift* set considerably. Only half of the CfA sample showed a clear photometric peak, and for SNe observed solely by *Swift* the lack of observations redward of the UVOT V band means that the peak of the SED, and hence the bulk of the light, was missed in every case. Of the PTF/iPTF SNe, most had to be rejected because they were observed only in the r band.

Table 2.1 lists the 85 SNe that fulfilled the criteria. The sample consists of 25 SNe Ib, 21 SNe Ic, 12 SNe Ic-BL, 10 GRB-SNe, 15 SNe IIb, and 2 SNe Ibc. (The SNe Ibc have an ambiguous classification; the data were not of sufficient quality to distinguish between the Ib and Ic subclasses.) SNe with full optical and near-infrared (NIR) coverage allowed the construction of an effective bolometric light curve as opposed to a pseudo-bolometric optical variant.

Table 2.1: The database of 85 SNe

SN	Type	μ [mag]	z	$E(B-V)_{\rm MW}$ [mag]	$E(B-V)_{\rm host}$ [mag]	references
1993J	IIb	27.8	-0.000113	0.071	0.1	(1)
1994I	Ic	29.6	0.0015	0.03	0.3	(2)
1996cb	IIb	29.95	0.0024	0.12	negligible	(3)
1998bw	GRB-SN	32.76	0.0087	0.052	negligible	(4),(5)
1999dn	Ib	32.93	0.0093	0.052	0.1	(6)
1999ex	Ib	33.44	0.0114	0.02	0.28	(7)
2002ap	Ic-BL	29.5	0.0022	0.071	0.008	(8),(9),(10)
2003bg	IIb	31.68	0.0046	0.02	negligible	(11)
2003dh	GRB-SN	39.21	0.168	0.025	negligible	(12)
2003jd	Ic-BL	34.43	0.019	0.06	0.09	(13)
2004aw	Ic	34.31	0.016	0.021	0.35	(14)
2004fe	Ic	34.28	0.018	0.0210	-	(15)
2004gq	Ib	32.09	0.0065	0.0627	0.095	(15)
2005az	Ic	33.14	0.0085	0.0097	-	(15)
2005bf	Ib	34.62	0.019	0.045	negligible	(16)
2005hg	Ib	34.68	0.021	0.0901	-	(15)
2005hl	Ib	34.92	0.023	0.073	-	(17)
2005hm	Ib	35.85	0.035	0.048	-	(17)
2005kl	Ic	31.64	0.0035	0.0219	-	(15)
2005kr	Ic-BL	38.91	0.134	0.087	-	(17)
2005ks	Ic-BL	38.21	0.099	0.05	-	(17)
2005kz	Ic	35.31	0.027	0.046	-	(15)
2005mf	Ic	35.27	0.027	0.0153	-	(15)
2006T	IIb	32.68	0.0080	0.0647	-	(15)
2006aj	GRB-SN	35.61	0.033	0.097	negligible	(18),(19),(20)
2006el	IIb	34.25	0.017	0.0973	-	(15)
2006ep	Ib	33.93	0.015	0.036	-	(15)
2006fe	Ic	37.41	0.07	0.098	-	(17)
2006fo	Ib	34.58	0.021	0.025	-	(15)
14475[a]	Ic-BL	39.17	0.149	0.072	-	(17)
2006jo	Ib	37.63	0.077	0.032	-	(17)
2006lc	Ib	34.13	0.016	0.057	-	(17)

2006nx	Ic-BL	38.97	0.137	0.108	-	(17)
2007C	Ib	32.15	0.0059	0.0363	0.73	(15)
2007D	Ic-BL	34.84	0.023	0.2881	-	(15)
2007Y	Ib	31.29	0.0046	0.022	0.09	(24)
2007ag	Ib	34.78	0.020	0.025	-	(15)
2007cl	Ic	34.84	0.022	0.02	-	(15)
2007gr	Ic	29.84	0.0017	0.055	0.03	(21)
2007kj	Ib	34.3	0.018	0.0691	-	(15)
2007ms	Ic	36.09	0.039	0.184	-	(17)
2007nc	Ib	37.91	0.087	0.025	-	(17)
2007qv	Ic	38.11	0.095	0.048	-	(17)
2007qx	Ic	37.71	0.08	0.023	-	(17)
2007ru	Ic-BL	34.04	0.016	0.27	negligible	(22)
2007sj	Ic	36.09	0.039	0.032	-	(17)
2007uy	Ib	32.48	0.0065	0.022	0.63	(23)
2008D	Ib	32.48	0.0065	0.02	0.63	(27),(15),(28)
2008ax	IIb	29.82	0.0019	0.022	0.278	(25),(26)
2008bo	IIb	32.06	0.005	0.0513	0.0325	(15)
2008hw	GRB-SN	42.35	0.53	0.42	negligible	(15)
2009bb	Ic	33	0.00988	0.098	0.482	(29)
2009er	Ib	35.9	0.035	0.0389	-	(15)
2009iz	Ib	33.8	0.014	0.0729	-	(15)
2009jf	Ib	32.64	0.0079	0.112	0.05	(30)
2010as	IIb	32.17	0.0073	0.15	0.42	(31)
2010bh	GRB-SN	36.94	0.059	0.12	0.14	(32)
2010ma	GRB-SN	42.40	0.552	0.019	0.04	(32)
2011bm	Ic	34.95	0.022	0.032	0.032	(33)
2011dh	IIb	29.48	0.0020	0.035	0.05	(34)
2011ei	IIb	33.09	0.0093	0.059	0.18	(35)
2011fu	IIb	34.36	0.019	0.068	0.015	(36)
2011hs	IIb	31.91	0.0057	0.011	0.16	(37)
2011kl	GRB-SN	43.09	0.677	0.019	0.038	(38)
2012ap	Ic-BL	33.45	0.012	0.045	0.4	(39)
2012bz	GRB-SN	40.31	0.28	0.037	negligible	(40)
2013cq	GRB-SN	41.19	0.34	0.02	0.05	(41)
2013cu	IIb	35.23	0.026	0.011	negligible	(42)
2013df	IIb	31.65	0.0024	0.017	0.08	(43)
2013dx	GRB-SN	39.04	0.145	0.04	0.10	(44)
2013ge	Ibc	31.87	0.0044	0.02	0.047	(45)
PTF09dh/2009dr	Ic-BL	37.60	0.076	0.022	-	-
PTF10gvb	Ic-BL	38.26	0.098	0.022	-	-
PTF10inj	Ib	37.31	0.066	0.01	-	-
PTF10qif	Ib	37.26	0.064	0.0587	-	-
PTF10vgv	Ic	34.01	0.015	0.145	-	(49)
PTF11bli	Ibc	35.81	0.034	0.013	-	-
PTF11jgj	Ic	36.15	0.04	0.027	-	-
PTF11klg	Ic	35.26	0.027	0.03	-	-
PTF11qiq	Ib	35.66	0.032	0.066	-	-
PTF11rka	Ic	37.61	0.074	0.03	-	-
PTF12gzk	Ic	33.8	0.014	0.14	negligible	(48)
PTF12os	IIb	31.89	0.0045	0.045	-	(50)
iPTF13bvn	Ib	31.89	0.0045	0.0278	0.0437	(46),(47)
iPTF14dby	Ic-BL	37.54	0.074	0.048	-	(51)

References: (1) Richmond et al. (1994), (2) Richmond et al. (1996), (3) Qiu et al. (1999), (4) Clocchiatti et al. (2011), (5) Patat et al. (2001), (6) Benetti et al. (2011), (7) Stritzinger et al. (2002), (8) Foley et al. (2003), (9) Gal-Yam et al. (2002), (10) Tomita et al. (2006), (11) Hamuy et al. (2009), (12) Deng et al. (2005), (13) Valenti et al. (2008), (14) Taubenberger et al. (2006), (15) Bianco et al. (2014), (16) Anupama et al. (2005), (17) Taddia et al. (2015), (18) Pian et al. (2006),(19) Mirabal et al. (2006), (20) Kocevski et al. (2007), (21) Hunter et al. (2009), (22) Sahu et al. (2009), (23) Roy et al. (2013), (24) Stritzinger et al. (2009), (25) Pastorello et al. (2008), (26) Taubenberger et al. (2011), (27) Mazzali et al. (2008), (28) Modjaz et al. (2009), (29) Pignata et al. (2011), (30) Valenti et al. (2011), (31) Folatelli et al. (2014), (32) Bufano et al. (2012), (33) Valenti et al. (2012), (34) Marion et al. (2014), (35) Milisavljevic et al. (2013a), (36) Kumar et al. (2013), (37) Bufano et al. (2014), (38) Greiner et al. (2015), (39) Milisavljevic et al. (2015b), (40) Melandri et al. (2012), (41) Melandri et al. (2014), (42) Gal-Yam et al. (2014), (43) Morales-Garoffolo et al. (2014b), (44) D'Elia et al. (2015), (45) Drout et al. (2015), (46) Fremling et al. (2014), (47) Srivastav et al. (2014), (48) Ben-Ami et al. (2012), (49) Corsi et al. (2012), (50) Fremling et al. (2016), (51) Corsi et al. (2016)

[a] SN 14475 was discovered in 2006 as part of the SDSS-II SN survey.

2.2 Constructing the bolometric light curve

2.2.1 Missing data

In order to derive the bolometric luminosity of a SN at a particular date, an SED constructed from the photometry is required. Thus, it was essential that there was photometry in the relevant bands at that time, which was not always the case. In order to attain temporal uniformity, the worst-sampled band was chosen to be a reference point and the remaining bands were fit with a linear spline. The magnitudes were interpolated on the dates of the reference band. Early-time data points are especially important as they help determine the rise time of the SN and constrain t_0, the time of explosion. However, these epochs also tended to be sparsely sampled, often with observations in just a couple of bands.

To obtain estimates of the early-time bolometric data points, two methods were used to extrapolate missing photometry provided that at least two bands were available and one of them was a V-band equivalent (e.g., an effective wavelength around 4000–5000 Å). If the temporal gap between the first date in two adjacent bands was no greater than a few days, then either a constant colour was assumed or the mean colour evolution of similar SN types was adopted. If it was not possible to use this method, but there were sufficient pre-peak data, then extrapolations were done via a low-order polynomial fit to the data. As per the previous method, this technique was limited to time periods on the order of a few days. Care was taken to avoid extrapolating early-time data points based upon the behaviour of the light curves near peak, as this would have underestimated the rate of change. Given the uncertain nature of the shape of the light curve outside the observed dates, large errors of ~ 1 mag on the extrapolations were assumed.

2.2.2 GRB-SNe and afterglow subtraction

The desire to include as many GRB-SNe as possible in the database is compromised by the difficulty in deconvolving the SN light from that of the GRB afterglow and host galaxy. For some SNe (e.g., SN 1998bw), the afterglow is negligible, so optical emission is dominated by SN photons; however, this is not usually the case. To calculate the afterglow component of the light curve, the spectrum is considered to follow a simple relation given by $F_\nu(t,\nu) \propto t^{-\alpha}\nu^{-\beta}$. I defer to the literature for the numerical values of the temporal and spectral indices and subtract the afterglow flux from the SEDs as required, these values are unique to each GRB. Additionally, it is common in the literature to fit the afterglow-SN-host light curve with a template SN based on SN 1998bw (Cano, 2013), but this method is not adopted here to avoid biasing any temporal characteristics that may be extracted from the light curve.

There are approximately 20 GRB-SNe given in the literature. Most are photometrically associated with the GRB (e.g., they show a late-time bump in the light curve), but unfortunately the majority of these are poorly observed, with few data points in only a few bands and showing large afterglow contamination. Consequently, the number of usable GRB-SNe is greatly restricted. It is an unfortunate irony that GRB-SNe in general have the best-known explosion date yet the most poorly constrained photometry.

SN 2003dh / GRB 030329

To form as complete a sample as possible, the light curve of SN 2003dh from Deng et al. (2005) is included in the database. The ultraviolet-optical-infrared (UVOIR) light curve is the result of synthetic photometry from spectra and a mean bolometric correction, derived from SN 1998bw, added to the photometric data. A consequence of this is that I do not desconstruct the light curve to obtain a *BVRI* variant and use the data as is.

Table 2.2: Redshift statistics of sample SNe by spectral type

Type	Median z	Mean z	Range	N
GRB-SNe	0.224	0.279	0.0087–0.677	10
Ic-BL	0.075	0.069	0.0022–0.149	12
Ic	0.022	0.031	0.0015–0.095	21
Ibc	0.019	0.019	0.0044–0.034	2
Ib	0.018	0.025	0.0045–0.087	25
IIb	0.0050	0.0076	< 0.0258	15

2.2.3 Distance

A primary goal of this study was to present a self-consistent set of bolometric light curves. In order to achieve this, it was necessary (where possible) to obtain a distance modulus for each SN adopting a standard cosmological model. Thus, the distance modulus of each SN was taken from the NASA/IPAC Extragalactic Database (NED)[2] for the host galaxy using the standard NED cosmological model (H_0 = 73.0 km s^{-1} Mpc^{-1}, Ω_m = 0.27, Ω_Λ = 0.73) and corrected for Galactic motion toward Virgo, the Great Attractor, and the Shapley Supercluster. These distances are entirely redshift-dependent and calculated from a cosmological model rather than measured, thus μ is taken as an absolute value throughout, this also aids easy conversion of individual SN peak luminosity values to different distances.

Figure 2.1 shows the redshift distribution of SNe within the database. 88% lie at $z < 0.1$, with the median being $z = 0.0189$. Statistics for the redshift distribution by spectral type are given in Table 2.2

2.2.4 Extinction

Correcting for $E\left(B-V\right)_{\rm tot}$ is important if one is to derive accurate values based upon luminosity. There are two main sources of line-of-sight attenuation; one associated with the Milky Way – $E\left(B-V\right)_{\rm MW}$ – and one associated with the host galaxy $E\left(B-V\right)_{\rm host}$.

[2]https://ned.ipac.caltech.edu/

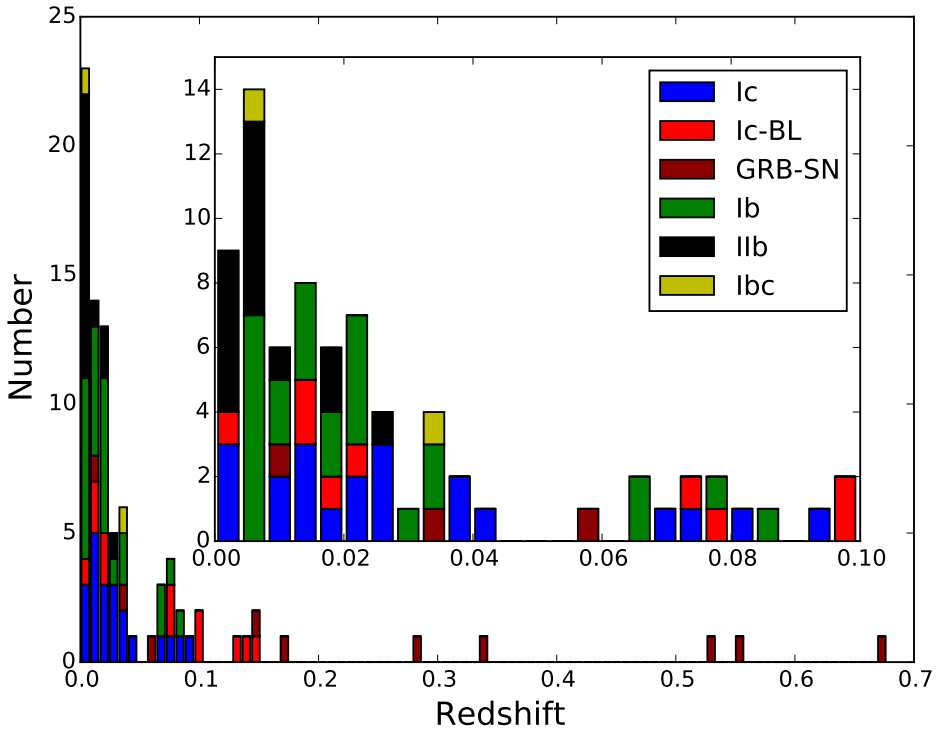

Figure 2.1: Redshift distribution of the SNe in the sample. The vast majority of SNe are found at $z < 0.1$, as demonstrated in the inset. It is clear that the high-z regime is dominated by GRB-SNe.

The values of $E\left(B-V\right)_{\rm MW}$ adopted here were either taken from the literature or from the dust maps of Schlafly and Finkbeiner (2011). Literature values of $E\left(B-V\right)_{\rm host}$ were only used if calculated from spectra, such as using the relationship between the equivalent width of Na I D absorption lines and $E\left(B-V\right)_{\rm host}$ (Poznanski et al., 2012). However, it was apparent that approximately half the SNe in my database do not have spectroscopically derived $E\left(B-V\right)_{\rm host}$.

A comparison of the mean $E\left(B-V\right)_{\rm MW}$ and $E\left(B-V\right)_{\rm host}$ of the SNe in this sample gives $\langle E(B-V)_{\rm MW}\rangle$ = 0.059 mag and $\langle E(B-V)_{\rm host}\rangle$ = 0.135 mag. Thus, on average the intrinsic attenuation is the greater of the two and failure to include the effect of host reddening results in less-luminous bolometric LCs for those SNe. By taking the host-galaxy reddening to be zero for some SNe, which is the lowest value possible, and then attempting to include them in population statistics I am actively biasing the distributions.

Table 2.3: $E\,(B-V)_{\rm host}$ statistics of different sub-populations.

SN Population	N	Median [mag]	Mean [mag]
IIP, IIL, II, IIb, IIn	25	$0.081\ ^{+0.130}_{-0.026}$	0.130
Ib	22	$0.2235\ ^{+0.305}_{-0.157}$	0.30
Ic, Ic-BL	27	$0.174\ ^{+0.187}_{-0.116}$	0.244
GRB-SN	22	$0.0325\ ^{+0.006}_{-0.024}$	0.040

As I want to maximise the number of SNe in the distributions, but do not want to include bolometric light curves calculated with zero host-extinction, I make the following assumption – SNe of a similar type have, on average, similar values for $E\,(B-V)_{\rm host}$. Thus, I searched the literature for core-collapse SNe, including all SNe II, and built a set of host-galaxy extinction functions by type. The host galaxies of observed GRB-SNe are known to be different from those of other core-collapse SNe in terms of metallicity (e.g., Modjaz et al., 2008; Graham and Fruchter, 2013) — so if the extinction is dependent on host, host inclination, and SN type, then the distributions should reflect this. A description of this work is presented in Appendix A, with the results given in Table 2.3.

For SNe without a literature value for $E\,(B-V)_{\rm host}$ I construct two bolometric light curves; one with no correction for intrinsic reddening and one which corrects for the median $E\,(B-V)_{\rm host}$ of that SN type. They are then used in the following way:

- The uncorrected bolometric light curve is used whenever the LC is plotted individually, or the properties of that individual SN are given in a table. This is the LC constructed with the fewest assumptions but any properties related to the luminosity should be considered a lower limit.

- I use the median $E\,(B-V)_{\rm host}$ corrected bolometric LC in distributions. This works on the basis that the extinction would be typically around this value and the number of SNe overcorrected would balance the number of SNe undercorrected. This increases the spread of the distribution but provides a better estimate of the median and mean than using lower limits.

All reddening corrections were applied using the extinction law given by Cardelli et al. (1989).

2.2.5 Constructing the SED

To construct the SED the photometry was corrected for Galactic extinction in the observer frame and, if possible, corrected for host extinction in the rest frame. Uncertainties in reddening were included in quadrature. When the monochromatic flux, calculated from the photometry (see Bessell et al. 1998; Fukugita et al. 1995), was shifted to the rest frame wavelength it was also multiplied by (1+z), which is a useful approximation in the absence of spectroscopically derived K-corrections. The process of flux conversion depends upon the filter system used. Data in the literature cover more than twenty years of observations and over this period there has been a shift in the usage of filters from Johnson-Cousins (J-C) *UBVRIJHK* (and minor variations) to SDSS type filters ($u'g'r'i'z'$) or some combination of these, as well as space telescope specific filters such as those on the *Swift*-UVOT. The two main standards use different flux units with the J-C system being based on Vega and SDSS on AB. As default all SEDs are constructed in units of erg s^{-1} cm^{-2} Å^{-1}. This required conversion of the SDSS filters which was achieved by using the relation $\lambda f_\lambda = \nu f_\nu$.

The rest frame flux was fit with a linear spline to create SEDs over the range 3000 Å to 10000 Å for *UBVRI*-equivalents, 4000 Å to 10000 Å for *BVRI*-equivalents, and 10000 Å to 24000 Å for NIR.

2.2.6 From SED to pseudo-bolometric luminosity

The rest-frame SEDs were then integrated over the wavelength range, assuming zero flux outside the limits. The effect due to redshift and the subsequent blueshifting of the effective wavelengths of the photometry is small (a few percent) out to $z \approx 0.1$. Beyond this, the bluest bands start to be shifted outside the integration range and the reddest effective wavelength shifts to a more central position; in this regime, the largest

uncertainty comes from the behaviour of the tail of the SED. If there is photometry in bands with effective wavelengths longer than I/i', I incorporate these into the optical SEDs, as they are blueshifted into the optical wavelength range or close to it.

I note that one might be tempted to fit a blackbody emission curve to the SEDs, but this is erroneous as the spectrum of a SN is not a blackbody. During the photospheric phase, the UV suffers line blanketing, the severity of which is related to the amount of iron-group elements (Mazzali, 2000) and the velocity of the ejecta, which causes line broadening. The photons scattered in this process eventually escape at redder wavelengths creating a flux excess at these points (e.g., Mazzali and Lucy 1993). In the nebular phase (> 60 days), the spectrum is dominated by line emission as the optically thin ejecta are excited via energy deposition from the γ-rays and positrons emitted during the decay of ^{56}Ni to ^{56}Fe (Mazzali et al., 2005).

The uncertainties were carried through the integration by evaluating the integral at the upper and lower errors of the flux. Once the bolometric flux was determined it was converted to bolometric luminosity using the distance.

2.3 Pseudo-bolometric light curves

In order to compare bolometric light curves effectively, a set of *BVRI*, *UBVRI*, and NIR (or equivalent) LCs were produced, where the data allowed. Table 2.4 lists the bands, total wavelength range, and reference name for the different light curves. Within the sample, 84 SNe have a *BVRI* LC, 44 have a *UBVRI* LC, and 24 have a NIR LC. Various extensions of the LCs can be made by combining the data (e.g., *UBVRI*NIR). In most cases, the NIR is less well sampled than the optical, so to construct an optical-NIR LC the ratio between the two datasets was calculated for coincident dates. This was subsequently fit with a linear spline, and the NIR flux was deduced by interpolation of the ratio and the value of the optical flux on the dates when NIR observations were absent. When the optical LC extended beyond the NIR, the flux ratio was kept constant beyond the boundaries.

Table 2.4: SED integration wavelength range and terminology.

Constituent bands	Wavelength range (Å)	Nomenclature
$BVRI/g'r'i'z'$	4000–10,000	$BVRI$
$UBVRI/u'g'r'i'z'$	3000–10,000	$UBVRI$
JHK	10,000–24,000	NIR

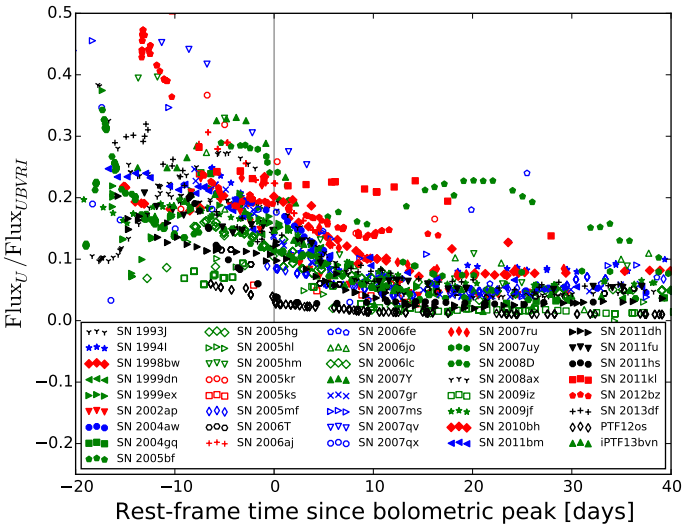

Figure 2.2: The ratio of the U/u'-band flux to the $UBVRI$ flux as a function of time. Open symbols represent SNe that have not had host-galaxy extinction corrections applied. The high host extinction of PTF12os is apparent in this diagram as the U/u' flux is negligible. The temporal evolution of peculiar SN Ib 2005bf is a noteworthy feature

Finally, the temporal evolution of the light curve was corrected to the rest frame and set with a fiducial $t(0)$ at the time of maximum luminosity with the following caveat: any peak caused by early-time shock breakout (e.g., SN IIb 2013df Van Dyk et al., 2014) is ignored, and the later peak powered by radioactive decay is selected. In the case of peculiar SN Ib 2005bf, with its double-peaked light curve (Tominaga et al., 2005), I took the first peak to be the result of the decay of ^{56}Ni and the second peak a different energy-injection process, specifically a magnetar (Maeda et al., 2007). For a different interpretation, see Folatelli et al. (2006).

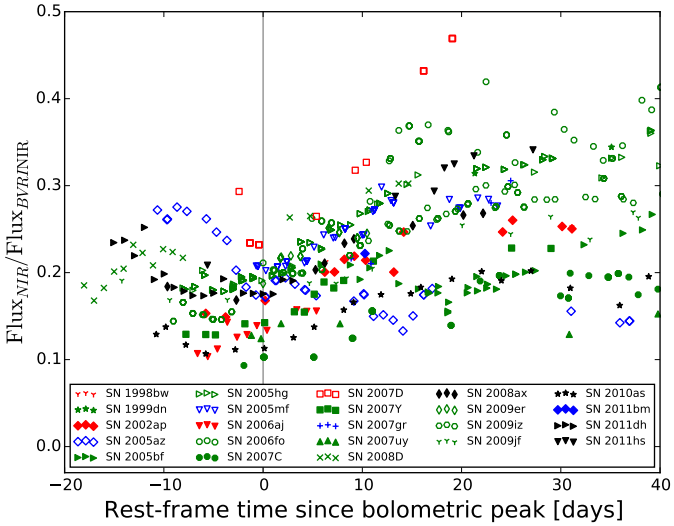

Figure 2.3: The ratio of NIR flux to *BVRI*NIR flux. Only dates when the optical and NIR observations were coincident are included.

2.3.1 The contribution of U to $UBVRI$

Figure 2.2 gives the time-dependent contribution of the U/u'-band flux to the total $UBVRI$ flux. As expected, the SNe are bluer at earlier times than later. Table 2.5 shows the statistics for the sample at bolometric peak by spectral type and with/without host-extinction corrections applied. Note that the statistics are derived from two overlapping populations and there is a bias in the non-host-corrected SN Ic values caused by a few SNe with poorly constrained u' photometry. The SNe Ic-BL are demonstrably bluer at this epoch than other SN types with a U flux contribution of $\sim 20\%$ as opposed to $\sim 16\%$ for the other types (host-extinction correction included). However, note the small sample size in some cases.

2.3.2 NIR contribution

Figures 2.3 and 2.4 show the contribution of the NIR to the *BVRI*NIR and *UBVRI*NIR light curves, respectively. The median, mean, and standard-deviation statistics are given in Table 2.5. There are insufficient numbers to split the sample into subtypes, so I perform the analysis on all available SNe, regardless of whether there is a host-galaxy

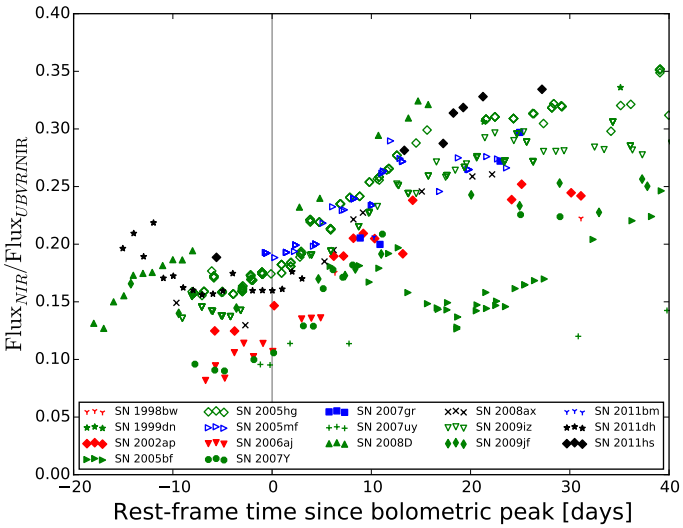

Figure 2.4: The ratio of NIR flux to *UBVRI*NIR flux. Only dates when the optical and NIR observations were coincident are included.

extinction value. I find that around peak, mean $\approx$ median, with a standard deviation of $\sim 4\%$ in both cases. It is possible that there is a bias in the sample given that the total number in each case is 18 and 12, which represents 21% and 14% of the total database, respectively. To test the probability of the statistical values being returned by chance, I run a Monte-Carlo simulation in which I randomly place 85 SNe with a uniform distribution in a NIR/ONIR "box" of varying width. From this box, 18 SNe (12 for NIR/*UBVRI*NIR) are randomly selected and their bulk median/mean ratio and standard deviation measured. I define an acceptable parameter set as $0.9 <$ ratio < 1.1 and standard deviation < 0.4; there is no constraint on the values of median or mean, only their ratio. If the returned values fulfil these criteria then it is considered a hit. I perform 5000 runs for each window and return P(ratio) = hit/runs. The results are sensitive to the allowed variation in the ratio and the standard deviation, both of which I choose to be in excess of the measured values. I find that for NIR/*BVRI*NIR, a window of > 0.16 gives $P < 0.025$, while for NIR/*UBVRI*NIR, a window of > 0.18 gives $P < 0.064$. I conclude that the observed median and mean are not a sampling bias caused by too few SNe; they represent typical values.

The contribution of the NIR is generally small throughout with the exception of SN 2005kl, which was extremely red and has a NIR to optical ratio > 1; consequently, it

Table 2.5: Flux-ratio statistics at bolometric peak.

U-band contribution to *UBVRI* with host extinction			
Type	median	mean	standard deviation
SNe Ic-BL/GRB-SNe	0.20	0.20	0.03
SNe Ic	0.15	0.15	0.02
SNe Ib	0.16	0.20	0.05
SNe IIb	0.16	0.17	0.06
U-band contribution to *UBVRI* without host extinction			
Type	median	mean	standard deviation
SNe Ic-BL/GRB-SNe	0.18	0.19	0.07
SNe Ic	0.16	0.19	0.09
SNe Ib	0.13	0.15	0.07
SNe IIb	0.11	0.14	0.07
NIR contribution to optical/NIR			
Type	median	mean	standard deviation
NIR/*BVRI*NIR	0.17	0.17	0.04
NIR/*UBVRI*NIR	0.14	0.15	0.03

has been omitted from Figure 2.3. Bianco et al. (2014) noted that this SN occurred in an H II region of NGC 4369, a galaxy with a high continuum gradient. They also do not attribute the red colour to high intrinsic extinction. Spectra of the object show that it is dominated by galactic emission and displays a red continuum. Accordingly, the red colour is attributed to host-galaxy extinction. On this basis it has not been included in the process of determining the NIR flux fraction.

2.4 Light-curve statistics

2.4.1 Light curves

The $BVRI$ LCs are shown by spectral type in Figures 2.5 and 2.6. The peak luminosity ranges from 5.6×10^{41} erg s^{-1} to $\sim 2.1 \times 10^{43}$ erg s^{-1}, a factor of ~ 100. Note that this range does not include PTF12os or SN 2005kl, both of which suffer from significant but unquantified host-galaxy extinction. 18 of the SNe available have sufficient photometry to be able to construct *UBVRI*NIR light curves. These SNe represent our "gold" sample and are shown in Figure 2.7. In some cases, the light curves are lower

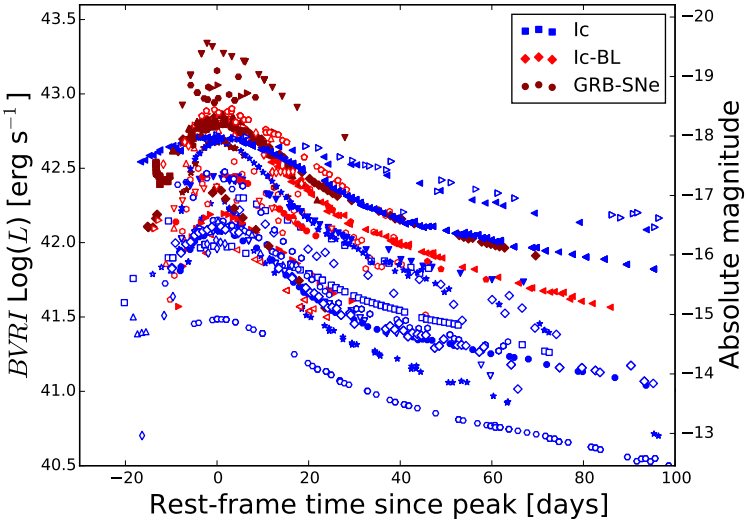

Figure 2.5: *BVRI* light curves of all Type Ic variants in the sample. SNe denoted by open markers have not been corrected for host-galaxy extinction. Markers may differ from the legend to aid the eye.

limits owing to the lack of information on host extinction.

The *BVRI* pseudo-bolometric light curves are shown en-masse in Figure 2.8. The final light curves will be uploaded to WISeREP[3] (Yaron and Gal-Yam, 2012).

2.4.2 Luminosity distributions

The luminosity distribution (see, for example, Li et al., 2011) for the *BVRI* sample, which includes those SNe where the median host-galaxy extinction has been included, is shown in Figure 2.9. Table 2.6 gives the statistics of the distribution; median and mean, while the standard deviation represents the intrinsic scatter within each distribution. The collective SN Ic-BL/GRB-SN group is most luminous, and while this is somewhat driven by the GRB-SNe, it can be seen from Figure 2.5 that SNe Ic-BL are typically more luminous than other SNe Ic. The least-luminous subpopulation is SNe IIb. The standard deviation derived for each subset shows that there is considerable overlap between SNe Ic, SNe Ib, and SNe IIb. Figure 2.10 shows the luminosity function for the 18 SNe with $UBVRI$NIR photometry.

[3]http://wiserep.weizmann.ac.il/

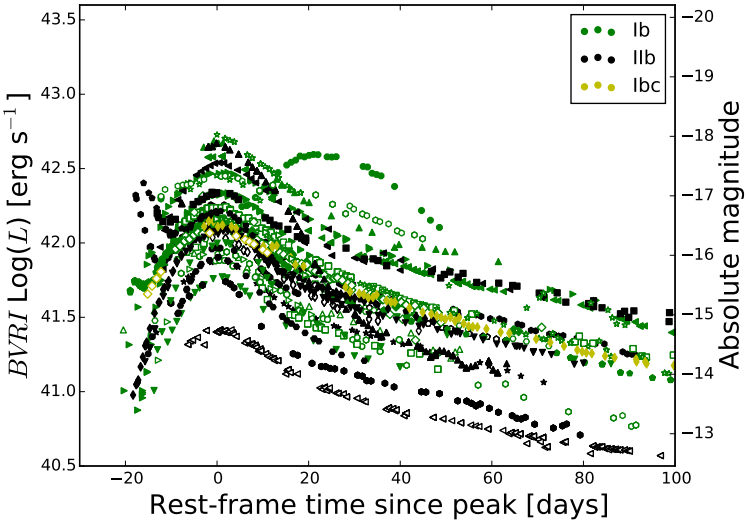

Figure 2.6: *BVRI* light curves of SNe Ib and SNe IIb in the sample. Open symbols represent SNe without a correction for host-galaxy extinction. Markers may differ from the legend to aid the eye.

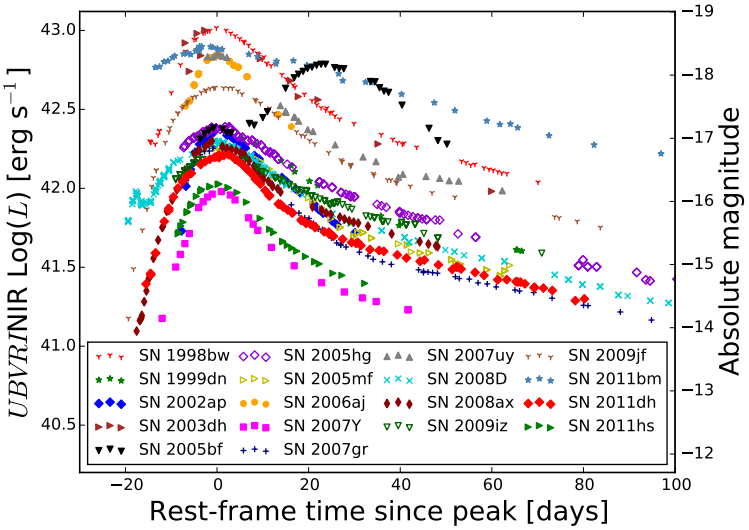

Figure 2.7: 18 *UBVRI*+ NIR pseudo-bolometric light curves constructed from optical and NIR photometry. Open symbols represent SNe without correction for host-galaxy extinction

Table 2.6: The *BVRI* $\log_{10}\left(L_{\rm p}/{\rm erg\ s^{-1}}\right)$ luminosity-function statistics.

Type	Median	Mean	Standard deviation	N
SNe Ic-BL/GRB-SNe	42.81	42.78	0.29	21
SNe Ic	42.29	42.36	0.28	21
SNe Ib	42.33	42.34	0.27	25
SNe IIb	42.19	42.14	0.26	15

SNe Ibc and GRB-SN 2003dh not included

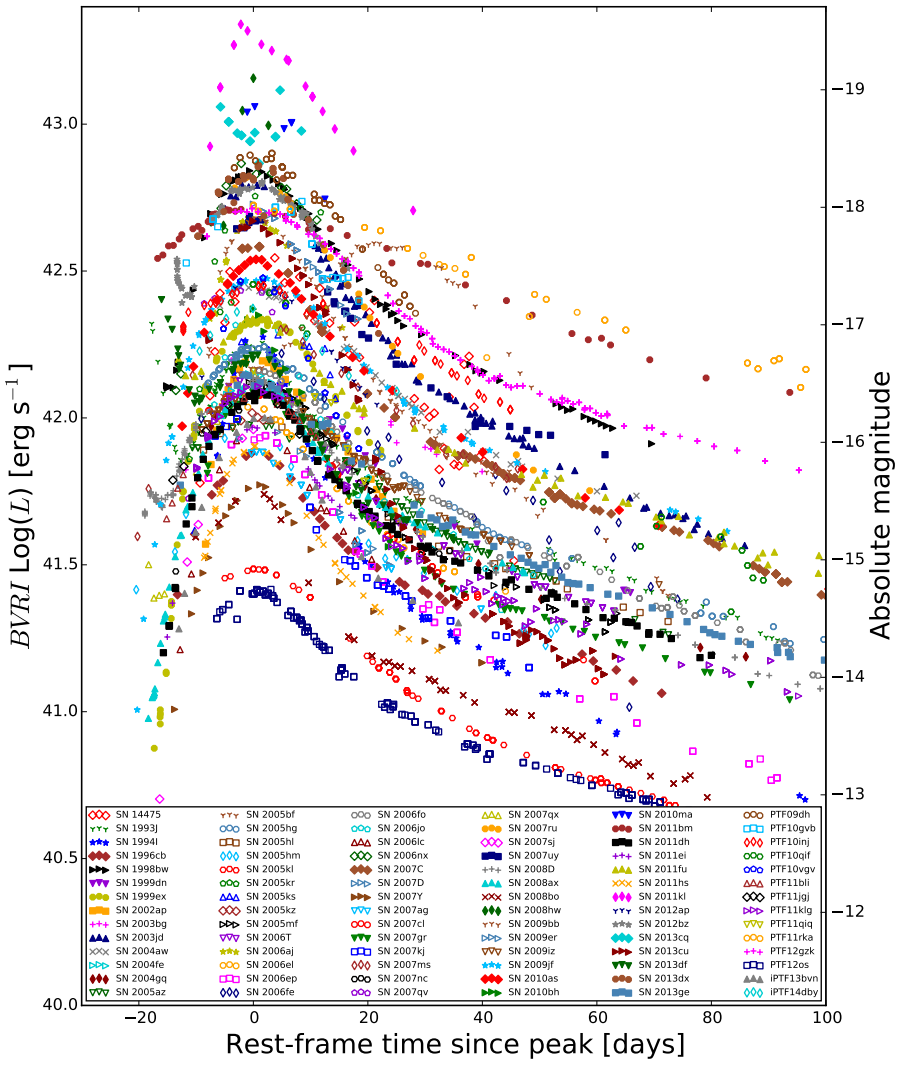

Figure 2.8: 84 *BVRI* light curves of all SN types in the sample. GRB-SN 2003dh is not included because it lacks a *BVRI* light curve. Note that GRB-SN 2013cq is extremely noisy, and its peak luminosity is constrained by a *Hubble Space Telescope* observation (Melandri et al., 2014). Open symbols represent SNe without corrections for host-galaxy reddening.

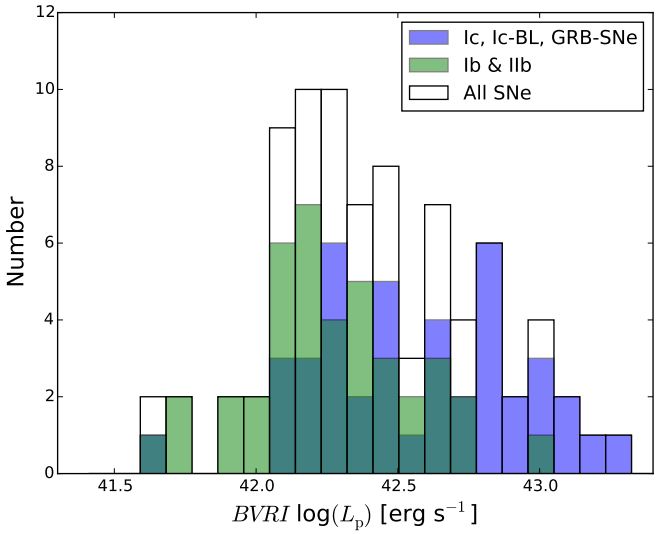

Figure 2.9: The *BVRI* pseudo-bolometric luminosity distribution of 82 SNe. The two SNe of Type Ibc are not included owing to ambiguity in their classification, nor is SN 2003dh owing to the lack of a *BVRI* LC. This distribution includes SNe with a correction for the median host-galaxy extinction of that type applied. The dark-green region represents the overlap of the blue and green distributions. The luminosity distribution for the combined green and blue distributions is shown in white.

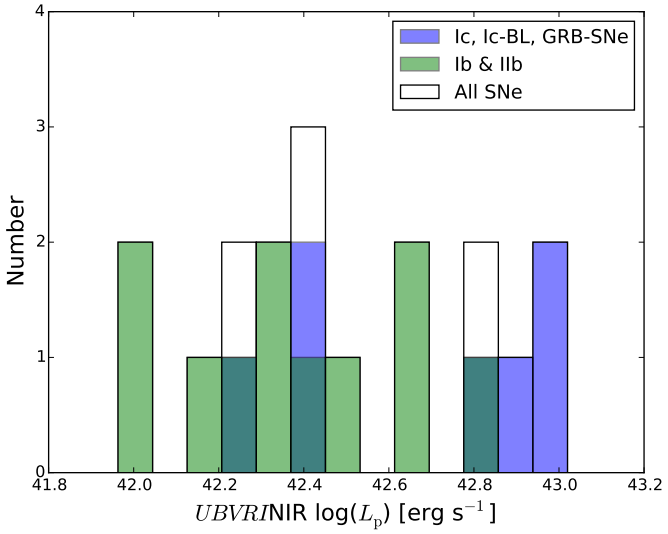

Figure 2.10: The luminosity distribution derived from the peak luminosity of the 18 *UBVRI*NIR light curves in the sample. Median host-galaxy extinction is assumed in three cases for statistical purposes. Colours are as described in Figure 2.9.

2.4.3 Parameter values and statistics

With the bolometric light curves complete, it is now possible to begin determining their properties. The following parameters are of interest:

- Peak luminosity — $L_{\rm p}$
- Rise time from explosion to $L_{\rm p}$ — $t_{\rm p}$
- Rise time from $L_{\rm p}$/2 to $L_{\rm p}$ — $t_{-1/2}$
- Decay time from $L_{\rm p}$ to $L_{\rm p}$/2 — $t_{+1/2}$
- Light-curve width — $t_{-1/2} + t_{+1/2}$
- Nickel mass — $M_{\rm Ni}$
- Ratio of ejecta mass to kinetic energy — $M_{\rm ej}^3/E_{\rm k}$

The statistics were found using the set of *BVRI* and *UBVRI*NIR-equivalent LCs. The first step was to determine the values of $L_{\rm p}$, $t_{-1/2}$, and $t_{+1/2}$. A fourth-order polynomial was fit to each light curve around the peak using CURVE_FIT from the PYTHON SCIPY[4] package. If the photometric coverage was sufficient, then the three parameters could be determined. However, in most cases only $L_{\rm p}$ plus one other of the temporal values was directly measurable. In the instances where the photometric observations did not extend sufficiently far before or after $L_{\rm p}$ to return $t_{-1/2}$ or $t_{+1/2}$, it may have been possible to extrapolate to this time if the initial/final luminosity was sufficiently close to $L_{\rm p}/2$. In an attempt to derive $t_{-1/2}$, a second-order polynomial was fit to the early-time observations up to the time of peak luminosity, provided a sufficient number of observations was available. If the fit could converge to a solution within two days of the boundary data point it was accepted. Conversely, on the rare occasion when $t_{+1/2}$ could not be taken directly from the observations, the late-time data were fit with a linear function and extrapolated out to five days to find a solution. The extrapolations were inspected visually for irregularities and accepted if they seemed reasonable. To

[4] www.scipy.org

derive estimates of the uncertainty, the upper and lower photometric errors were fitted in a similar fashion as previously described. In some cases, it was not possible to determine one or more of these parameters, and so these SNe are omitted from the initial studies involving this parameter.

Table 2.7 gives the median temporal characteristics as derived from the *BVRI* group; I note that these values remain consistent with those derived for the *UBVRI*, *BVRI*NIR, and *UBVRI*NIR samples. I caution that the median width is not the sum of the median values of $t_{-1/2}$ and $t_{+1/2}$ but is the median of the sum of the two parameters for SNe where both have been derived. This means that the median width is drawn from a smaller sample size than either $t_{-1/2}$ or $t_{+1/2}$. In particular the large median value of $t_{+1/2}$ for SNe Ic is largely driven by the extremely broad light curves of SNe 2011bm (Valenti et al., 2012) and PTF11rka, neither of which can be included in the calculation of median width because they lack a value for $t_{-1/2}$. The relationship between $t_{-1/2}$ and $t_{+1/2}$ is considered in more detail in Section 2.6.2.

In Appendix B, Table B.1 and Table B.2 give the values derived for individual SNe from the *BVRI* sample and the *UBVRI*NIR-equivalent sample, respectively.

2.4.4 Determining Errors

The error in any particular value derived is related to the uncertainties in the photometry and the extinction. In certain situations the photometric errors are very small, perhaps unjustly so, which is the cause of very small uncertainties in the values determined in this section. Very small uncertainties lead to a higher degree of certainty in a value than is justified, and they have the effect of biasing possible correlations between parameters by increasing the weighting of the values for a particular SN. Ideally, a well-observed SN with good Galactic and host-galaxy extinction would have such an effect, but there are some SNe which fall short of this standard display extremely small uncertainties in their photometry. It can be seen in the LCs of these SNe that the uncertainties are unjustified, as they show variability which is greater than the photometric errors bars.

Table 2.7: Median temporal values derived from the *BVRI* data.

Type	$t_{-1/2}$ (N) (days)	$t_{+1/2}$ (N) (days)	Width (N) (days)
SNe Ic-BL/GRB-SNe	$8.6\pm^{1.9}_{1.1}$ (15)	$15.1\pm^{1.0}_{2.0}$ (14)	$24.7\pm^{2.7}_{2.3}$ (11)
SNe Ic	$9.3\pm^{2.6}_{1.1}$ (11)	$19.2\pm^{4.7}_{5.4}$ (15)	$23.8\pm^{7.3}_{5.4}$ (7)
SNe Ib	$11.2\pm^{2.2}_{1.4}$ (11)	$17.0\pm^{2.8}_{2.9}$ (23)	$26.4\pm^{3.6}_{3.9}$ (11)
SNe IIb	$10.1\pm^{1.2}_{0.4}$ (11)	$15.3\pm^{2.8}_{1.6}$ (15)	$25.4\pm^{2.3}_{0.8}$ (11)

2.4.5 Rise time

The parameter with the largest uncertainty is rise time, $t_{\rm p}$, principally because it requires well-covered photometry pre-peak and because of the uncertain behaviour of the light curve at very early times. Generally, only GRB/XRF SNe have an observed value of t_0 and hence a well-constrained $t_{\rm p}$, although the explosion time of SNe IIb with prominent early-time emission (e.g., SN 1993J, Matheson et al. 2000a; SN 2013df, Van Dyk et al. 2014; SN 2011dh, Arcavi et al. 2011; SN 2013cu, Gal-Yam et al. 2014) caused by the cooling of the stellar surface following shock breakout (Woosley et al., 1994) can be estimated to within a day or two of explosion. If the SN is found in a host galaxy that is regularly observed, then t_0 can be constrained between the detection and nondetection dates assuming that $\langle {\rm d}L/{\rm d}t \rangle$ is sufficiently large at early epochs so as to minimise the "dark time" (the period between explosion and detectability) of the SN (e.g., PTF10vgv; Corsi et al., 2012). Of course, this method is limited to the time interval between the two dates, which ideally should be on the order of a few days. Values for $t_{\rm p}$ from the literature are given in Table 2.10.

2.4.6 Comparison between optical and optical/NIR light curves at peak

I took the step of plotting the *UBVRI* luminosity at maximum versus *UBVRI*NIR maximum luminosity to investigate the possibility of determining some form of "bolometric correction" for the much larger *BVRI*-only sample. The results of this test are shown in Figure 2.11. It is apparent, at a glance, that all SNe in this set follow a very tight

correlation between the two values, and while caution must be exercised when dealing with values in log-log space, it appears that a simple linear fit would produce the desired results. The data were fit with a simple linear polynomial of the form given by the equation

$$\log(L_{UBVRI\mathrm{NIR}}) = a_1 + a_2 \log(L_{UBVRI}) \tag{2.1}$$

The best fit gives $a_1 = 1.62$ and $a_2 = 0.96$ with the standard deviation of the residual distribution equal to 0.02, which is adopted as the uncertainty in the fit. The SN with maximum displacement from the best-fit line shows a difference of $< 20\%$ between the value returned from the polynomial and the photometric value.

Overall, it appears that the variation in spectral shape is less important outside the optical wavelengths. This correlation is also very strong for *BVRI* against *BVRI*NIR. Thus, the conversion to fully bolometric luminosity requires little more than a simple multiplicative factor that is proportional to the optical flux. This implies that, around peak luminosity, the absorption and re-emission of photons as they diffuse through the ejecta happens primarily in the optical regime. Consequently, the NIR region is effectively the Rayleigh-Jeans tail of a blackbody with a temperature that gives an optical integrated flux similar that of the SN optical SED.

2.5 Pseudo-bolometric to fully bolometric

The disparity in number of SNe with *BVRI* data compared with *UBVRI*NIR data presents a challenge to efforts to reveal the statistics of the explosion, especially the luminosity distribution and the mass of ^{56}Ni synthesised in the first seconds after core collapse. Here I detail how I construct fully bolometric peak luminosity values for all the SNe in the sample using the results from earlier sections.

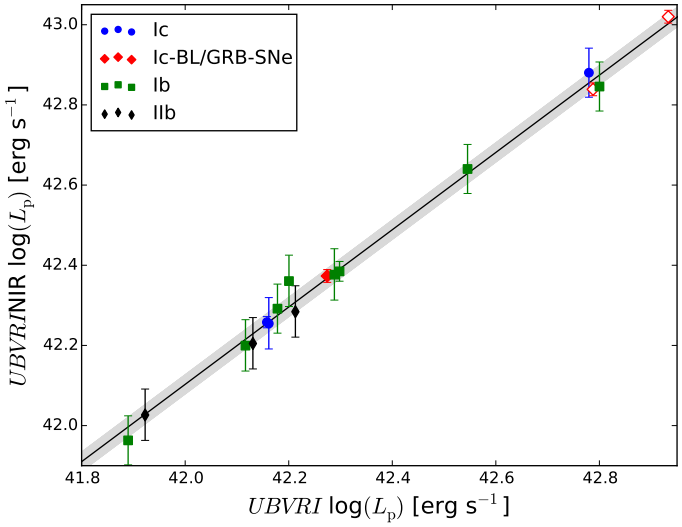

Figure 2.11: *UBVRI*+NIR peak luminosity as a function of *UBVRI* peak luminosity. The correlation appears to be independent of SN type. The grey area represents the 1σ uncertainty in the fit determined by the standard deviation of the residuals. The error bars are representative of the uncertainty only in the NIR contribution. Open symbols represent GRB-SNe.

2.5.1 The conversion method

To minimise the amount of uncertainty in each SN, the shortest method of obtaining the fully bolometric peak luminosity was used. The details of this procedure are outlined here.

Conversion from *BVRI* to *UBVRI* at peak

Approximately half of the SNe in the database lack U/u' photometry. To compensate for this, I use the results of Section 2.3.1 and apply a correction to account for the missing photometric band to the *BVRI* flux of these SNe. I use Table 2.5 to assign a correction value depending on SN type and whether there is a value for host-galaxy extinction. I assume the errors are commensurate with the standard deviation of each distribution. As a justification, I note that from Table 2.5 the median U fraction is always between 15% and 20%.

Conversion from *UBVRI* to *UBVRI*NIR

There are two pathways to convert the *UBVRI* flux to *UBVRI*NIR flux. In the first instance I can use the NIR data where they exist and combine their peak value with that of the *UBVRI* flux. The second method utilises Equation 2.1 and the values for the *UBVRI* to *UBVRI*NIR conversion as given in Section 2.3.2.

*UBVRI*NIR to fully bolometric

I finalise the conversion of *UBVRI*NIR $L_{\rm p}$ to a fully bolometric value by assuming a 10% contribution from unobserved wavelengths. I justify this value by integrating a Planck function at temperatures between 4000 K and 8000 K, which is typical for SE-SNe at peak, and comparing the flux ratio of our *UBVRI*NIR wavelength range to that of the flux outside it. I find that the UV and far-infrared can account for between $\sim 7\%$ and $\sim 20\%$ of the total flux but is typically $\sim 10\%$. If I assume some reprocessing of UV photons into the optical regime then this value can be lower. Thus, I take the error to be $+10\%$–5%. I do not attribute any particular fraction of this amount to IR or UV, the latter of which is small for SE-SNe (Pritchard et al., 2014).

2.5.2 Luminosity distribution for the bolometric sample

The resulting fully bolometric luminosity distribution for the entire SN sample is shown in Figure 2.12 and the statistics are shown in Table 2.13. The SN Ic/Ic-BL/GRB-SN group remains the most luminous population. SNe Ic and SNe Ic-BL can be found throughout this distribution while GRB-SNe occupy the upper end.

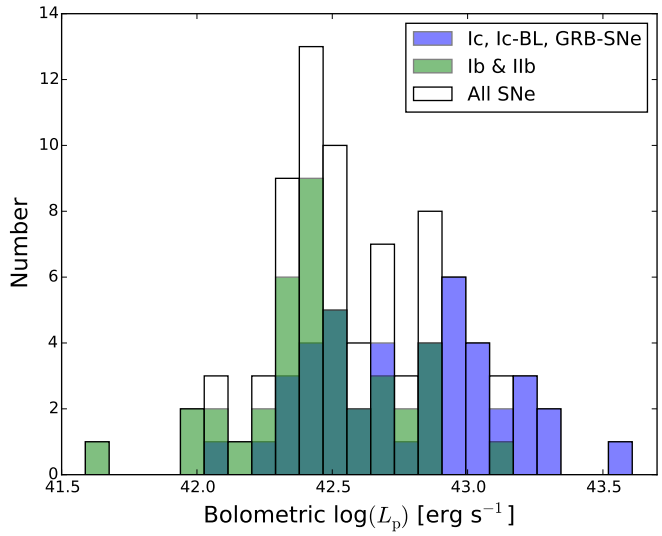

Figure 2.12: Fully bolometric luminosity distribution of the entire sample. Median host-galaxy extinction is adopted when the actual value is absent. Colours are as described in Figure 2.9.

Table 2.8: Spearman rank correlation results for $L_{\rm p}$ against $t_{+1/2}$

Type	ρ	p-value	N
All	-0.02	0.84	69
GRB-SNe	-0.8	0.10	5
Ic-BL	-0.14	0.76	7
Ic	0.30	0.24	17
Ib	-0.07	0.77	23
IIb	0.22	0.43	15

2.6 Temporal properties

2.6.1 $L_{\rm p}$ as a function of $t_{+1/2}$

The value of Type Ia SNe for cosmological studies owing to the correlation between *B*-band peak and light-curve decline over 15 days (Phillips, 1993) is well known. All previous attempts to find a similar relation for core-collapse SNe have returned negative results (Drout et al., 2011; Lyman et al., 2014). Figure 2.13 shows how the *BVRI* pseudo-bolometric peak of our sample compares with $t_{+1/2}$.

The results of a Spearman rank correlation test on $L_{\rm p}$ and $t_{+1/2}$ are given in Table 2.8. With p-values > 0.05 throughout, it is apparent that there is no equivalent "Phillips

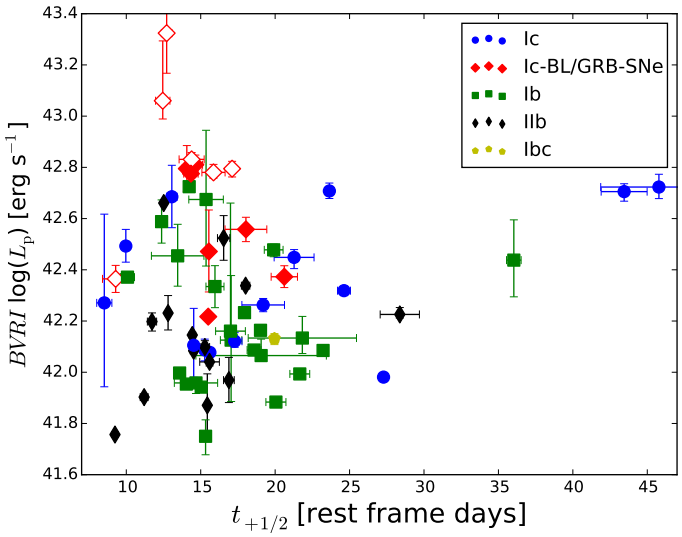

Figure 2.13: $L_{\rm p}$ as a function of $t_{+1/2}$ for the *BVRI*-equivalent light curves. There is no correlation between either parameter. Open symbols represent GRB-SNe.

Table 2.9: Spearman rank correlation results for $t_{+1/2}$ against $t_{-1/2}$

Type	ρ	p-value	N
All	0.66	0.000005	39
GRB-SNe	0.69	0.19	5
Ic-BL	0.30	0.62	5
Ic	0.93	0.0008	8
Ib	0.69	0.018	11
IIb	0.68	0.022	10

relation" for any SN type used here, thus confirming earlier studies and indicating that the dynamics of the explosion mechanism of SE-SNe and the relationship to the ejecta is non-uniform.

2.6.2 Is there a relationship between $t_{-1/2}$ and $t_{+1/2}$?

Photometric coverage in not consistent across the whole sample, so a full set of temporal parameters is available only for a small number of SNe. Motivated by the desire to maximise the statistics derived from our sample, I examined temporal parameter values as a function of other temporal characteristics where the values were known. A plot of $t_{-1/2}$ and $t_{+1/2}$, Figure 2.14 suggests that a correlation exists. SNe that showed an excess of luminosity caused by shock breakout and non-radioactive power have been

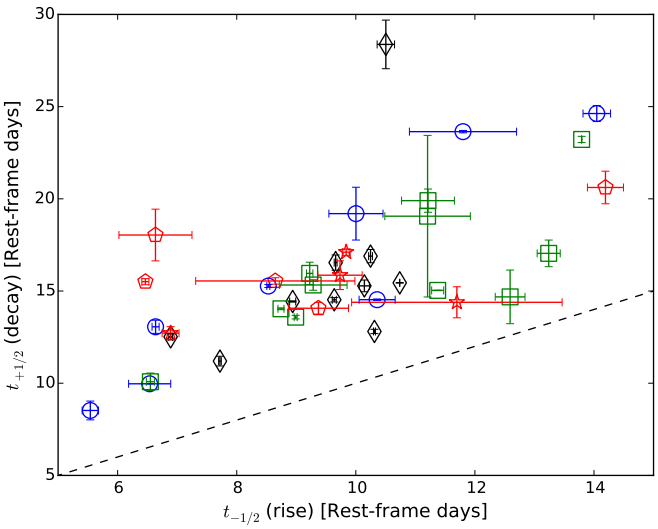

Figure 2.14: $t_{+1/2}$ as a function of $t_{-1/2}$. The dashed line is the line of unity and Open symbols represent GRB-SNe. All SNe have $t_{-1/2} < t_{+1/2}$.

omitted, which further strengthens the apparent correlation between the two properties. The results of a Spearman rank correlation are given in Table 2.9 and shows that indeed, the entire same is well correlated, as are SNe Ic, Ib, and IIb with p-values < 0.05. Again, the numbers in each sample are small.

However, this is at odds with the results of Taddia et al. (2015), where the Kolmogorov-Smirnov (K-S) tests on the value of Δm_{-10} (rise) and Δm_{15} (decay) for the r band for 40 SNe indicated that they were drawn from the same population and that no correlation between the rise and the decay of the light curve around maximum light.

Consequently, I performed a similar analysis on my $t_{+1/2}$ values. Figure 2.15 shows $t_{+1/2}$ as a function of $t_{-1/2}$. It can be seen that although there is a general trend to a slower decline for a slower rise, there is a considerable spread in the values. I plotted cumulative distribution functions (CDFs) for all $t_{+1/2}$ values derived in the sample and split them by type, as seen in Figure 2.16. K-S tests indicate that most of the distributions are drawn from the same population ($P > 0.05$) with the exception of the SN Ic/IIb group ($P = 0.048$), although the SN Ic/Ic-BL group returns $P = 0.061$ which is marginally over the threshold. I can attribute this entirely to the presence of broad light curve SNe Ic 2011bm and PTF11rka in conjunction with the relatively small number of SNe throughout: 12, 14, 23, and 13 for SNe Ic-BL, Ic, Ib, and IIb, re-

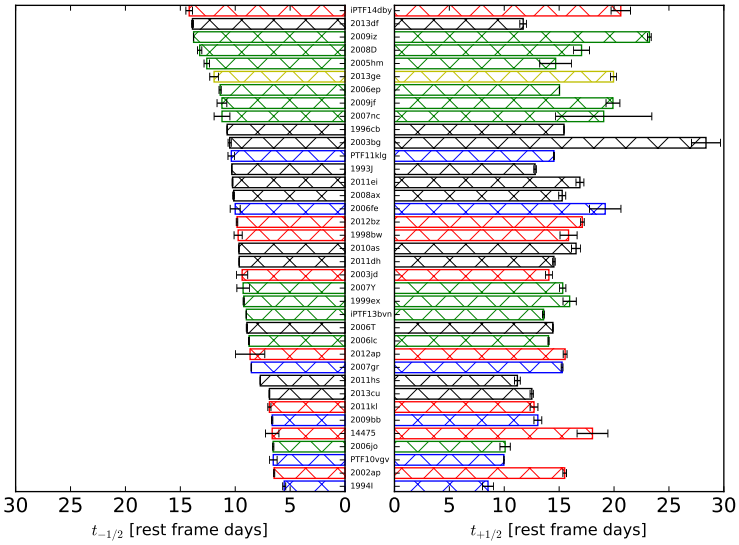

Figure 2.15: The $t_{-1/2}$ and $t_{+1/2}$ values for the SNe in the sample with both parameters. The range of values in $t_{+1/2}$ is readily apparent despite a trend of the decay time to increase as the rise time increases. SNe Ib are shown in green, Ic-BL/GRB-SNe are red, Ic are blue, IIb are black, and Ibc are yellow.

spectively. It is clear that these two SNe disproportionately affect the sample, because without their presence the SN distributions are very similar, sharing a similar median $t_{+1/2}$ of ~ 15 days. The implication is that one should not treat the SN subtypes separately, at least for this sample size. Next I performed a K-S test on the entire sample of $t_{-1/2}$ and $t_{+1/2}$. With $P = 2 \times 10^{-10}$ it is clear that the two are not drawn from the same population.

My results are contrary to those in Taddia et al. (2015), I find a clear correlation between the characteristic rise times and decay times.

However, despite the while the trend is toward a longer decay for a longer rise, the variance along the trend, which is not measured by the Spearman rank correlation, makes it unreliable as a method for converting one to the other.

2.6.3 Correlation between $t_{\rm p}$ and $t_{-1/2}$

It is pertinent to see if the time for rise to peak of the SN is in some way correlated with the rise from $L_{\rm p}/2$ to $L_{\rm p}$, as it would lead to a method to estimate the SN rise

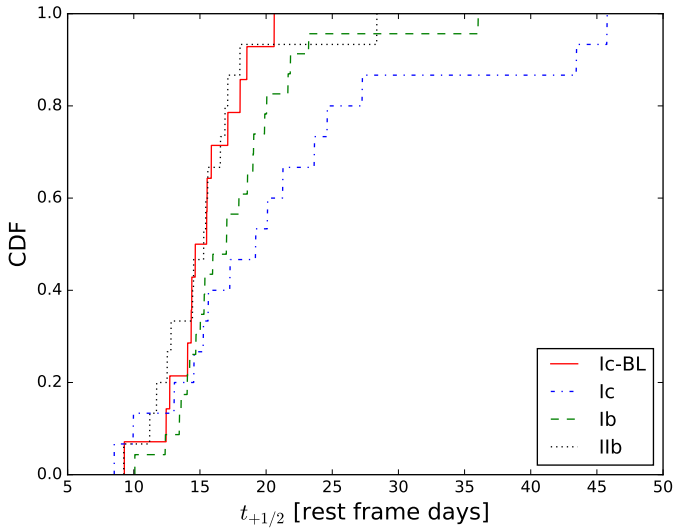

Figure 2.16: The cumulative distribution function of all the $t_{+1/2}$ values in the sample sorted by spectral type. The effect of the extremely slowly declining Type Ic SNe 2011bm and PTF11rka on the SN Ic CDF is clearly seen.

time from $t_{-1/2}$. The limitations of such an assessment are apparent, as few SNe have known explosion times. Thus, I take the GRB-SNe with their known t_0, some of the SN IIb set (because their explosion times can be constrained from the initial shock-breakout peak), plus any SN with well-constrained explosion time owing to the short interval between nondetection and detection. Figure 2.17 shows $t_{\rm p}$ against $t_{-1/2}$; it is apparent that there is some correlation which appears to be independent of SN type. Using a linear fit as before, defined as

$$t_{\rm p} = \alpha t_{-1/2}, \tag{2.2}$$

I find $\alpha = 1.5$. To determine uncertainties in the fit I took the standard deviation of the distribution of the residuals as described previously, which I find to be 1.68 days. SNe were omitted from the fitting procedure if the early-time emission was dominated by shock breakout. These were typically SNe IIb or GRB-SNe for which $t_{-1/2}$ was poorly constrained owing to two components, and well-defined explosion times heavily influenced the result.

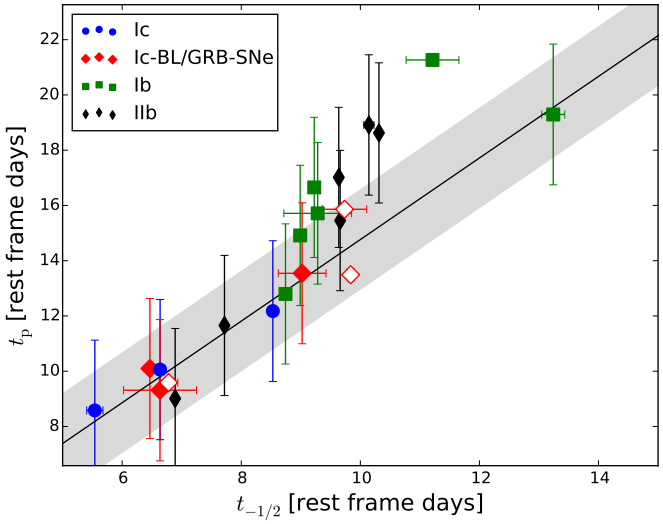

Figure 2.17: $t_{\rm p}$ as a function of $t_{-1/2}$ for SNe in the sample having both parameters. The black line represents the best fit to the data incorporating errors in both the ordinate and abscissa. The grey region represents the standard deviation of the residuals from this line, which is taken to be the uncertainty in the fit. Open symbols represent GRB-SNe.

2.6.4 Inferred rise time $t_{\rm p}$

Table 2.10 shows the inferred rise time for the sample as derived by the previously described correlation. Note that the rise times for GRB-SN 1998bw ($\sim$ 16 days) and GRB-SN 2006aj ($\sim$ 10 days) are recovered within the uncertainties of the extrapolated explosion time. Notable exceptions are as follows. (i) SNe that show relatively slowly declining shock break-out emission so that it is a non-negligible contributor to the flux of the SN during the rise (e.g., SN 2008D, SN 2011hs). (ii) The case of SN 2011kl, associated with ultra-long GRB 111209A (Greiner et al., 2015); this SN is interesting with regard to the explosion mechanism.

First, I must consider an explanation for the correlation between $t_{-1/2}$ and $t_{\rm p}$. This can be explained by the interplay with ^{56}Ni $\rightarrow$ ^{56}Co $\rightarrow$ ^{56}Fe energy injection and the light-curve rise time, which is itself a function of opacity, ejecta mass, and photospheric velocity (Arnett, 1982). Because the derivative of the energy injection rate is constant, the shape of the light curve is determined solely by the diffusion time. Altering the diffusion time means the peak may move, but the way the light curve rises to the peak retains the same relative shape provided the nickel distribution remains located

centrally. This is not necessarily the case for an alternate energy source such as a magnetar, where the magnetar rotational energy can be deposited into the ejecta on a timescale much less, or much greater, than the diffusion time, or the case where shock breakout (particularly for SNe IIb) or GRB afterglow contribute to the optical flux. For all GRB-SNe, except SN 1998bw where the GRB afterglow was negligible, afterglow subtraction is a major issue for accurately determining $t_{-1/2}$; fortunately, the need for this value is made redundant by a known explosion date.

2.7 Explosion properties

2.7.1 The synthesis of ^{56}Ni

With the fully bolometric $L_{\rm peak}$ and $t_{\rm p}$, it is now possible to estimate the amount of ^{56}Ni synthesised in the explosion. To obtain a value for $M_{\rm Ni}$, I used the formulation from Stritzinger and Leibundgut (2005) which is based upon "Arnett's rule" (Arnett, 1982): the approximation that the maximum luminosity of a SN powered by the decay of ^{56}Ni is equal to the energy released by radioactive decay at that time:

$$\begin{aligned}\frac{M_{\rm Ni}}{\rm M_{\odot}} =& L_{\rm p} \times \left(10^{43}\text{erg s}^{-1}\right)^{-1} \\ & \times \left(6.45 \times e^{-t{\rm p}/8.8} + 1.45 \times e^{-t{\rm p}/111.3}\right)^{-1}\end{aligned} \tag{2.3}$$

I use equation 2.3 to evaluate $M_{\rm Ni}$ for the *BVRI*, *UBVRI*NIR, and the fully bolometric sample. I adopt the exact value of $t_{\rm p}$ if known; failing that, I adopt the $t_{-1/2}$ to $t_{\rm p}$ conversion (Equation 2.2) to reduce the propagation of uncertainties. The result of this is given in Table B.3. The $M_{\rm Ni}$ distribution for the whole sample, highlighting SNe Ic/Ic-BL and GRB-SNe, is shown in Figure 2.18, whereas Figure 2.19 the whole sample emphasises SNe Ib and SNe IIb. The spread of synthesised $M_{\rm Ni}$ varies between SN types. The SN Ic group shows the largest spread while the SN Ib and SN IIb populations cluster toward the lower end of the distribution. The normal (i.e., non-

Table 2.10: Rest-frame $t_{\rm p}$ values.

SN	Literature $t_{\rm p}$ (days)	$t_{\rm p}$ from $t_{-1/2}$ (days)
1993J	19.15±0.03	16.32±1.65
1994I	12.25±0.21	8.77±1.66
1996cb	-	16.99±1.65
1998bw	15.86±0.18	15.41±1.69
1999dn	13.92±2.84	-
1999ex	18.35±0.04	14.60±1.65
2002ap	13.01±0.00	10.23±1.65
2003bg	-	16.62±1.66
2003dh	12.65±1.66	-
2003jd	12.50±0.18	14.83±1.73
2004fe	-	14.68±1.65
2005bf	18.32±0.35	-
2005hm	-	19.93±1.67
2005kr	-	11.41±1.67
2005ks	-	12.37±1.66
2006T	-	14.15±1.65
2006aj	9.59±0.04	10.73±1.66
2006ep	-	18.00±1.65
2006fe	-	15.83±1.71
2006jo	-	10.37±1.65
14475	-	10.50±1.76
2006lc	-	13.84±1.65
2006nx	-	14.28±1.70
2007Y	18.76±0.35	14.69±1.75
2007gr	13.15±0.23	13.50±1.65
2007ms	-	22.23±1.67
2007nc	-	17.73±1.80
2007qx	-	15.09±2.76
2007ru	10.24±0.05	-
2007sj	-	14.54±1.66
2007uy	19.08±0.28	-
2008D	19.29±0.23	20.95±1.66
2008ax	19.28±0.13	16.05±1.65
2008hw	12.31±0.10	-
2009bb	12.63±0.10	10.50±1.65
2009iz	-	21.83±1.65
2009jf	21.27±0.16	17.74±1.71
2010as	12.44±0.12	15.29±1.65
2010bh	12.74±0.10	5.20±1.68
2010ma	10.33±4.34	-
2011bm	34.59±0.15	-
2011dh	15.71±0.02	15.25±1.65
2011ei	17.73±0.03	16.22±1.65
2011hs	8.59±0.06	12.21±1.65
2011kl	15.17±0.07	10.90±1.66
2012ap	13.19±0.31	13.69±2.12
2012bz	13.49±0.22	15.57±1.65
2013cq	13.00±2.00	-
2013cu	9.01±0.08	10.90±1.65
2013df	21.79±0.10	21.99±1.65
2013dx	12.26±5.48	-
2013ge	-	18.88±1.70
PTF10vgv	-	10.35±1.69
PTF11bli	-	20.63±1.66
PTF11jgj	-	22.07±2.17
PTF11klg	-	16.39±1.68
PTF12gzk	16.35±0.46	-
iPTF13bvn	15.95±0.10	14.23±1.65
iPTF14dby	-	22.46±1.68

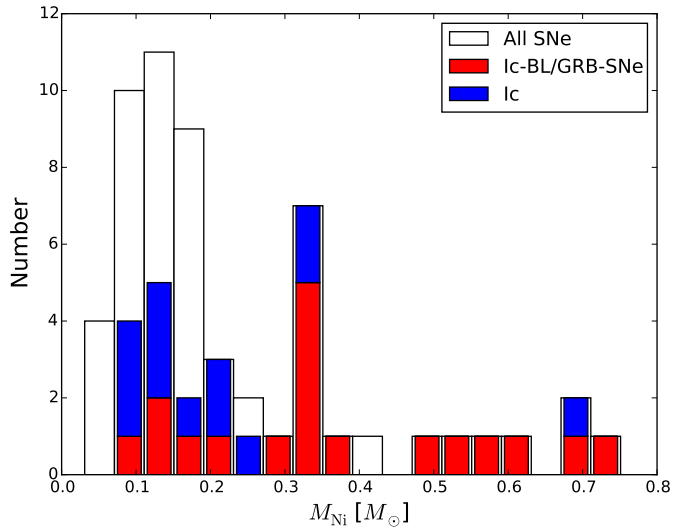

Figure 2.18: The ^{56}Ni distribution for the fully bolometric sample with the normal SNe Ic and the SNe Ic-BL/GRB-SNe in blue and red, respectively. Consistent with our procedure for the bulk analysis, corrections for median host-galaxy extinction have been applied. The bulk nickel-mass distribution, for SNe where the nickel mass can be derived, is shown in white.

broad-lined) SNe Ic also include the non-GRB-SN with the largest nickel mass, SN 2011bm, which is a consequence of its exceptionally broad light curve. Figure 2.20 gives peak bolometric luminosity as a function of $M_{\rm Ni}$ for the sample.

2.7.2 Characteristic timescales, kinetic energy, and ejecta mass

The rise time of the SN is linked to the powering mechanism, the spatial distribution of ^{56}Ni, the opacity of the ejecta (κ), the mass of the ejecta ($M_{\rm ej}$), and the photospheric velocity at luminosity peak $v_{\rm ph}$ via the formulation for the parameter τ_m given by Arnett (1982),

$$\tau_m = \sqrt{2}\left(\frac{k}{\beta c}\right)^{\frac{1}{2}}\left(\frac{M_{\rm ej}}{v_{\rm ph}}\right)^{\frac{1}{2}}. \tag{2.4}$$

For ejecta of uniform density undergoing spherically symmetric free expansion ($R(x,t) = v(x)t$), I can convert $v_{\rm ph}$ to $E_{\rm k}$ via Equation 2.5,

$$E_{\rm k} = \frac{3}{10} M_{\rm ej} v_{\rm ph}^2, \tag{2.5}$$

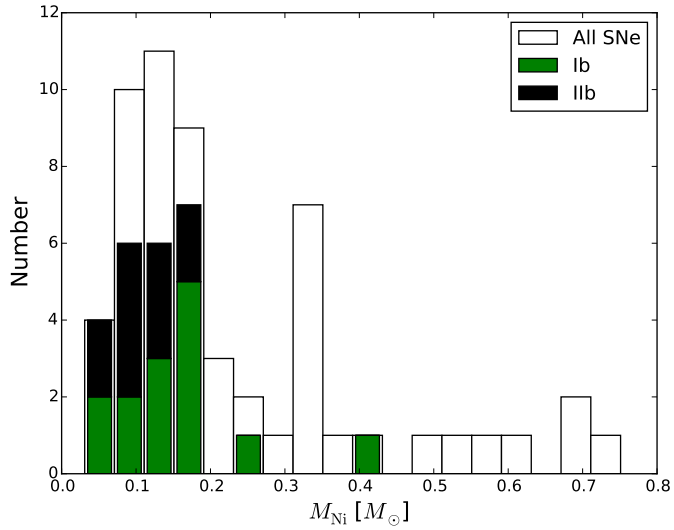

Figure 2.19: The ^{56}Ni distribution for the fully bolometric sample with the normal SNe Ib and SNe IIb in green and black, respectively. Corrections for median host-galaxy extinction have been applied. The white region is the same as in Figure 2.18.

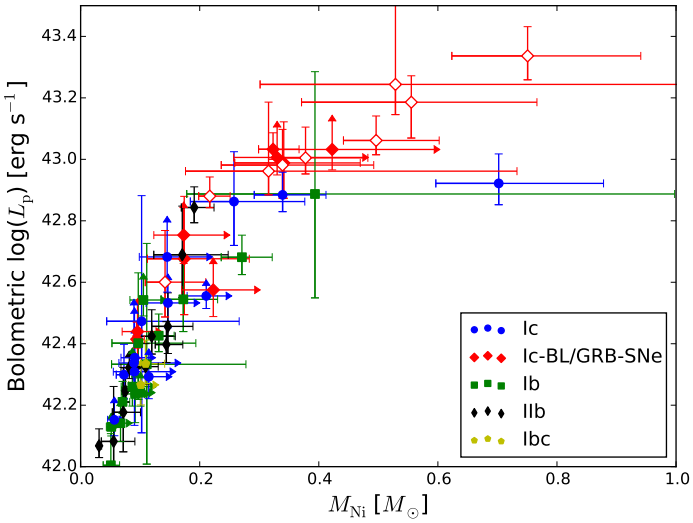

Figure 2.20: Peak bolometric luminosity as a function of nickel mass. Open symbols represent GRB-SNe.

which leads to

$$\tau_m = \left(\frac{\kappa}{\beta c}\right)^{\frac{1}{2}} \left(\frac{6M_{\rm ej}^3}{5E_{\rm k}}\right)^{\frac{1}{4}}, \tag{2.6}$$

where c is the speed of light and β is a constant of integration with value of ~ 13.7. The parameter τ_m, which defines the scale time of the light curve, is similar to the rise time of the SN but typically lower by ~ 2 days. However, by assuming that $t_{\rm p} \approx \tau_m$, I can estimate a value for $M_{\rm ej}^3/E_{\rm k}$ for a range of opacities; see Table B.4. Note that this model assumes that κ is independent of time and constant across the ejecta — but this is not true for any SN, especially SNe Ib and SNe IIb. In these cases the opacity of the He shell is extremely low owing to the paucity of He lines in the optical. Consequently, the value for $M_{\rm ej}$ derived from τ_m underestimates the total mass of the ejecta because the photons emitted from the photosphere diffuse through this shell with little overall interaction (also see Wheeler et al., 2015). Furthermore, $E_{\rm k}$ is approximated by assuming a constant density throughout the ejecta. This is not the case and the density profile of the ejecta defines the total kinetic energy, this is discussed further in Chapter 3. On this basis no value is calculated for $M_{\rm ej}$ or $E_{\rm k}$, and so $M_{\rm ej}^3/E_{\rm k}$ is left as the scaling for the light curve rise time (assuming all other parameters are constant). Finally, to test the overall accuracy of this method I compare these results with that of spectral modelling, (see Mazzali et al., 2000, 2002, 2003; Sauer et al., 2006; Mazzali et al., 2009, 2013, 2017), although even these methods are still sensitive to the estimated explosion date and $\sim 30\%$ in $M_{\rm ej}$ (Ashall et al., 2017).

I plot $L_{\rm p}$ and $M_{\rm Ni}$ as a function of $M_{\rm ej}^3/E_{\rm k}$ in Figures 2.21 and 2.22. There is considerable scatter in each plot, but for a given value of $L_{\rm p}$ or $M_{\rm Ni}$ the value of $M_{\rm ej}^3/E_{\rm k}$ tends to be higher for SNe Ic, SNe Ib, and SNe IIb compared with SNe Ic-BL. The width of SN 2011bm leads to a large value for $M_{\rm ej}^3/E_{\rm k}$, which in turn necessitated the use of a logarithmic abscissa. These distributions (Ic/Ib/IIb against Ic-BL/GRB-SNe) can be approximated by considering the means and standard deviations of the two parameters in the x and y directions. The distributions overlap in the $M_{\rm ej}^3/E_{\rm k}$ direction ($\sim 3 \pm 2.5$ against $\sim 0.9 \pm 0.7$ respectively), and in the $M_{\rm Ni}$ direction ($\sim 0.14 \pm 0.05$ against $\sim 0.34 \pm 0.2$), however, with a mean $\log_{10}(L_{\rm p})$ of 43.0$\pm$0.3 erg s^{-1} for Ic-BL and 42.44$\pm$0.25 erg s^{-1} for the rest of the SNe, the 1 sigma region of these two distribu-

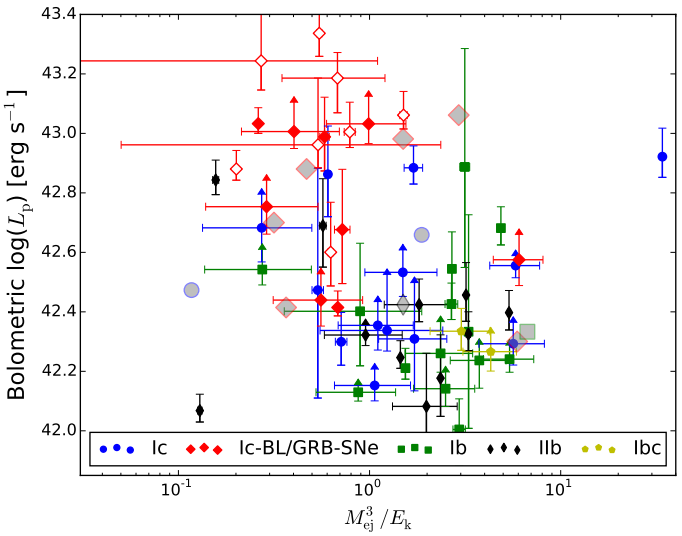

Figure 2.21: Peak bolometric luminosity as a function of $M_{\rm ej}^3/E_{\rm k}$. Open symbols represent GRB-SNe. Grey filled symbols represent the results of spectroscopic modelling and shows that the two methods are broadly consistent for positioning of SN types with SNe Ic, Ib and IIb occupying the lower right region and SNe Ic-BL (including GRB-SNe) taking the upper left.

tions do not overlap in the y direction and so they do not overlap at all. This shows that there are two different distributions in Figure 2.21.

2.8 Comparison with multiband photometry

2.8.1 Deriving multiband parameters

The multiband photometry of each SN was fit using the same process as described in Section 2.4.3. The raw photometry was dereddened for Galactic extinction in the observer frame and host-galaxy extinction in the rest frame, where possible.

2.8.2 Colour curves

The diversity of filters used in the observations implies that there is no single colour that can be used to represent every SN in the sample as is; this requires the use of some filter conversion to homogenise the sample. I utilise the colour corrections of Jordi et al. (2006) to convert *B* and *V* to g' and *R* to r', so as to present the $g' - r'$ colour for

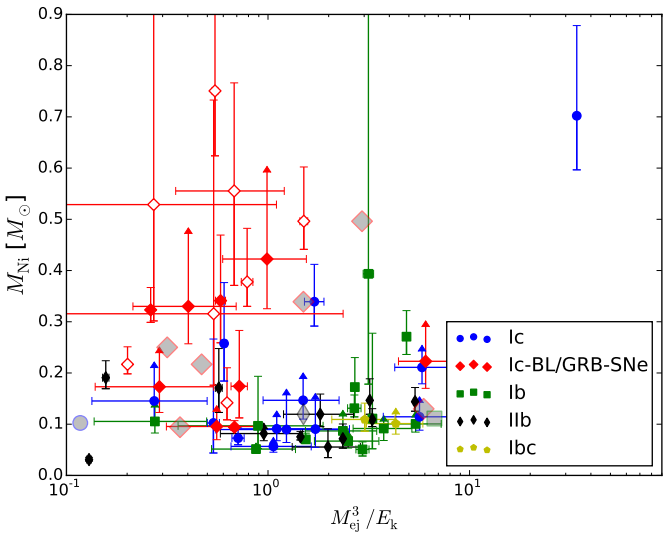

Figure 2.22: Nickel mass as a function of $M_{\rm ej}^3/E_{\rm k}$. Open symbols represent GRB-SNe. Grey filled symbols represent the results of spectroscopic modelling, as in Figure 2.21, the results are broadly consistent.

all of the SNe. This is the most sensible choice for conversion because g' lies between *B* and *V* while r' lies blueward of *R*, so the conversions fall between the available photometry. I note that this process is not perfect and stellar colour transformations can be poor for emission-line objects. However, it should be less of an issue during the photospheric phase ($\lesssim 40$ days) when the spectrum can be more closely approximated by a blackbody.

As a test of the accuracy of this conversion I utilise SN PTF12gzk, which has photometry in *UBVRIgriz*. I find that the transformed colour falls within the uncertainties of that determined directly from the photometry, giving confidence that this method is sufficiently accurate within the bounds of the photometric uncertainties.

I take the approach of plotting the colours of all SNe at $z < 0.05$ with extinction corrections applied only when the reddening is known. The limit on distance is chosen so as to minimise the need for K-corrections, which become more important at $z > 0.05$. This importance is amplified by the behaviour of g' and r', as they lie on opposite sides of the SED peak for most SNe until times much later than the peak of the bolometric LC. The behaviour of the K-correction is dependent on the underlying spectrum, the epoch, and the redshift, which can have a dramatic effect on the colours as g' and r'

can be corrected in opposite directions. For example, at ~ 10 days past bolometric maximum and in the $z < 0.05$ regime, the K-correction in the g' band is typically ~ 0 mag, but it begins to rise rapidly to ~ 0.1 mag as z tends to 0.05. In the r' band the behaviour is more complex, with the low-z K-correction taking small positive or negative values but tending toward lower values as z increases. At other times the behaviour can be different and more extreme, especially with increasing redshift. Hence, I limit this effect by restricting the sample to low z.

Figure 2.23 shows the $g' - r'$ colour evolution over the photospheric phase; SNe without known host-galaxy extinction are plotted in transparent markers to separate them. When host extinction is applied the spread of colours narrows, and at ~ 10 days past bolometric peak it forms a "bottleneck"; see Figure 2.24. This behaviour is similar to that seen by Drout et al. (2011) in the $V - R$ colours of their sample, and was similarly observed for SNe with $g - r$ by Taddia et al. (2015). The colour evolution of SN 2005bf is unique and appears to reflect the light curve, with the blue dips being approximately coincident with the luminosity peaks. If one was to take the second peak as the bolometric maximum, then the colour curve would shift to the left by 20 days and line up with the other SNe. Type IIb SN 2011hs, $E_{\rm host}(B-V) = 0.16 \pm 0.07$ mag (Bufano et al., 2014), is a notable outlier in Figure 2.24. Bufano et al. (2014) find that $g' - r'$ is ~ 0.6 mag around the time of g' maximum and there is a ~ 0.5 mag difference between the colours of SN 2011hs and SN 2008ax. The result here is comparable, with $g' - r' \approx 0.6$ mag in the few days before bolometric maximum and a similar difference between the two SNe, which is consistent with the period around g' maximum. It may be that the host extinction has been underestimated in this case, or it could be indicating that not all SNe sit within the main distribution.

Figures 2.25 and 2.26 show the colour evolution of SNe split by spectral type for all SNe Ic and SNe Ib/IIb, respectively. The "bottleneck" is more readily apparent in the SN Ic/Ic-BL/GRB-SN population than it is for SNe Ib/IIb, providing further caution in attempting to use colours as a basis of determining host extinction. Note that for clarity, uncertainties are not shown in these figures.

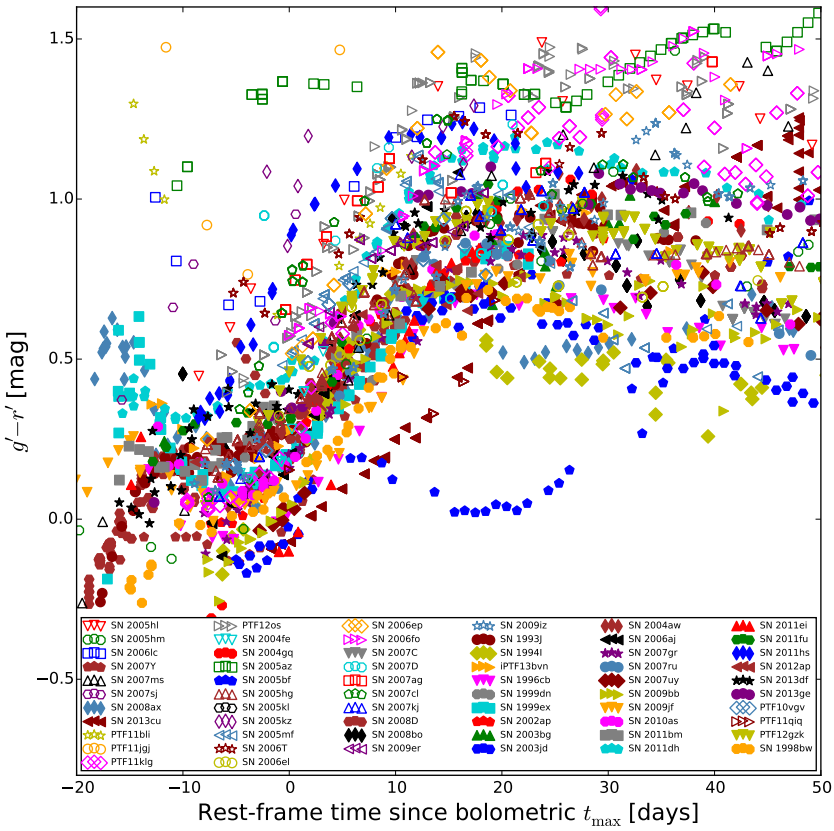

Figure 2.23: $g' - r'$ colour of the SNe in the sample at $z < 0.05$. Open markers indicate SNe where $E(B-V)_{\rm host}$ is not known. To see how correcting the colour curves for host extinction affects the spread, see Figure 2.24.

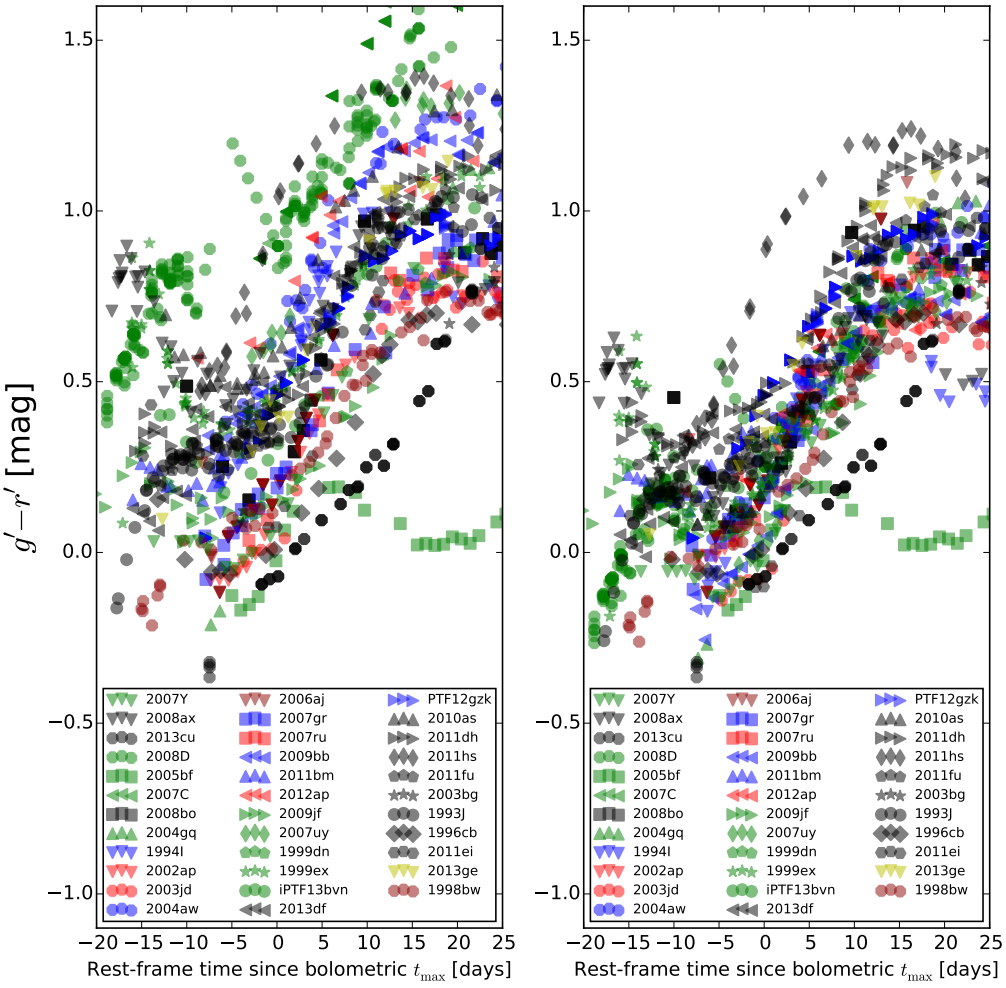

Figure 2.24: $g' - r'$ colour curves of the SNe in the sample at $z < 0.05$, sorted by spectral type, showing before (left) and after (right) correction for host extinction. SNe of Types Ic, Ic-BL, Ib, IIb, Ibc, and GRB-SNe are shown in blue, red, green, black, yellow, and dark red, respectively.

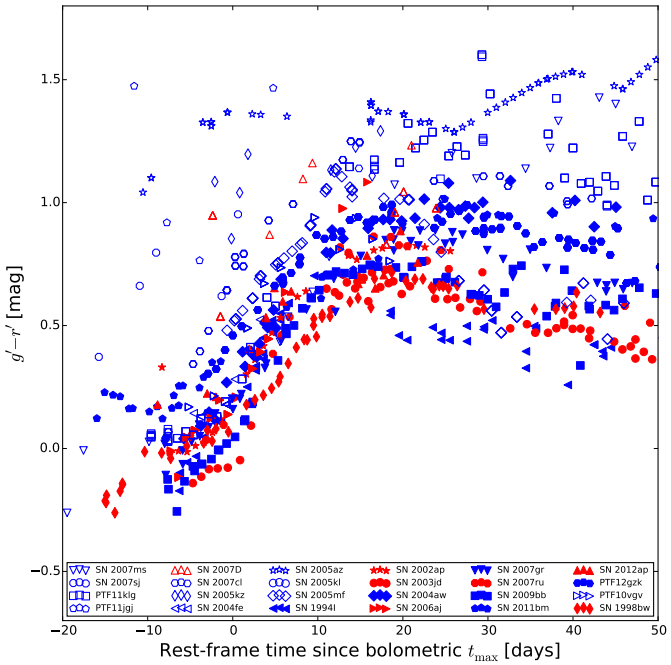

Figure 2.25: $g' - r'$ colour of the SNe Ic in the sample at $z < 0.05$. Open markers indicate SNe where $E(B-V)_{\rm host}$ is not known.

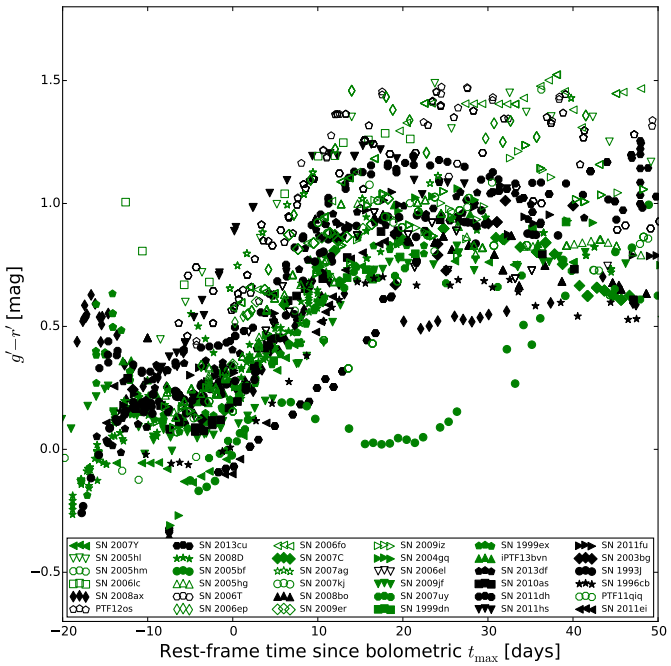

Figure 2.26: $g' - r'$ colour of the SNe Ib and SNe IIb in the sample at $z < 0.05$. Open markers indicate SNe where $E(B-V)_{\rm host}$ is not known.

Table 2.11: Effective wavelength when photometry peak matches bolometric peak.

SN Type	Median λ (Å)	$\langle\lambda\rangle$ (Å)	σ (Å)
Ic-BL	5449	5369	536
GRB-SNe	4869	5065	419
Ic	5616	5452	826
Ib	5416	5454	500
IIb	5308	5277	334

2.8.3 Comparing the multiband and bolometric peak time

The time of peak of the photometry is a function of the effective wavelength of the band, with blue bands peaking earlier than red bands (Taddia et al., 2015). This can be explained by the evolution of the underlying spectrum and the cooling of the photosphere, although absorption features can affect the temporal evolution of the photometry. By using the photometry and interpolating the time of peak between the bands I can estimate the wavelength peak that coincides with $t_{\rm p}$. Table 2.11 gives the average wavelength where the photometry would peak at $t_{\rm p}$; it can be seen that the values are around that of the *V* band, $\lambda_{\rm eff} = 5505$ Å. For GRB-SNe the SED can be "contaminated" by afterglow flux, which is preferentially blue, leading to a bluer SED peak. Unfortunately, it is hard to account for GRB afterglow beyond simple empirical methods (see Section 2.2.2). For comparison, the spectra of GRB-SN 1998bw are red, broad-lined, and almost featureless owing to the comprehensive reprocessing of optical photons to lower frequencies by the high-energy ejecta.

2.8.4 Bolometric corrections

In the era of large-scale surveys [e.g., PTF, iPTF, the Panoramic Survey Telescope and Rapid Response System (Pan-STARRS); the future Large Synoptic Survey Telescope (LSST) and the Zwicky Transient Facility (ZTF)], where the number of transients discovered has increased (and will continue to increase) by orders of magnitude, it is apparent that with a limited number of telescopes available, long-term multiband

follow-up observations of single objects become more time consuming. Bolometric corrections are a useful way of approximating the bolometric luminosity from a single band or colour (Lyman et al., 2014), which in turn enables the determinations of the bolometric properties of the SN. To this end, I investigate the bolometric corrections (BCs) in single bands for our database.

The BC is defined as

$$M_{\rm band} - {\rm BC} = M_{\rm bol}. \tag{2.7}$$

To estimate the BC, I subtract $M_{\rm bol}$ at the time of bolometric peak from $M_{\rm band}$ at the time of peak in that band and calculate a distribution. The mean and standard deviation of each distribution is given in Table 2.12; the standard deviation is taken to be the error of the bolometric correction δBC. It is apparent that the band with the least scatter is *R*, where $\delta BC = 0.13$ mag, followed by I ($\delta BC = 0.18$ mag); r' and i' are less constrained, with $\delta BC = 0.28$ mag and 0.27 mag (respectively). This is an issue for calculating BCs via this method because it relies on the spectral differences of each SN being outside the band in question. If *R* ($\lambda_{\rm eff} = 6580$ Å) and I ($\lambda_{\rm eff} = 8060$ Å) define such a region, then it should be expected that i' ($\lambda_{\rm eff} = 7630$ Å) would also be a tracer for the bolometric luminosity, but the scatter is actually considerably greater for this band. The reason behind this could possibly be systematics (e.g., relatively poor photometry), but this would have to be applicable to a large number of observations across many years to avoid being lost in the noise of better observations.

There is insufficient evidence to suggest that any particular band is a superior tracer of the bolometric light curve at peak. Additionally, if one were to apply the BC to some SNe, the returned luminosity would be poorly constrained. This is because the standard deviation of the spread of residuals from the BC, which is taken to be the uncertainty in the resulting luminosity, corresponds to approximately a quarter of the value returned. Here I have yet to even consider errors in the input photometry. Given that the spread of SN luminosities typically ranges between 10^{42} erg s^{-1} and 10^{43} erg s^{-1}, this uncertainty represents a significant fraction of the parameter space; hence, the BCs are not applied here.

Table 2.12: Bolometric corrections derived from single-band photometry.

Band	Mean BC (mag)	σ (mag)	N
B	0.19	0.27	40
g'	-0.058	0.33	12
V	-0.34	0.21	40
r'	-0.43	0.28	27
R	-0.45	0.13	25
i'	-0.38	0.29	27
I	-0.51	0.18	24

2.9 Discussion

2.9.1 Biases

It would be remiss to fail to appreciate the biases involved in the data used for this study. SNe were rare discoveries until the early/mid 1990s. Typically fewer than 20 per year were discovered, but as technology improved and more large-scale surveys were initiated, the number count increased from a few tens per year to the few hundred discovered each year now (e.g., Gal-Yam et al., 2013a). However, telescope time and funding are of limited supply; thus, the sample of SNe is affected in numerous ways. For example, many of the SNe are objects of interest; they display some unusual property that makes them targets for follow-up observations when they are spectroscopically confirmed, or they are nearby and bright. This is especially true of GRB-SNe and XRF-SNe, which are discovered only as a result of the detection of the high-energy transient event with which they are associated. Consequently, GRB-SNe and XRF-SNe are found at much greater distances that other SE-SNe and in different host environments.

Some SNe are serendipitous discoveries in surveys designed for research in other areas, typically searches for SNe Ia, so unless the SE-SN is an object of interest it is not monitored. Furthermore, if a SE-SN is discovered as a result of a targeted survey in which particular galaxy types are observed at regular intervals because they display a propensity for SNe, then events that occur in less optimal environments will be missed.

This means that the SNe in this sample are a mix of targeted (e.g., Lick Observatory Supernova Search; LOSS, the Chilean Automatic Supernova Search; CHASE, most amateur discoveries) and untargeted surveys (e.g., PTF, the Catalina Real-time Transient Survey; CRTS, ATLAS).

Intrinsically fast evolving and dim supernovae may well also be missed. Even with wide-field surveys that have a regular cadence these objects are hard to identify against other dim and fast evolving transients (e.g., comets, stellar flares), automated pipelines may not be optimised to flag such objects. Additionally, highly extinguished SNe may be missed. This could be because the host has a high inclination or that the SN occurs close to the nucleus.

The cost of observing transients over numerous bands has resulted in an increase of single-band observations of SNe. If spectra are available it may be possible to estimate the bolometric properties of the the SN by assuming its evolution is the same as that of a SN with a similar spectrum. Finally, observations favour SNe in less dusty regions of the host galaxy and those that are intrinsically luminous because their apparent brightness is greater. This leads to sampling of a larger comoving volume for more luminous SNe (Malmquist bias).

There are several consequences for our study. First, the luminosity distributions are effectively luminosity distributions for $z < 0.1$ because only the GRB-SNe and some SNe Ic-BL are sampled at higher redshifts. Second, the luminosity distributions themselves may be overestimating the median luminosity if the non-detection of low-luminosity SNe is a significant issue. This is unquantifiable because rates of intrinsically dim SNe are unknown; however, a low-luminosity, nearby SN would be an object of interest (provided this is not a consequence of reddening). Our study shows that there appears to be a clear reduction in the number of SNe with $\log(L_{\rm p}) \approx 41.7$, yet there are clearly well-sampled SNe significantly below this luminosity. Given that the majority of these SNe are found at low redshift, and so would be observable at these luminosities, it appears that intrinsically dim SNe are not being missed in large numbers in the comoving volume that are being sampled. It must also be considered that SNe with relatively low ejecta and nickel masses are not seen; for example, SN 1994I was found

Table 2.13: Median values for the fully bolometric sample.

SN Type	$\log(L\mathrm{p})$	M_{Ni} ($\mathrm{M}_{\odot}$)
Ic-BL/GRB-SNe	$43.00\pm^{0.21}_{0.21}$	$0.34\pm^{0.13}_{0.19}$
Ic	$42.51\pm^{0.06}_{0.36}$	$0.16\pm^{0.03}_{0.10}$
Ib	$42.50\pm^{0.10}_{0.20}$	$0.14\pm^{0.04}_{0.04}$
IIb	$42.36\pm^{0.26}_{0.11}$	$0.11\pm^{0.04}_{0.04}$

to have $M_{\mathrm{ej}} < 1\mathrm{M}_{\odot}$ (Iwamoto et al., 1994), while SN 2007Y synthesised just $0.051\mathrm{M}_{\odot}$ of ^{56}Ni. This raises interesting questions of the SN mechanism and whether there is a lower limit on ejecta mass and nickel synthesis. Finally, I consider the effect of peculiar objects on our sample. This is generally minimised because peculiar objects (e.g., SN 2003bg, Mazzali et al. 2009; PTF12gzk, Ben-Ami et al. 2012; SN 2011bm, Valenti et al. 2012) do not constitute a significant proportion of each subtype, and if there are enough of them they become subtypes in their own right (e.g., SNe Ic-BL, GRB-SNe). I note that a good example of observational bias toward interesting objects is seen with the number of GRB-SNe that could be included in this study. There are 10 GRB-SNe that fulfil the criteria for inclusion, and this represents a significant fraction of those discovered.

2.9.2 Explosion characteristics

The median population statistics and relevant 1σ uncertainties for the fully bolometric sample are given in Table 2.13. As per Table 2.6, a hierarchy of peak luminosities is evident, with SNe Ic-BL/GRB-SNe generally more luminous than the SN Ic, IIb, and Ib populations. In terms of M_{Ni}, I find that most types of SNe synthesise similar amounts of ^{56}Ni with the exception of the broad-lined SNe Ic, where the median value for M_{Ni} is more than double that of the others. Additionally, the median $t_{-1/2}$ is found to be shorter for these SNe compared to their less-energetic cousins. The degeneracy between M_{ej} and E_{k} in Equation 2.6 means that without photospheric velocities, found

from spectral modeling, it is not possible to tell whether the typically narrower light curves of the SNe Ic is a consequence of smaller ejecta masses, more energetic explosions, or some amount of ^{56}Ni in the outer ejecta. Ejecta with significant amounts of ^{56}Ni mixed into the outer layers will rise more quickly as the diffusion time for the photons emitted in these regions will be less than that emitted more centrally. The models of Arnett (1982) assume that all light-curve powering sources are located centrally; if ^{56}Ni is located further out, then this model will return less-accurate values for the light-curve parameters.

2.9.3 Photometry

The scatter of light-curve colours at peak is unsurprising; there is no homogeneous explosion mechanism for SE-SNe as there is for SNe Ia. The reason for the narrowing of the colour curves after ~ 10 days is harder to explain. Attempts have been made to use this as a way of deriving host-galaxy extinction (e.g., Drout et al., 2011; Taddia et al., 2015), but this method is sensitive to the underlying spectrum, K-corrections, the quality of the photometry, the colours used, and the type of SN. It may have most applicability for low-redshift SNe.

The SNe Ic-BL appear to have bolometric peak coincident with the SED peak to the blue side of *V*, comparable to SNe IIb which are known for their blue spectra. This cannot be accounted for in the scatter of the distribution, as it falls short of covering the effective wavelength of *V*. A thorough investigation of this result cannot be undertaken with photometry and will require the use of spectra.

2.10 Summary

I have taken 85 SE-SNe from the literature and used the available photometry to build a set of optical pseudo-bolometric light curves and optical/NIR bolometric light curves. By using the same method and the same cosmological model, the database is as self-

consistent as possible. The photometry was corrected for Galactic and host-galaxy extinction where such information was available. I found that fewer than 50% of the SNe had known host extinction values, so I searched the literature for SNe Ib/c and SNe II with this information known. From these data a series of distributions was constructed, and the median host extinction for each SN type was found and used as an estimate to correct for reddening when deriving bulk statistics.

The light curves were then analysed to reveal the peak luminosity and various temporal properties which were used to investigate the characteristics of SE-SNe. The analysis revealed that $t_{-1/2}$ is correlated with $t_{+1/2}$ but showed significant scatter around this value. K-S tests of the cumulative distribution functions for the decay times of the SNe revealed that most were likely drawn from the same population with the exception of SNe Ic/Ic-BL and SNe Ic/IIb. However, the presence of the Type Ic SNe PTF11rka and 2011bm, which display broad light curves, and a relatively small sample size skew the SN Ic CDF. Conversely, it is found that the SNe Ib and IIb generally take longer to rise than the SN Ic population. Using the equations of Arnett (1982), one can estimate the mass to kinetic energy ratio of the ejecta, which is related to the rise time. These properties are degenerate and can only be fully determined via spectral modelling; consequently, I make no comment on the size, mass, or structure of the progenitor star.

It was also found that, in the absence of a known explosion time, the rise time of a light curve could be estimated from $t_{-1/2}$. A comparison between the peak values of the *UBVRI* pseudo-bolometric light curves and *UBVRI*NIR light curves of those SNe having enough data to build both revealed that a tight correlation forms in the $L_{\mathrm{p},UBVRI}$–$L_{\mathrm{p},UBVRI\mathrm{NIR}}$ parameter space that is independent of SN type, allowing the conversion of one value to the other. These relationships were then used to produce bolometric statistics for nearly all of the SN database.

It is shown that SNe Ic-BL and GRB-SNe occupy the upper part of the SE-SN luminosity distribution, with SNe IIb at the bottom. SNe Ic and SNe Ib show similar median peak luminosities. Using an approximation of "Arnett's law," the amount of ^{56}Ni synthesised in the core collapse of the stars that eventually go on to form the SN Ic-BL population is on average twice that of SNe Ic, Ib, and IIb. This is partly driven by the

fact that all GRB-SNe are broad-lined and luminous.

The colour curves of the multiband photometry in the sample were analysed. The peak magnitude, time to peak, $t_{-1/2}$, and $t_{+1/2}$ were calculated for each band and compared with those of the bolometric light curve. To determine the colour curves and the colour at maximum, for each SN *BgVRr* photometry was converted to g' and r' where necessary. Our results confirm that there is evidence of a narrowing in the spread of $g' - r'$ for SNe with Milky Way and host-galaxy extinction corrections applied at ~ 10 days past bolometric maximum, though there is still a large range of possible values in this region. It is shown that the approximate wavelength of temporally coincident peaks between the multiband photometry and the bolometric LC occurs around the peak of the V band ($\lambda_{\rm eff} = 5505$ Å) for all but GRB-SNe, which are blueward of this. The photometry allowed us to investigate the possibility of using single-band observations and a BC to derive the bolometric parameters. The smallest spread in values was found for the *R* and *I* bands, but this was not replicated with i', which has an effective wavelength between these two Johnsons-Cousins filters. The uncertainties involved would lead to poorly constrained luminosities; thus, I reject the notion of using a single band as a proxy for the bolometric light curve at peak.

The importance of knowing the host-galaxy extinction cannot be understated. The peak luminosity of a SN, and all of the subsequent characteristics derived from that, depend on knowing this property. As such, I suggest that future work involving SE-SNe place a high priority on calculating or estimating the extinction at the source. This could be done through medium/high-resolution spectra and analysis of the Na I D absorption lines, via some method involving the colour evolution, or preferably both. If the colour method is used it is imperative that K-corrections are included. It is appreciated that these methods are not without their problems, however, and further analysis of the extinction in the environments of SE-SNe is needed.

Finally, each subtype presented here suffers from small-number statistics; hence, I identify the need for well-sampled SE-SN follow-up observations, particularly in volume-limited surveys, in order to improve the statistics and enhance our understanding of the evolutionary paths of massive stars.

Chapter 3

Spectral analysis and classification

In Chapter 2 I investigated the physical properties derived from the bolometric light curves of 85 stripped envelope supernovae. These were sorted according to subtype and revealed that SNe Ibc are largely heterogeneous in their light curve behaviour. In this chapter I will consider the properties of SE-SNe that can be derived through analysis of their spectra.

The analysis of photospheric-phase spectra reveals important information about the physical properties of the SN. Unlike the bolometric light curves, physical information can by obtained directly from the spectra in the form of line velocities and equivalent widths. Several questions can be asked of the spectra of SE-SNe

- Is there a continuum in H line strength between H-rich and H-poor SNe?
- Is there a continuum in He line strength between He-rich and He-poor SNe?
- Can line blending be quantified?

In this chapter spectra are examined using empirical methods to classify and sort via envelope stripping and line blending. The results are then compared with parameters found through spectral models and the results used to investigate the relationship between different physical characteristics and SN type.

3.1 Method - Visual inspection

The SNe analysed here are listed in Table C.1 and were mostly selected from the SESNe database of Chapter 2 so as to provide comparative light curve properties, in particular the epoch of each spectrum with reference to bolometric maximum. I increased this sample by also including Ic-BL SN 1997ef (Mazzali et al., 2000; Iwamoto et al., 2000) and Type Ic SN 2004dn (Drout et al., 2011; Lennarz et al., 2012) as the former is an interesting object spectroscopically and the latter had photometry that was not previously available. I also include preliminary analysis on Type Ic SNe 2012ej, 2016P, 2016iae (Prentice et al. in preparation) and 2016coi[1] (Prentice et al., 2018). The public spectra for each SN were downloaded from WISeRep[2] (Yaron and Gal-Yam, 2012) and supplementary photometry from the Open Supernova Catalog (OSC)[3] (Guillochon et al., 2016).

Each spectrum was shifted to the rest-frame wavelength as given in Table C.1 however the spectra were not corrected for any kind of extinction, for two reasons. The first is that, even though Galactic extinction is known, host extinction is usually unknown and as host extinction normally dominates Galactic extinction then the bulk of the total extinction is unknown. Secondly, the analysis performed here relies on relative flux rather than absolute flux and is derived over $\sim$ 1000 Å regions which are small enough to mitigate the differences associated with extinction differential over wavelength. However, for aesthetic reasons extinction corrections were applied to plotted spectra if $E(B-V) > 0.1$ mag.

The next step was to visually inspect the spectra in our sample in bins of 5 days, from -12.5 to $+12.5$ days from bolometric maximum. If there were multiple spectra in each bin I chose the spectrum closest in time to the mid-point however, I also considered S/N and would prefer a spectrum if it was significantly better than the others. To mitigate the possibility of bias in the grouping, the spectra were not labelled with either name or classification.

[1] aka ASASSN-16fp
[2] http://wiserep.weizmann.ac.il/
[3] https://sne.space/

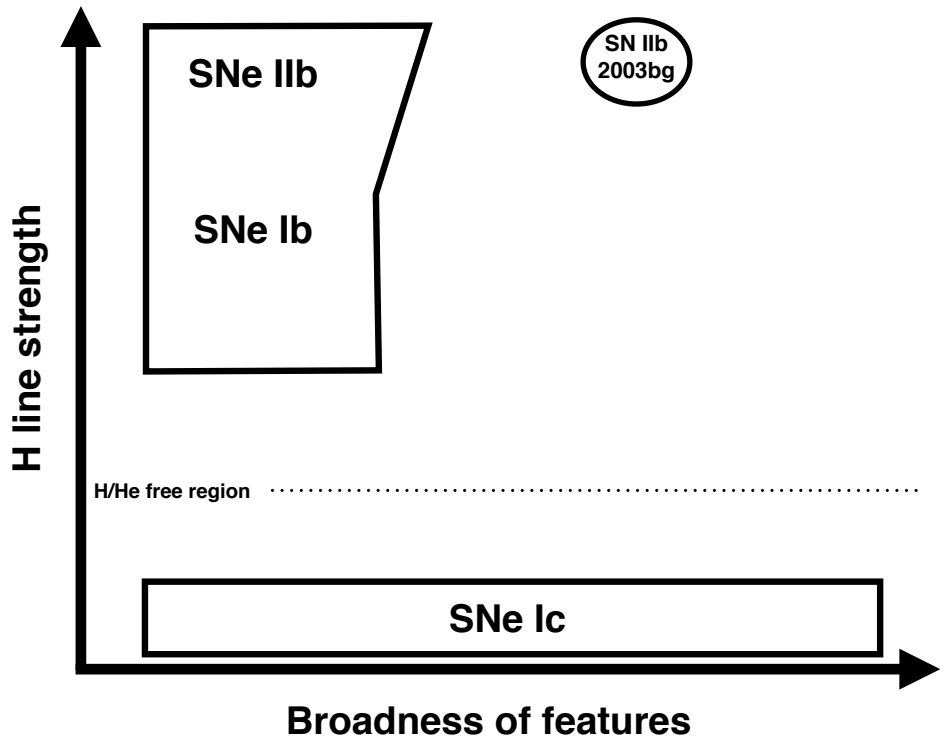

Figure 3.1: A visualisation of the two-axes categorisation of the spectra of the SNe. SNe IIb and Ib predominantly fell into the narrow-line and H/He-rich upper left quadrant. While some SNe IIb appeared to have slightly broader lines than others, the broad lined type IIb SNe 2003bg was a clear outlier. The SNe Ic, devoid of H and He, were sorted according to line broadness.

I grouped the spectra along two axes; hydrogen line strength, and broadness of absorption lines. This produced a sequence of He-rich SNe from IIb to Ib while the clear absence of H/He lines in SNe Ic created an immediate separation between these and SNe Ib/IIb. The "line broadness" axis was dominated by the sequence of SNe Ic from narrow lined to broad lined. This is visualised in Figure 3.1.

An example of the Hα line filtering process is demonstrated in Figure 3.2, which shows this region for a single pre-max spectrum for each SN sorted by the apparent strength of the absorption feature.

I then followed two separate analytical pathways which I describe in Section 3 for the SNe Ib/IIb (He-rich) and Section 5 for the SNe Ic (He-poor).

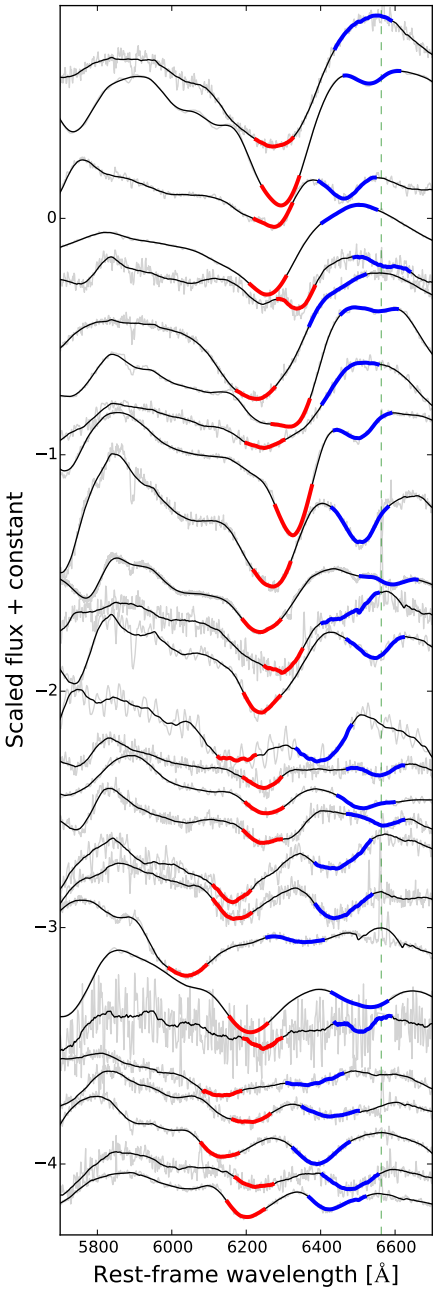

Figure 3.2: A simple example of a visual comparison between the Hα region of the SNe Ib/IIb sample at $t < t_{\rm max}$, with one spectrum per SN, sorted by apparent relative strength of the absorption to emission component. The red line represents the Hα absorption while the dashed line represents the rest wavelength of Hα, the blue line represents the position of He I 6678 Å at the velocity as derived from He I 5876. The Doppler shifted He I 6678 Å line is used to provide a lower limit to the velocity of the H absorption, but is not always present in early spectra. Ideally analysis of a single SN should be performed using many spectra with a clear temporal evolution to a few days beyond $t_{\rm max}$. The spectra have been normalised to their maximum flux and smoothed with an Savitzky-Golay filter.

3.2 He-rich SNe: The issue of hydrogen

The presence of hydrogen in SE-SNe has previously been discussed in the literature with Elmhamdi et al. (2006) and Deng et al. (2000) using SYNOW to identify Hα in various SNe Ib while Branch et al. (2006) and Parrent et al. (2016) find that SNe Ic as well as SNe Ib may have some remaining H. Tominaga et al. (2005) found signs of hydrogen in the peculiar Type Ib SN 2005bf while Fremling et al. (2016) presented the possibility of weak H in the optical and infrared spectra of SN Ib iPTF13bvn. Folatelli et al. (2014) suggested using used the H velocity profile as a way of separating SNe IIb and H-rich SNe Ib into different groups. Hachinger et al. (2012) used non-local thermodynamic equilibrium (NLTE) models to determine that less than $0.1 M_{\odot}$ of H can be present in SNe Ib before H lines begin to appear, but they speculated that the Hα line may be a Hα/Si II blend.

Figure 3.3 shows the canonical Type IIb SN 2011dh (Bersten et al., 2012; Arcavi et al., 2011; Ergon et al., 2014; Soderberg et al., 2012); the P-Cygni profiles of the hydrogen Balmer series are prominent in the spectra. On the other hand, there is also SN Ib 1999dn (Deng et al., 2000; Benetti et al., 2011) for which it is unclear if there is H present in the spectra. The P-Cygni profile at the position of the Hα line (~ 6200 Å) is weak and there is no indication of the higher Balmer lines. This line could also be due to Si II λ 6355 as in SNe Ic and Ia; a discussion of this can be found in Section 3.2.1, however I will refer to this feature as Hα throughout the discussion of He-rich SNe.

3.2.1 Hα or Si II 6355?

The positive identification of Hα in H-poor SNe is complicated due to the possible presence of the Si II 6355 Å line. This line is such that it differs from Hα by $\sim 10,000$ km s^{-1}, meaning that the $\sim$ 6200 Å feature could represent Si II at $6,000$ km s^{-1} or Hα at $16,000$ km s^{-1}, both of which are valid velocities for these atomic species in SN ejecta. The presence of Si II in SE-SNe is not unexpected because SNe Ic, like SNe Ia, show an absorption feature associated with this ion (see, for example, Parrent et al.,

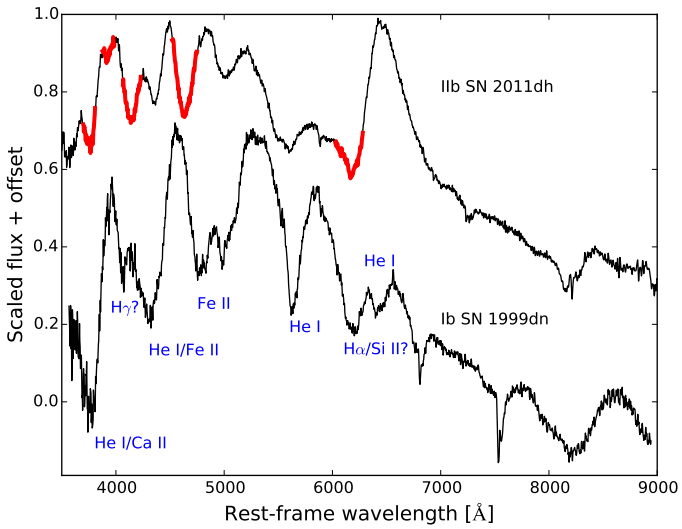

Figure 3.3: A comparison of the pre-peak spectra of Type IIb SN 2011dh and Type Ib SN 1999dn. Highlighted in red on the SN 2011dh spectrum are the Balmer series of absorption lines associated with H$\alpha-\epsilon$ which indicate a H rich outer ejecta. Comparatively, in SN 1999dn, aside from a feature in a similar position to Hα there is no clear indication of the higher Balmer lines.

2016). I show the $\sim$ 6200 Å region for examples of SNe Ib, Ic, and Ia in Figure 3.4.

In SNe IIb the absorption component of the Hα P-Cygni profile dominates any contribution from Si II, which is also likely constrained to a shell that is below the photosphere for some significant period of the evolution of the SN. Indeed, the unambiguous identification of this ion in SNe IIb is extremely difficult as the Hα line remains sufficiently dominant in the spectrum well past the photospheric phase ($\sim +40$ days).

If SNe Ib are considered, the lack of higher Balmer lines in the spectra, in addition to the potential presence of Si II, makes identification of the atomic species responsible for the feature at $\sim$ 6200 Å ambiguous. Matters are further complicated by the evolution in the spectra. H lines are expected to be stronger at very early times because little else is above the photosphere and Si II should be restricted to layers well below that of the H envelope (Sauer et al., 2006; Nakamura et al., 2001; Hachinger et al., 2012). As time progresses a Si II line should become more prominent as the photosphere recedes in velocity space, revealing the deeper laying ejecta. Conversely, H should reach a limiting velocity corresponding to the bottom of the shell with the line becoming progressively weaker as the ejecta expand and the optical depth of the

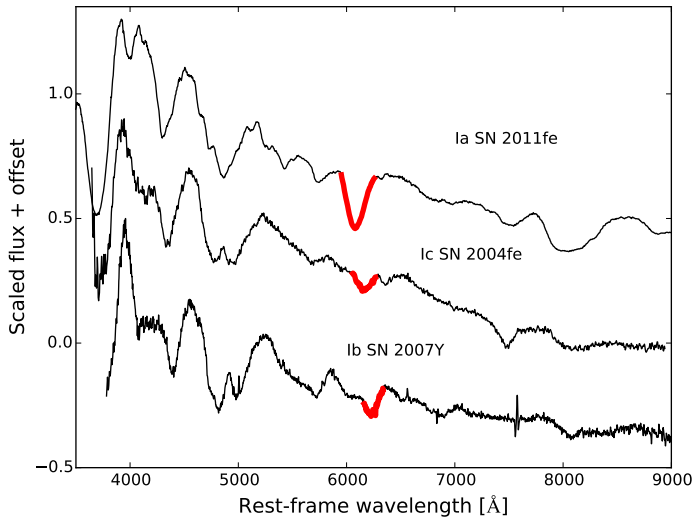

Figure 3.4: A comparison of the $\sim$ 6200 Å feature between SN Ia SN 2011fe (Mazzali et al., 2014), SN Ic 2004fe (Modjaz et al., 2014), and SN Ib 2007Y (Stritzinger et al., 2009). In SNe Ia and Ic this feature is attributed to Si II 6355, for SNe Ib such an assertion is less certain due to the presence of He in the outer ejecta which means that Si is buried deeper in the ejecta and there is a possibility of H in the outer layers of the ejecta. In SNe Ic and Ia the feature immediately redward of Si II 6355 is C II 6580 while in SNe Ib this line is dominated by He I 6678.

H envelope decreases. If the relative velocity of the two shells is $\sim 10,000$ km s^{-1} then it may be possible for the ~ 6200 Å feature to transition from being H-dominated to being Si II-dominated, with little more than an asymmetrical absorption component to indicate that this has happened.

I investigate this degeneracy by calculating the velocity of the ~ 6200 Å feature for our SN Ib sample and for narrow-lined SNe Ic while insisting on a logical stratification to the ejecta (Hachinger et al., 2012; Iwamoto et al., 1994) so that $v_{\rm H} > v_{\rm He} > v_{\rm SiII}$. The final discriminator is to ensure that the absorption feature does not extend significantly redwards of 6355 Å, the rest wavelength of the Si II line, as this would represent an unphysical situation. The result is shown in Figure 3.5.

With the exception of SN 2007uy and PTF12gzk most of the SNe occupy a similar region in the time/velocity plane. However, the velocities of SNe Ic are typically higher than those of SNe Ib. In addition to this, some SNe Ib show velocities that drop below that of the rest wavelength of the Si II line, which is a situation that is irreconcilable with the line being of that element. In most cases, for both SN types, the line disappears

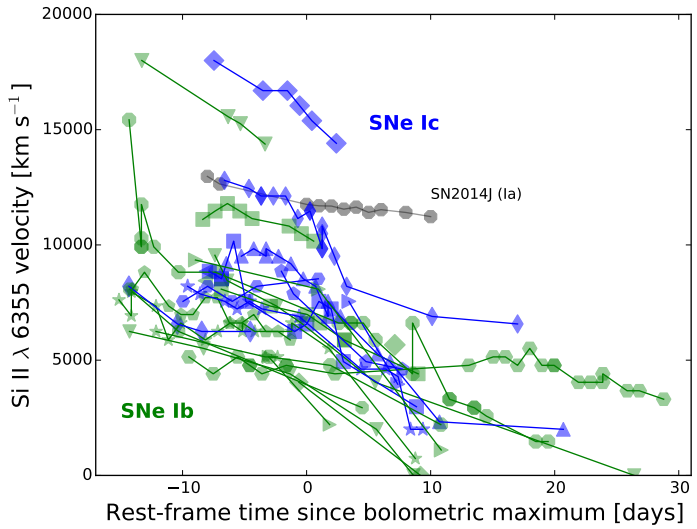

Figure 3.5: The velocities of the absorption line $\sim$ 6200 Å if attributed to Si II 6355. The line is followed from the time it unambiguously appears until it disappears or the feature is ambiguous. On average the velocity for SNe Ib is lower than that for the Ic SNe, though there are exceptions, notably Type Ib SN 2007uy where the velocity is extremely large. For some of the SNe Ib the feature drops below the rest-frame wavelength of Si II 6355, an unphysical situation indicating that the line is not produced by Si. For comparison is the Si II velocity for Type Ia SN 2014J (Ashall et al., 2014)

before it reaches a static velocity that would be indicative of the base of a shell.

The disappearance of the line in SNe Ib represents a serious problem if the feature at $\sim$ 6200 Å is attributed to Si II. With a He shell above the Si layer, the Si II strength should increase with time as more Si is exposed by the receding photosphere. Instead it is seen that the $\sim$ 6200 Å feature is strong initially (line strength for this feature is presented via equivalent width in Section 3.2.4) before fading and disappearing around ten days after peak. This is likely an issue with opacity, where the line forming region has insufficient density and so $\tau \sim 1$. If this is the case then the line-forming region should be in the outer layers of the ejecta, which is inconsistent with the position of a Si shell. For SNe Ic there is no He envelope and so Si should be exposed rapidly as the photosphere sits within the CO core material.

This reasoning does not mean that the presence of the Si II ion can be ruled out, but it does mean that H is taken to be a valid source for the line opacity and so I henceforth refer to the $\sim$ 6200 Å feature in SNe Ib as Hα.

3.2.2 H and He Line velocities

The velocity evolution for H and He is calculated from the Hα and He I 5876 Å lines using the maximum depth of the absorption feature and in most cases the lines were sufficiently well defined with no evidence of blending. However, at early times and shortly after maximum the features can be blended or less pronounced. In a situation whereby an absorption feature shows two minima I would consider the later evolution of the feature in order to attribute the minima to the correct species. The line velocities for each SN were fit with a low order spline and an approximate velocity was calculated for every day relative to maximum light. This was then used to calculated the mean velocity of all the SNe in each daily bin.

The velocity measurements are shown in Figure 3.6 for Hα and He I 5876. The velocities are broadly consistent with those found in Liu et al. (2016) for a slightly different data set. There is a continuum of $v_{\rm H}$ values but little overlap between SN sub-types. The situation for He I is different as the velocities do show considerable overlap, although some SNe Ib can show higher line velocities in individual cases. The He I 5876 measurement is of importance because the identification of this line is not ambiguous and will provide a useful reference point with regard to the structure of the SN ejecta.

Finally, the Hα feature itself is transient, especially in SNe Ib, and its lifetime can be limited to ~ 10 d past maximum light.

3.2.3 Is there evidence of Hα in the nebular phase?

Absorption

Modelling of the nebular data of SN 1993J at ~ 150 days by Houck and Fransson (1996) indicates that an absorption feature around 6380 Å, on the blue-wing of the [O I] 6300, 6363 Å line, is Hα absorption corresponding to a shell with width ~ 1000 km s^{-1} and an expansion velocity of $\sim 10,000$ km s^{-1}. Maurer et al. (2010) find that similar absorption features can be found in the [O I] line for other SNe of Type Ib and

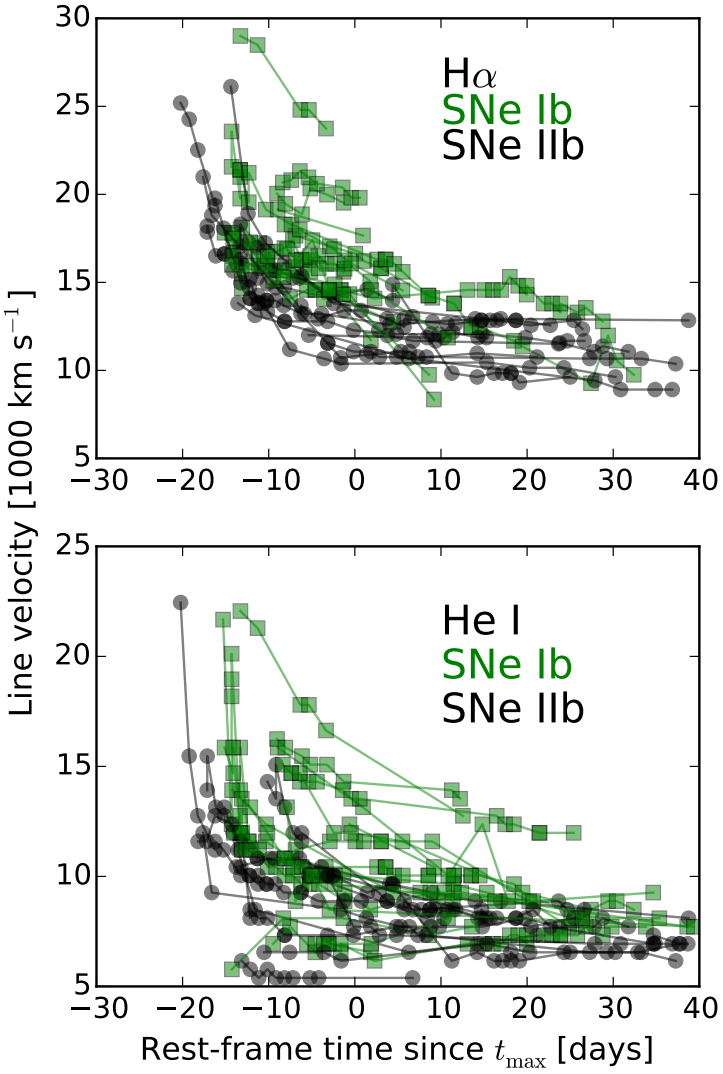

Figure 3.6: (Top) The Hα velocity curves for SNe IIb (black) and SNe Ib (green). For clarity no error bars are included but uncertainties are typically less than ± 500 km s^{-1}. The SN Ib velocities are typically higher than that for SNe IIb. (Bottom) The He I 5876 Å velocity curves, these lines show far more overlap in the values between subgroups than for hydrogen although SNe Ib show higher velocities on average.

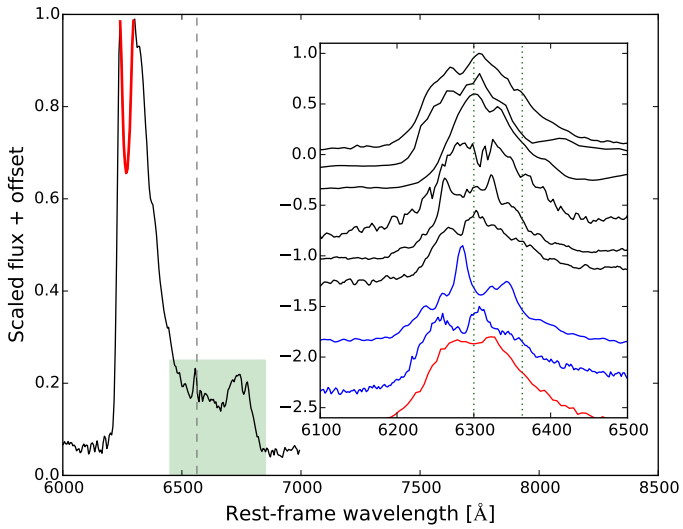

Figure 3.7: The nebular profile of Type IIb SN 2011fu at $+281$ days. The green region highlights the "flat-top" emission profile that is occasionally seen in He-rich SE-SNe, the dashed line at 6563 Å gives the rest wavelength of Hα, and the red region shows a possible absorption by Hα on the [O I] 6300, 6363 emission line. (Inset) The two dotted lines at 6300 and 6363 Å demonstrate that although the [O I] is a doublet, of which the 6300 Å component is the stronger part of the two, the split feature is not due to the doublet nature of the line. This line profile is common, but not ubiquitous, to He-rich SE-SNe. Various SNe IIb are in black, SNe Ib 2009jf and 2008D in blue, and Type Ic SN 2011 is included for reference in red.

IIb, as demonstrated for SN 2011fu in Figure 3.7, which they attribute to Hα. Thus, from this absorption feature a velocity can be calculated which would be expected to correspond to the densest part of the H shell, the base. The nebular Hα velocity as a function of the minimum photospheric Hα velocity is shown in Figure 3.8. Some of the SNe appear to have similar photospheric and nebular phase velocities while others do not. To test a possible linear correlation I apply the Pearson correlation coefficient to the data, the corresponding values of $r = 0.33$ suggests a weak correlation but at a p-value $= 0.32$ this is not significant.

Another cause of a double-peaked [O I] emission line is asphericity (Mazzali et al., 2005; Maeda et al., 2008), whereby the principle mass of O is ejected in a torus leading to a line profile that is viewing-angle dependent. This could be typical of a more energetic explosion, as is characteristic of some SNe Ibc, while the only comparatively energetic Type IIb is SN 2003bg Mazzali et al. (2009); Hamuy et al. (2009). It cannot be discounted that there is some degree of asphericity in the explosion of SNe IIb contribute to the splitting of the [O II] line. Indeed, both SN 2005bf (Tominaga

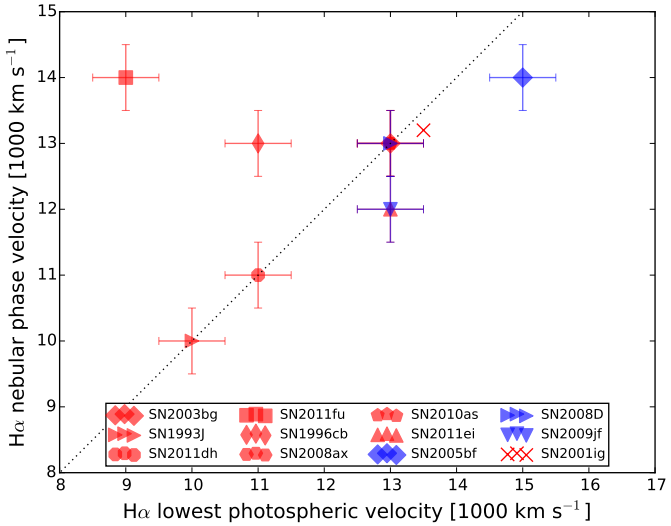

Figure 3.8: The velocity of the Hα absorption profile on [O I] 6300, 6363 during the nebular phase as a function of minimum photospheric velocity for the supernovae in our sample and that of SN 2001ig (Maurer et al., 2010). The dotted line represents the line of unity. Velocity measurements were approximated to the nearest integer value and an uncertainty of ± 0.5 included. There is a tendency for some of the SNe for the two velocities to take similar values but there are also some clear outliers, most notably SN 2011fu where $v_{\rm neb}$ is amongst the largest measured and $v_{\rm phot}$ the lowest.

et al., 2005) and SN 2008D (Mazzali et al., 2008) have been suggested to have significant deviations from spherical symmetry and their nebular [O I] line profiles are split. Another clue can be determined by the profile of [O I] 5577, where by intrinsic asymmetries should be apparent in this line as well, but this is not seen.

An alternative approach to asphericity is considered by Morales-Garoffolo et al. (2014a) with respect to SN 2011fu, whereby they attribute the double peak to a "blob" of O at ~ 4000 km s^{-1} in the direction of the observer. To investigate this possibility further the nebular profiles of several Type IIb and Ib SNe are plotted in the inset of Figure 3.7. Typically they all show some degree of offset with respect to the doublet lines, all in the direction of the observer with velocities of $\sim 2000 - 3000$ km s^{-1}, and most have a peak centred on 6300 Å. Neither approach is wholly convincing because every SNe IIb shows a blueshifted double peaked [O I] emission (with the exception of SN 2011hs where the [O I] line is single peaked but shows a high of asymmetry). The probability that all the SNe show motion towards the observer, or are viewed from the same angle, is very small. Yet such a thing would be required for all the nebular [O I] lines to be

Table 3.1: The profile of [O I] at nebular epochs

SN	Type	SN	Type
Double		Single	
1993J	IIb	2007Y	Ib
1996cb	IIb	2011hs*	IIb
2003bg	IIb	1999dn	Ib
2008ax	IIb	2007kj	Ib
2011dh	IIb	iPTF13bvn	Ib
2011ei	IIb	2005hg	Ib
2011fu	IIb	2007C	Ib
2005bf	Ib		
2010as	IIb		
2008D	Ib		
2009jf	Ib		
2004gq	Ib		

blueshifted or double peaked. I also conclude that the horns of the O I 6300, 6363 emission are not due to a doublet component. A similar conclusion was reached by Modjaz et al. (2009) and Tanaka et al. (2009c) in relation to SN 2008D, although the latter did attribute the line profile to a toroidal O distribution contaminated with host [O I] emission. Milisavljevic et al. (2010) investigated the nebular spectra of 5 SE-SNe and concluded that the [O I] line profile was probably not a consequence of toroidal ejecta or non-spherical geometry (in contrast to Modjaz et al., 2008) but instead suggested that the profile could be due to internal scattering or that the far side of the ejecta could be obscured by dust.

It is clear there are a variety of views as to the nature of the double-peak in He-rich SNe, our results, in conjunction with those of Houck and Fransson (1996); Maurer et al. (2010) suggest that Hα absorption may well be responsible for this feature. The reason for single profile nebular phase [O I] lines in H-poor He-rich SNe is that there is insufficient densities of H at late times, this could be reflected in the transient nature of the absorption line during the photospheric phase where it disappears before reaching a constant velocity. The profile of the nebular emission lines for the He-rich SNe in the sample are given in Table 3.1 and it can be seen that the more H-rich SNe show double peaked emission while those with less H can show single-peaked emission.

Emission

I now consider if it is possible to see Hα emission in the nebular phase. SNe IIb typically show a flat-top emission feature centred on the rest wavelength of Hα which has been attributed to the [N II] 6548, 6583 doublet (Jerkstrand et al., 2015) from N in the He shell, see Figure 3.7. However, I take the initial view that this feature could also be due to Hα, likely as a result of X-rays from ejecta/CSM interaction exciting the unshocked H shell (e.g., Houck and Fransson, 1996; Maurer et al., 2010; Matheson et al., 2000a; Maeda et al., 2015). I investigate this possibility by measuring the velocity of the redward edge of the feature, which defines the upper limit of the expansion velocity, although this is sensitive to density. I also consider the edge of the flat top, which represents the inner boundary (hence velocity) of the shell containing the line-forming region. Our results suggest that the apparent "minimum" velocity is always lower than the lowest H velocity derived in the photospheric phase. Inspection shows that the maximum and minimum velocities derived for the ~ 6500 Å region is broadly consistent with the He I 5876 velocities found in the photospheric phase which would tend to agree with the assessment of Jerkstrand et al. (2015) though some emission component due to Hα cannot be ruled out (For a discussion on Hα emission in the He shell see Maurer et al., 2010).

3.2.4 Hα and He I 5876 Equivalent width

The equivalent width EW for Hα, and for comparison He I 5876, is calculated in order to establish the temporal evolution of the line strength and to provide another comparative characteristic between the lines. The continuum level for the wavelength region in question was approximated by fitting the spectra with either a quadratic or linear spline in a range of a few thousand angstroms either side of the feature. Each continuum fit was inspected by eye and in most cases provided a reasonable fit to the continuum level. In the few instances where the fit was clearly inaccurate the spectrum was removed from the sample. The EW is then:

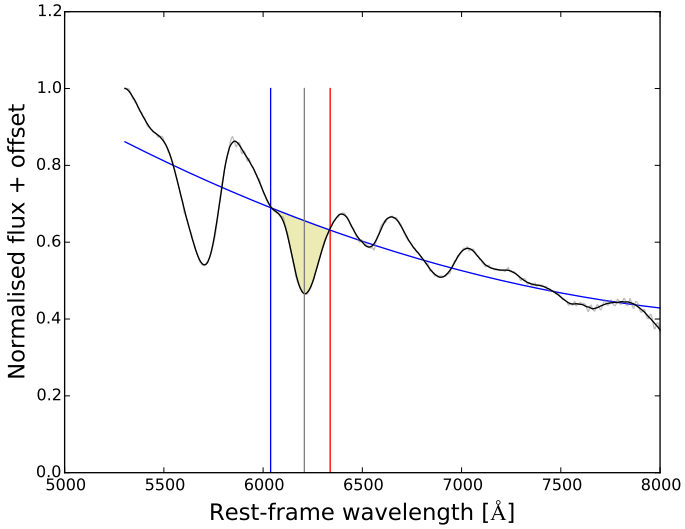

Figure 3.9: A demonstration of the results of the equivalent width fitting code. A pseudo-continuum, either linear or quadratic, is fit to the normalised and smoothed spectrum around the absorption feature. The yellow shaded region is then used to calculate EW.

$$EW = \int_{\lambda_a}^{\lambda_b} [1 - F(\lambda)/F_{\rm c}(\lambda)]\, d\lambda \tag{3.1}$$

where λ_a and λ_b are the wavelength boundaries, $F(\lambda)$ is the flux of the spectrum at λ and $F_{\rm c}(\lambda)$ is the continuum flux at λ. The largest sources of uncertainty come from the continuum fit and the boundary limits. In the former case the problem arises when there are significant emission peaks masking the underlying continuum. In the latter case one would ideally want to place limits at the edges of the absorption feature but multi-component lines require some estimation of where the boundary is. Fortunately these two uncertainties are rarely seen together, as spectra with prominent emission also tend to have well defined absorption profiles and spectra with multi-component lines tend to have less emission. A demonstration of this procedure is shown in Figure 3.9.

The curves of the total mean EW of Hα, and He I 5876, for the He-rich SNe are shown in Figures 3.10. Our results are consistent, in terms of relative positioning of the EW curves of the SN types, with Liu et al. (2016) for their sample, see Figure 3.11. Our actual values differ but this can be explained by the different methods used to process the spectra and calculate EW, the definition of "continuum", and different samples of SNe.

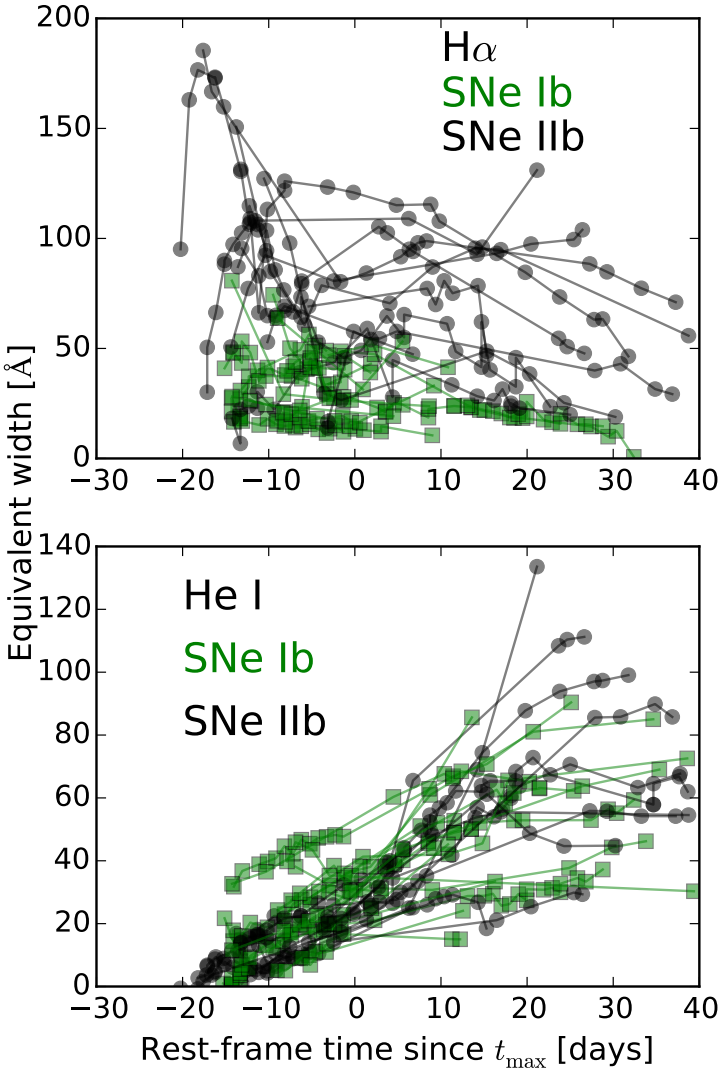

Figure 3.10: (Top) EW as a function of time for the Hα absorption feature. The strong H absorption of the SNe IIb is prominent, and show considerable scatter, but there is overlap with the strongest Hα lines of the SNe Ib sample. (Bottom) The same but for He I 5876, this line grows in strength over time but is especially strong in some SNe Ib.

In Figure 3.10 it can be seen that EW of Hα is weak in some SNe IIb shortly after explosion. This is because the temperature of the ejecta at this epoch is sufficient to ionize H and so there is little neutral H above the photosphere to provide line opacity. As the photosphere cools the absorption increases in strength to around bolometric maximum. For the SNe Ib the feature is typically weaker although the line strength of some SNe Ib overlaps with that of the weaker SNe IIb.

The EW of the He I 5876 line (Figure 3.10) is quite similar for most of the SNe with the line increasing in strength over time. This occurs because the photosphere gradually exposes the denser regions of He in addition to the increased γ-ray flux as the photosphere moves towards more ^{56}Ni rich regions which allows non-local thermodynamic equilibrium (NLTE) excitation of the exposed He (Lucy, 1991).

3.2.5 Hα emission to absorption ratio $f_{\rm em}/f_{\rm abs}$

As previously noted, the SNe were ordered based upon the relative strength of the H features, especially Hα, and it is apparent that there is a diversity of spectral shape within this region. In particular the relative intensity of the absorption component to the emission component varies amongst SNe and as a function of time within each SN.

I define a value $f_{\rm em}/f_{\rm abs}$, which is the ratio of the maximum intensity of the emission peak, relative to the local continuum, to the minimum intensity of the absorption trough. The local pseudo-continuum is calculated by using a linear function fitted to two points either side of the features and the errors on the ratio calculated by allowing these points to vary by 40 Å as shown in Figure 3.12. $f_{\rm em}$ and $f_{\rm abs}$ are then calculated by taking the absolute value of the continuum-subtracted maximum/minimum intensity. This value is derived from the P-Cygni profile and so is a useful measure of the extent of the envelope and the distribution of material within it. Very H-rich SNe have dominant emission peaks due to an extended H envelope.

I then calculate the mean of this value for early-time up to $t_{\rm max}$ but because spectral coverage is not so ordered as to provide one spectrum per day for every SN I interpolate

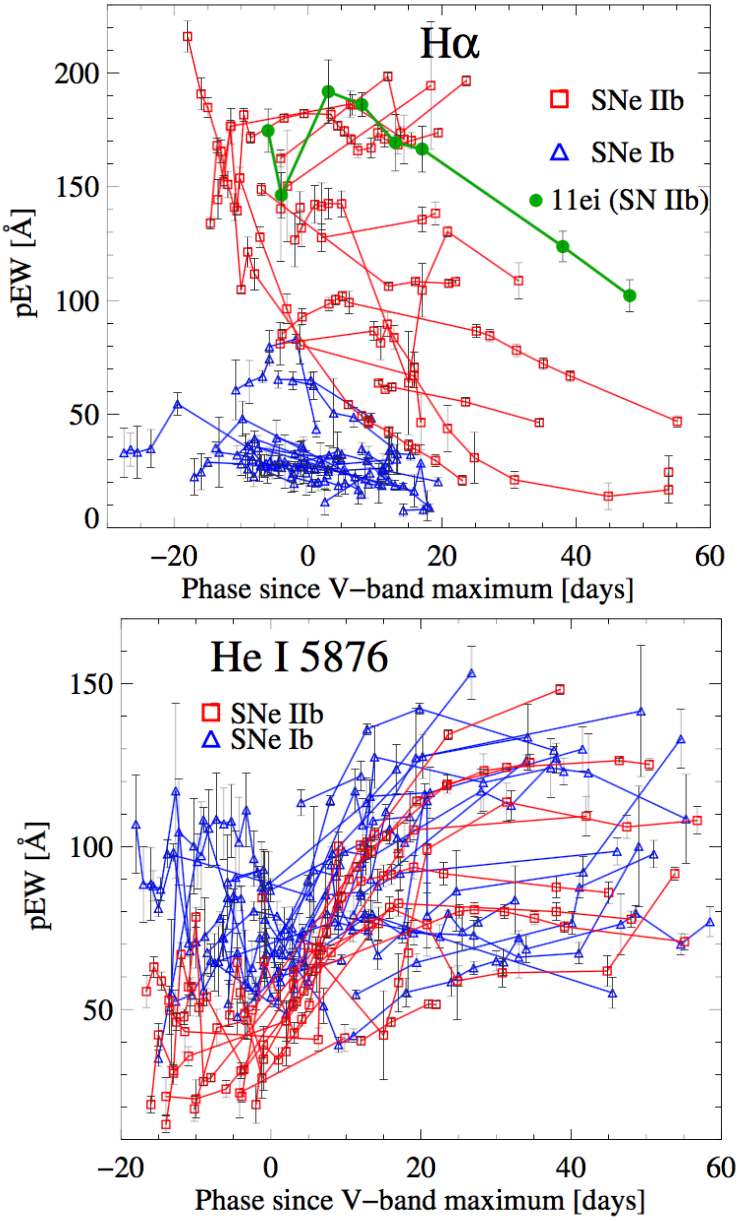

Figure 3.11: The EW curves of Hα and He I λ 5876 from Liu et al. (2016). Similarity in evolution and relative positions of the EW curves for the SN types can be seen with respect to Figure 3.10

the value of $f_{\rm em}/f_{\rm abs}$ between an early epoch, usually defined as the earliest possible spectrum, to the spectra around $t_{\rm max}$. I then take a value for each day and divide by the total number of days to give a pre-peak $\langle f_{\rm em}/f_{\rm abs}\rangle$ and repeat this method for EW. On this basis I aim to smooth out any weighting due to clustering of spectral observations and return a robust $\langle f_{\rm em}/f_{\rm abs}\rangle$ and $\langle EW\rangle$ that is representative of the early data. A final point is that I omitted the early phases of SNe that displayed indications of shock-breakout because the lack of lines in these SNe is reflective of high ionisation and not low neutral H opacity.

Typically the errors are relatively small, with the largest errors appearing when the emission component is weak. There is a note of caution with regard to this measurement in that the Doppler shifted absorption of He I λ 6678 can be present as a "v" shaped feature on top of the Hα emission. The effect can be to reprocess photons in the region between 6563 Å and the absorption feature effectively flattening the region around the emission peak. This will decrease the value of $f_{\rm em}$ and so decrease $\langle f_{\rm em}/f_{\rm abs}\rangle$. In theory this could lead to a SN positioned marginally in one subclass moving to the H-poor subclass below. However, this effect is mitigated in several ways; i) by the decaying strength of Hα emission and increasing strength of He I absorption over time, ii) that we're considering pre-peak data when the former is strongest and the latter weakest, and iii) when Hα emission is clear, it is easy to "subtract" the He I absorption from the profile. Thus the SNe most affected by this are the ones already weakest in H – SNe Ib, hence their classification will not change.

3.2.6 Other Balmer lines

Lines of the Balmer series other than Hα are normally a prominent feature of Type IIb SNe, however the identification of these lines in some of the SNe IIb is not clear. In Figure 3.13 it is shown that Type IIb SN 2010as lacks prominent Hβ and Hγ lines whereas Type Ib SN 2005bf shows hints of Hβ in its spectra. Similar features are not seen in other SNe in the sample because, in the regime under examination, Hβ must be strong enough to have some influence on the spectrum but not so strong that it forms

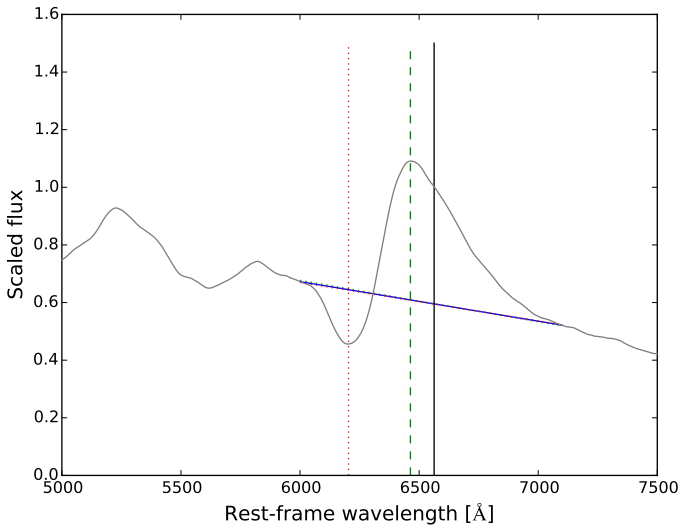

Figure 3.12: A demonstration of the $f_{\rm em}/f_{\rm abs}$ process. A smoothed and normalised spectrum is fit with a short linear continuum and the difference between the flux of the continuum and flux of the base (absorption) and peak (emission) is calculated. the ratio $f_{\rm em}/f_{\rm abs}$ is returned as an absolute value. Errors are calculated by allowing the limits of the continuum to vary over 40 Å.

a line which, along with S/N, limits numbers. Without the higher Balmer lines, the certainty of H being present in the ejecta diminishes significantly. This is why it is useful to trace the evolution of these lines and the properties of the Hα profile across the range of He-rich SNe as it demonstrates the pathway from H-rich to H-poor ejecta.

3.3 He-rich SNe - Reclassification

This work has shown the Hα region provides a continuum of line profiles and strengths for those SNe canonically classified as Type IIb (H-rich) and Type Ib (H-poor). I seek to re-evaluate these SNe in line with the degree of envelope stripping using the Hα line as the discriminator. In Figure 3.14 I plot $\langle EW \rangle$ as a function of $\langle f_{\rm em}/f_{\rm abs} \rangle$ for spectra up to the time of maximum light, giving a comparison of line strength against the line profile, Table 3.2 gives the values per SN. Examination of the figure shows that the IIb SNe take the most extreme values of $\langle f_{\rm em}/f_{\rm abs} \rangle$ and $\langle EW \rangle$ but there are regions of some similarity. While it may be compelling to view the distribution as evidence of two clear classes the separation is actually an artefact of the classification process.

Table 3.2: $\langle f_{\rm em}/f_{\rm abs}\rangle$, $\langle EW\rangle$, and classification of the He-rich SNe.

SN	$\langle f_{\rm em}/f_{\rm abs}\rangle$	$\langle EW\rangle$ [Å]	Old Classification	New Classification
SN2008bo	1.10	70.2	IIb	IIb
SN2011ei	2.06	93.7	IIb	IIb
SN2006T	1.96	97.5	IIb	IIb
SN2011hs	1.35	67.3	IIb	IIb
SN2011fu	2.74	28.8	IIb	IIb
SN2011dh	1.99	94.1	IIb	IIb
SN2003bg	2.34	75.2	IIb	IIb
SN1993J	3.16	35.6	IIb	IIb
SN2010as	0.32	78.3	IIb	IIb(I)
SN2008ax	0.54	108.0	IIb	IIb(I)
SN2006el	0.45	69.1	IIb	IIb(I)
SN1996cb	0.90	129.	IIb	IIb(I)
SN2008D	0.68	27.7	Ib	Ib(II)
SN2005bf	0.37	46.7	Ib	Ib(II)
SN1999dn	0.53	47.5	Ib	Ib(II)
SN2006ep	0.32	21.1	Ib	Ib(II)
SN1999ex	0.77	49.3	Ib	Ib(II)
SN2007kj	0.61	38.4	Ib	Ib(II)
SN2007Y	0.89	45.4	Ib	Ib(II)
SN2009jf	0.30	13.4	Ib	Ib
SN2009iz	0.21	26.3	Ib	Ib
SN2007uy	0.07	45.1	Ib	Ib
SN2005hg	0.26	14.9	Ib	Ib
iPTF13bvn	0.29	42.7	Ib	Ib
SN2009er	0.26	26.6	Ib	Ib
SN2004gq	0.28	18.3	Ib	Ib
SN2006lc	0.10	39.8	Ib	Ib

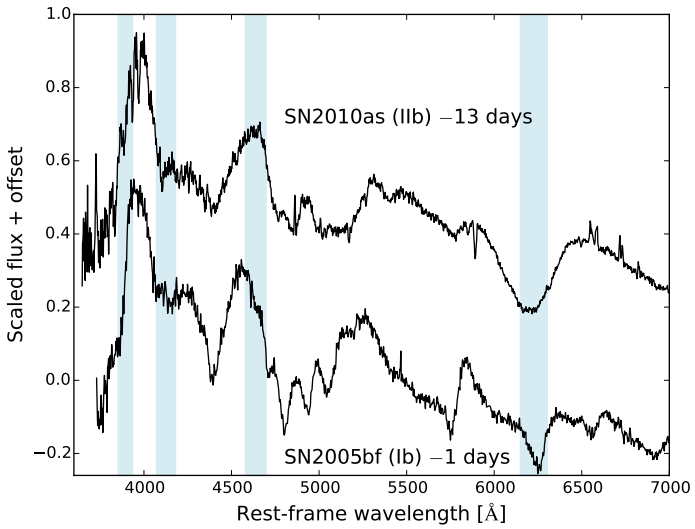

Figure 3.13: Example spectra of Type IIb SN 2010as and Type Ib SN 2005bf showing the regions (blue) occupied by H$\alpha - \delta$ at $v \sim 14,000 - 17,000$ km s^{-1}. In SN 2010as, at 13 d before maximum, there is no clear indication of the H lines other than Hα and nor do these lines appear at later times. In SN 2005bf (1 d before the first peak) there is a notch on the emission profile which may be an indication of Hβ, but there is no evidence of H lines at wavelengths shorter than this and this feature disappears after a few days.

In this case there is a "race to the middle ground" as over time SNe are classified due to spectral similarity with earlier SNe and their spectra become reference spectra (e.g., Modjaz et al., 2015) which broadens the definition until the two labels meet at some position in the middle. This appears to be linked to the visibility of the Balmer lines at λ shorter than Hα. The consequence of this is that the distinction between H-rich and H-poor SNe becomes arbitrary and does not reflect the continuum of H abundances.

Using these characteristics as a way of defining the Hα feature I propose the following classification system for the SNe listed in Table 3.2.

SNe IIb

These SNe have a pre-peak $\langle f_{\rm em}/f_{\rm abs}\rangle > 1$ indicating an emission dominated P-Cygni profile. These SNe are H-rich and all display a prominent series of Balmer lines in their spectra well past peak. In our sample every SN that falls into the IIb category was originally classified as a Type IIb SN and remains so here. In Figure 3.15 I show SN2011fu as an example for this group and demonstrate its evolution over the course

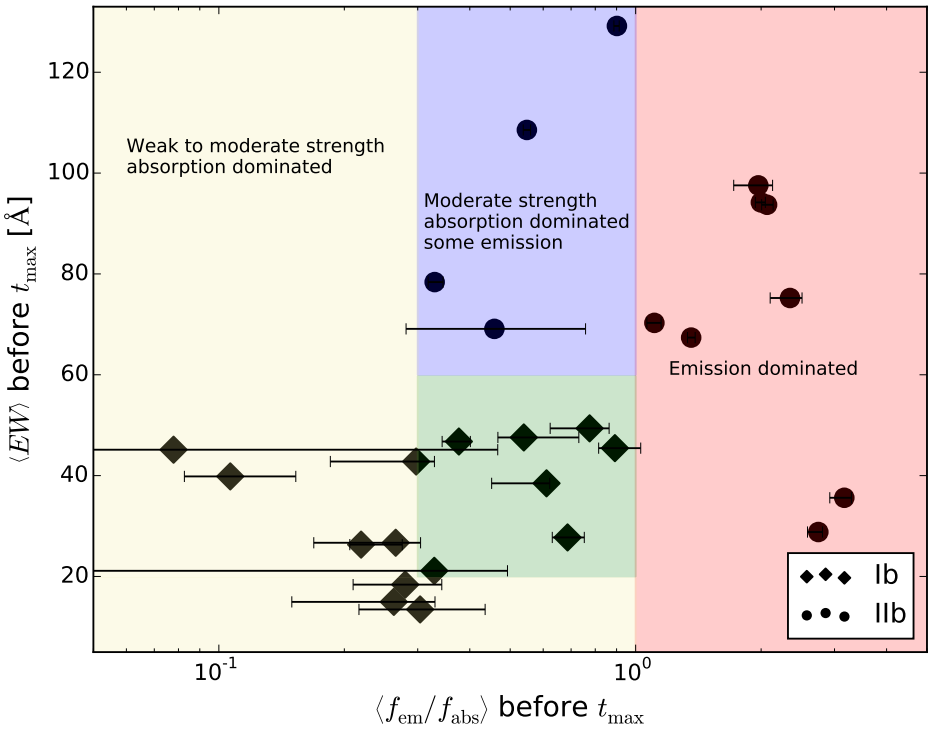

Figure 3.14: $\langle EW \rangle$ of Hα as a function of $\langle f_{\rm em}/f_{\rm abs} \rangle$ before peak, with this ratio being presented in logarithmic space for clarity. The plot is segmented to show that some SNe (red) have a flux excess $\langle f_{\rm em}/f_{\rm abs} \rangle > 1$, so the emission component dominates the absorption component, these SNe also tend to have moderate to large EW values. The group in the blue region have $0.3 < \langle f_{\rm em}/f_{\rm abs} \rangle < 1.0$, denoting absorption dominance but they also have strong lines with $\langle EW \rangle > 60$ Å. Below this is a group (green) with similar line profiles but overall weaker line strength with $20 < \langle EW \rangle < 60$ Å. Supernovae with either very absorption dominated line profiles and/or weak lines are found in the yellow region. The SNe appear to split between SNe Ib occupying the green and yellow regions while the SNe IIb are in the red and blue regions, because they are classified by similarity to reference spectra. This figure indicates there is a transition from Type IIb to Type Ib SNe through the blue and green regions as these SNe are separated by line strength. The distinct separation between SNe Ib and IIb is due to the "race to the middle ground" that occurs due to classification by spectral similarity.

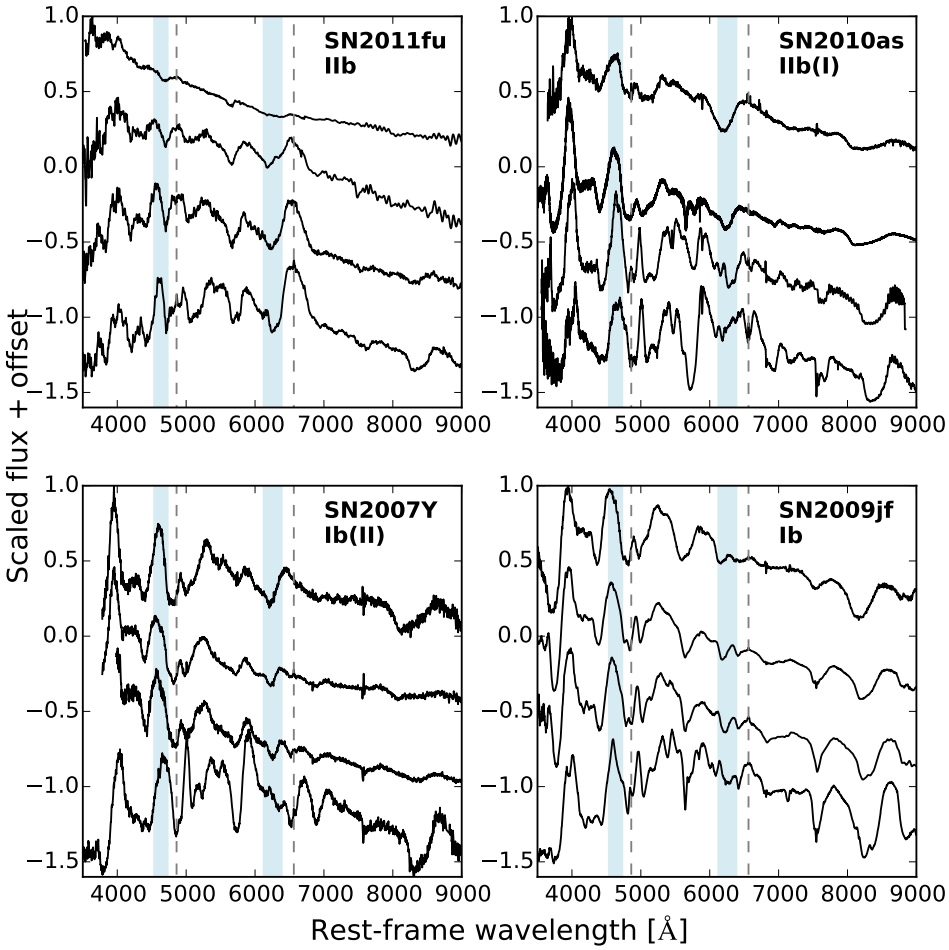

Figure 3.15: The evolution of representative spectra for SNe in the groupings related to the Hα $\langle EW \rangle$/ $\langle f_{\rm em}/f_{\rm abs} \rangle$ plane over the course of a month from the earliest spectrum available with an approximate cadence of 7 days. The dashed lines are placed at the rest wavelength of Hα and Hβ while the blue regions signify $8,000 < v_{\rm H} < 20,000$ km s^{-1} and define the region of interest. (Top left) H-rich IIb SN 2011fu shows many defining characteristics of SNe IIb; a hot shock-breakout phase early on followed by very prominent H lines with a strong Hα emission component. (Top right) SN 2010as is an example of the IIb(I) group, clearly the Hα profile is weaker than in SN 2011fu and decays strongly over time. The later spectra are He I and Fe II dominated blueward of Hα with no sign of Hβ. (Lower left) SN 2007Y, a member of the Ib(II) group, shows indications of a moderate to weak Hα line but there is ambiguity due to the presence of He I 6678, which cuts in to the Hα emission region. The early line profile shows some similarities to that of SN 2011fu and SN 2010as. (Lower right) The Type Ib SN 2009jf displays a weak feature around 6200 Å which is very quickly overwhelmed by He I 6678. The presence of any amount of H is unclear here and it may be possible to entirely attribute the line to Si II.

of a month.

IIb(I)

The IIb(I) group are defined by $0.3 < \langle f_{\rm em}/f_{\rm abs} \rangle < 1$ and $\langle EW \rangle > 60$ Å. They typically show strong H line profiles pre-peak but these lines weaken greatly over time. Their mean Hα P-Cygni profile is dominated by the absorption component and in some cases the remaining Balmer series lines can be weak or even unidentifiable. Of our sample all these SNe were originally classified as Type IIb and I use SN 2010as as a representative for this group in Figure 3.15.

Ib(II)

The Ib(II) group shows approximately half the Hα line strength of the IIb(I) group, $20 < \langle EW \rangle < 60$ Å, but occupy the same $\langle f_{\rm em}/f_{\rm abs} \rangle$ range. There is no obvious indication of the Balmer series of lines above Hα here. The SNe that are found in this region were all originally classified as Type Ib, however, analysis suggests that the SNe in this group have some amount of H in their ejecta but that it is relatively small compared to the IIb and IIb(I) groups, and so they represent the transition point between H-rich and H deficient SNe. An example of this group, SN 2007Y, is shown in Figure 3.15.

Ib

The final group is defined by typical SNe Ib. The SNe have weak absorption features around 6200 Å but the sheer lack of strength in emission is such that $\langle f_{\rm em}/f_{\rm abs} \rangle < 0.3$. The weak feature, in conjunction with He I line scattering in the same region, results in an ambiguous identification of this line. The 6200 Å line could be due to a very small mass of H or due to Si II. I use SN 2009jf as the representative of this group and plot it in Figure 3.15.

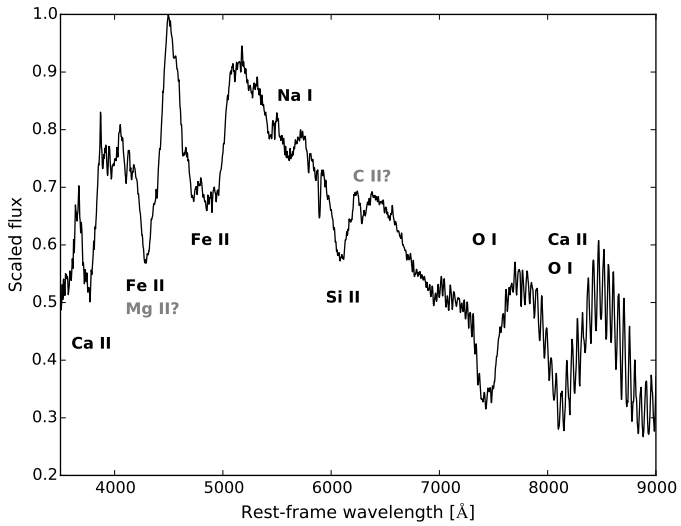

Figure 3.16: A spectrum of Type Ic SN 2004aw (Taubenberger et al., 2006) showing the ions that are responsible for the most prominent absorption features in a typical Type Ic SN. As with any expanding atmosphere, the lines are blue shifted in relation to the velocity of the material that is responsible for the line forming regions, in this case by $10,000 - 15,000$ km s^{-1}. The diversity of type Ic spectra is principally a product of the velocity and degree of blending of these lines.

3.4 He-poor SNe: Type Ic

The initial analysis described in Section 3.1 showed that there was a clear division between the He-rich SNe and the He-poor SNe; those of Type Ic (for an innovative investigation into the presence of He in SNe Ic see Modjaz et al., 2015). Unlike the He-rich SNe, in which the spectra are dominated by H and or He lines, SNe Ic are dominated by Fe II, Si II, O I, Ca II, and possibly Mg II and C II as shown in Figure 3.16.

Here SNe Ic are analysed within the context of line broadening because this is the defining characteristic used to classify them. If the SN shows "narrow" lines (e.g. SN 1994I Filippenko et al., 1995) it will be labelled as a Type Ic, while if the SN has "broad" lines it will be labelled Ic-BL. Unfortunately, the definition of "broad-lined" is subjective and tells us little about the properties of the spectra other than the SN has broader lines than SN 1994I. To confuse matters, the earliest spectrum of SN 1994I also showed shallow, broad lines before giving way to narrower features a day later, as shown in Figure 3.17. Had SN 1994I exploded a decade later then it is probable that it would have been classified as Ic-BL, at least initially. With more data it is now

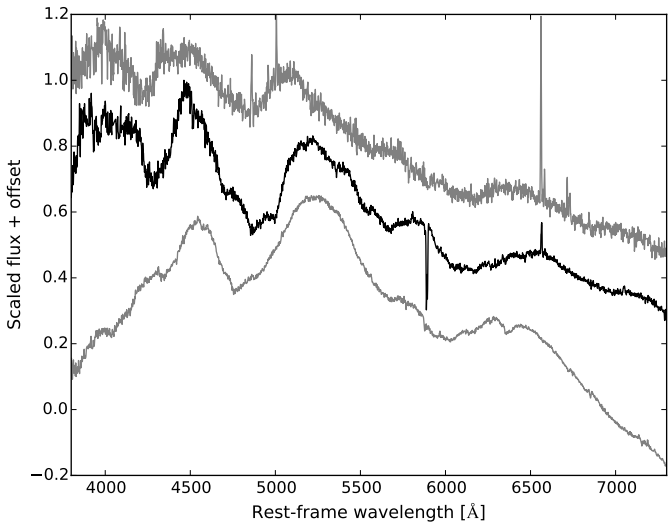

Figure 3.17: A comparison of the first spectrum of SN 1994I a few days after explosion (black) with Ic-BL SNe SN 2003jd (top) and SN 2002ap (bottom). The spectrum of SN 1994I shows similarities with both SNe and although it is considered a typical SN Ic and the lines narrow shortly after this time, it does demonstrate the subjective nature of the Ic-BL categorisation.

possible to quantify the degree of line broadening and provide useful information in the classification scheme.

3.4.1 Methodology - Counting features

I adopt a straight forward method to analyse the spectra of SNe Ic by counting the number of absorption features N that are visible. By doing this I take a measure of the degree of line blending which can then be related to $M_{\rm ej}$, $E_{\rm k}$, and the properties of their light curves. The intention is that this procedure should be easily replicable and provide information about the explosion characteristics but without the need for more complex analytic methods or modelling.

The first step is to note the constraints this method must work under, thus one must account for the range of wavelengths covered by different spectrographs and their respective S/N and "a feature" must be defined in such a way that is not ambiguous. With this in mind I take a core wavelength range of $4000-8000$ Å as this is within the range of most spectrographs. I then define a set of characteristic features within this range and one outside, as defined by the lines given in Table 3.3. I include the Ca II NIR

Table 3.3: Prominent spectral lines used to determine N

Ion	λ/ [Å]
Fe II	4924
Fe II	5018
Fe II	5169
Na I	5895
Si II	6355
O I	$\sim$7774 triplet
Ca II	NIR triplet

triplet because it is often, but not always, covered by spectroscopy and its presence is ubiquitous in SE-SNe. Furthermore I can infer properties of this line by observing the O I 7774 triplet as well as the Ca II H&K lines if the spectrum extends sufficiently far to the blue. For the former case the shape of the line will indicate a lack of blending if the line is sufficiently narrow and the spectrum extends far enough to capture the rise of the red-wing of the line. For the latter the velocity of Ca II can be measured, given that velocities of less than $\sim 27,000$ km s^{-1} are unlikely to result in line blending. The C II 6580 Å line, which is normally identifiable, is not counted because it is relatively weak and is close in velocity space to the much stronger Si II line.

Next, the lines in the spectra are examined noting which are blended and which are absent, and calculating the line velocity from the bottom of the absorption profile. Velocities are measured up to 30,000 km s^{-1}, although values in excess of this are difficult to measure as such velocities also lead to line blending.

Note that by attributing a feature to one of these lines I do not suggest it is a positive identification of that element. This is especially relevant to the region occupied by Na I D and Si II 6355 as several unidentified features can appear here. Thus I count a maximum of two features in this region. I define a feature as being a significant change in the spectrum that cannot be attributed to noise. Finally, I do not count all the visible features in a spectrum because each feature should be identifiable in other SNe spectra and the evolution of these features should be easily traceable.

Noise and other sources of contamination

The method of counting features is sensitive to the resolution and noise of the individual spectra. Noisy spectra make feature identification difficult particularly if there are groups of lines in close proximity to each other (e.g., the Fe II lines around 5000 Å) or in the case where features become very broad and shallow, such as with hypernovae (e.g., SN 2002ap and SN 1998bw). I provide an example of how resolution and S/N affects the spectra in Figure 3.18. Additionally, contamination from emission by other processes (e.g., host-galaxy, GRB afterglow) must also be considered because such processes can mask the SN spectrum leading to an absence of certain absorption lines which results in a flat region of the spectrum. This can be a serious problem for GRB/XRF SNe because the afterglow flux follows a power law decay in temporal and wavelength space which means that the contribution to the total flux from this component is stronger during the critical early phases.

To deal with this the first option is to check spectra taken shortly before and after the spectrum in question. This may allow a more robust estimate of the lines and their evolution at the epoch in question rather than relying on the noisy spectrum. The second option is to give a lower limit to the number of features. Given that noise primarily affects the Fe II lines around 5000 Å this provides an uncertainty of 2 lines. If the noise was excessive enough to mask other lines then the spectrum would be rejected.

Broad lines and $E_{\rm k}/M_{\rm ej}$

The importance of N is that it is a measure of the degree line blending and broadening in SNe, which is linked to the intrinsic density profile of the ejecta and which in turn affects $E_{\rm k}$. The total kinetic energy $E_{\rm k}$ of the ejecta is a measure of the energy of the explosion while ejecta mass, $M_{\rm ej}$, can give indications as to the zero-age main sequence (ZAMS) mass of the progenitor whereby a larger $M_{\rm ej}$ correlates with a greater $M_{\rm ZAMS}$ (Nomoto et al., 1994). $E_{\rm k}/M_{\rm ej}$ is the specific kinetic energy, giving the kinetic energy per unit mass, and as $E_{\rm k}$ is dominated by high velocity material it is also related to the

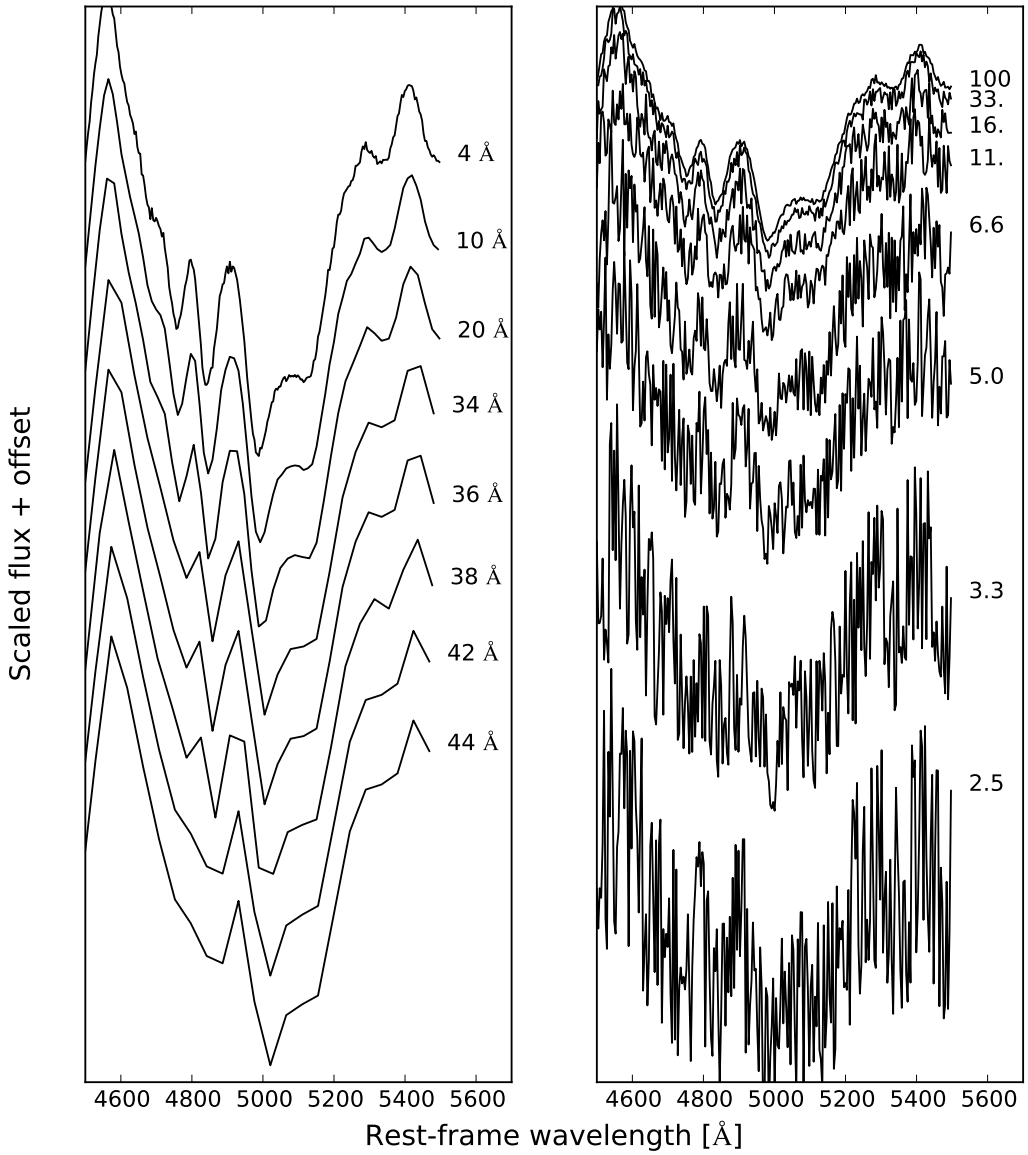

Figure 3.18: An example the effect of resolution (left) and S/N (right) on spectra. (Left) A spectrum of SN 2016iae has been binned in progressively larger wavelength bins. The key Fe II $\lambda\lambda$ 4924 and 5018 lines cannot be differentiated with a wavelength resolution greater than $\sim$ 44 Å. (Right) The same spectrum with random noise. Between a S/N of 5 and 3.3 the Fe II lines cannot be distinguished.

explosion mechanism. This is due to the fact that the total $E_{\rm k}$ is sensitive to the shape of the outer part of the ejecta density profile because a shallower density profile adds mass, and therefore opacity, at higher velocities. The addition of a small amount of mass a $v > 25,000$ km s^{-1} can add $\approx 10^{52}$ erg to the kinetic energy (see, for example, Mazzali et al., 2000, 2013; Nakamura et al., 2001).

3.5 Results

Figure 3.19 shows the results found when applying this method to three SNe covering narrow to broad absorption features. The need for good S/N is clearly seen when considering the Fe II regions.

N evolves differently over time for each SN but during the period before peak, and for some days afterwards, N increases as a function of time and never decreases. At later times the identification of features becomes more difficult as the continuum flux decreases, especially in the blue near the Fe II lines, and the density of the outer ejecta decreases sufficiently to significantly reduce opacity in some lines, in addition to this the structure of the spectra becomes more complex as low velocity elements become more prominent. The evolution of N before this epoch is towards 6 and 7 in most cases but in some situations (e.g. SN 1998bw, PTF10vgv (Corsi et al., 2012)) significant line blanketing around 5000 Å masks Fe II lines in this region, restricting the value of N.

As an example of the evolution of N, Figure 3.20 shows the $t_{\rm max}$ spectrum and the evolution of N in relation to the light curve for four SNe in our sample; SN 1998bw (Patat et al., 2001), SN 2002ap (Mazzali et al., 2002; Foley et al., 2003), SN 1994I (Richmond et al., 1996; Filippenko et al., 1995; Sauer et al., 2006), and SN 2007gr (Valenti et al., 2008; Mazzali et al., 2010). There is clear diversity in the shape and temporal characteristics of each SN and the evolution of N is not predictable or uniform although N never decreases with time. This latter behaviour allows upper limits on N to be placed at times earlier than the first spectrum.

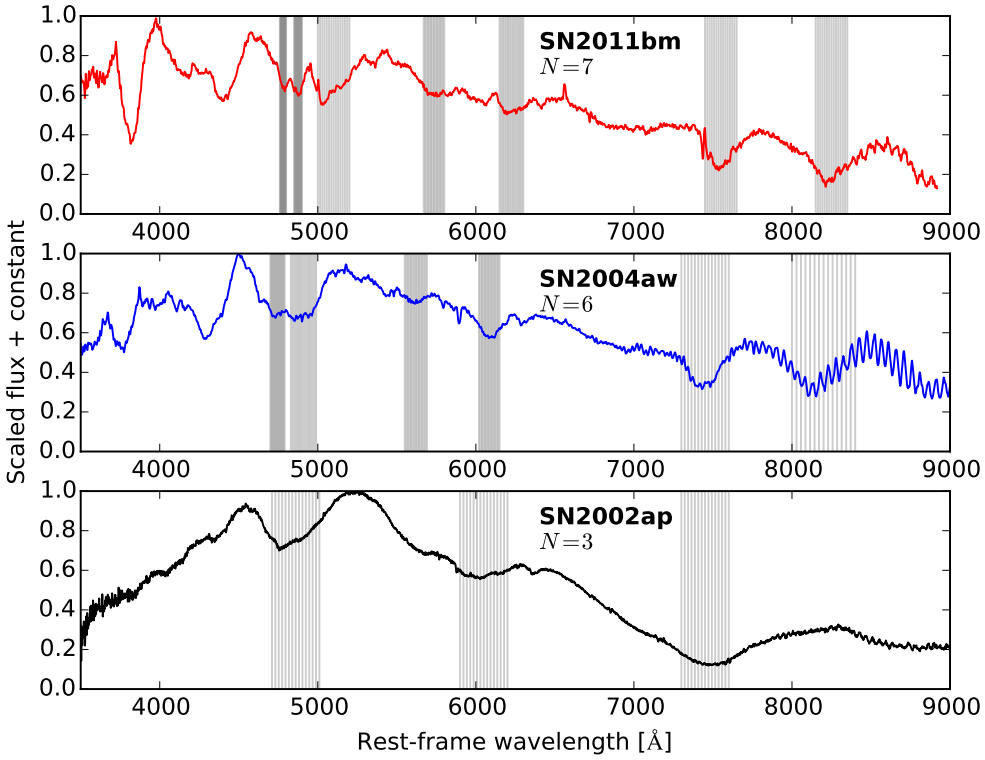

Figure 3.19: An example of SNe with different N, the lines counted towards N are denote by the grey regions. (Top) A spectrum of SN 2011bm with $N = 7$, as can be seen the Fe II 4924 and 5018 lines are clearly unblended. Because of the limited wavelength range of many spectrographs I do not count anything blueward of the Fe II 4924 line, however, if present the Ca II H&K lines can be used to limit the velocity of the Ca II shell. The absorption feature directly blueward of the Fe II 4924 line is a further series of Fe II lines. (Middle) SN 2004aw shows blended Fe II lines although the rest of the designated features are unblended. (Bottom) A spectrum of SN 2002ap indicating severe line blending. The Fe II lines are completely blended as are O and Ca. The Si II 6355 feature is broad, however it is not blended with the Na I D line, which itself is not clearly apparent. It may be appearing around ~ 5700 Å but is not counted here.

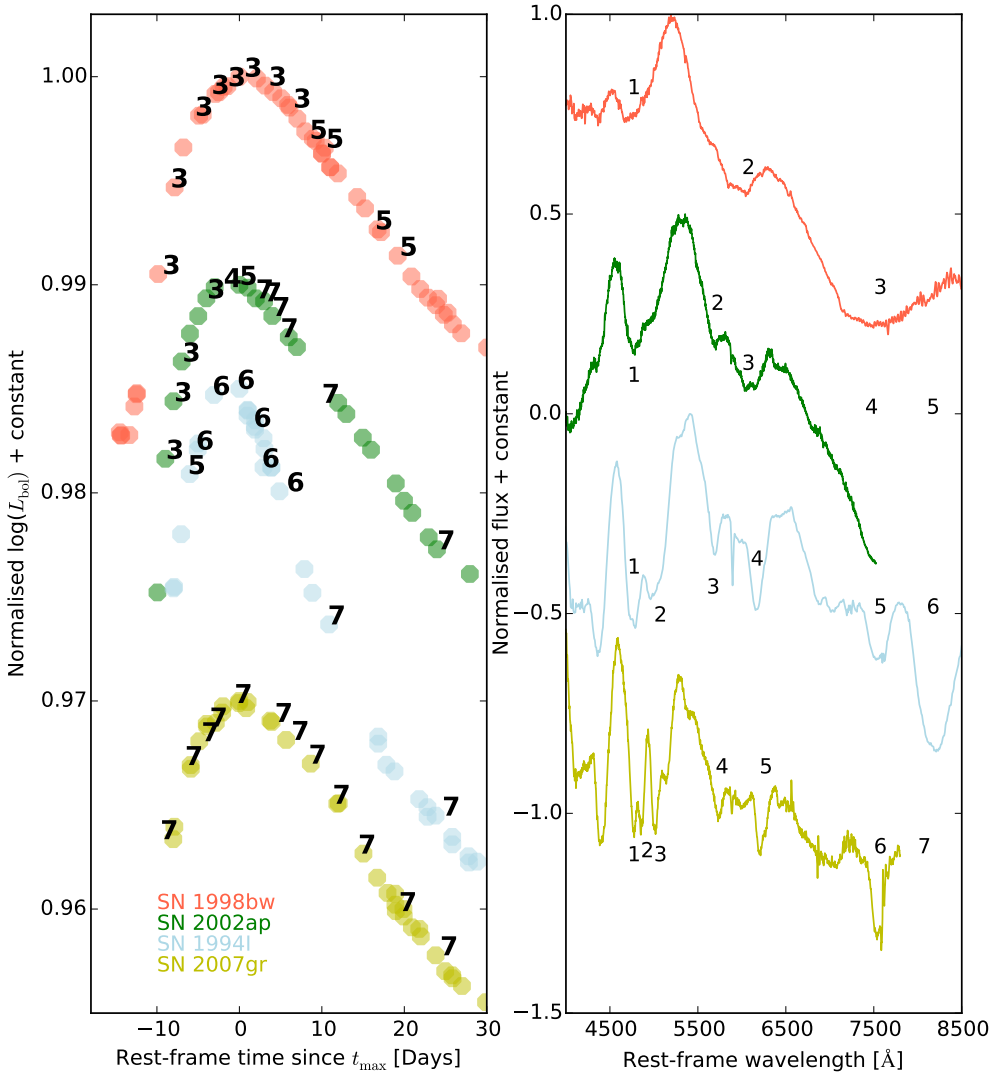

Figure 3.20: (Left) The normalised and offset bolometric light curves of our reference SNe. The number of features N in the spectra is shown as a function of epoch, the evolution of N is not entirely predictable as shown by SN 2002ap where $N = 3$ before maximum but rapidly evolves to $N = 7$ shortly after maximum while SN 1994I takes much longer to reach $N = 7$. (Right) The maximum light spectra of the reference supernovae, the number of features counted and their location. The Ca II NIR triplet is present in SN 2007gr at this epoch however the spectrum does not extend sufficiently far to the red to show it, while in SN 2002ap there is enough evidence in spectra around this epoch to suggest that the lines are in the process of separating.

N at $t_{-1/2}$, $t_{\rm max}$, and $t_{+1/2}$

N can be evaluated as a function of time but because of the discrete values of N and the different temporal characteristics of each SN I consider just the value of N at comparative epochs in the evolution of the LC. The time of bolometric maximum $t_{\rm max}$ is used as a fiducial t_0. I also consider two other reference times, the first is $t_{-1/2}$, which is the time taken for the light curve to rise from $L_{\rm p}/2$ to peak luminosity $L_{\rm p}$, $t_{-1/2}$. The second is $t_{+1/2}$, the time taken for the light curve to decay from $L_{\rm p}$ to $L_{\rm p}/2$. These times are used to investigate the number of features in the spectra scaled to a similar epoch in the evolution of the light curve. Spectra are selected within a bin around ±2 days for $t_{-1/2}$, ±4 days for $t_{\rm max}$ and ±6 days for $t_{+1/2}$, where the windows reflect the fact that a day represents a greater proportion of the evolved time earlier in the light curve.

In some cases there was sufficient photometry to measure $t_{-1/2}$ for individual bands but insufficient photometry to construct a bolometric LC. To compensate for this I took the SNe with bolometric $t_{-1/2}$ and investigated how the multi-band $t_{-1/2}$ varied in comparison. It is found that $t_{-1/2}$ for the *gVR* bands were generally within two days of the bolometric $t_{-1/2}$, and for most SNe it was closer to one day. Thus, for SNe which lacked a bolometric $t_{-1/2}$ but had earlier photometry I used the $t_{-1/2}$ for *VRg*, prioritised by their respective order.

Table 3.4 gives the line velocities and overall N of SNe with spectra at $t_{-1/2}$ while Table 3.5 gives the same for spectra at $t_{\rm max} \pm 4$ days. Finally, the spectral velocities at $t_{+1/2}$ are given in Table 3.6; I do not list N here because the degree of blending in the Fe II region between $4500 - 5000$ Å is ambiguous owing to the decaying strength of these lines in some of the spectra. If the S/N is sufficiently good then in most cases N takes a value of 6 or 7. The post peak evolution of He-poor SNe spectra is discussed in Section 3.8.2.

Table 3.4: N and estimated velocities in SNe Ic at $t_{-1/2}$

SN	Type	Epoch [days]	Fe II 4924 [km s^{-1}]	Fe II 5018 [km s^{-1}]	Fe II 5169 [km s^{-1}]	Na I [km s^{-1}]	Si II [km s^{-1}]	O I [km s^{-1}]	Ca II [km s^{-1}]	N
1994I	Ic	-5.26	16,000		16,000	11,000	11,000	11,000	17,000	6
1998bw	GRB-SN	-9.33		Blended		Blended		Blended		3
2002ap	Ic-BL	-6.98		Blended		Flat	23,000	Blended		3
2004dn	Ic	-9.52		Blended?		10,000?	9,000	10,000	15,000	¿5[a]
2004fe	Ic	-7.8	13,000		13,000	9,000	9,000	11,000	16,000	6
2006aj‡	XRF-SN	- 5.3		Blended		Flat	14,000	Flat		2
2007gr	Ic	-8.6	11,000	11,000	11,000	10,000	9,000	10,000	14,000	7
2009bb	Ic-(BL?)	-4.3		Blended		30,000	30,000	17,000	30,000	5
2010bh*	GRB-SN	-5.2		Blended			Flat			1
PTF10vgv	Ic	-7.4		Blended?		Flat	15,000	Flat	¡10,000	¿3
2011bm*†	Ic	-14.2	10,000	10,000	10,000	9,000	6,000?	10,000	10,000	7
PTF12gzk*	Ic	-8.5	27,000 (Blended)		27,000	22,000	21,000	23,000	23,000	6

[a] N is almost certainly 6 or 7

‡ SN 2006aj is severely contaminated by afterglow and host-galaxy lines

*$t_{-1/2}$ estimated from V or R band photometry

† $t_{-1/2} \sim 22$ days, this spectrum is the first with decent S/N

Table 3.5: Number of features and estimated velocities in SNe Ic at $t_{\max}$

SN	Type	Epoch [days]	Fe II 4924 [km s^{-1}]	Fe II 5018 [km s^{-1}]	Fe II 5169 [km s^{-1}]	Na I [km s^{-1}]	Si II [km s^{-1}]	O I [km s^{-1}]	Ca II [km s^{-1}]	N
1994I	Ic	0.7	13,000		13,000	11,000	9,000	11,000	>13,000	6
1997ef	Ic-BL	-3.0	20,000			flat	13,000	17,000	20,000	4
1998bw	GRB-SN	0.58	Blended			X	15,000	Blended		3
2002ap	Ic-BL	0.0	>15,000			11,000	9,000	10,000	15,000	5
2003jd	Ic-BL	0.25	>15,000			13,000	13,000	>15,000	-	>4
2004aw	Ic	0.3	15,000		15,000	14,000	11,000	13,000	15,000	6
2004fe	Ic	0.0	11,000		11,000	10,000	8,000	<12,000†	<17,000†	6
2005az	Ic	1.0	8,000	8,000	8,000	6,000	11,000	-	-	7‡
2006aj	XRF-SN	0.4	21,000	21,000	21,000	X	21,000	15,000	21,000	6
2007gr	Ic	-0.6	10,000	10,000	10,000	9,000	7,000	9,000	<13,000†	7
2009bb	Ic-BL	1.6	Blended?			22,000	20,000	19,000	24,000	>5^{a}
2010ah	Ic-BL	-1.5	Blended			X	18,000	Blended		3
2010bh	GRB-SN	0.0	Blended			25,000	32,000	-	37,000	4
2011bm	Ic	0.0	-	-	-	-	-	-	-	7‡
PTF10vgv	Ic-(BL?)	3.4	Blended			Flat	7,000	10,000	15,000	¿4
2012ej	Ic	2	7,000	7,000	7,000	7,000	5,000	-	-	7
PTF12gzk	Ic	-0.6	22,000		22,000	19,000	17,000	16,000	21,000	6
2016P	Ic-BL	-3.0	Host contamination			14,000	Host contamination	-	16,000	6
2016coi	Ic-BL	0.0	Blended			14,000	14,000	Blended		4
2016iae	Ic	-0.1	13,000	13, 000	13,000	11,000	9,000	11,000	16,000	7

† Upper limit derived from earlier epochs

‡ For SN 2005az spectra do not extend redward of 7000 Å but the number of features is almost certainly 7 as the FeII lines are unblended. For SN 2011bm I am able to give the number of features because they had split before the time of bolometric maximum

- denotes that the feature is not covered by spectrum

[a] Contamination by host galaxy lines and depressed flux in blue, likely $N = 6$ or 7

X denotes that the feature is not visible

Table 3.6: The estimated velocities in SNe Ic at $t_{+1/2}$. All Fe II lines are given one velocity, the degree of blending in many cases is unknown at this epoch.

SN	Type	Epoch [days]	Fe II 4924 [km s^{-1}]	Fe II 5018 [km s^{-1}]	Fe II 5169 [km s^{-1}]	Na I [km s^{-1}]	Si II [km s^{-1}]	O I [km s^{-1}]	Ca II [km s^{-1}]
1994I	Ic	8.7		10,000		10,000*	4,000	8,000	10,000
1997ef	Ic-BL	24		10,000		7,000†	4,000	-	-
1998bw	GRB-SN	16.4		15,000		11-13,000	6,000	5-7000	15,000
2002ap	Ic-BL	15		10-15,000		7-11,000	4,000	6-8,000	10-15,000
2003jd	Ic-BL	17.9		15,000		12,000	7,000	-	-
2004aw	Ic	20		12-15,000		7-9,000	7,000	10,000	10,000
2005az	Ic	27		9,000		7,000	13,000	-	-
2006aj	XRF-SN	9		20-23,000		flat	15,000	15,000	20-23,000
2007gr	Ic	14.4		7,000		7,000	4,000‡	7,000	7-8,000
2009bb	Ic-BL	15.5		13-25,000		16,000	12,000	13,000	16-22,000
2010bh	GRB-SN	10		Blended		flat	30,000	flat	30-40,000
2011bm	Ic	43		6,000		6,000	flat	7,000	6,000
PTF10vgv	Ic-(BL?)	7.3		12,000		Flat	5,000	10,000	12,000
PTF12gzk	Ic	26		17,000		12,000	8,000	10,000	17,000

*possibly dominated by He I 5876

† Multi-component base, velocity of red component used

‡ Ambiguous identification

Table 3.7: Common line blending combinations

N	Description
3	Fe II blend, Si II, O I/Ca II blend
4	Same as $N = 3$ but with visible Na I
6	Fe II 4924 and 5018 blended, all other lines separate
7	All lines separate

3.5.1 The effect of line-blending on N

The value of N is a discrete number and there is a prevalence for certain values which correspond to particular sets of line blending, which are listed in Table 3.7. Figure 3.19 shows three example SNe with the features highlighted. The effect of line blending and broadening is apparent as one looks down the plot and the importance of the Fe II 4924 and Fe II 5018 lines, and O I and Ca II NIR to the value of N is also apparent.

The blending of absorption features gives clues as to the shape of the density profile of the ejecta and, by proxy, $E_{\rm k}$. In this section I discuss the situations in which lines transition from being blended to being separate.

Line velocity and spread, and the effect on line blending

The two main regions of interest are the blending of Fe II 4924, Fe II 5018, and the Fe II 5169, 5169, 5235 group with each other and the blending of the O I 7774 triplet and Ca II NIR triplet. In velocity space the Fe II lines are separated by ~ 5600 km s^{-1} (for Fe II 4924 and 5018) and $\sim 10,500$ km s^{-1} (for Fe II 5018 and Fe II 5169) while the O I 7774 triplet and Ca II NIR lines are separated by $\sim 27,000$ km s^{-1}. This represents a good sampling of log-spaced velocity, which is why line blending is sequential. Thus from this cursory analysis one can expect that very high velocity ejecta is required to blend O and Ca II, whereas the Fe II lines require a less substantial velocity differential. Note that it is not sufficient for the ejecta to be high velocity; the values given here are the velocity differentials, that is the spread Δv over which the atom or ion must provide sufficient opacity. If the lines were simply offset by $27,000$ km s^{-1} then O I 7774 and Ca II NIR would not blend, as can be seen in PTF12gzk (Ben-Ami et al., 2012) where

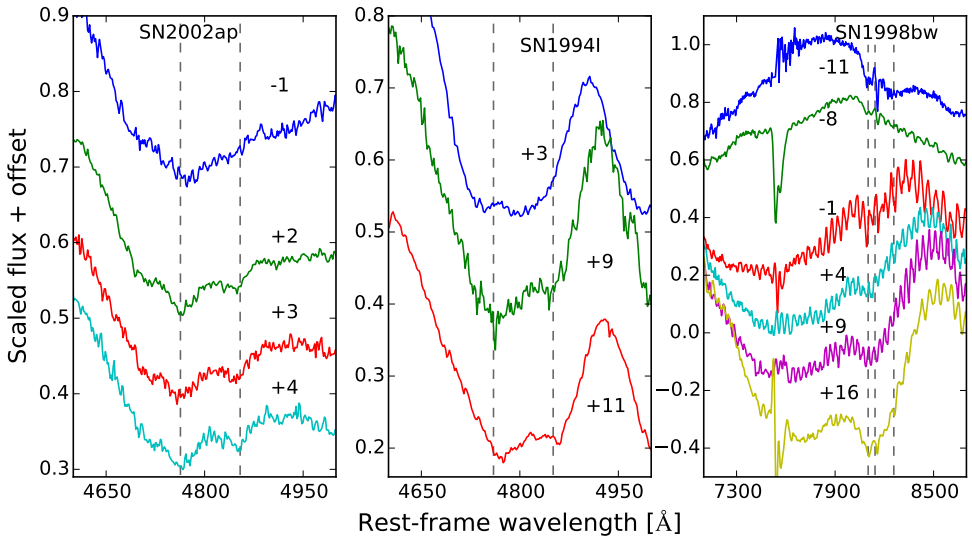

Figure 3.21: (Left) The evolution of the Fe II 4924 and 5018 features in SN 2002ap; the grey dashed line represents the lines shifted by $\sim 10,000$ km s^{-1}. The two lines emerge out of the broader feature over a period of two days. (Centre) The same as SN 2002ap but for SN 1994I. The velocity of the Fe II lines is $\sim 10,000$ km s^{-1} but they are weaker and take longer to appear in terms of light curve evolution than for SN 2002ap. (Right) The evolution of the O I and Ca II blend for SN 1998bw. At -11 days there is an indication of material contributing to the opacity which would match Ca II at $\sim 15,000$ km s^{-1}, however it is not possible to say if this is Ca II or not. After peak the Ca II NIR triplet lines become prominent at a velocity of $\sim 13,000$ km s^{-1}.

the line velocities are typically $> 20,000$ km s^{-1} but $\langle N \rangle = 6$.

Deblending

Figure 3.21 shows how various lines become deblended in the spectra, although it is noticeable that this tends to occur around or after peak in most SNe. The broad-lined supernovae provide a useful study into this process because they represent the largest possibility for change in the spectra. Lines deblend as the opacity velocity differentials decrease because of ejecta expansion and the changing slope of the density profile.

3.5.2 $\langle N \rangle$ as an aid to classification

Having established how I count N and what it represents I now consider $\langle N \rangle$, the mean N, which is calculated from the $t_{-1/2}$ and $t_{\max}$ spectra and is used as a measure of the

pre-peak spectral evolution. In the absence of spectra at $t_{-1/2}$ the earliest spectrum after this time is used, alternatively the value at $t_{\rm max}$ is used. If there are no spectra at $t_{\rm max}$ then $N(t_{\rm max})$ is interpolated from spectra before and after. $\langle N \rangle$ is taken to be an integer and so non-integer values are rounded up. In general $N(t_{+1/2})$ cannot be used to reliably estimate $\langle N \rangle$ and the issues affecting post-maximum classification of SE-SNe are discussed in Section 3.8.2.

Using this information it is now possible to adjust the existing classification system to include information about the degree of line blending in the SNe, which is done by including $\langle N \rangle$ in the "Ic" nomenclature and dispensing with the ambiguous "Ic-BL". For example, broad-line Ic SN 2002ap becomes "Ic-4", whereas narrow lined Ic SN 2007gr becomes "Ic-7". Table 3.8 gives the new classification for the SNe used here. This method is advantageous because the relative degree of line broadening between SNe is clearly given.

Figure 3.23 shows representative spectra for SNe of type Ic-3, Ic-4, Ic-6, and Ic-7 while Figure 3.22 shows how many SNe fall into each Ic-$\langle N \rangle$ category. That there appears to be as many SNe with significant line blending compared to those with well defined lines is partly a consequence of a bias in the prioritisation of SN observations and of these SNe tending to be more luminous on average (Prentice et al., 2016).

3.6 Taxonomy

In Section 3.5.2 $\langle N \rangle$ was established as a means of characterising the spectra of SNe Ic, and in Section 3.7 I compare $\langle N \rangle$ with physical parameters derived from the bolometric light curves of the SNe. From this it can be seen that $\langle N \rangle$ is weakly correlated with line velocity, as would be expected, but no correlation with any other property. Consequently, with two addition parameters, I can further expand on this method by including $v_{\rm SiII}$ at peak in units of 1000 km s^{-1}, and $t_{+1/2}$ in days, which gives Ic-$\langle N \rangle$ $\left(v_{\rm p,SiII}/t_{+1/2}\right)$. These measurements provide a useful at-a-glance comparison between He-rich SNe. This taxonomic scheme is applied to the He-poor SNe in our

Table 3.8: Ic classification including information on N

SN	Ic$\langle N \rangle$
1994I	Ic-6
1997ef	Ic-4
1998bw	Ic-3
2002ap	Ic-4
2003jd*	Ic-4
2004aw	Ic-6
2004dn	Ic-6
2004fe	Ic-6
2005az	Ic-7
2006aj†	Ic-6
2007gr	Ic-7
2009bb	Ic-6
2010ah	Ic-3
2010bh*	Ic-3
PTF10vgv	Ic-5
2011bm	Ic-7
2012ej	Ic-7
PTF12gzk	Ic-6
2016P	Ic-6
2016coi	Ic-4
2016iae	Ic-7

† $\langle N \rangle$ is an upper limit, from $t_{\max}$ spectrum only
*Lower limit due to contamination or poor S/N

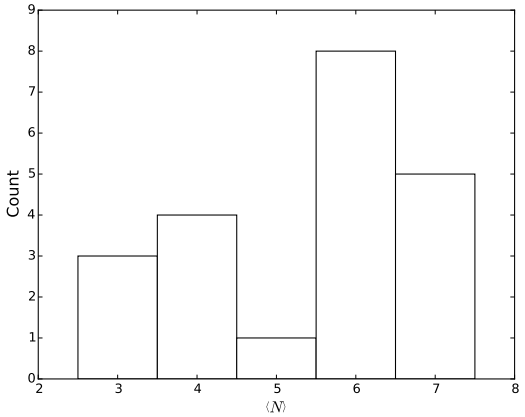

Figure 3.22: The number of SNe within the category Ic-$\langle N \rangle$. The values $\langle N \rangle = 3, 4, 6, 7$ represent common sets of line blends whereas the Ic-5 group appears to be transitional between Ic-4 and Ic-6, however, there is just one example; PTF10vgv. There is uncertainty in the categorisation of a few SNe due strong host-galaxy emission lines (e.g., SN 2016P), which is not reflected here.

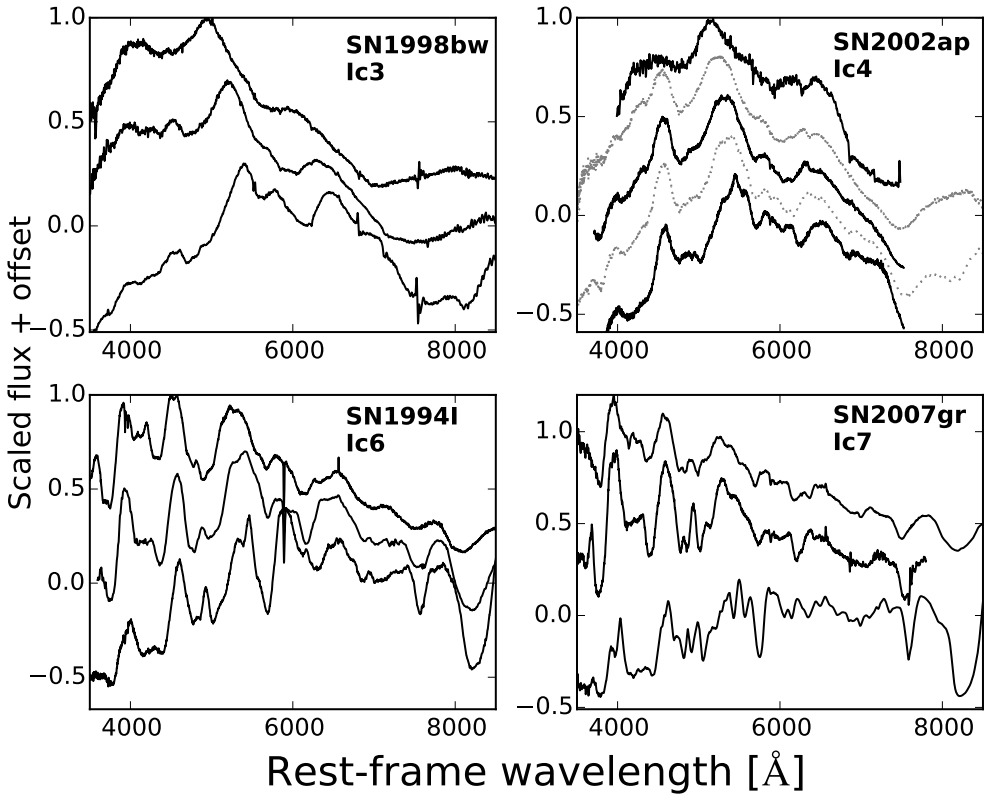

Figure 3.23: The $t_{-1/2}$, $t_{\max}$, and $t_{+1/2}$ spectra of four representative SNe for the SN Ic classification scheme presented in this work. Only the first two spectra are used in defining $\langle N \rangle$, the last is given to show spectroscopic evolution. (Top left) GRB-SN 1998bw is a model for the Ic-3 group, and it displays blended Fe II lines, O I and Ca II, and a single Si II feature until well after maximum. The deblending of the Fe II lines is affected by the depressed flux blueward of 5000 Å. (Top right) Here SN 2002ap is used to show the effects of early deblending. The early spectrum shows similarity to SN 1998bw at a relative epoch. The grey dotted spectra are a few days later than the reference spectra and are used to show the evolution of the O I/Ca II blend. By maximum SN2002ap has deblended O I and Ca II lines, a distinct Na I line and the Fe II lines, while still blended, are beginning to separate. (Lower left) SN 1994I shows the evolution of Ic-6 SNe. Generally the only blend is of the Fe II 4924 and 5018 lines and these separate shortly after maximum. Notice that, except for similarities between SN 2002ap and SN 1994I at $t_{+1/2}$, particularly around 4500 - 5500 Å and 6200 to 7000 Å. (Lower right) Ic-7 are well demonstrated by SN 2007gr, the lines are narrow and well defined throughout.

Table 3.9: The reclassification of SNe Ic

SN	Previous classification	Reclassification
1994I	Ic	Ic-6(11/9)
1997ef	Ic-BL	Ic-4(13/45)
1998bw	GRB-SN	Ic-3(15/16)
2002ap	Ic-BL	Ic-4(9/16)
2003jd*	Ic-BL	Ic-4(13/14)
2004aw	Ic	Ic-6(11/21)
2004dn	Ic	Ic-6(9/15)
2004fe	Ic	Ic-6(8/u)
2005az	Ic	Ic-7(11/29)
2006aj*	GRB-SN/Ic-BL	Ic-6(21/14)
2007gr	Ic	Ic-7(7/15)
2009bb	Ic-BL	Ic-6(20/13)
2010ah	Ic-BL	Ic-3(18/17)
2010bh*	GRB-SN	Ic-3(32/9)
PTF10vgv	Ic	Ic-5(7/10)
2011bm	Ic	Ic-7(6/43)
2012ej	Ic	Ic-7(7/20)
PTF12gzk	Ic	Ic-6(17/24)
2016P	Ic-BL	Ic-6(u/14)
2016coi	Ic-BL	Ic-4(14/20)
2016iae	Ic	Ic-7(9/14)

*$\langle N \rangle$ Lower limit due to contamination or poor S/N
u: insufficient data to calculate

sample in Table 3.9. Note that for GRB-SNe the reclassification does not supersede the "GRB-SN" label and I find that all SNe associated with GRBs are classified as Ic-3.

Figure 3.24 shows the distribution of $t_{+1/2}$ for all the SNe Ic in the sample used here, plus those from Prentice et al. (2016) that did not make the cut here. This figure is a useful reference when considering how a value of $t_{+1/2}$ sits in relation to other SNe. It is apparent that $t_{+1/2} < 20$ d in most cases but that in a few extreme examples $t_{+1/2}$ can be around double this.

3.7 $\langle N \rangle$ in relation to other parameters

$\langle N \rangle$ is a measure of line blending, reflecting the density profile of the ejecta above the photosphere which has an effect on $E_{\rm k}/M_{\rm ej}$. However, more information can be

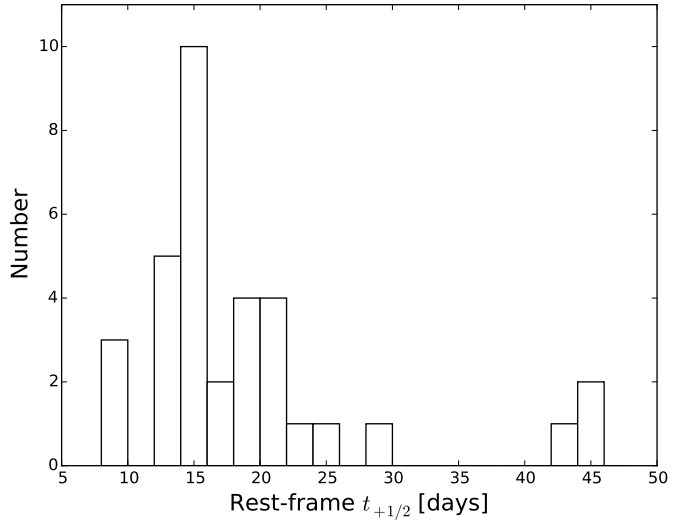

Figure 3.24: For reference, the distribution of $t_{+1/2}$ for 34 SNe Ic. As noted in Section 3.5, $t_{+1/2}$ is usually calculated from the bolometric light curve but the *VRgr* bands also provide good approximations.

extracted from the spectra and from the light curves so there exists a series of properties that can be investigated in relation to $\langle N \rangle$ which should help reveal the properties of SE-SNe and the diversity within. From the spectra I can extract line velocities for most SNe (principally those that do not show excessive line blending), or provide estimates on the ejecta velocity, and by using photometric information the temporal and physical characteristics of the LCs can be compared with $\langle N \rangle$.

3.7.1 $\langle N \rangle$ in comparison with line velocities

Of interest are the line velocities at maximum as a function of $\langle N \rangle$, shown in Figure 3.25, of Si II, Fe II, and O I, the first of which is taken as an approximation of the photospheric velocity $v_{\rm ph}$. It can be seen that a possible relationship may exist between $\langle N \rangle$ and the velocities of Si II, and Fe II, although some uncertainty in measurements of $\langle N \rangle$ adds to the scatter of the values. A test using the Pearson correlation coefficient on $v_{\rm SiII}$ yields $r = -0.54$ and $p = 0.029$ which suggests that as $p < 0.05$ the correlation may be statistically significant, but this is based on a very limited data sample of 16. Comparatively, for $v_{\rm FeII}$ and a sample size of 13 I find $r = -0.43$ and $p = 0.15$

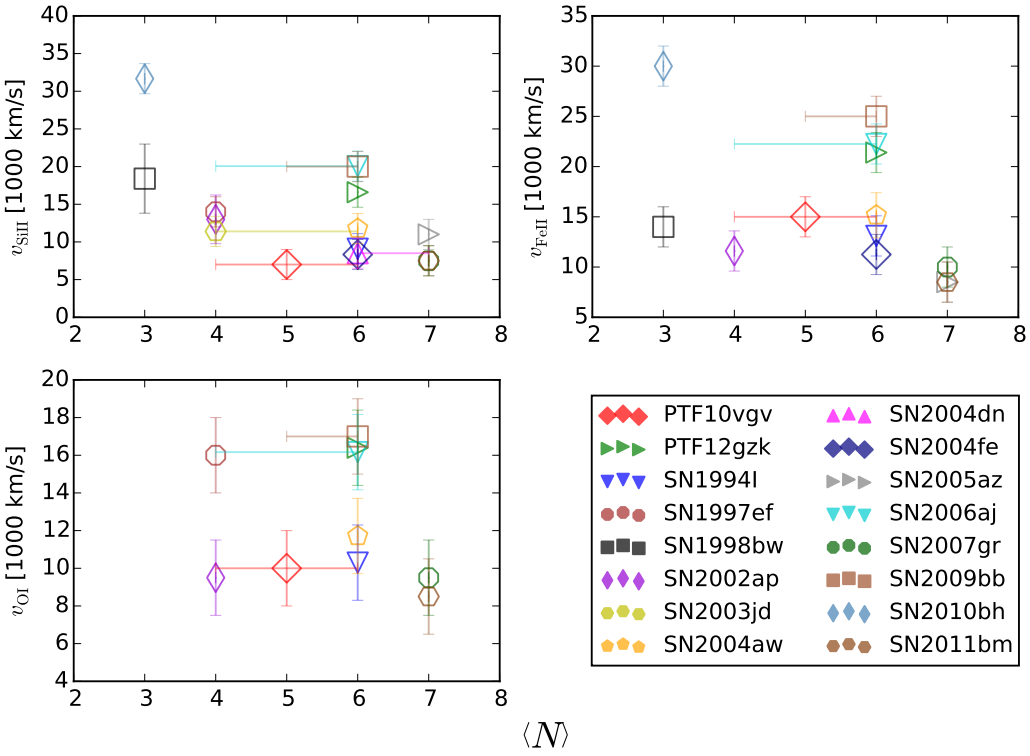

Figure 3.25: Line velocities around maximum light of Type Ic SNe as a function of $\langle N \rangle$. (Top left) The Si II line velocities show a possible relationship between the velocity of the photosphere and $\langle N \rangle$, there is uncertainty with $\langle N \rangle$ in some SNe due to contamination from other emission sources, poor S/N, restricted wavelength or temporal coverage. (Top right) The same as before but for Fe II (note $v_{\rm FeII} \approx v_{\rm CaII}$), the relationship between line number and the velocity of a line is also present. The number of visible iron lines is related, at least partially, to the iron velocity because this series of lines (Fe II 5169, 5169, 5235) represents two sources of blending when considering $\langle N \rangle$. The positioning of SN 1998bw and SN 2002ap in this plot is interesting because the Fe II lines in these SNe at this epoch are on the verge of deblending (This is discussed in Section 3.5.1. (Lower left) the O I lines do not show the same relationship with $\langle N \rangle$ and are more scattered, however this is partially because it has not been possible to estimate the O I velocity when it is blended with the Ca II NIR triplet.

suggesting that a correlation is not significant. It is likely that the sample sizes here are far too small to extract any meaningful analysis however.

Should a correlation between $\langle N \rangle$ and line velocities be expected? Line broadening is associated with high energy ejecta which places some material at high velocities. That some SNe show broad lines but their peak velocities settle around the typical value of SNe Ic (SN 1998bw, SN 20002ap) while others retain high velocity lines, either blended (SN 2006aj, SN 2010bh)) or unblended (PTF12gzk) is indicative of the energy distribution in the ejecta. In the former case the energy is primarily ejected into material in the outer layers creating a high velocity region with a flatter density profile. The most energetic SNe tend to be associated with GRBs.

3.7.2 $\langle N \rangle$ and light curve parameters

Having considered how various line velocities relate to $\langle N \rangle$ one can investigate the relationship between $\langle N \rangle$ and properties of the light curve: $t_{-1/2}$, $L_{\rm p}$, $M_{\rm Ni}$, and $t_{+1/2}$ which is plotted in Figure 3.26. The values for these three properties are taken from Prentice et al. (2016) and their derivation described therein. The optical ($4000 - 10000$ Å) pseudo-bolometric $L_{\rm p}$ is used here in order to maximise the available SNe.

It appears that $\langle N \rangle$ is weakly correlated with $L_{\rm p}$, however this is driven by the GRB-SNe, which are exclusively Ic-3 and significantly more luminous on average than other He-poor SNe, and the choice of SNe used here. In the absence of the GRB-SNe there is no relation between $L_{\rm p}$ and $\langle N \rangle$, nor is there a correlation with any of the other parameters investigated.

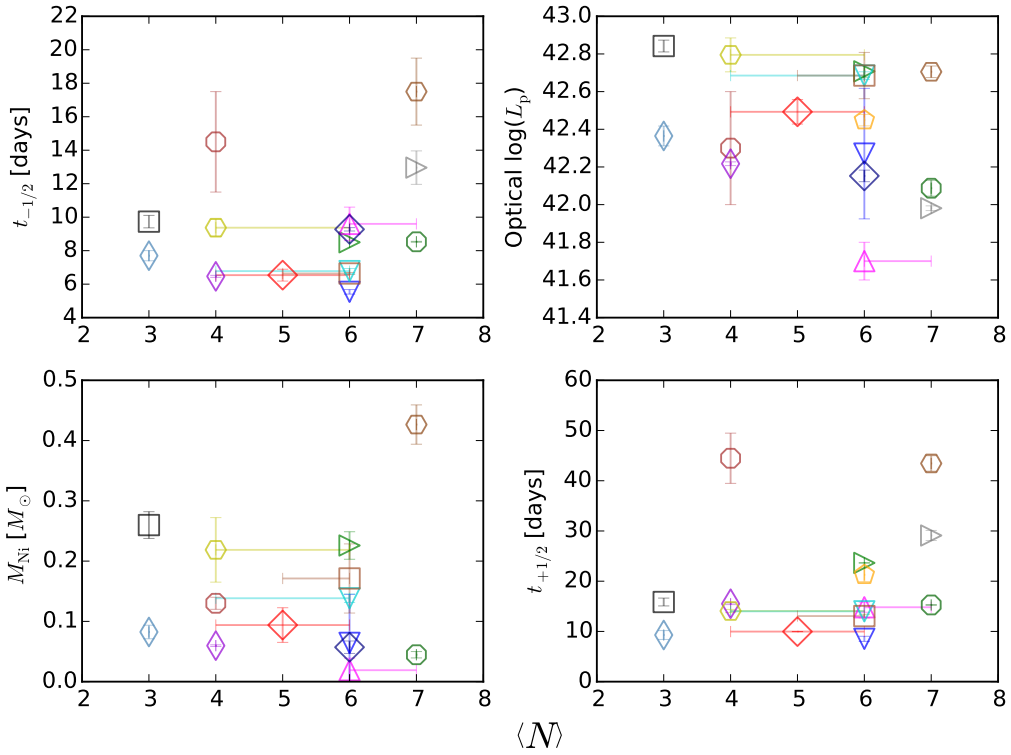

Figure 3.26: Second parameters when considering $\langle N \rangle$. (Top left) $t_{-1/2}$, (top right) optical pseudo-bolometric peak luminosity L_p, (lower left) M_{Ni} as derived from the previous value of L_p, (lower right) $t_{+1/2}$. L_p and M_{Ni} include host-galaxy extinction when known but some are lower limits, SN 2004dn in particular appears heavily extinguished. None of the parameters individually show a correlation with $\langle N \rangle$ but they are all related to each other through the photon diffusion and ejecta expansion times scales (Arnett, 1982). SN labels as the same as in Figure 3.25

3.8 Discussion

3.8.1 He-rich SNe

The method for characterising the $\sim$ 6200 Å region used for the He-rich SNe has allowed for the separation of these SNe into four separate groups defined by where they sit in the $\langle EW \rangle / \langle f_{\rm em}/f_{\rm abs} \rangle$ plane, which represents the degree of certainty that there is H in the ejecta. For the IIb and IIb(I) sub-groups this is definite as the Hα P-Cygni profile is a prominent feature and Hβ and Hγ are present in most cases. For SNe Ib(I) the presence of H is likely, implied by the transition in strength of the $\sim$ 6200 Å feature across the IIb(I) SNe to the Ib(II) SNe, but supporting evidence such as higher Balmer lines is absent and the spectra are dominated by strong He I from early epochs. Si II 6355 may well account for some of the opacity that results in the $\sim$ 6200 Å absorption feature. The Ib group displays a weak absorption around the 6200 Å region, and an even weaker emission peak, that is most likely attributable to Si II 6355, with little, if any, contribution from Hα. If H is present in these SNe it is likely diffuse very soon after explosion and so provides little opacity.

The analysis presented here suggests that most He-rich SNe are not stripped down to their He layer but retain some amount of H in their ejecta. Four of the SNe IIb (1993J 2011hs, 2011dh, 2011fu) display an early rapidly decaying phase in their light curve that can be interpreted as cooling of the stellar surface following shock-breakout. The timescale of shock-breakout, and its luminosity are related to the radius of the progenitor, ejecta mass, and explosion energy (see Nakar and Piro, 2014; Piro, 2015). A more extended progenitor has a longer cooling timescale and greater luminosity, which is expected to be seen in the light curve as a rapid initial peak ($\sim$ half a day) followed by decline over a few days (for a more extended envelope). No such early time emission is seen for any other IIb or IIb(I) SNe in our sample and, while for most of the SNe this could be due to lack of detection at a sufficiently early time, the lack of a declining phase in the light curve puts an upper limit on the extent of the progenitor's envelope. This discrepancy has been used to make the case that SNe IIb can occur

from both compact ($\sim$ a few solar radii) and extended ($\sim$ a few hundred solar radii) progenitors (e.g., Bersten et al., 2012; Folatelli et al., 2014). Interestingly, two of the Ib(II) SNe have shown a similar emission; the peculiar SN 2008D/XRF080109 (Mazzali et al., 2008; Soderberg et al., 2008; Modjaz et al., 2009), and SN 1999ex (Hamuy et al., 2002; Stritzinger et al., 2002) where the early emission has been attributed to shock-breakout from the stellar surface, or in the case of SN 2008D, to the failure of a relativistic jet to pierce the stellar envelope Mazzali et al. (2008). Our results are consistent with more H-rich SNe also being more extended.

3.8.2 He-poor SNe (SNe Ic)

A comparison of $E_{\rm k}$/$M_{\rm ej}$ with N

It was noted in Section 3.4 that a small amount of mass at high velocity can increase the kinetic energy of the ejecta by nearly 10^{52} erg and that $E_{\rm k}/M_{\rm ej}$ was significantly affected by the shape of the outer density profile. The variation in density profile can be explained by small masses of material projected to high velocities, as could happen in the case of an asymmetric explosion. In this case one may expect to see widely separated peaks in the nebular phase [O I] 6300, 6363 Å line (see Mazzali et al., 2005; Maeda et al., 2008) and relatively broad, but not necessarily blended, lines for an off axis jet (e.g., SN 2003jd) or extremely broad and long-lived absorption features as with GRB-SNe if viewing the jet on-axis (this would also explain why the GRB is detected in some Ic with low $\langle N \rangle$ and not in others[4]).

I now compare $\langle N \rangle$ with $E_{\rm k}/M_{\rm ej}$ derived from spectral modelling or hydrodynamic simulations, as these are most reliable for calculating $E_{\rm k}$. Simpler methods (e.g., "Arnett") cannot account for the changes in density profile of the ejecta and so only provide coarse estimates of the kinetic energy. The number of SNe available for this kind of analysis is small, so there are just a few key examples which fortunately cover a good range of $E_{\rm k}/M_{\rm ej}$. Figure 3.27 shows the relationship between $E_{\rm k}$/$M_{\rm ej}$ and the number

[4]Although the detection rate for GRBs is not 100 percent

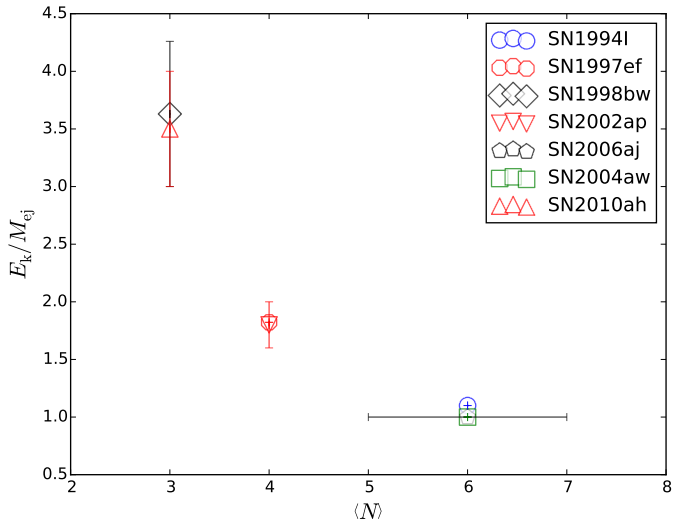

Figure 3.27: E_k/M_{ej} as a function of $\langle N \rangle$ for SNe with the former values derived from spectral modelling rather than analytical methods. The plot indicates that, for SNe with such values available, $\langle N \rangle$ is related to E_k/M_{ej}. That the two parameters should be linked is a product of the outer density profile whereby a small amount of high velocity mass results in a large increase in kinetic energy. SN 2006aj is an unusual case because $\langle N \rangle$ is difficult to define as it is likely that the spectra are contaminated by other sources of emission. This plot also demonstrates the need for more SNe Ic to be modelled spectroscopically as the commonly used analytical methods cannot account for the diverse range of density profiles.

of features for the SNe that fulfil our requirements. It can be seen that E_k/M_{ej} scales with smaller $\langle N \rangle$ although the case of SN 2006aj is extremely uncertain as the pre-max spectra show contamination from the host-galaxy and the XRF afterglow (Pian et al., 2006).

The density profile of the ejecta is an important part of what defines the value of E_k/M_{ej} (Mazzali et al., 2013). It is typically modelled with a steep index before reaching a turn-over at lower radial coordinates (Mazzali et al., 2000). In a simple model I can define three cases:

Case 1: A steeper density profile provides more mass towards the core, at lower velocities. The photosphere evolves slower through velocity space in this environment as the increasing density of the material passing through the photospheric boundary offsets the decrease in density due to expansion. Line formation should be relatively narrow in velocity space as the opacity outside the photosphere rapidly drops due to the steep profile. This is typical of larger $\langle N \rangle$.

Case 2: Flatter density profiles can project more material to higher velocities. For a fixed mass M such a profile would have a higher overall $E_{\rm k}$ than for a steeper density profile, however the photosphere would recede more rapidly in velocity space. Such a profile should allow somewhat broad, but not necessarily blended, lines which would reduce in velocity rapidly. $E_{\rm k}/M_{\rm ej}$ would be larger than for Case 1.

Case 3: A steep density profile with a flatter outer part has already been discussed, but to summarise it would result in long-lived blended lines as the photosphere recedes slowly in the steep part of the density profile but the flatter part provides sufficient opacity to greater velocities resulting in line blending. This allows the larger mass of the steeper density profile to combine with the larger kinetic energy of the flatter density profile leading to a larger $E_{\rm k}/M_{\rm ej}$ than Case 2. This situation would result in a very low $\langle N \rangle$.

A relationship between $\langle N \rangle$ and the outer density index n is suggested in that a lower value of one represents a lower value of the other. For SN 1998bw $n = 2$ and $\langle N \rangle = 3$, while for SN 1994I $n = 7$ and $\langle N \rangle = 6$. It may be possible that with more work a set of models could be used to provide an analytical estimate of the total kinetic energy of the SN by using $\langle N \rangle$ as a proxy for n.

Post-peak spectral similarity

I have considered spectra at times before and around maximum light. However, many SNe are classified at a later epoch and while it is clear that early spectra, even with relatively poor S/N, can be categorised but it is not clear that this true of later times. Table 3.6 indicates that the line velocities of many SNe fall within a relatively narrow range that does not correspond with their velocities at earlier times. In Figure 3.28 I plot the spectra of several supernovae where the spectra appear to be similar. The epochs are all post-maximum but vary in relation to the evolution of the light curve (i.e., they are not all around $t_{+1/2}$). While the order of spectra are grouped in terms of early spectral similarity it is clear that, aside from the Ic-7 SNe (SN2011bm and SN 2007gr, where the narrow lines remain prominent), the remaining SNe have spectral

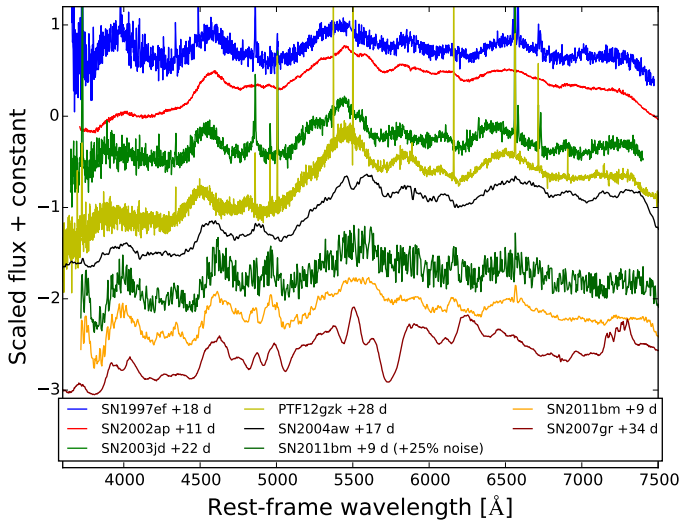

Figure 3.28: Various spectra that appear somewhat similar post-maximum, this is particularly the case for the top five SNe for which $\langle N \rangle = 3, 3, 3, 5, 5$ respectively . Only the spectra of Ic-7 SN 2011bm and Ic-7 SN 2007gr show clear deviation from the general characteristics of the other spectra. I include a version of the observed SN 2011bm spectrum where 20 percent noise has been introduced, which shows that S/N is important for classification after peak as this spectrum could be mistaken for belonging to the group of spectra above it.

similarity on at lease one occasion during their evolution. To test the effect of noise on the Ic-7 SNe I include two versions of the same spectrum of SN 2011bm in which I artificially introduce noise at the 20 percent level to one of the spectra. Both the noisy and observed spectra show similarity to the spectra above them in the region redward of 5000 Å. The key difference is in the region between $4000 - 5000$ Å where the Fe II lines lose their definition with increasing noise. While it is still possible to see a positive comparison between the two SN 2011bm spectra and that of SN 2007gr it is also possible to see similarity between the noisier SN 2011bm spectrum and the spectra above. A further increase in noise also increases the ambiguity of the spectrum and could make misclassification more likely. Such problems may well occur often as classification spectra are typically taken with shorter exposure times than science spectra and consequently a lower S/N. This can have an effect on the statistics of SN rates as post-peak classification is ambiguous.

Sample size

Our sample has relatively few SNe with spectra or light curves early enough to investigate N at $t_{-1/2}$. Although this number increases for $t_{\max}$, it is evident that with 5 subgroups more data is required in order to effectively probe the parameter space. I can trace three issues that result in a dearth of numbers. The first is biases in observations, where rare SNe such as GRB-SNe or those with broad lines are followed in more detail than normal SNe Ic. The second is data with low S/N; it is understandable that spectroscopy can be time intensive for all but the brightest targets but information on the SN is lost if S/N is too low. The third is the lack of data made publicly available, which is especially relevant to spectra which cannot be accommodated in the literature in the way light curve information can. A significant proportion of the data on WiseRep has been supplied by 2014 Harvard-Smithsonian Centre for Astrophysics (CfA) data release (Modjaz et al., 2014). More data will allow more robust analysis to build on this work.

3.9 Conclusions

The publicly available spectra for the SNe in the sample of Prentice et al. (2016), plus that of SN 1997ef, SN 2004dn, and unpublished data for SN 2012ej, SN 2016P, SN 2016coi, and SN 2016iae has been analysed, using an empirical method to group the spectra according to the presence and strength of H lines, He lines, and line broadening. From this, there was found to be a clear distinction between SNe of Type Ic (He-poor) and those of Type Ib/IIb (He-rich), the analysis then proceeded along two separate pathways

3.9.1 He-Rich SNe

The He-rich SNe were analysed for the presence and strength of H in their spectra. Measurements were made of the velocity, equivalent width, and ratio of absorption to

emission of the feature around 6200 Å which is typically attributable to Hα. An alternate explanation for this feature could be Si II 6355 as is found in Type Ia and Ic SNe, however the analysis presented here suggests that, while Si II 6355 may contribute to the opacity in this region, Hα is more likely the dominant component for most He-rich SNe.

The spectra were also examined for the presence of Balmer lines beyond Hα, which are prominent in H-rich SNe but rapidly decrease in strength with decreasing Hα strength. It is found that some classical IIb SNe do not display clear H absorption beyond Hα while some SNe Ib show hints of these features that are broadly in line with a continuum of H line strength.

The mean pre-peak contrast ratio between $\langle f_{\rm abs}/f_{\rm em}\rangle$ and the mean pre-peak equivalent width $\langle EW\rangle$ have been used to systematically categorise the ~ 6200 Å feature, and from this the He-rich SNe are able to be placed into four groups:

- IIb - H-rich, Hα emission dominates absorption
- IIb(I) - moderately H-rich, Hα absorption dominates emission
- Ib(II) - Likely shows some Hα but lacks any definite signatures. Like IIb(I) but with a weaker line profile
- Ib - Weak 6200 Å feature, probably Si II dominated

An emission dominated Hα feature relates to a strong P-Cygni line profile, which is indicative of an extended H envelope. Such a large distribution of emitting material in the outer ejecta is incompatible with the location and abundances of Si found in He-rich SNe. Finally, the results here are consistent with the conclusions driven from analysis of the early time declining phase of the light curve of some SNe IIb in that the most H-rich SNe are also the most extended because their outer envelope would be H dominated.

3.9.2 Type Ic SNe

The method adopted to analyse the spectra of type Ic SNe was to count the number of absorption features N present in the spectra at key epochs. 7 key features have been selected due to their prominence and ubiquity in SE-SNe spectra, because they allow for an investigation into the velocity spread over which blending occurs, and due to the wavelength constraints of commonly used spectrographs. Because line blending is related to the specific kinetic energy of the ejecta this is a useful diagnostic for classification and provides information about the properties of the SNe without resorting to more complex processing methods.

By taking a mean value for N before bolometric maximum and comparing this value with the velocities of Si II, Fe II, and O I it is found that there is a relationship between $\langle N \rangle$ and line velocity, although this should be expected as sufficient mass at high velocity, along with a steep density profile in the outer ejecta, is required to form broad lines. Comparison with the properties of the SNe light curves ($L_{\rm p}$, $t_{-1/2}$, $t_{+1/2}$) as well as $M_{\rm Ni}$ reveals that there is no connection between $\langle N \rangle$ and any of these properties. However, the specific kinetic energy $E_{\rm k}/M_{\rm ej}$, using values derived from spectral modelling or hydrodynamical simulations, may be related to $\langle N \rangle$. This is because line blending requires an outer, flatter component to the density profile of the ejecta which increases the mass at high velocity, and with it $E_{\rm k}$, but without significantly increasing the overall mass. This could be a consequence of ejecta with a jet like structure as is expected with GRB-SNe. High velocities alone do not translate into a large $E_{\rm k}/M_{\rm ej}$. If the lines are relatively narrow then the density profile is steeper in front of the photosphere.

To reflect the findings here I adapt the common nomenclature for SN classification by including $\langle N \rangle$, $v_{\rm SiII}$ at peak, and $t_{+1/2}$ so as to give a clearer picture of the degree of line blending in SNe Ic and to provide physical information about the explosion. The adopted form of the taxonomical system is as follows: Ic-$\langle N \rangle$ $\left(v_{\rm p,SiII}/t_{+1/2}\right)$, with $v_{\rm SiII}$ in units of 1000 km s^{-1}. With this modification the properties of SNe Ic can be compared at a glance and the arbitrary nature of the "broad-line" definition is removed.

Chapter 4

Observations of SE-SNe

Previous chapters have dealt with the photometric and spectroscopic properties of large samples of SE-SNe. In particular, in Chapter 3 it was noted that we are now entering a time when we can begin to see further divisions within the SN classification scheme. This led to my proposed sub-classifications of SE-SNe in line with the degree of envelope stripping (for He-rich SNe) and for quantifying line blending (SNe Ic). I made an important note that there is a dearth of well sampled SNe Ibc – those caught early and with high quality data. This limits the analysis that can be done.

To build on the work already described in Chapters 2 and 3, and to examine the diversity of SE-SN properties from an independent body of data, I now present observations and analysis of 19 SNe. I will compare the properties of these SNe with those found in Chapter 2 while utilising the classification scheme presented in Chapter 3. I will be aiming to see if there are similarities and differences in the properties of these SNe and to assess if we have well sampled the SN Ibc parameter space.

4.1 Target selection and data sources

In the time frame 2015 – 2017, approximately 6 – 12 objects per year were classified as SE-SNe. I aimed to follow as many objects as possible with no bias towards those

that may be designated as "objects of interest", for example GRB-SNe. However, with limited telescope time, and in order to maximise the scientific potential, I limited observations to SNe classified pre-maximum light and that were at $z < 0.05$ in order that they remain bright enough to observe into the nebular phase. Exceptions to this only came when I observed objects in collaboration with the Public ESO Spectroscopic Survey of Transient Objects (PESSTO) and extended PESSTO (ePESSTO) and so was able to access spectroscopy from larger telescopes.

Of the 19 SNe listed in Table 4.1, 15 of these were obtained as part of my own observing programmes; these SNe were discovered from 2015 onwards. Three further supernovae are included as part of the work I led on the PESSTO/ePESSTO observations of stripped envelope supernovae. The remaining SN is 2012ej, which after some work, was deemed to have insufficient data to publish as a stand-alone object. Two of these SNe in this sample have been the subject of published work; GRB-SN 2016jca (Ashall et al., 2017) and Ic-4 SN 2016coi (Prentice et al., 2018). In the latter we presented comprehensive photometric and spectroscopic observations of the SN along with analysis and spectral modelling. This object is discussed briefly in Section 4.4.3 with regards to its unusual nature – residual He in the outer ejecta.

Telescopes and instruments

Primarily, I used the Liverpool Telescope (LT) (Steele et al., 2004) and the Las Cumbres Observatory (LCO) network of 2.0 m robotic telescopes (Brown et al., 2013) to obtain photometric and spectroscopic data. The LT was the primary source of data, with the LCO network used as an auxiliary source. The 2.0 m Liverpool Telescope is located in the Northern hemisphere at the Roque de los Muchachos Observatory (ORM) on the island of La Palma, Spain. The LCO telescopes are located in the North at the Haleakala Observatory, USA, and South at the Siding Spring Observatory, Australia. PESSTO/ePESSTO objects were supplemented with additional spectra from the European Southern Observatory (ESO) Faint Object Spectrograph and Camera2 (EFOSC2) on the 3.6 m New Technology Telescope (NTT), based at La Silla, Chile.

On the LT the primary instruments were the optical wide-field camera IO:O for photometry and the Spectrograph for the Rapid Acquisition of Transients (SPRAT) (Piascik et al., 2014) for spectroscopy. The LCO telescopes are clones of the LT, but the instrument package is different. On both there is a Spectral optical imaging camera and a Floyds spectrograph. The latter has variable slit widths, from 1.2" to 6.0" and a wide wavelength range; 3200 Å to 10000 Å. The low resolution EFOSC2 covers a wavelength range 3050 – 11000 Å

Table 4.1: The properties of the new SNe

SN	type	μ [mag]	z	$E(B-V)_{\rm MW}$ [mag]	$E(B-V)_{\rm host}$ [mag]	$\log_{10}(L_{\rm p})$ [erg s^{-1}]	$M_{\rm Ni}$ [M$_\odot$]	$t_{-1/2}$ [d]	$t_{+1/2}$ [d]	$t_{\rm p}$ [d]	$v_{\rm ph}$ [km s^{-1}]	$M_{\rm ej}$ [M$_\odot$]
2012ej	Ic-7	32.98	0.00898	0.09	0.14±0.14	42.1±0.1	0.08±0.01	-	18±2	15	5000	1.14
2013bb‡	IIb(I)	34.52*	0.017595	0.014	0.3±0.3	42.0±0.05	0.07±0.02	-	56±10	23	7000	4.1
2014L‡	Ic-7	30.92	0.008	0.034	0.5±0.5	42.2±0.2	0.06±0.04	10±1	13.9±0.2	15.5	8500	2.24
2014ad‡	Ic-3	32.12	0.00572	0.04	0.05±0.05	42.50±0.05	0.12±0.01	7±1	13.3±0.2	11	30000	4.37
2015ah‡	Ib	33.86	0.016	0.071	0.02±0.02	42.28±0.01	0.075±0.007	-	17.0±0.1	14	6000	1.3
2016P‡	Ic-6	34.17	0.0146	0.024	0.05±0.05	42.39±0.01	0.09±0.02	9.86±0.08	13.9±0.2	14	7000	1.51
2016bau	Ib	29.81	0.0038	0.018	0.2±0.2	41.26±0.02	0.00875±0.001	11.08±0.03	13.3±0.1	18	7500	2.68
2016coi	Ic-4	31	0.0036	0.075	0.125±0.125	42.29±0.02	0.09±0.01	11±1	19±1.5	16	12000	3.3
2016frp‡	Ib	35.23*	0.027	0.031	negligible	42.32±0.01	0.08±0.007	-	21.6±0.7	16	9000	2.50
2016iae‡	Ic-7	31.19	0.003646	0.014	0.65±0.65	42.4±0.2	0.13±0.08	9.3±0.1	17.7±0.1	17	9000	3.2
2016jca	GRB-SN	39.1*	0.145	0.03	negligible	42.96±0.08	0.27±0.01	5±2	14±2	10	28000	3.08
2016jdw	Ib	34.66*	0.0189	0.01	negligible	42.08±0.04	0.06±0.01	-	17.1±0.5	19	11000	3.5
2017bgu	Ib	33.2*	0.0085	0.029	0.02±0.02	42.16±0.02	0.07±0.01	-	22.5±0.6	18	8500	2.87
2017dcc‡	Ic-3	35.06*	0.0245	0.041	negligible	42.8±0.1	0.17±0.01	-	15.5±0.5	11	12000	1.32
2017ein	Ic-7	32.7†	0.0027	0.019	negligible	42.31±0.01	0.09±0.01	9.1±0.1	16.1±0.2	15	7000	1.76
2017gpn	IIb(I)	29.79	0.0073	0.3	negligible	41.04±0.1	0.005±0.001	9.9±0.1	17.3±0.5	15	8000	1.98
2017hyh‡	IIb(I)	33.54*	0.012	0.118	0.04±0.04	42.11±0.1	0.062±0.001	8±1	13±0.1	16	11000	3.0
2017ifh	Ic-4	35.97*	0.039	0.117	0.05±0.05	42.6±0.1	0.161±0.01	-	14.7±0.3	13	16000	2.98
2017iuk‡	GRB-SN	36*	0.037	0.045	negligible	42.51±0.03	0.12±0.01	6.8±0.5	15±2	14	15000	3.23

Distances from redshift (*), spectral modelling (†), or otherwise T-F median

‡ Target observed as part of PESSTO/ePESSTO

4.1.1 Photometric calibration

The nightly photometry from the LT and LCO comes reduced (e.g., bias subtraction, flat fielding) through their own pipelines. This leaves photometric calibration down to the user. I developed a short pipeline to align and the calibrate the images in order to process light curves of the objects observed. This pipeline utilises PYRAF as part of the UREKA package.

Standard star lists are obtained from the Sloan Digital Sky Survey data releases 4 – 9 and the American Association of Variable Star Observers Photometric All-sky Survey (APASS). The latter are observed in $ugriz$ and the former in $BVgri$. Use of the SDSS stars is preferential as the fields are well observed, with sources to ~ 24 mag, whereas the APASS fields can be sparse, with few stars in the field and a limit of ~ 17 mag.

Host subtraction is desirable for some SNe, particularly if they explode in a bright H II region. Without host subtraction the late time light curves ($\sim$ hundred days) are flattened as the host flux begins to dominate over the SN flux. At maximum light the host-flux is negligible compared to that of the SN. Unfortunately suitable frames for host subtraction require very good seeing conditions < 1.1 arcsec, a total of 15 – 20 minutes of exposure time per band, and be taken at least three years after the SN explodes. Hence, given that telescope time is limited, observations of new objects were prioritised over host-subtraction exposures for the two pre-2014 SNe.

Image preparation

The pipeline flow is shown in Figure 4.1 and was based upon the method described in Ashall et al. (2014). The pipeline starts aligning the nightly exposures to a reference image (usually r) using IRAF.DAOFIND to obtain the physical coordinates of sources within the reference image and then IRAF.IMALIGN to align the remaining exposures to it. If there are multiple exposures in the same band these are then stacked using IRAF.IMCOMBINE.

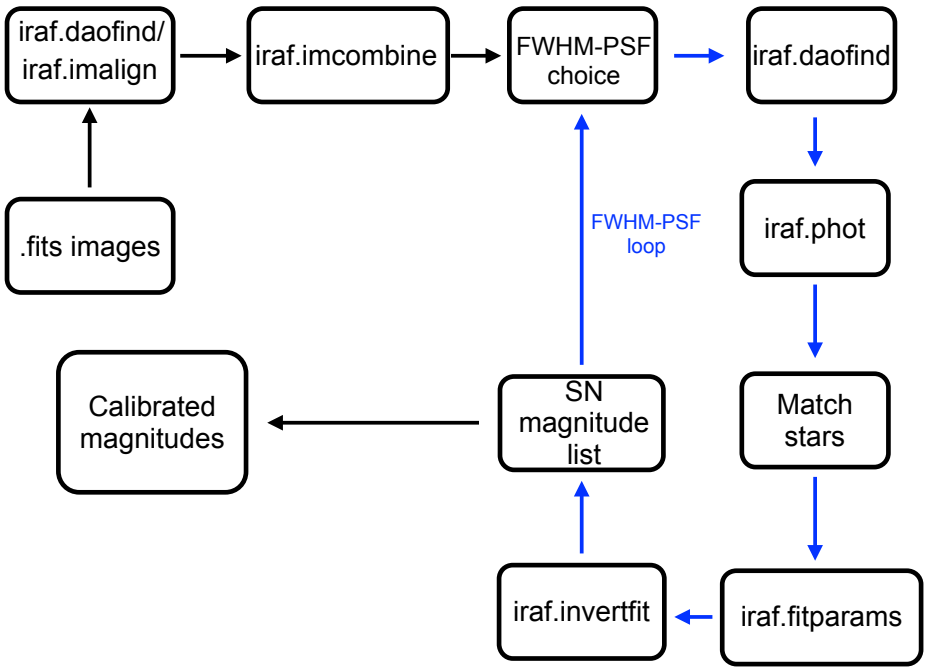

Figure 4.1: Flow diagram of the photometry pipeline. The "FWHM-PSF loop" is shown in blue, this loop is repeated for varying FWHM-PSF values between 1 and 20 pixels.

Finding instrumental magnitudes

The pipeline begins the "FWHM-PSF loop" – an iteration through a list of Full-width half-maximum (FWHM) values that define the point spread function (PSF) used, normally 10 values in the range 1 – 20 pixels. This method evolved because measured FWHM of the SN did not always return well behaved photometry. Hence the range of FWHM values allows a variety of possibilities to be tested. Its value is seen further when, on rare occasions, just one FWHM-PSF value works.

The aligned frames and FWHM-PSF are passed to the main pipeline which uses IRAF.DAOFIND to find all the sources in the frames. These sources are then passed to IRAF.PHOT which performs aperture photometry using the FWHM-PSF to find the instrumental magnitudes. These sources are then cross-correlated with the RA and DEC of the standard stars and the supernova via a custom PYTHON script named MATCH STARS which returns a list of the standard stars and their instrumental magnitudes.

Photometric equations and calibration

This list is passed to IRAF.FITPARAMS which fits a simple linear equation in the form of

$$m_{\rm inst} = m_{\rm standard} + Zp \tag{4.1}$$

where $m_{\rm inst}$ is the instrumental magnitude, $m_{\rm standard}$ the magnitude of the standard star, and Zp is the zero point, in order to compare the standard stars with the instrumental magnitudes and hence calibrate the photometry for a particular band. Note the absence of a colour term and an airmass term. The exposures are all at approximately the same airmass, so an airmass term would be effectively zero. On the other hand, a colour term based on the standard stars was originally used in Equation 4.1 in the form

$$m_{\rm inst} = m_{\rm standard} + A + B \times C \tag{4.2}$$

where A and B are constants and C is a colour term based upon the calibrate magnitudes of the standard stars (e.g., $g - r$ or $B - V$). A consistency check found that the form of the equation without the colour term returned calibrated magnitudes of the standard stars that were closer to measured magnitudes of those stars, or no worse. This is because, if one exposure of one of the reference bands in the colour term was poor, it would then affect the photometry for any other band where this term was used.

The photometric equations and instrumental magnitudes are then passed to IRAF.INVERTFIT which applies the equations to the sources in the field and returns the calibrated magnitudes. The calibrated magnitudes of the SN is extracted from the output and appended to a list

Final output

The code then either repeats the "FWHM-PSF loop" with the next FWHM-PSF value or ends if this process is complete. If complete, the pipeline takes the median magnitude for each band from the SN magnitude list as the calibrated photometry of the SN. Uncertainties on this value are either the standard deviation on the distribution of calibrated magnitudes or the mean error from the fit to the photometric equations (these are the errors derived from the least-squares fit applied to find the parameters of the photometric equations)

Testing

The pipeline developed over the course of 2016 to 2017 and underwent a series of consistency checks during its development in order to determine its reliability. The key test was to ensure that the calibrated photometry was accurate. To do this, the magnitudes of the standard stars were compared with those output by the pipeline, as demonstrated in Figure 4.2. Typically, the pipeline output was found to return the magnitudes of the standard stars with a median percentage difference of < 2 percent. The best calibrated stars were those that were bright and unsaturated, while the scatter increased towards the magnitude limit defined by the exposure time and weather conditions of the night.

The final test is on the actual light curves themselves. If the pipeline is sensitive to systematics that result in significant ($>$ a few percent) deviations in calibration then this would show as random scatter in the light curves, or offsets in the case of photometric observations taken at different latitudes. This is not seen, the light curves are well behaved when the standard stars are well behaved, the SN has a good S/N, and when the weather conditions are fine.

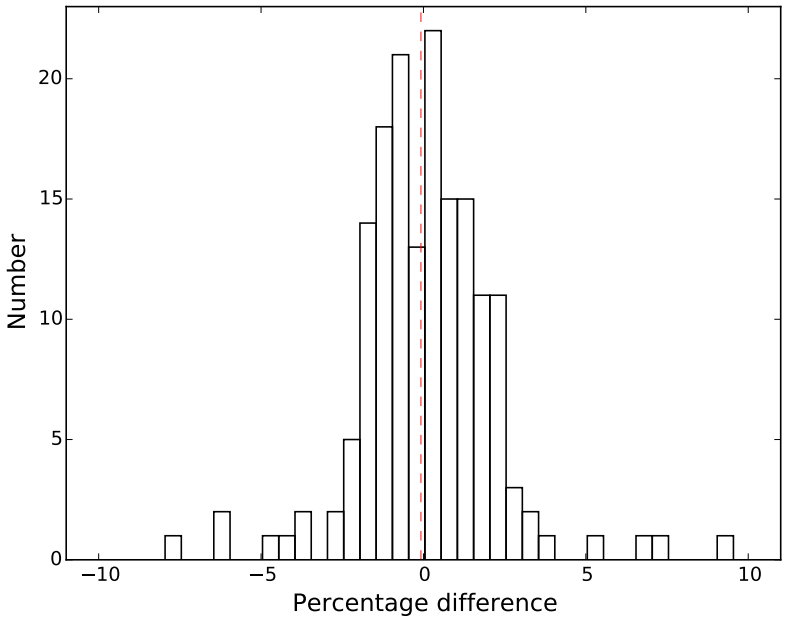

Figure 4.2: Histogram of the percentage difference between r-band standard star magnitudes and calibrated magnitudes. The absolute mean of the distribution is 0.08 percent, the absolute median is 0.09 percent (magenta dotted line), and the standard deviation on the distribution is 2 percent.

4.1.2 Spectral data reduction

The amount of spectroscopic data reduction required depends upon the instrument, the pipeline it passes through before being passed to the user, and the output of that pipeline.

Spectroscopic data from SPRAT on the LT undergoes a reduction pipeline before being released to the user (Piascik et al., 2014). Prior to 2017 this required the user to perform the final step of flux calibrating the spectra. In this case the wavelength calibrated output of the SPRAT pipeline was calibrated to the sensitivity function of a spectroscopic standard star via IRAF.CALIBRATE. However, a later adjustment to the pipeline produced flux calibrated spectra, albeit in relative flux units in most cases.

On the occasions where the source was not automatically located by the SPRAT pipeline a manual extraction and wavelength/flux-calibration was required. I developed a short pipeline that wavelength calibrates the spectra to the Xe arc spectra taken the same night, and then flux calibrates the spectra to the response of the spectroscopic stan-

dard star. The pipeline uses IRAF.APALL to extract a spectrum from a user defined aperture (manual centering, trace, and background subtraction). For the nightly arc exposures, the resulting spectrum is then compared with defined a Xe line list using IRAF.IDENTIFY to set the wavelength calibration for that night. The wavelength calibration derived from the arc exposure is applied to the object spectrum via IRAF.DISPCOR using the wavelength calibrated arc spectrum as a reference. This wavelength calibrated spectrum is then flux calibrated using the same procedure as described previously.

Data from the FLOYDS spectrographs on the LCO telescopes also passes through a pipeline, but this has a tendency to fail at the final step in the process necessitating a manual extraction of the already flux and wavelength-calibrated spectra.

Aside from LT/SPRAT and LCO/Floyds, spectra from other sources were shared with me, these are –

- The Device Optimized for the LOw RESolution spectrograph (DOLORES) on the Telescopio Nazionale Galileo (TNG) located at the ORM
- The Yunnan Faint Object Spectrograph and Camera (YFOSC) on the Li-Jiang 2.4 m telescope (LJT)) at Li-Jiang Observatory of Yunnan Observatories (YNAO)
- Bei-Jing Faint Object Spectrograph and Camera (BFOSC) on the Xing-Long 2.16 m telescope (XLT) at Xing-Long Observation of National Astronomical Observatories (NAOC)
- Intermediate Dispersion Spectrograph (IDS) on the 2.5m Issac Newton Telescope (INT), at the ORM
- Kast Double Spectrograph on the Shane 3m telescope at the Lick observatory
- DEep Imaging Multi-Object Spectrograph (DEIMOS) located on the Keck II telescope
- Wide-Field Spectrograph (WiFeS) on the Australian National University 2.3 m telescope, Siding Spring Observatory (as part of PESSTO)

4.1.3 Calculating host extinction

Being able to quantify the effect of host extinction of a SN is important in order to derive properties that relate to the luminosity and the spectral shape. There are two methods commonly used in the literature. The first method is through measurements of the equivalent width of the Na I D doublet absorption feature (Poznanski et al., 2012), although there are limitations to this method when applied to low resolution spectra (Poznanski et al., 2011). Accurate measurement of the equivalent width of the Na I line is best achieved with high S/N spectra with good resolution. This method also assumes a Milky Way type $R_V = 3.1$, which does not necessarily apply to other galaxies (e.g., Ashall et al., 2014; Stritzinger et al., 2018b). The choice of continuum will affect the resulting equivalent width. Also the equations used to derive $E\left(B-V\right)_{\rm host}$ are very sensitive to the equivalent width and when the lines saturate the relationship is no longer valid.

The second method is through the colour curves of the SN, whereby a "bottleneck" appears to occur in $V-R$ at ~ 10 days past R-band maximum (Drout et al., 2011). A similar relationship was used for $g-r$ (Taddia et al., 2015; Stritzinger et al., 2018b). However, neither method is without issues. The colour method suffers from large uncertainties due to the scatter of the host-corrected colour curves (see Chapter 2) and relies on other methods to define $E\left(B-V\right)_{\rm host}$ for the SNe in the distribution in the first instance.

The equivalent width of the Na I D line is calculated in relation to a "local continuum", a line of best fit to the data around the the Na I absorption line. If the intensity of the Na I absorption is less than the variance (e.g., noise) of the line of best fit minus the flux then an upper limit is obtained. This method is used to provide a range of values for $E\left(B-V\right)_{\rm host}$ in order to determine the mean extinction and the standard deviation of the distribution, which is taken to be the uncertainty. While it is found that S/N and the estimated local continuum affect the value of the equivalent width, the largest contribution to the error is the uncertainties given in Poznanski et al. (2012). A final consistency check is to compare the $E\left(B-V\right)_{\rm tot}$ corrected spectra with other SNe at

similar epochs. Late-time spectra are especially useful in this regard as over-correction leads to abnormally blue spectra.

I calculate $E\left(B-V\right)_{\rm host}$ for all the SNe used previously that lacked this, in addition to those introduced here, using the equivalent width of the Na I D absorption lines while comparing these values to the that derived from the $g-r$ colour curves. The updated $E\left(B-V\right)_{\rm host}$ values, and new bolometric parameters for previously examined SNe are presented in Table D.1.

4.1.4 Distances

In Chapter 2, distances were given as the z-dependent distance based upon the given cosmology. Here, to better reflect the calculated distances to the host galaxy, I use either the median distance modulus derived from the Tully-Fisher (TF) method, or if this is not present I use the z-dependent distance. This is because peculiar motions of galaxies have an important effect on the apparent redshift in the local $(z < 0.05)$ universe, a region that encompasses the vast majority of the SNe observed here. In the future, the uncertainty in the distance to local SN hosts may be worthy of further investigation.

4.1.5 Calculating $t_{\rm p}$, $M_{\rm Ni}$, and $M_{\rm ej}$

To determine $M_{\rm Ni}$ and the time from explosion to maximum light $t_{\rm p}$ I use the analytical models of Arnett (1982) as given in Valenti et al. (2008)

$$L(M_{\rm Ni},t,\tau_{\rm m}) = M_{\rm Ni}e^{x^2} \times \left[(\epsilon_{\rm Ni}-\epsilon_{\rm Co})\int_0^x A(z)dz + \epsilon_{\rm Co}\int_0^x B(z)dz\right] \qquad (4.3)$$

where $A(z) = 2ze^{-2zy+z^2}$ and $B(z) = 2ze^{-2zy+2zs+z^2}$ with $x = t/\tau_{\rm m}$, $y = \tau_{\rm m}/(2\tau_{Ni})$, and $s = [\tau_{\rm m}(\tau_{\rm Co}-\tau_{\rm Ni})/2\tau_{\rm Co}\tau_{\rm Ni}]$

$\tau_{\rm m}$ is a characteristic time-scale of the model, $\epsilon_{\rm Ni}$ and $\epsilon_{\rm Co}$ are the luminosity per unit mass of ^{56}Ni and ^{56}Co; i.e., 3.90×10^{10} erg s^{-1} g^{-1} and 6.78×10^{9} erg s^{-1}g^{-1} respectively.

This model assumes homologous expansion, a constant opacity, spherical symmetry, and that ^{56}Ni is located centrally. The light curve model was fit to the data using a Monte-Carlo routine that allowed the time of explosion $t_{\rm exp}$, $\tau_{\rm m}$ and $M_{\rm Ni}$ to vary.

The light curve is not fit in its entirety, with emphasis being placed on the rise and the peak. After this the light curve deviates from the model for two reasons. The first is that, as the ejecta expands, the opacity to γ-rays decreases and energy escapes. This simple model assumes full trapping. Next is that the light curve model is that of the bolometric LC, however, here we deal with pseudo-bolometric light curves, typically over the range $4000 - 10000$ Å, which covers $\sim 70 - 80$ percent of the total flux. Consequently, as the SN evolves, the peak in the spectral energy distribution shifts red-wards leading to a loss of flux in the integration range compared with the early epochs. Each case results in an increase in the light curve decay rate and deviation from the model some weeks after maximum light.

The explosion time $t_{\rm exp}$ is limited so that it cannot take a value that is after the date of discovery, and it must be no more than 35 d before $t_{\rm max}$. The reason for this latter condition is that some light curves find a "best fit" as the tail of the model passes through the plateau of the light curve peak. When examined in the broader context of the light curve it is clear that the fit is inappropriate. Information on discovery dates and corresponding photometry was found via Bright Supernova[1] (Gal-Yam et al., 2013b).

For the rise time estimated by the fit to the light curve model, $M_{\rm ej}$ can be calculated by rearranging Equation 2.4 for mass

$$M_{\rm ej} = \frac{1}{2}\left(\frac{\beta c}{\kappa}\right)\tau_{\rm m}^2 v_{\rm sc} \tag{4.4}$$

$v_{\rm sc}$ is a scale velocity, a "characteristic" velocity of the ejecta. There are large uncer-

[1] http://www.rochesterastronomy.org/snimages/

tainties with this method as κ and $v_{\rm sc}$ are degenerate, and the model is highly sensitive to $t_{\rm p}$, which is used to approximate $\tau_{\rm m}$. κ is often taken to be $0.07 - 0.1$ cm^2 g^{-1} (Chugai, 2000; Cano, 2013; Wheeler et al., 2015; Taddia et al., 2018b), but in reality is variable throughout the SN ejecta. Defining a "typical" velocity in the form of $v_{\rm sc}$ is difficult, as the ejecta has a continuous velocity profile. It is commonly taken to be the photospheric velocity, $v_{\rm ph}$, at maximum light or some estimated expansion velocity. Measurements used may be that of the Fe II λ 5169 or Si II λ 6355 lines, but these tend to cover the maximum and minimum measured velocities in the ejecta at peak and lead to large uncertainties. The photospheric velocity, by definition, is below the velocity of both these lines.

Here I use $\kappa = 0.07$ cm^2 g^{-1}, and take $v_{\rm sc}$ to be the velocity of the line with the lowest velocity at $t_{\rm max}$, as an approximation for $v_{\rm ph}$. In the case of He-poor SNe, this is Si II λ 6355, and for He-rich SNe it is O I λ 7774 if present, He I λ 5876 if not.

4.2 Analysis and results

The intrinsic light curves of the 19 SNe are shown in Figures 4.3, 4.4, and 4.5, with their associated physical parameters and classification listed in Table 4.1. In Figure 4.6 the extinction corrected $g - r$ colour curves of the SNe are shown compared to the larger sample. The corrections bring the SNe into the same region as occupied by other SE-SNe, supporting the consistency of the methods of Poznanski et al. (2012) and Drout et al. (2011).

The maximum light spectra of the SNe presented here, sorted according to type, are shown in Figure 4.7. In Figure 4.8 are nebular spectra of those SNe where observations could be take at a late enough epoch. Table 4.2 lists the spectroscopic observations presented here, all spectra are presented in Appendix E.

Table 4.2: Journal of spectroscopic observations

MJD	$t-t_{\max}$ [rest-frame days]	Telescope/instrument	λ range [Å]	Exposure time [s]
		SN 2012ej		
56170	3	TNG/DOLORES	3000 – 8000	1200
56172	5	TNG/DOLORES	3000 – 8000	1200
56186	19	TNG/DOLORES	3000 – 8000	1500
56213	45	TNG/DOLORES	3000 – 8000	1800
56275	107	TNG/DOLORES	3000 – 10000	2400
56325	157	TNG/DOLORES	3000 – 10000	3600
		SN 2013bb		
56388.25	-5.6	NTT/EFOSC2	3000 – 10000	1500
56395.20	1.1	NTT/EFOSC2	3000 – 10000	1500
56401.16	7.0	NTT/EFOSC2	3000 – 10000	1600
56508.99	112.9	NTT/EFOSC2	3000 – 10000	2700
56717.27	317.6	NTT/EFOSC2	3000 – 10000	2400
		SN 2014L		
56688.72	-8.4	ANU/WiFeS	3300 – 9000	1200
56689.30	-7.8	NTT/EFOSC2	3000 – 10000	900
56694.33	-2.8	NTT/EFOSC2	3000 – 10000	900
56696.35	-0.8	NTT/EFOSC2	3000 – 10000	900
56712.60	15.2	ANU/WiFeS	3300 – 9000	1200
56730.60	33.1	ANU/WiFeS	3300 – 9000	1200
56738.51	40.9	ANU/WiFeS	3300 – 9000	1200
		SN 2014ad		
56730.62	-9.4	ANU/WiFeS	3300 – 9000	1200
56733.51	-6.5	ANU/WiFeS	3300 – 9000	1800
56734.54	-5.5	ANU/WiFeS	3300 – 9000	1800
56735.61	-4.5	ANU/WiFeS	3300 – 9000	1800
56738.46	-1.6	ANU/WiFeS	3300 – 9000	1200

56744.52	4.3	ANU/WiFeS	3300 – 9000	1000
56749.64	9.4	ANU/WiFeS	3300 – 9000	1200
56763.48	23.1	ANU/WiFeS	3300 – 9000	1800
56768.15	27.8	NTT/EFOSC2	3000 – 10000	900
56770.45	30.1	ANU/WiFeS	3300 – 9000	1200
56777.19	36.8	NTT/EFOSC2	3000 – 10000	1200
57100.31	358.1	NTT/EFOSC2	3000 – 10000	1800
		SN 2015ah		
57243.42	-5.0	LT/SPRAT	4000 – 8000	1800
57244.51	-3.9	LT/SPRAT	4000 – 8000	1800
57247.55	-0.9	LCO/Floyds	3200 – 10000	1800
57248.32	-0.1	NTT/EFOSC2	3000 – 10000	1200
57249.10	0.5	LT/SPRAT	4000 – 8000	1200
57251.00	2.4	LT/SPRAT	4000 – 8000	1200
57250.55	2.0	LCO/Floyds	3200 – 10000	1800
57253.19	4.6	NTT/EFOSC2	3000 – 10000	900
57253.53	4.9	LCO/Floyds	3200 – 10000	1800
57254.15	5.5	LT/SPRAT	4000 – 8000	1200
57256.49	7.8	LCO/Floyds	3200 – 10000	1800
57257.17	8.5	LT/SPRAT	4000 – 8000	1200
57257.96	9.3	LT/SPRAT	4000 – 8000	1200
57271.52	22.6	LCO/Floyds	3200 – 10000	2700
57277.53	28.5	LCO/Floyds	3200 – 10000	2700
57294.55	45.3	LCO/Floyds	3200 – 10000	3600
57301.22	51.8	NTT/EFOSC2	3000 – 10000	1800
57308.31	58.8	LCO/Floyds	3200 – 10000	3600
57396.5	145.6	Keck/DEIMOS	4000 – 10000	1800
		SN 2016P		
57408.14	-7.8	LT/SPRAT	4000 – 8000	300
57410.23	-5.8	LT/SPRAT	4000 – 8000	600
57413.29	-2.8	LT/SPRAT	4000 – 8000	600

57415.30	-0.8	NTT/EFOSC2	3000 – 10000	1500
57423.13	6.8	LT/SPRAT	4000 – 8000	600
57423.34	7.0	NTT/EFOSC2	3000 – 10000	1500
57430.13	13.7	LT/SPRAT	4000 – 8000	700
57434.29	17.8	NTT/EFOSC2	3000 – 10000	1800
57443.28	26.7	NTT/EFOSC2	3000 – 10000	1800
57466.02	49.1	LT/SPRAT	4000 – 8000	400
		SN 2016bau		
57462.05	-15.0	LT/SPRAT	4000 – 8000	400
57463.07	-14.0	LT/SPRAT	4000 – 8000	400
57464.11	-12.9	LT/SPRAT	4000 – 8000	300
57465.13	-11.9	LT/SPRAT	4000 – 8000	900
57465.89	-11.2	LT/SPRAT	4000 – 8000	300
57466.95	-10.1	LT/SPRAT	4000 – 8000	300
57475.88	-1.2	LT/SPRAT	4000 – 8000	100
57478.94	1.7	LT/SPRAT	4000 – 8000	300
57479.53	2.3	LCO/Floyds	3200 – 10000	250
57480.85	3.6	LT/SPRAT	4000 – 8000	100
57483.91	6.7	LT/SPRAT	4000 – 8000	100
57487.91	10.7	LT/SPRAT	4000 – 8000	300
57488.92	11.7	LT/SPRAT	4000 – 8000	125
57500.36	23.1	LCO/Floyds	3200 – 10000	1250
57508.97	31.6	LT/SPRAT	4000 – 8000	750
57515.91	38.6	LT/SPRAT	4000 – 8000	750
57525.89	48.5	LT/SPRAT	4000 – 8000	900
57703.16	225.1	LT/SPRAT	4000 – 8000	1500
		SN 2016coi		
57536.19	-13.1	LT/SPRAT	4000 – 8000	200
57537.13	-12.2	LT/SPRAT	4000 – 8000	100
57539.88	-9.5	LJT/YFOSC	3500 – 9200	1800
57540.11	-9.2	LT/SPRAT	4000 – 8000	100

57541.59	-7.8	LCO/Floyds	3200 – 10000	1200
57541.87	-7.5	LJT/YFOSC	3500 – 9200	1800
57542.17	-7.2	LT/SPRAT	4000 – 8000	100
57546.56	-2.8	LCO/Floyds	3200 – 10000	1200
57548.14	-1.2	LT/SPRAT	4000 – 8000	100
57549.15	-0.2	LT/SPRAT	4000 – 8000	100
57551.14	1.6	LT/SPRAT	4000 – 8000	100
57552.67	3.2	LCO/Floyds	3200 – 10000	1200
57553.07	3.6	LT/SPRAT	4000 – 8000	100
57554.67	5.2	LCO/Floyds	3200 – 10000	400
57557.11	7.6	LT/SPRAT	4000 – 8000	100
57557.53	8.0	LCO/Floyds	3200 – 10000	1200
57558.07	8.6	LT/SPRAT	4000 – 8000	100
57561.04	11.5	LT/SPRAT	4000 – 8000	100
57563.74	14.2	XLT/BFOSC	3600 – 8800	2400
57566.51	17.0	LCO/Floyds	3200 – 10000	1200
57570.59	21.0	LCO/Floyds	3200 – 10000	1200
57574.20	24.6	LT/SPRAT	4000 – 8000	150
57574.59	25.0	LCO/Floyds	3200 – 10000	1200
57575.14	25.6	LT/SPRAT	4000 – 8000	150
57581.01	31.4	LT/SPRAT	4000 – 8000	150
57583.59	34.0	LCO/Floyds	3200 – 10000	1800
57584.72	35.1	LCO/Floyds	3200 – 10000	1800
57588.14	38.5	LT/SPRAT	4000 – 8000	200
57591.58	41.9	LCO/Floyds	3200 – 10000	1800
57593.12	43.5	LT/SPRAT	4000 – 8000	300
57602.65	53.0	XLT/BFOSC	3600 – 8800	2700
57602.68	53.0	LJT/YFOSC	3500 – 9200	1800
57603.53	53.9	LCO/Floyds	3200 – 10000	1800
57613.59	63.9	LJT/YFOSC	3500 – 9200	2700
57613.93	64.2	LT/SPRAT	4000 – 8000	1000

57614.47	64.7	LCO/Floyds	3200 – 10000	1800
57620.57	70.8	LJT/YFOSC	3500 – 9200	2700
57623.69	73.9	LJT/YFOSC	3500 – 9200	2700
57625.66	75.9	LJT/YFOSC	3500 – 9200	2700
57628.62	78.8	LCO/Floyds	3200 – 10000	1500
57636.50	86.7	LCO/Floyds	3200 – 10000	1500
57636.99	87.2	LT/SPRAT	4000 – 8000	700
57656.36	106.5	LCO/Floyds	3200 – 10000	1800
57661.5	111.6	INT/IDS	3700 – 7600	3600
57662.20	112.3	Lick/Kast	3400 – 10000	2700
57677.20	127.3	LCO/Floyds	3200 – 10000	1800
57678.41	128.5	LCO/Floyds	3200 – 10000	1800
57693.84	143.8	LT/SPRAT	4000 – 8000	1500
57701.32	151.3	LCO/Floyds	3200 – 10000	1800
57703.57	153.5	LJT/YFOSC	3500 – 9200	2400
57724.11	174.0	Lick/Kast	3400 – 10000	1200
57728.84	178.7	LT/SPRAT	4000 – 8000	1500
57736.23	186.1	LCO/Floyds	3200 – 10000	1800
57744.21	194.0	LCO/Floyds	3200 – 10000	1800
57898.5	347.8	Keck/DEIMOS	4000 – 10500	900
57990.94	439.9	LT/SPRAT	4000 – 8000	2400
		SN 2016frp		
57638.13	0.1	NTT/EFOSC2	3000 – 10000	1800
57638.00	0.0	LT/SPRAT	4000 – 8000	900
57642.28	4.2	NTT/EFOSC2	3000 – 10000	1800
57650.98	12.6	LT/SPRAT	4000 – 8000	900
57651.10	12.8	NTT/EFOSC2	3000 – 10000	1800
57655.19	16.8	NTT/EFOSC2	3000 – 10000	2700
57664.19	25.5	NTT/EFOSC2	3000 – 10000	2700
		SN 2016iae		
57705.11	-8.6	LT/SPRAT	4000 – 8000	400

57707.42	-6.3	LT/SPRAT	4000 – 8000	1000
57708.02	-5.7	LT/SPRAT	4000 – 8000	400
57708.58	-5.2	LT/SPRAT	4000 – 8000	1000
57710.01	-3.8	LT/SPRAT	4000 – 8000	400
57710.28	-3.5	NTT/EFOSC2	3000 – 10000	900
57711.26	-2.5	NTT/EFOSC2	3000 – 10000	1500
57712.00	-1.8	LT/SPRAT	4000 – 8000	400
57712.09	-1.7	NTT/EFOSC2	3000 – 10000	1800
57713.09	-0.7	NTT/EFOSC2	3000 – 10000	1800
57714.08	0.2	NTT/EFOSC2	3000 – 10000	1800
57718.24	4.3	NTT/EFOSC2	3000 – 10000	1800
57723.22	9.3	NTT/EFOSC2	3000 – 10000	2700
57740.23	26.3	NTT/EFOSC2	3000 – 10000	1500
57759.22	45.2	NTT/EFOSC2	3000 – 10000	1800
57771.09	57.0	NTT/EFOSC2	3000 – 10000	1800
57779.13	65.0	NTT/EFOSC2	3000 – 10000	2400
57789.08	74.9	NTT/EFOSC2	3000 – 10000	2900
57803.05	88.9	NTT/EFOSC2	3000 – 10000	2700
		SN 2016jdw		
57756.21	-6.7	LT/SPRAT	4000 – 8000	700
57757.20	-5.8	LT/SPRAT	4000 – 8000	1000
57762.27	-0.8	LT/SPRAT	4000 – 8000	700
57764.27	1.1	LT/SPRAT	4000 – 8000	700
57770.24	6.9	LT/SPRAT	4000 – 8000	500
57788.19	24.6	LT/SPRAT	4000 – 8000	700
57789.10	25.5	LT/SPRAT	4000 – 8000	700
57790.15	26.5	LT/SPRAT	4000 – 8000	900
57812.11	48.0	LT/SPRAT	4000 – 8000	700
57824.20	59.9	LT/SPRAT	4000 – 8000	900
57846.03	81.3	LT/SPRAT	4000 – 8000	900
57866.91	101.8	LT/SPRAT	4000 – 8000	1000

57892.07	126.5	LT/SPRAT	4000 – 8000	1300
		SN 2017bgu		
57811.24	-7.0	LT/SPRAT	4000 – 8000	700
57812.27	-6.0	LT/SPRAT	4000 – 8000	700
57813.25	-5.0	LT/SPRAT	4000 – 8000	700
57814.27	-4.0	LT/SPRAT	4000 – 8000	250
57820.24	1.8	LT/SPRAT	4000 – 8000	200
57824.27	5.8	LT/SPRAT	4000 – 8000	200
57828.20	9.7	LT/SPRAT	4000 – 8000	200
57839.17	20.6	LT/SPRAT	4000 – 8000	200
57853.02	34.3	LT/SPRAT	4000 – 8000	250
57902.98	83.8	LT/SPRAT	4000 – 8000	750
57931.90	112.5	LT/SPRAT	4000 – 8000	1000
58000.85	180.9	LT/SPRAT	4000 – 8000	1000
		SN 2017dcc		
57865.27	-3.5	NTT/EFOSC2	3000 – 10000	300
57866.29	-2.5	NTT/EFOSC2	3000 – 10000	1500
57867.09	-1.7	LT/SPRAT	4000 – 8000	200
57872.08	3.0	NTT/EFOSC2	3000 – 10000	1500
57874.21	5.1	NTT/EFOSC2	3000 – 10000	1500
57879.02	9.8	LT/SPRAT	4000 – 8000	360
57884.93	15.6	LT/SPRAT	4000 – 8000	500
57905.10	35.3	NTT/EFOSC2	3000 – 10000	1800
		SN 2017ein		
57902.04	-12.5	LT/SPRAT	4000 – 8000	650
57903.88	-10.7	LT/SPRAT	4000 – 8000	250
57906.05	-8.5	LT/SPRAT	4000 – 8000	150
57907.90	-6.7	LT/SPRAT	4000 – 8000	150
57909.88	-4.7	LT/SPRAT	4000 – 8000	150
57911.89	-2.7	LT/SPRAT	4000 – 8000	150
57913.90	-0.7	LT/SPRAT	4000 – 8000	150

57914.90	0.2	LT/SPRAT	4000 – 8000	210
57917.88	3.2	LT/SPRAT	4000 – 8000	210
57921.94	7.2	LT/SPRAT	4000 – 8000	210
57925.89	11.2	LT/SPRAT	4000 – 8000	210
57932.96	18.2	LT/SPRAT	4000 – 8000	210
57939.94	25.2	LT/SPRAT	4000 – 8000	360
57948.92	34.1	LT/SPRAT	4000 – 8000	600
58055.24	140.2	LT/SPRAT	4000 – 8000	1500
58102.25	187.1	LT/SPRAT	4000 – 8000	1200
		SN 2017gpn		
57995.06	-7.3	LT/SPRAT	4000 – 8000	900
57996.04	-6.4	LT/SPRAT	4000 – 8000	900
58000.04	-2.4	LT/SPRAT	4000 – 8000	300
58003.01	0.5	LT/SPRAT	4000 – 8000	300
58007.02	4.4	LT/SPRAT	4000 – 8000	300
58015.00	12.4	LT/SPRAT	4000 – 8000	360
58020.09	17.4	LT/SPRAT	4000 – 8000	360
58024.97	22.3	LT/SPRAT	4000 – 8000	360
58030.14	27.4	LT/SPRAT	4000 – 8000	420
58036.93	34.1	LT/SPRAT	4000 – 8000	600
58043.92	41.1	LT/SPRAT	4000 – 8000	600
58074.88	71.8	LT/SPRAT	4000 – 8000	600
58106.87	103.6	LT/SPRAT	4000 – 8000	1000
		SN 2017hyh		
58070.32	-6.1	NTT/EFOSC2	3000 – 10000	300
58071.07	-5.4	LT/SPRAT	4000 – 8000	1000
58074.23	-2.2	LT/SPRAT	4000 – 8000	600
58077.03	0.4	LT/SPRAT	4000 – 8000	360
58088.11	11.4	LT/SPRAT	4000 – 8000	360
58102.06	25.2	LT/SPRAT	4000 – 8000	360
58108.97	32.0	LT/SPRAT	4000 – 8000	360

		SN 2017ifh		
58076.00	-2.5	LT/SPRAT	4000 – 8000	900
58088.09	9.0	LT/SPRAT	4000 – 8000	900
58102.00	22.4	LT/SPRAT	4000 – 8000	1200
58107.96	28.1	LT/SPRAT	4000 – 8000	1200
		SN 2017iuk		
58102.20	-4.7	LT/SPRAT	4000 – 8000	1200
58107.23	0.0	LT/SPRAT	4000 – 8000	1200

4.2.1 Line velocities

The line velocities for the SNe are calculated as described in Chapter 3 and the resulting velocity curves are plotted in Figure 4.9. The Ic-3/4 SNe are not included due to the large uncertainties in velocity caused by the broad and blended lines. The 6200 Å feature in the H-poor/He-rich SNe is treated as Hα. There are several interesting features to note

- Type IIb(I) SN 2017hyh has high velocity lines. With a Hα velocity of ~ 16000 km s^{-1} and He I velocity of ~ 11000 km s^{-1} at maximum light it has more in common with the velocities of the H-poor/He-rich SNe than the other H-rich SNe (see Figure 3.6). Its early Fe II line velocity at $t_{\rm max}$ of ~ 13000 km s^{-1} even exceeds that of some He-poor SNe (Figure 3.25; top right panel)
- There is a difference in the behaviour of the Fe II velocity between the He-rich and He-poor SNe. In the former the velocity tends to decrease throughout, whereas in the the latter the velocities level off to around 8000 km s^{-1}
- The velocities of He-poor SNe are typically larger than those of He-rich SNe (see Fe II λ 5169 and Ca II NIR). The Ic-7 velocities have a small range, although the low velocities of SN 2012ej make it an outlier.

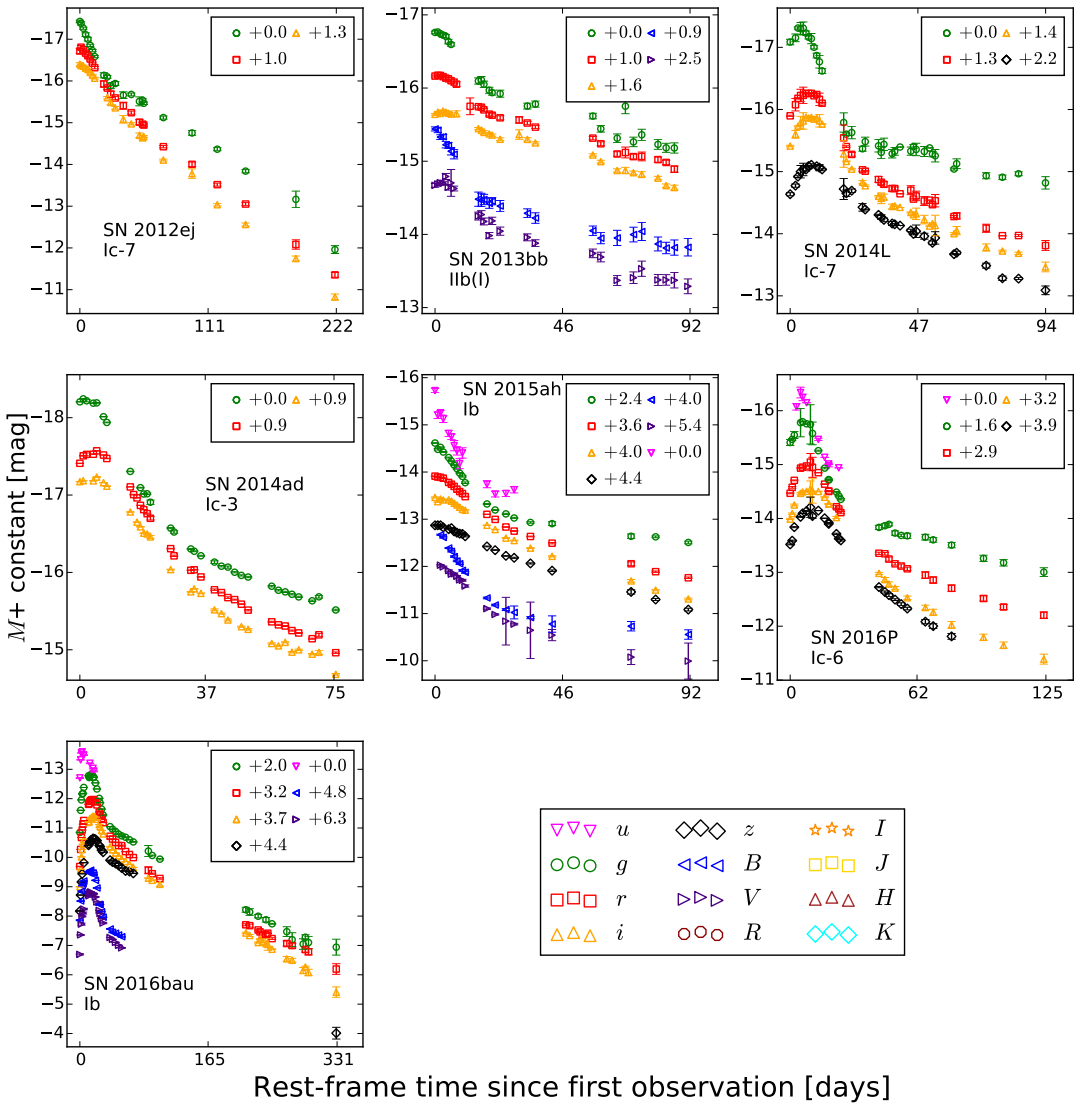

Figure 4.3: The intrinsic light cures of SNe included in the observations sample (1/3). All SNe are corrected for $E\,(B-V)_{\rm tot}$ and cosmological time-dilation. The SN types are listed in Table 4.1

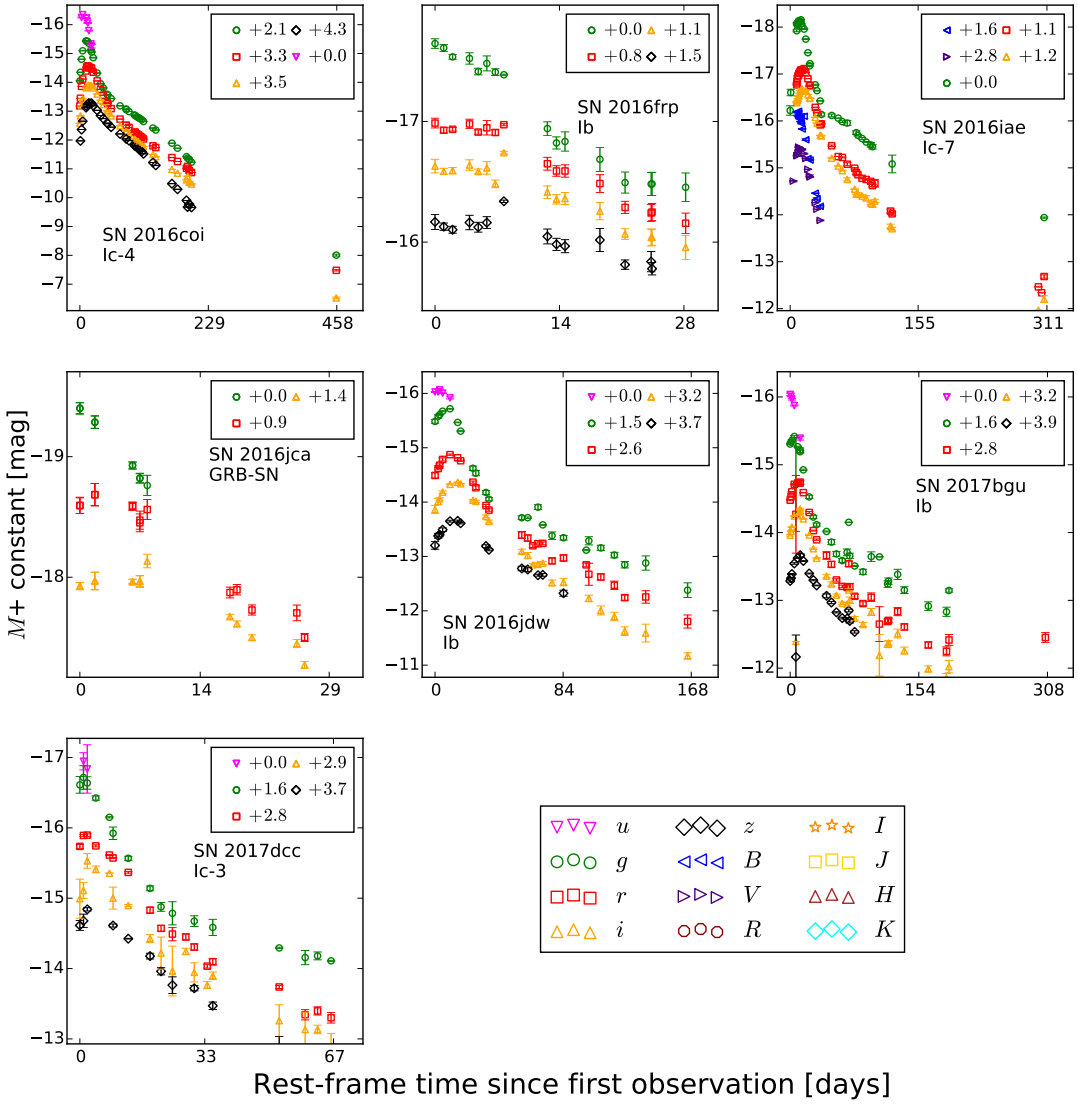

Figure 4.4: The intrinsic light cures of SNe included in the observations sample. As Figure 4.3 (2/3).

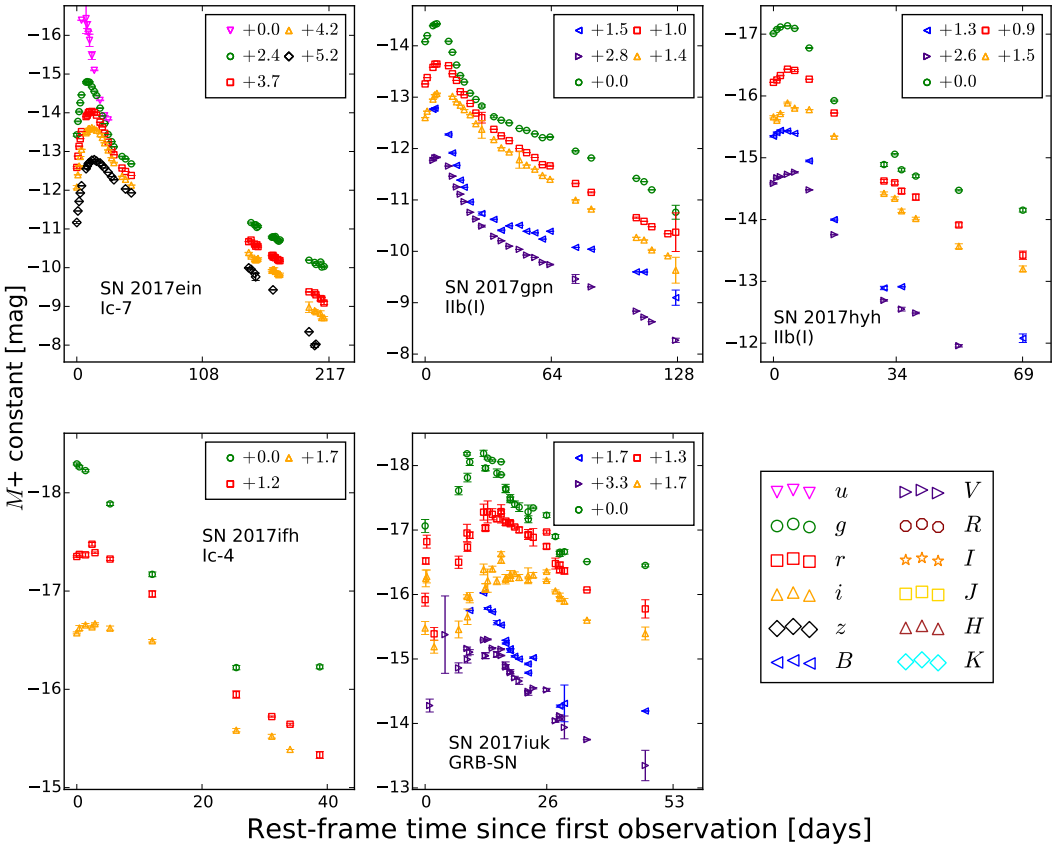

Figure 4.5: The intrinsic light cures of SNe included in the observations sample. As Figure 4.3 (3/3)

4.3 Comparison with bulk distributions

Figure 4.10 shows the distributions of $t_{-1/2}$ and $t_{+1/2}$ for the SN subtypes. These distributions include two extra SNe in addition to the sample of Chapter 2; SN IIb(I) 2008aq and SN Ic-7 2004dn, their parameters are listed in Table D.2. The absence of spectra, sufficiently early spectra, or the quality of the data, means that many of the SNe in the sample used in Chapter 2 cannot be reclassified into the scheme detailed in Chapter 3. Additionally, it would be desirable to build distributions based upon a single SN subtype, however there are insufficient numbers to do this in most cases. Because of this, the SNe are grouped as IIb + IIb(I), Ib(II) + Ib, Ic-5/6/7, Ic-3/4, GRB/XRF-SNe. SNe which I have been unable to reclassify are placed in the closest relative group (e.g., H-rich SNe in IIb + IIb(I))

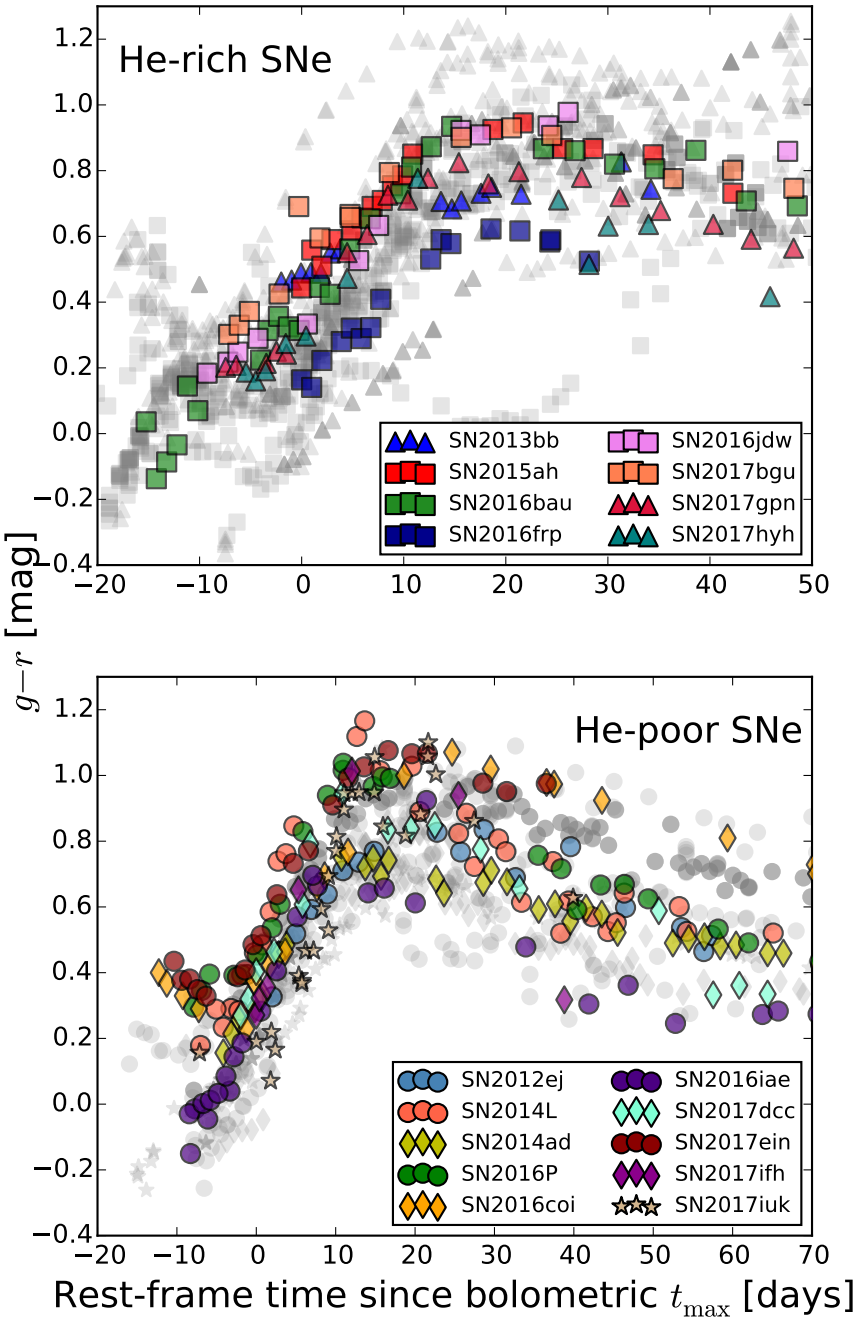

Figure 4.6: Updated $g-r$ colour curves of SE-SNe (grey) with inclusion of the new SNe located at $z < 0.05$. Markers are H/He-rich (triangles), H-poor/He-rich (squares), Ic-5/6/7 (circles), Ic-3/4 (diamonds), GRB-SNe (stars). Only those SNe with calculated $E\,(B-V)_{\rm host}$ are included. The correction for $E\,(B-V)_{\rm host}$ of the new SNe, independently calculated from host Na I D line strength, brings them into the larger distribution.

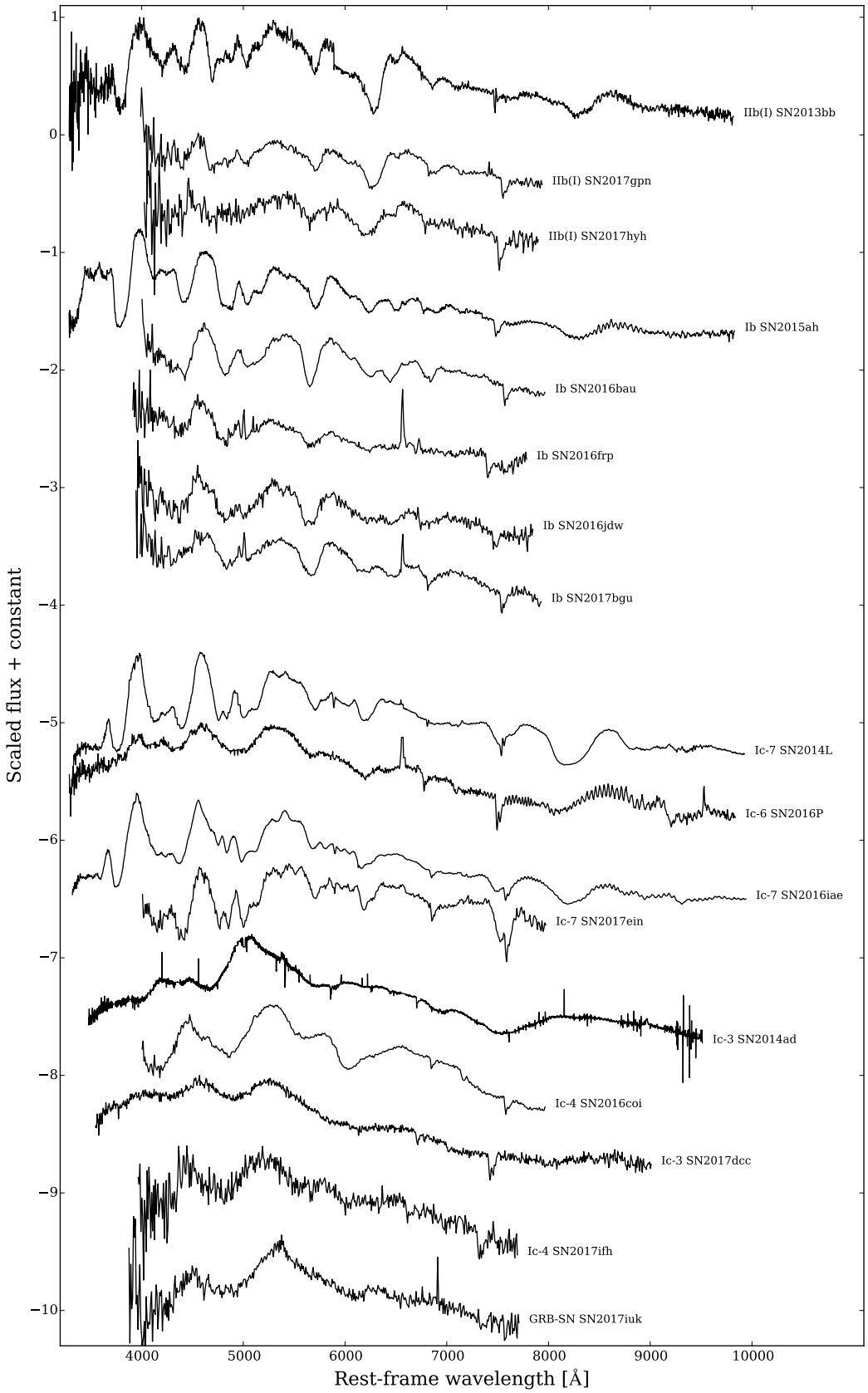

Figure 4.7: Spectra of the new SNe as close as possible to $t_{\max}$, excluding GRB-SN 2016jca, sorted according to type. SNe 2016P, 2014L, and 2014ad have had host galaxy emission lines removed.

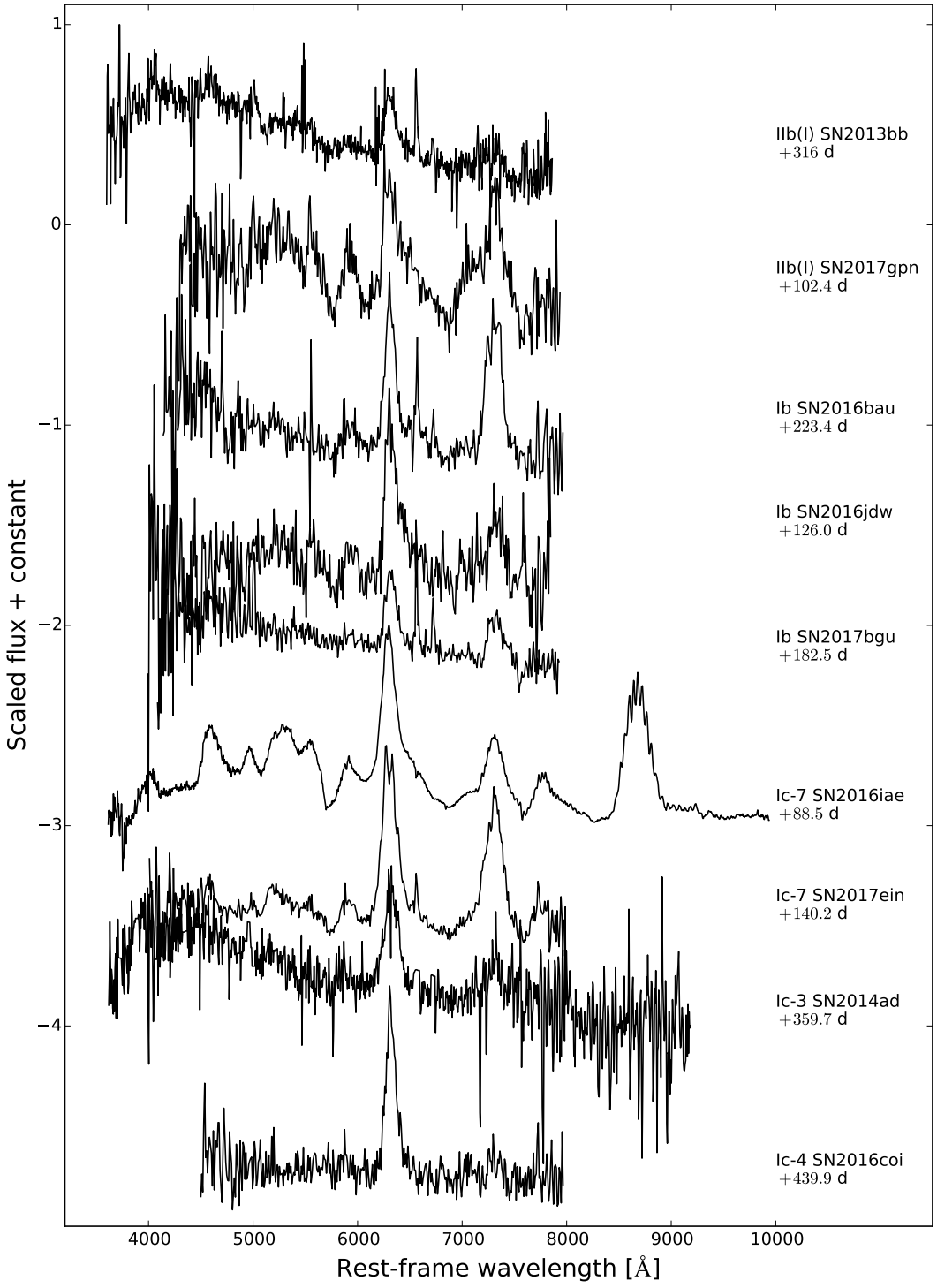

Figure 4.8: Nebular phase spectra of the SE-SNe observed in the course of this work.

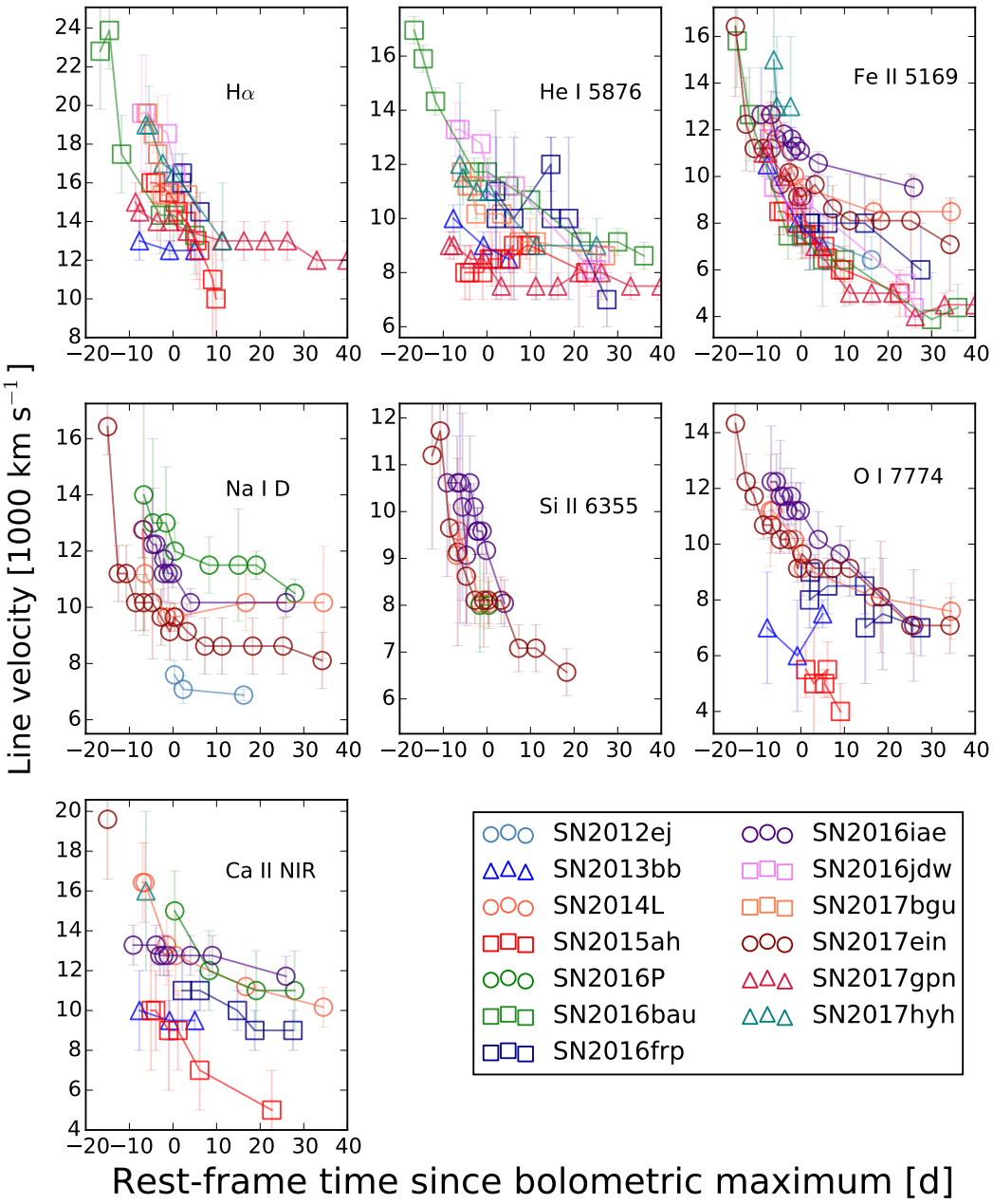

Figure 4.9: Velocity curves of the new SNe to +40 d. Markers are as in Figure 4.6.

4.3.1 $t_{-1/2}$ and $t_{+1/2}$ distributions

The distributions for the characteristic time-scales $t_{-1/2}$ and $t_{+1/2}$ are shown in Figure 4.10. For all SN types the medians of the respective distributions are comparable.

The clear outlier in the IIb + IIb(I) distribution is SN 2013bb which has a $t_{+1/2}\sim 56$ d compared with the median of ~ 15 d. Unfortunately, the rise was not observed for this SN. SN Ib 2017bgu is found a little outside the $t_{+1/2}$ one sigma region of the Ib(II) + Ib distribution. The rise was not sampled sufficiently well to determine $t_{-1/2}$ but a by-eye estimate from the light curve suggests it would be between 10 and 15 d, thus within the one sigma region. SN 2016coi is a marginal outlier in both $t_{-1/2}$ and $t_{+1/2}$ within the Ic-3/4 distributions, having both values a little greater than one sigma from the median. A direct comparison of $t_{-1/2}$ and $t_{+1/2}$ for each SN can be seen in Figure 4.11. That SN 2016coi is long in both time scales is apparent, although there are other SNe with long time-scales.

Both SN 2013bb and 2016coi are "objects of interest" and are discussed further in Section 4.4

4.3.2 Peak luminosity and $M_{\rm Ni}$ distributions

Figure 4.12 shows the $\log_{10}(L_{\rm p})$ distributions of this sample, constructed from 4000 – 10000 Å SEDS. Only SNe with an estimated $E(B-V)_{\rm host}$ are used here. Most of the SNe fall within one sigma of their respective distributions, but there are two clear outliers; SN IIb(I) 2017gpn and SN Ib 2016bau. The two main causes for underluminosity is an underestimate in either $E(B-V)_{\rm host}$ or μ.

SN 2016gpn (in NGC 1343, $z = 0.0074$) was calculated to have negligible $E(B-V)_{\rm host}$, which was also seen by its position in the $g-r$ colour curves. Distances to the host galaxy vary from 28.14 mag to 31.73 mag with a mean of 29.79 mag as per the TF method. A redshift-derived distance gives $\mu = 32.6$ mag. Hence, it is clear that the distance to the host is uncertain and it is possible that the distance used here is an underestimate rather than SN 2017gpn being intrinsically dim.

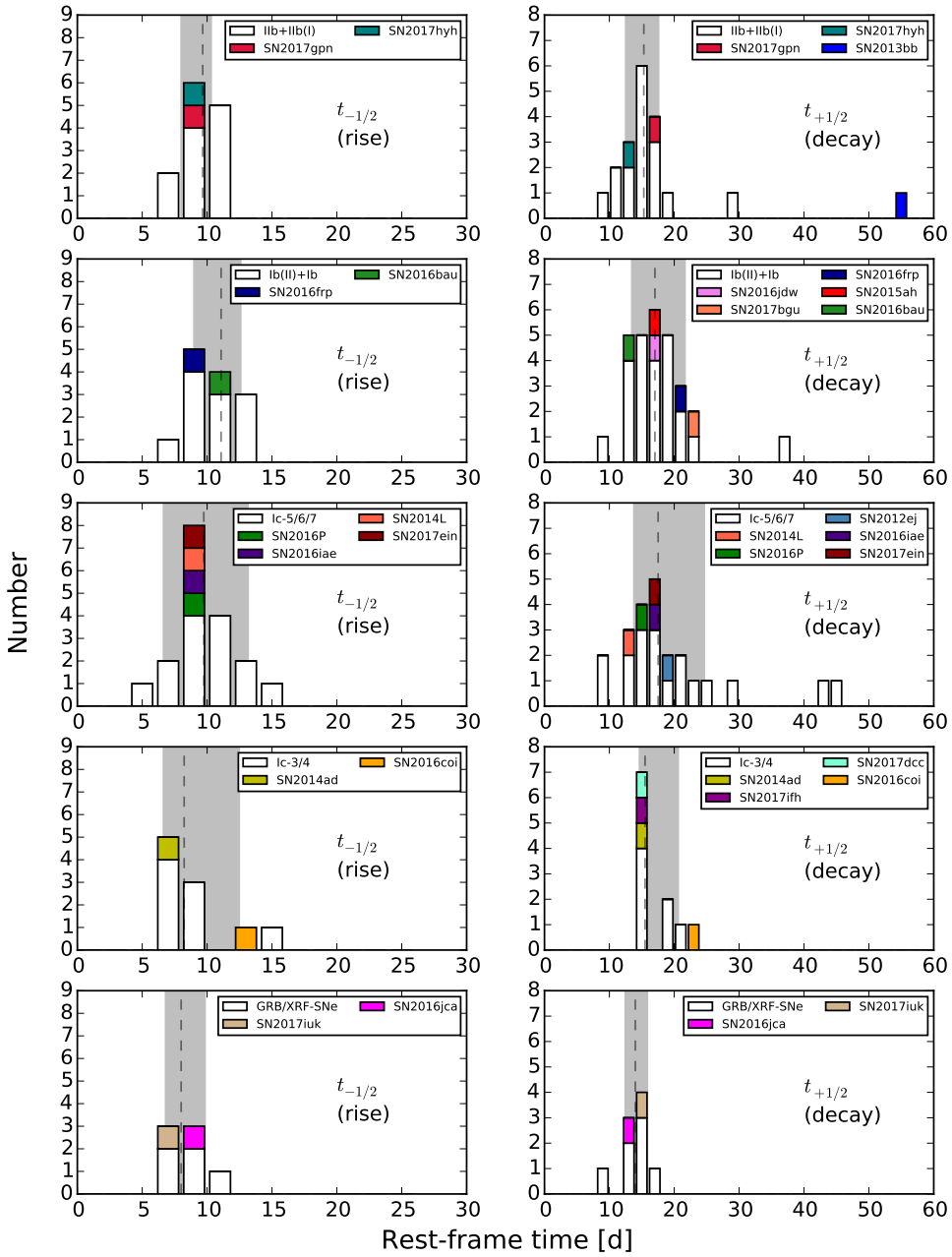

Figure 4.10: The distributions for $t_{-1/2}$ and $t_{+1/2}$ for the SN subtype groupings considered here. The dashed line represents the median of each distribution and the grey region represents the one sigma range, within which 68 percent of the values are found. SN 2013bb is a very clear outlier in the IIb + IIb(I) distribution.

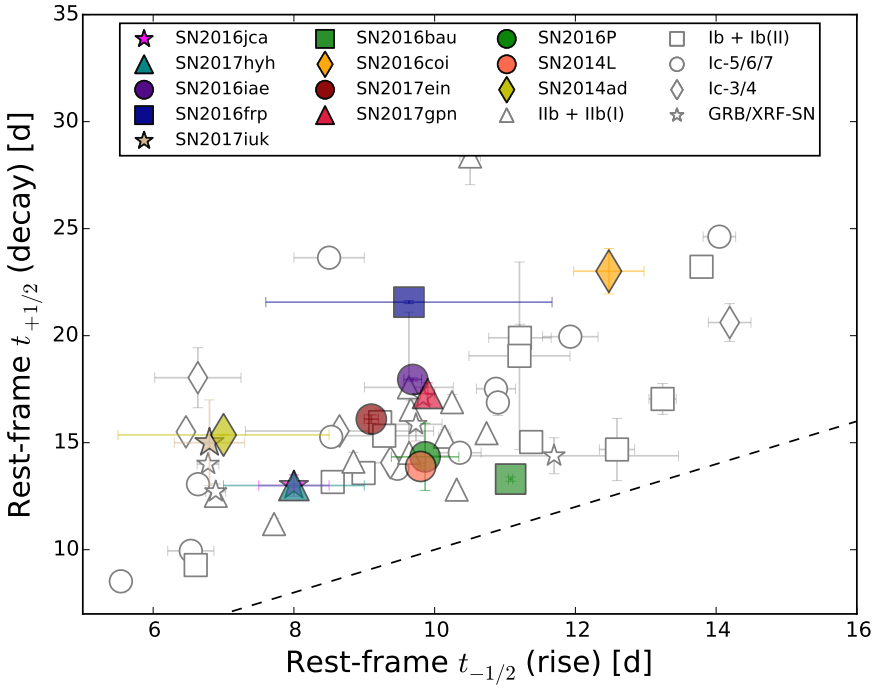

Figure 4.11: $t_{+1/2}$ against $t_{-1/2}$ for the SNe where both values have been derived. The dotted line denotes $t_{+1/2} = t_{-1/2}$ and shows that all SNe have $t_{+1/2} > t_{-1/2}$. The absence of early data means that some extreme SNe (SN 2013bb, SN 2011bm, PTF11rka) are not shown. These SNe all have $t_{+1/2} > 35$ d

SN 2016bau faces a similar problem; the TF measurements to the host, NGC 3631 vary from 29.12 mag to 31.67 mag with a z-dependent distance modulus of 31.73 mag. Adopting the larger distance modulus returns $\log_{10}(L_{\rm p}) = 42.8$ erg s^{-1}, which is still more than one sigma below the median. This implies that SN 2016bau is intrinsically a dim supernova.

The results for GRB-SN 2017iuk are preliminary but suggest that the SN is at the lower end of the luminosity distribution, which is occupied by XRF-SNe. At $z = 0.039$ the SN is the second closest GRB-SN (after SN 1998bw) but should be sufficiently far into the Hubble flow that the peculiar motion of the host galaxy can be neglected, however $E(B-V)_{\rm host}$ is quite uncertain. There are no obvious host Na I D lines in the spectra and the $g-r$ colour curves suggest that $E(B-V)_{\rm host}$ negligible. GRB-SNe are known for being discovered in "clean" environments and show little attenuation at source. In reality this is likely a bias in the observations as the less luminous and extinguished GRB-SNe are significantly harder to observe at the typical distances for

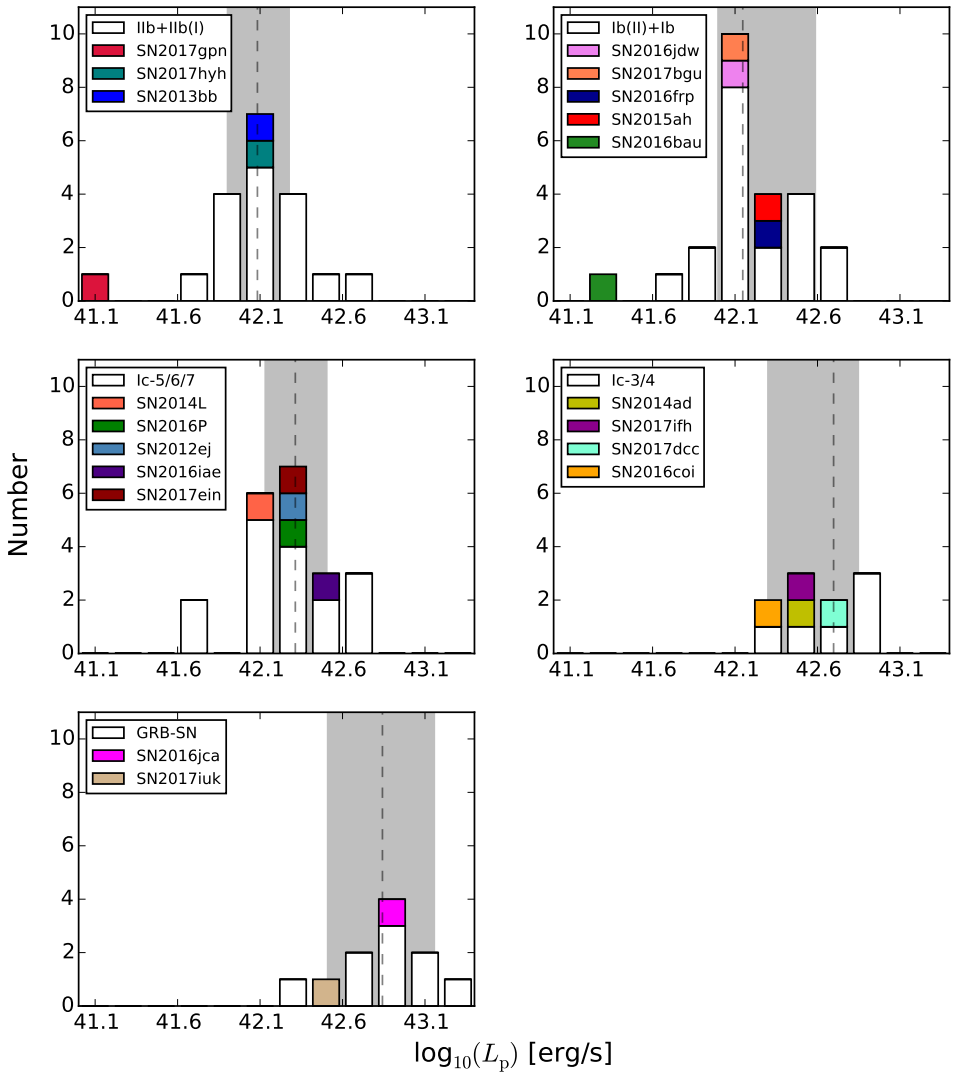

Figure 4.12: $\log_{10}(L_{\rm p})$ as derived from the 4000 – 10000 Å SEDs for SNe with a calculated value for $E(B-V)_{\rm host}$. These distributions reaffirm that found in Chapter 2; SNe Ic are more luminous on average than He-rich SNe, and GRB-SNe are the most luminous overall. SNe 2017gpn, 2016bau, and 2017iuk are discussed in the text.

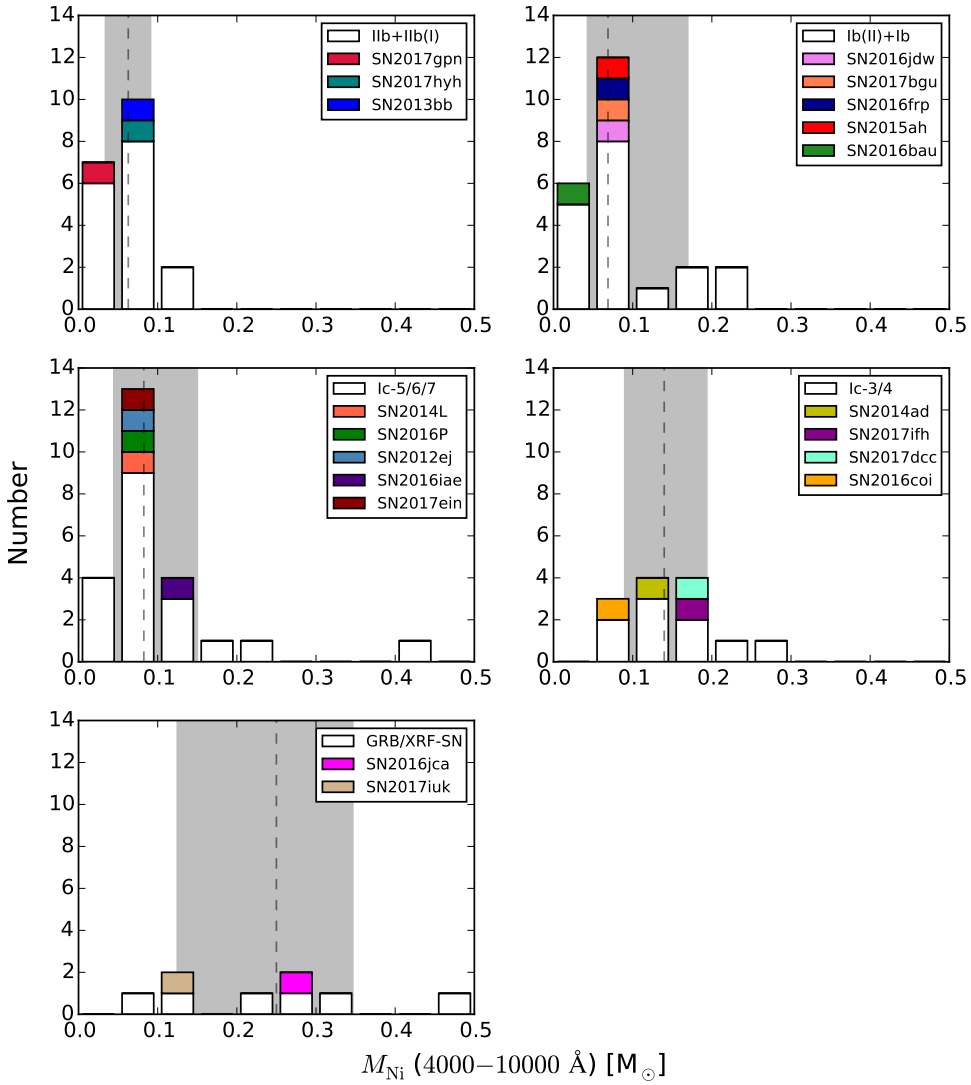

Figure 4.13: $M_{\rm Ni}$ calculated from analytical light curve fits to the 4000 – 10000 Å pseudo-bolometric light curves and distributed according to SN subtype.

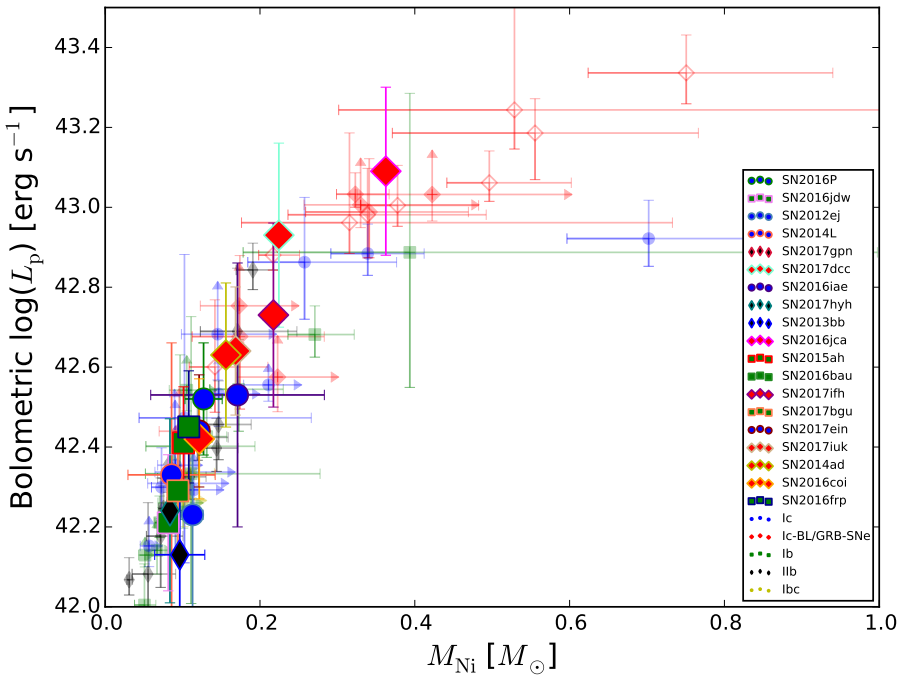

Figure 4.14: Updated $\log_{10}(L_{\rm p})$ against $M_{\rm Ni}$ including the new SNe introduced here. They continue to follow the same pattern as found before.

GRB-SNe. SN 2017iuk may just represent the lower part of the luminosity function that, as yet, remains ooorly-sampled.

The $M_{\rm Ni}$ distributions in Figure 4.13 show that ^{56}Ni synthesis is greater in Ic-3/4 and GRB-SNe than in Ic and He-rich SNe; this echoes the findings of Chapter 2. The new SNe all fall within one sigma of the median of their respective distributions.

red

4.3.3 $\log_{10}(L_{\rm p})$ v $M_{\rm Ni}$ v $M_{\rm ej}^3/E_{\rm k}$

In chapter 2 I showed Figures that investigated the relationships between $\log_{10}(L_{\rm p})$, $M_{\rm Ni}$, and $M_{\rm ej}^3/E_{\rm k}$. I update these plots in Figures 4.14, 4.15, 4.16 to include the SNe analysed in this Chapter. As can be seen, the SNe lie in similar regions to those found previously. There are no very luminous SNe here however, although there are some low luminosity SNe (SN 2016gpn and SN 2016bau)

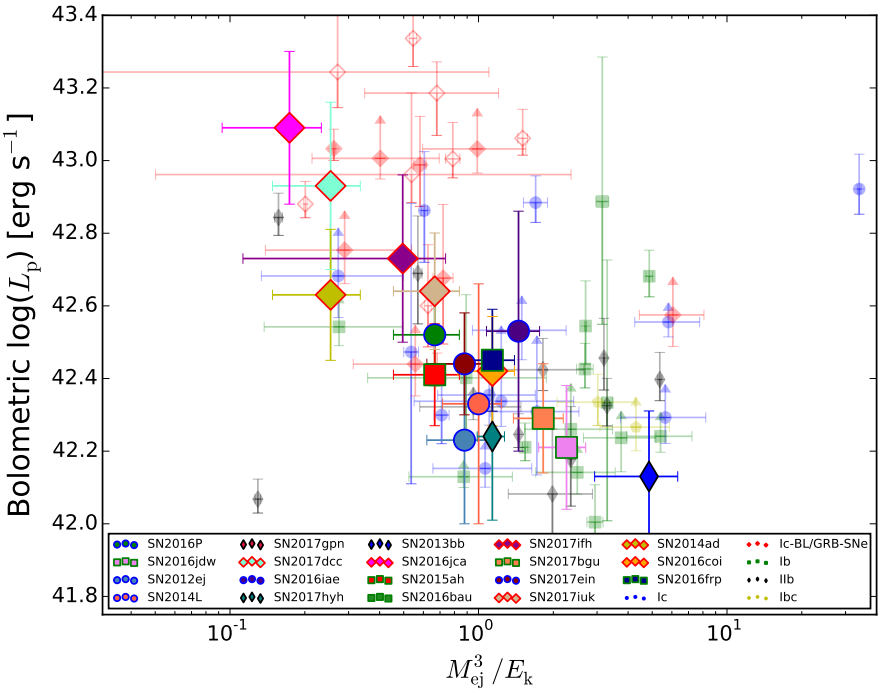

Figure 4.15: $\log_{10}(L_p)$ against M_{ej}^3/E_k updated to include the new SNe in the sample. As before, the SNe types occupy similar positions with SNe Ic, Ib, and IIb tending towards the lower right and the more energetic SNe to the upper left.

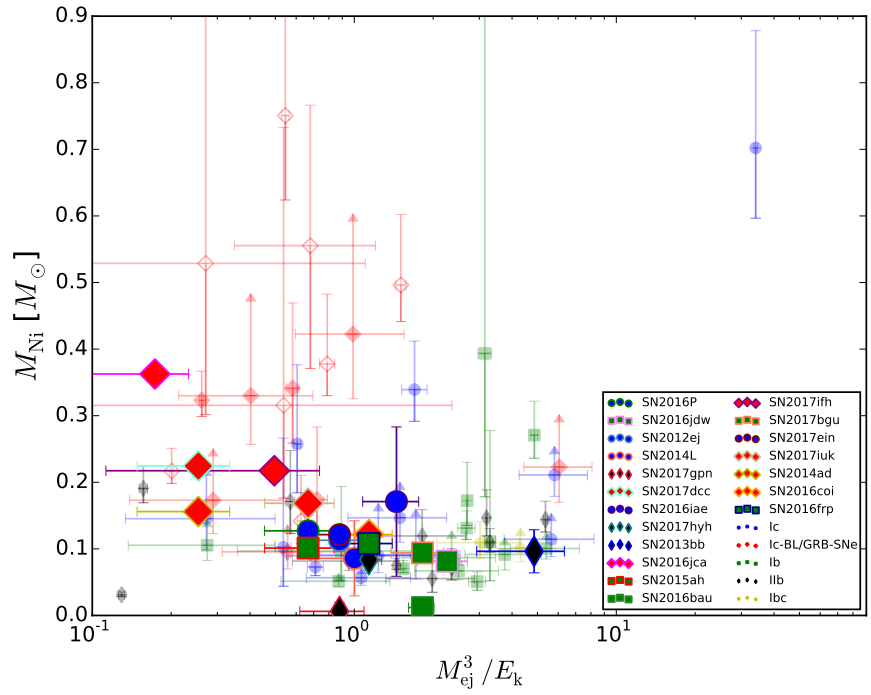

Figure 4.16: M_{Ni} against M_{ej}^3/E_k updated to include the new SNe in the sample. As before, the SNe types occupy similar positions with SNe Ic, Ib, and IIb tending towards the lower right and the more energetic SNe tending towards the upper left.

4.3.4 Ejecta mass

With a large sample of SNe it is now possible to get a clearer picture of the ejecta mass distributions for the individual subtypes and for all SE-SNe, these are shown in Figure 4.17 and the individual $M_{\rm ej}$ values listed in Table D.3. It is seen that there is considerable overlap between the distributions. The method itself comes with two caveats –

i) For the He-rich SNe it is important to note that helium has little effect on the light curve because its opacity is low (Piro and Morozova, 2014; Wheeler et al., 2015), thus $M_{\rm ej}$ may better measure the C/O core mass and underestimate the total ejecta mass in these SNe. This may be compensated for by dynamical effects however – the transparent He still needs to be energised, which leads to lower ejecta velocities for SNe with He and for a fixed $E_{\rm k}/M_{\rm ej}$.

ii) An issue may also arise if there is a large velocity gradient (e.g., as found in GRB-SNe), where a significant fraction of mass can pass through the photosphere before maximum light, when $v_{\rm ph}$ is measured, leading to an underestimate of $M_{\rm ej}$. This is why $M_{\rm ej}$ for SN 1998bw, for example, varies between spectral modelling (10 $M_{\odot}$– Mazzali et al., 2013) and light curve fitting ($\sim$5 $M_{\odot}$; e.g., this work, Lyman et al., 2016).

Table 4.3 compares the results of masses derived in this work with those from spectral or explosion modelling. The methods are broadly consistent in their results. Interestingly, the outliers have large velocity gradients and long rise times (16 – 19 days), while others with large velocity gradients but short rise times (10 – 12 days, e.g. SNe 2002ap, 2003dh, 2010ah) are in agreement, this supports the statement made previously about discrepancies. High velocity ejecta in a SN with a long rise time ejects more mass before $t_{\rm max}$ when $v_{\rm ph}$ is measured at peak and velocities are closer to that of normal SE-SNe. That the same is not seen for quick-rising SNe suggests that the key time is the days before $t_{\rm max}$, when the density of material passing through the photosphere is higher than at earlier times but the ejecta velocity at these times is still relatively high.

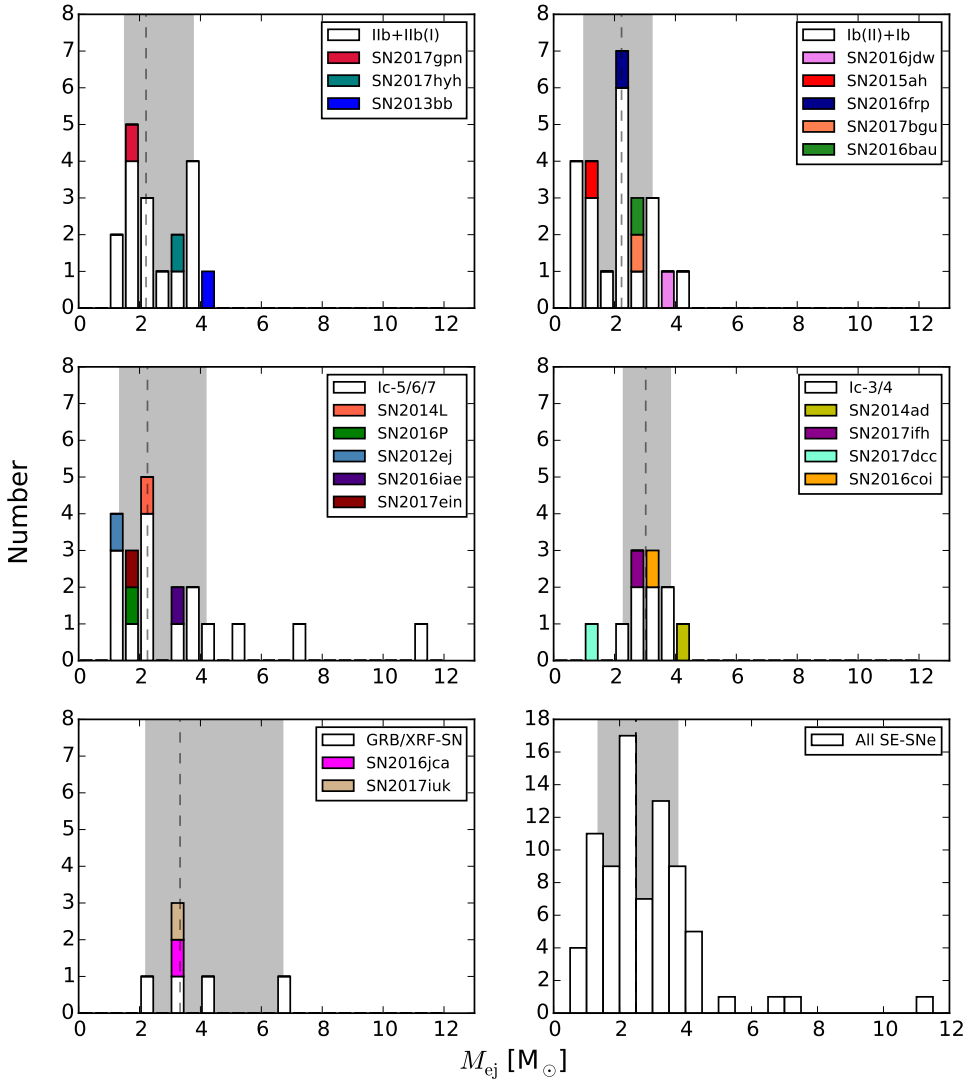

Figure 4.17: $M_{\rm ej}$ distributions and derived using the analytical light curve model of Arnett (1982).

Table 4.3: $M_{\rm ej}$ derived here compared with spectral modelling

SN	type	$M_{\rm ej}$ (this work) [$M_\odot$]	$M_{\rm ej}$ (literature) [$M_\odot$]	Ref
1993J	IIb	3.3	2.5 – 3	(Woosley et al., 1994)
1994I	Ic-6	1.04	0.95	(Sauer et al., 2006)
1998bw	GRB-SN	4.3	10	(Mazzali et al., 2013)
2002ap	Ic-4	2.3	2.5	(Mazzali et al., 2002)
2003dh	GRB-SN	6.7	8	(Mazzali et al., 2003)
2003bg	IIb-BL	3.7	4	(Mazzali et al., 2009)
2004aw	Ic-6	4.2	3-5	(Mazzali et al., 2017)
2005bf	Ib-pec	0.9	0.1 – 0.4†	(Maeda et al., 2008)
2006aj	XRF-SN	2.2	2	(Mazzali et al., 2006)
2008D	Ib-pec	2.9	7	(Mazzali et al., 2008)
2010ah	Ic-3	3.4	3	(Mazzali et al., 2013)

† From nebular models. O constitutes the majority of $M_{\rm ej}$ in SNe Ibc.

Considering the distributions, the He-rich SNe are found to have $M_{\rm ej}$ between 1 – 4 $M_\odot$, as do the Ic-3/4 SNe, although the latter are more massive on average. Comparatively the Ic-5/6/7 show a large spread of values from 1 $M_\odot$ to 11 $M_\odot$ but with a median comparable to the He-rich SNe. The GRB/XRF-SNe are comparable in median mass to the Ic-3/4 SNe but cover a larger range of values.

There are a number of outliers, mostly marginally outside one sigma of the distribution; SN 2013bb, SN 2016jdw, SN 2014ad are all significantly above their respective medians while SN 2017dcc is below. SN 2017dcc is an Ic-3 SNe with line velocities are significantly below those of the archetypal "broad-line" SN 1998bw. An uncertain rise means that it may be more massive but high mass is not a requirement for highly blended lines, only high velocities and a large $E_{\rm k}/M_{\rm ej}$ (e.g., iPTF16asu; Whitesides et al., 2017).

Comparison with $M_{\rm ej}$ calculated in other samples (Drout et al., 2011; Cano, 2013; Lyman et al., 2016; Taddia et al., 2015) is given in Table 4.4. Mostly, the ejecta masses overlap although differences are seen in the medians and means. In these works the procedure for determining $M_{\rm ej}$ was similar to here; using the method of Arnett (1982), and in most cases $\kappa = 0.05 - 0.07$ g cm^{-2} was used. However in some cases (Drout et al., 2011; Cano, 2013) a typical value for $v_{\rm ph}$ was used rather than a measured value. In this work we ensure that the photospheric velocity is always below that of the lowest

measurable velocity at $t_{\rm max}$, though this is not the case in other works and can go some way to explaining different results (see Table 4.4). It should be noted that no method is more valid than another here as $v_{\rm sc}$, of which $v_{\rm ph}$ is a proxy, has little physical meaning. The density of the ejecta is not constant across the velocity profile (e.g. Nomoto et al., 1994), but this is assumed in Equation 4.4. Thus, it is assumed the majority of mass resides below $v_{\rm sc}$, and measurements of line velocities in the spectra may provide some estimate of this.

Interpreting the results

The overlap in the $M_{\rm ej}$ distributions for different SN sub-types suggests that the progenitors of many of these SNe may be similar. If one assumes a 1.4 M$_\odot$ remnant then $M_{\rm ej} + M_{\rm remnant} = M_{\rm COcore} < 5$ M$_\odot$ for the vast majority of SNe. Given that if there are two progenitor pathways, one from low mass with binary interaction and one from high mass single stars, it should be expected that there would be two distributions present. The distribution of SNe Ic is very broad, and it may well be possible that it represents two separate pathways. There is not enough data yet to see if a bimodal distribution is present. Nor is any bimodality immediately apparent in the ejecta mass of all the SE-SNe, what is seen is a skewed distribution with more low $M_{\rm ej}$ trailing off to high $M_{\rm ej}$.

I interpret this as evidence for a dominance of one pathway over the other, that is, the low median $M_{\rm ej}$ (~ 2.5 M$_\odot$) and unimodality is consistent with stars with $M_{\rm ZAMS} < 25$ M$_\odot$ being stripped primarily via interaction with a binary companion.

Consequences of low $M_{\rm ZAMS}$

It has been shown that SE-SNe occur from low mass progenitors, and that high metallicity is not required to strip the star of its outer envelope (as is required in the single star scenario) so these events can occur earlier in the history of the universe. Consequently, these SNe and their progenitors can have several significant impacts:

- The $M_{\rm ZAMS}$ of type Ibc progenitors overlaps the theoretical $M_{\rm ZAMS}$ of SNe II (12 – 25 $M_{\odot}$). Thus, more massive stars typically do not explode, instead they collapse into black holes. As the binary fraction of massive stars is large, this gives a source of high mass black holes, such as those for GW150914 (Abbott et al., 2016). It also means their elemental yields are lost.

- Low mass binary progenitors resulting in SNe Ibc means the formation of NS binaries. The binary system is required to be close in order to strip the more massive star, leading to a larger gravitational potential, which in turn may prevent the system becoming unbound when one or the other star explodes. Consequently, SE-SNe are likely the progenitor sources of short GRBs and kilonovae.

- The pre-explosion star will be highly stripped and hot – either a WR star or a He star. These stars emit copious amounts of UV flux which an ionize the surrounding ISM. My results show that these stars could have been present in the low metallicity environment of the early universe, thus contributing to the epoch of re-ionization.

- For an observed fractional rate of events, the O yield per SE-SN is lower for the binary pathway than for single stars, so the overall O yield per CC-SN decreases. Removing the metallicity dependence allows type Ibc SNe to explode in the early universe but their progenitor masses are in the theoretical mass regime of SNe II meaning that these stars would explode regardless. Conversely, SE-SNe tend to be more energetic than SNe II so the dynamical impact on CC-SNe on their local environment may be underestimated.

However, I acknowledge that there are weaknesses in the relationship between $M_{\rm ZAMS}$ of the progenitor and $M_{\rm ej}$ derived here due to the uncertainties in the light curve fitting method and the uncertainty in the total $M_{\rm ej}$ of He-rich SNe. What is required is spectral modelling in order to investigate the abundance tomography (e.g., the elemental abundance as a function of mass and velocity) of the explosion then linking this back to theoretical models of pre-explosion massive stars. Also, it was previously mentioned that $M_{\rm ej}$ of GRB-SNe could be underestimated with this method and that

Table 4.4: $M_{\rm ej}$ statistics in comparison with other work

Type†	median [$M_\odot$]	mean [$M_\odot$]	N
	This work		
IIb + IIb(I)	$2.2\pm^{1.5}_{0.7}$	2.6 ± 0.9	18
Ib(II) + Ib	$2.2\pm^{1.0}_{1.2}$	2.2 ± 0.9	24
Ic-6 + Ic-7	$2.3\pm^{1.9}_{0.9}$	3.1 ± 2.4	20
Ic-3 + Ic-4	$3.0\pm^{0.8}_{0.7}$	3.1 ± 0.8	11
GRB/XRF-SNe	$3.3\pm^{3.3}_{1.1}$	3.8 ± 1.4	6
	Drout et al. (2011)		
Ib	-	$2.0\pm^{1.1}_{0.8}$	8
Ic	-	$1.7\pm^{1.4}_{0.9}$	11
Ic-BL	-	$4.7\pm^{2.3}_{1.8}$	4
"Engine-driven SNe"	-	$3.6\pm^{2.0}_{1.6}$	3
	Cano (2013)		
Ib	3.89	4.72 ± 2.77	19
Ic	3.4	4.55 ± 4.51	13
Ic-BL	3.9	5.42 ± 3.44	9
GRB/XRF-SNe	5.91	6.11 ± 3.87	20
	Taddia et al. (2015)		
Ib	-	3.6 ± 0.63	6
Ic	-	5.75 ± 2.09	3
Ic-BL	-	5.39 ± 1.30	4
	Lyman et al. (2016)		
IIb	-	2.2 ± 0.8	9
Ib	-	2.6 ± 1.1	13
Ic	-	3.0 ± 2.8	8
Ic-BL	-	2.9 ± 2.2	9

†See text for how the classification schemes relate

spectral modelling has shown these SNe to have $M_{\rm ej} \sim 10$ $M_\odot$ (Mazzali et al., 2003, 2013; Ashall et al., 2017). In this case a bimodality would appear with a second peak around 10 $M_\odot$, and in this case it may point to GRB-SNe resulting from a different population to other SE-SNe. However, as these occur in low-metallicity environments (Modjaz et al., 2008) their progenitors may still have had significant binary interaction in order to lose their H and He envelopes.

4.4 Unusual objects

Three of the SNe observed have some quality that marks them as an "object of interest". I briefly discuss these three objects here.

4.4.1 SN 2013bb

It was noted that in the distribution of $t_{+1/2}$ for H/He-rich SNe, one object was significantly outside the mean. This SN is the H/He-rich IIb(I) SN 2013bb. Figure 4.18 shows how the bolometric light curve of this supernova compares with SNe of a similar type, and is compared with the decay rate of ^{56}Co. It is evident that SN2013bb declines at a much slower rate than these SNe, and this is seen by how closely it matches the ^{56}Co line. The decay time $t_{+1/2}$ is extremely long at ~ 56 d, as traced by the r- and i-band flux. Such a long time decay time is rare in normal SE-SNe and those examples that are comparable are expected to have extremely massive cores (e.g., SN 2011bm, iPTF15dtg Valenti et al., 2012; Taddia et al., 2016)

Unfortunately, the rise of this SN was not observed, and the constraint on explosion time is limited to the discovery date, which is less than 10 days before maximum light. A rise time of ~ 23 days, as derived from the light curve model, is only marginally longer than that of existing events (e.g, SN 1993J; 21 d). $t_{+1/2}$ is almost a factor of 4 longer ($\sim$56 days to 13 days) which suggests that the rise time could be longer too, perhaps between 25-35 days, if one assumes that the rise time and $t_{+1/2}$ are loosely proportional. This would increase the ejecta mass to ~ 9 M$_\odot$with the methods used here. The estimated ejecta mass is larger than that of SN 1993J, $M_{\rm ej}\sim 1.5-3.5$ M$_\odot$ (Nomoto et al., 1993; Filippenko et al., 1993; Woosley et al., 1994) (assuming a 1.4 M$_\odot$ remnant), and that of SN 2003bg (Mazzali et al., 2009), which had ejecta mass of ≈ 4 M$_\odot$. Neither SN showed efficient trapping of gamma-rays at late times hence both showed late decay rates that deviated from that of ^{56}Co, and on this basis it may be expected that SN 2013bb is significantly more massive then either SN.

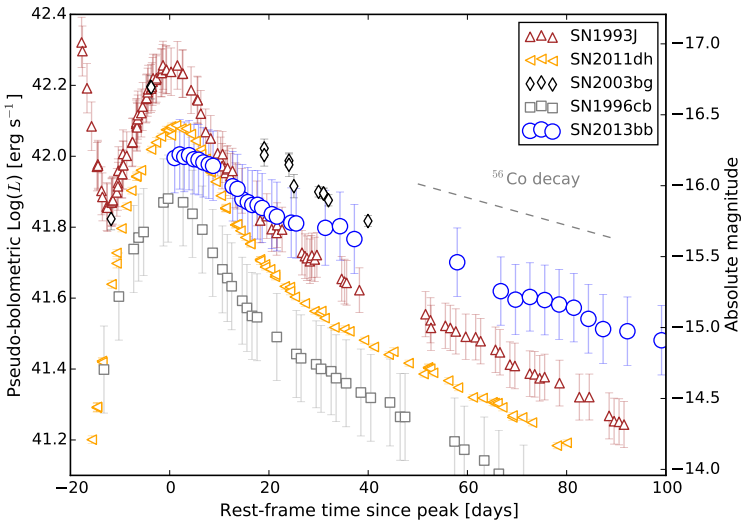

Figure 4.18: The bolometric light curve of SN 2013bb compared with other H/He-rich SNe. SN 2013bb decays at a much slower rate, one that almost matches the decay rate of ^{56}Co.

4.4.2 SN 2014ad

The spectra of SN 2014ad, Figure 4.19, show broad absorption lines and few distinctive features. At first glance this SN is similar to many Ic-3/4 SNe like SN 1998bw (Iwamoto et al., 1998) or SN 2002ap (Mazzali et al., 2002), however there are key differences. The first is that it is difficult to attribute any particular feature to any series of lines, with the possible exception of the series of Fe II lines around $4500 - 5000$ Å. The Si II line, which is prominent in Ic-3/4 SNe pre-peak is one of two features around ~ 6000 Å that appear around peak in SN 2014ad. It may be tempting to attribute the red one to Si II and the blue one to Na I D but in this case the Na I velocity is lower than half that of Si II, suggesting that this is not responsible for the blueward feature. In the redder part of the spectrum (7500 – 8000 Å) a broad absorption feature appears, this undoubtedly contains Ca II NIR as the emission profile can be observed at its rest wavelength. In Ic-3/4 this absorption feature separates into Ca II NIR and O I λ 7774 around maximum light, however Figure 4.19 shows that this separation does not occur in SN 2014ad prior to $\sim$ 38 d. Additionally, the blue side of the absorption profile represents an O I velocity of > 25000 km s^{-1} throughout.

Assumptions can be made about line velocities by assuming that Fe II $\lambda\lambda$4924, 5018, 5169, Si II λ6355, and Ca II NIR are broadly responsible for the features in the spectra.

In this case all the line velocities exceed 30000 km s^{-1} to maximum light.

Note, that the upper limit on O I is not consistent with these velocities and suggests that O I is not a part of large absorption feature at $7500 - 8000$ Å.

These velocities are exceedingly high, even compared with the majority of GRB-SNe. The closest analogue before maximum light of SN 2010bh/GRB 100316D (Cano et al., 2011; Bufano et al., 2012), which showed consistently high velocities (> 30000 km s^{-1}) in its spectra. After maximum light the ejecta velocity in SN 2014ad decreases and the SN begins to resemble SN 1998bw (Galama et al., 1998; Patat et al., 2001). There are some important key differences here that are emphasised on the $+29.4$ d (+42.2 d, SN 1998bw) spectrum (Figure 4.19, right). The pseudo-emission peaks at ~ 5200, 6200, and 7100 Å are in the same place, and the shape of the 5200 Å feature is similar. However, the two absorption features around 5500 and 6000 Å are different, with the minima of each feature being closer together in SN 2014ad compared with SN 1998bw. In SN 1998bw, these lines are attributed to absorption by Na I D (blueward) and Si II λ 6355 (redward) and have $v_{\rm NaI} > v_{\rm SiII}$, which is typical in SNe Ic. In SN 2014ad however, if the features are also produced by these ions then $v_{\rm NaI} < v_{\rm SiII}$ at 10000 km s^{-1} and 16000 km s^{-1} respectively. The Ca II NIR absorption ~ 8200 Å also suggests a higher velocity in SN 2014ad than in SN 1998bw at these times.

It is unlikely that the O I λ 7774 line is part of the broad absorption feature around 7500 – 8300 Å either, as the edge of the blue wing of this feature is at $v < 25000$ km s^{-1} from -4.9 d, low considering the other line velocities here. This broad feature is seen at higher velocities pre-peak in SN 1998bw, yet for SN 2014ad and SN 2010bh they are similar. Another, relatively shallow, absorption feature appears ~ 7000 Å at -3.9 d and this is consistent with O I $\lambda\lambda$ 7774 at ~ 35000 km s^{-1}. Stevance et al. (2017) suggest that the ejecta has a high and low velocity O I component, which may be the reason for the velocity discrepancies here.

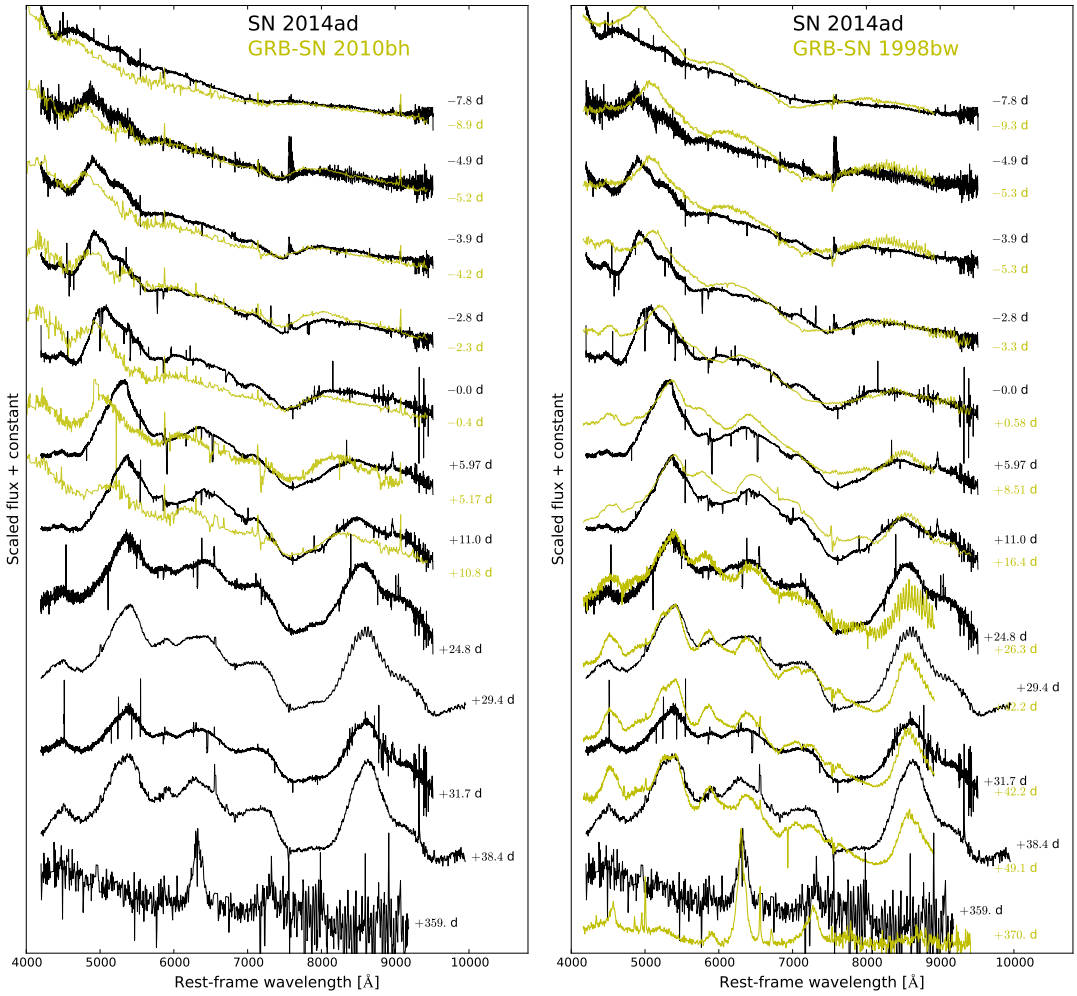

Figure 4.19: The spectra of SN 2014ad in comparison with GRB-SNe 2010bh (left) and 1998bw (right). Up to maximum light SN 2014ad is better represented by SN 2010bh, while after this the ejecta velocity of SN 2014ad decreases and it begins to look more like SN 1998bw. Identification of common line transitions in the spectra of SN 2014ad are difficult because the velocity stratification, which is normally predictable does not appear to be in evidence here; this is especially relevant to Na I D, Si II λ 6355, and O I λ 7774

4.4.3 Ic-4 SN 2016coi

SN 2016coi was determined by Yamanaka et al. (2017) to be a SNe Ic with helium. Prentice et al. (2018) presented a larger data set and analysis of this object with empirical analysis on the spectra and spectral modelling.

Figure 4.20 shows the early time spectra of SN 2016coi in comparison with He-rich SN 2008D (Modjaz et al., 2009) and Ic-4 SN 2002ap (Gal-Yam et al., 2002). The positions of the apparent He lines are indicated. It is clear that, as time progresses, any He present in the ejecta of SN 2016coi does not behave in the same way as that in He-rich SNe, and in particular the lines attributed to He weaken over time, while the opposite happens in SN 2008D.

The He I lines all form in the same line forming region, hence a comparison of the spectra in the velocity space, centred on the rest wavelength of the prominent lines; those ar 5876 Å, 6678 Å, and 7065 Å provide a useful test of this. Figure 4.21 demonstrates this by comparing the early spectra of SN 2016coi, for reference the genuine He-rich SN 2016jdw is included to show the effectiveness of this technique. From Figure 4.21 it is difficult to prove that the absorption features are aligned and of a similar shape. This may be due to the highly blended nature of the lines, which would serve to mask the position of the absorption minima. However, another option is the that lines themselves are not due to helium and the position of the features with respect to He I at some Doppler shifted velocity is purely coincidence.

It took spectral modelling to provide some answers to this question, in Prentice et al. (2018) it was shown that the strong line around 5500 Å could be reproduced by either Na or He, but that the abundance of Na significantly exceeded that which would expected in any massive star in a region approximately one third solar metallicity (Asplund et al., 2009). The models utilise a He mass fraction of ~ 3 percent and steadily decrease this as a function of velocity while the contribution of Na remains constant. This leads to a steady mapping of the transition from He I to Na I D in the ~ 6200 Å feature. The results led to the conclusion that residual He was present in the C/O layer. The abundance tomography of SN 2016coi from Prentice et al. (2018) is shown

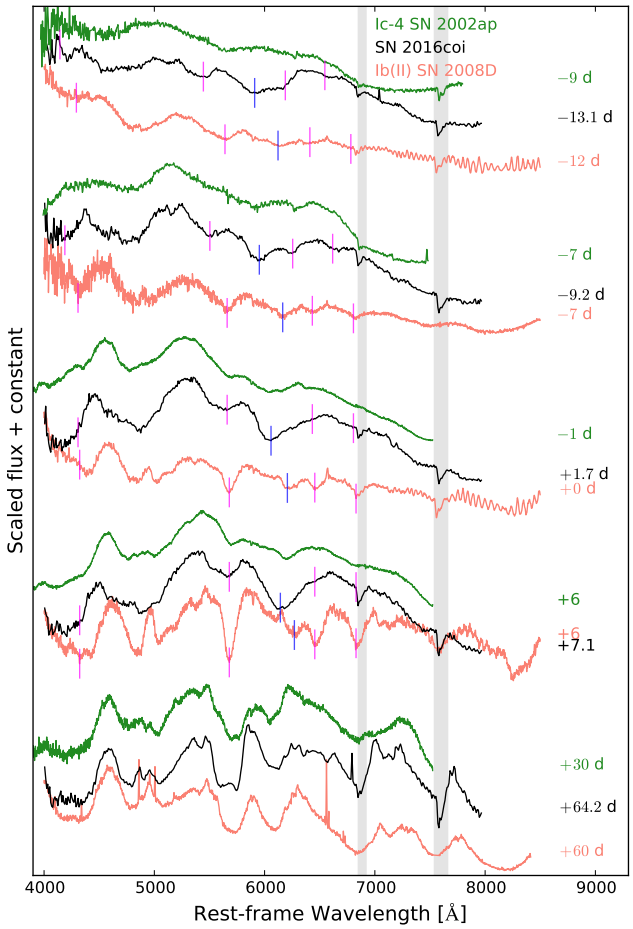

Figure 4.20: From Prentice et al. (2018), the spectra of SN 2016coi (red) in comparison with Ic-4 SN 2002ap (grey) and He-rich SN 2008D at various epochs. Magenta/blue lines show the position of Doppler shifted He I and Si II lines The evolution of SN 2016coi is slower than that of SN 2002ap, which is to be expected as the time-scales are longer for SN 2016coi. It is noticeable that SN 2016coi has more features visible in the early spectra, especially with respect to the Na I D line at $\sim$ 5500 Å. It can also be seen that the SN 2016coi line velocities are lower than those of SN 2002ap at very early times but are higher by peak. SN 2008D initially has broad lines that give way to a spectrum with strong narrow lines and dominated by He at peak.

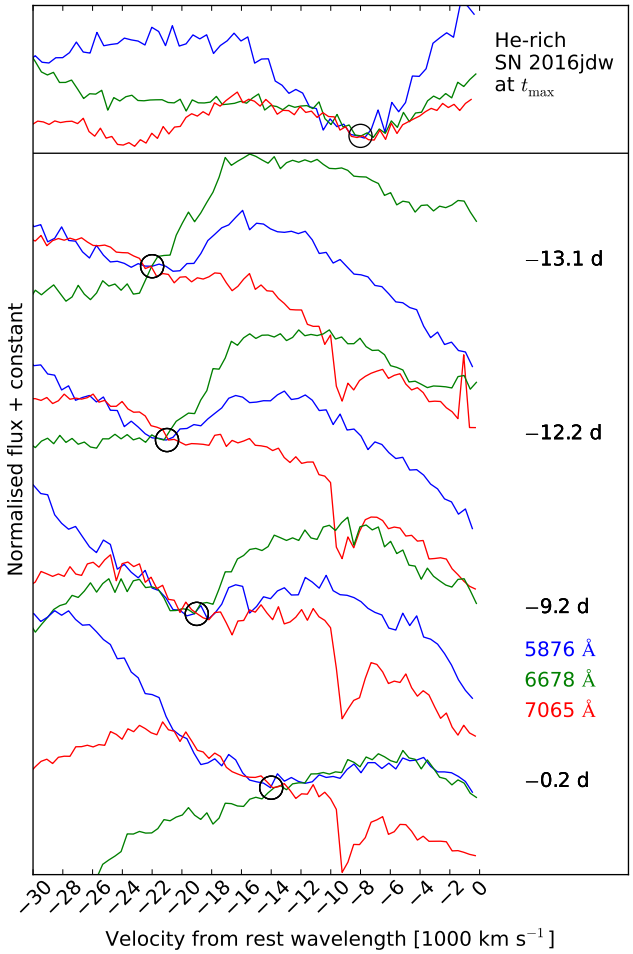

Figure 4.21: From Prentice et al. (2018). In order to test line profiles for a common origin we plot the pre-peak spectra of SN 2016coi, in velocity space relative to the rest wavelength of the He λ 5876 (blue), λ 6678 (green), and λ 7065 (red) lines. The flux at a common velocity, as determined by the velocity measured from the 5876 Å, relative to the rest wavelength is used to normalise each spectral region. For comparison the maximum light spectrum of the He-rich SN 2016jdw is included, which demonstrates how He forms within a common line-forming region. In SN 2016coi, the 5876 Å line profile occasionally matches the shape of one of the other two in either the red or the blue, but at no point do the absorption features well match each other.

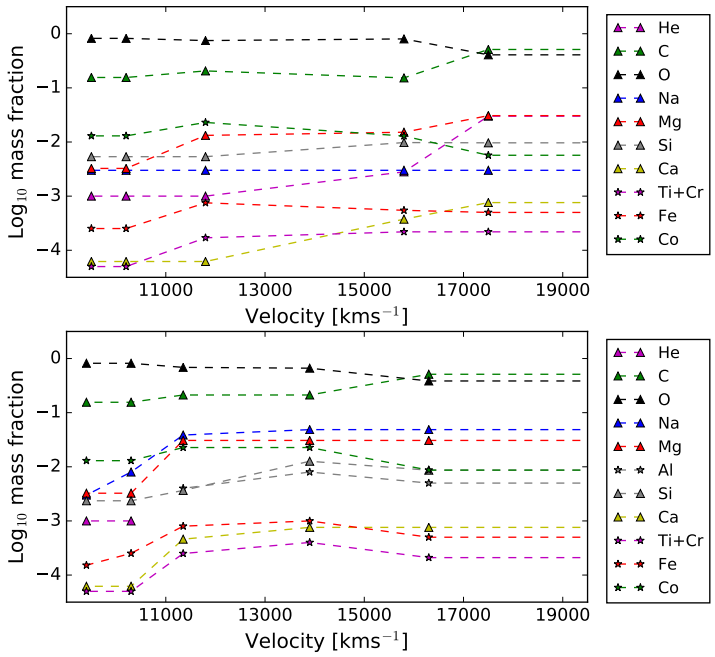

Figure 4.22: From Prentice et al. (2018), the abundance of SN 2016coi as a function of mass and velocity (Prentice et al., 2018). The upper panel uses He to explain the feature at $\sim$ 5300 Å and shows that the He mass fraction remains low. At very early times it has an effect on spectral line formation before being dominated by Na a week before maximum light. The lower panel shows an abundance plot for purely Na, this distribution leads to an excessively large Na abundance for a star of $M_{\rm ZAMS}\sim$ 23 $M_{\odot}$ at one third solar metallicity.

in Figure 4.22.

From this I concluded that SN 2016coi is the best example of a SN stripped of its He layer but with the C/O shell intact.

4.5 Summary

In this chapter I have presented the observations and analysis of 19 SE-SNe. In Chapter 3 it was noted that there were less than 20 SE-SNe with good spectroscopic and photometric data coverage (pre-peak photometry, good quality spectra from pre-peak to nebular phase). This work increases that number by 14 and thus significantly contributes to the body of data on SE-SNe.

Comparison of the SNe with the bulk properties described in Chapter 2, and expanded with new SNe and under the taxonomic scheme described in Chapter 3 reveals that,

while many of the SNe are "normal", several of the objects have some property that significantly deviates from the mean of the respective distribution.

I have identified three supernovae as significantly unusual objects; SN 2013bb, SN 2014ad, and SN 2016coi. This is in addition to the two GRB-SNe; SNe 2016jca and 2017iuk. SN 2013bb is a very massive type IIb(I) SN with an extremely long $t_{+1/2}$ of ~ 53 days. It may be the best example of a H-rich SE-SN that arises from a single star rather than a binary. SN 2014ad is a highly energetic Ic-3 event, with broad blended lines that persist at least three weeks past bolometric maximum. This event has been shown to be highly aspherical in the literature, however no GRB was detected around its discovery. SN Ic-4 2016coi is the best example of a type Ibc SN stripped down to its C/O core. Spectral modelling has revealed traces of He in the outer ejecta at a level of a few percent. This SN is unique in its early spectroscopic evolution with broad lines, but a very strong feature around 5500 Å.

The most important result of this chapter is analysis of the ejecta mass distributions for 81 SNe Ibc. The lack of clear bimodality in the distributions and the low median $M_{\rm ej}$ suggests that these events primarily arise from progenitors of low $M_{\rm ZAMS}$ ($\sim< 25$ $\rm M_{\odot}$) which are stripped via binary interaction. This low mass pathway removes the metallicity dependence on SE-SNe events, allowing them to occur in the early universe. Stripped stars are a significant source of ionizing UV photons, thus the progenitors of SE-SNe may have contributed significantly to the epoch of re-ionization. There are further implications as it sets out SNe Ibc as progenitors of short GRBs and kilonovae while greatly reducing the explodability of more massive stars. If these stars to not explode they likely collapse to a black hole and are the source of high stellar mass binaries in the universe.

This work shows the importance in ongoing observations of SE-SNe in order to probe the parameter space in which they reside and to provide good quality data sets for spectral modelling, the results of which can then be linked back to theoretical stellar evolution models and help determine the nature of the progenitor stars.

Chapter 5

Conclusions and future work

In Chapter 2 I presented analysis on the bolometric light curves of 85 SE-SNe. The resulting distributions of the fully bolometric peak luminosity showed that SNe IIb were least luminous with a mean $\log_{10}(L_{\rm p}) = 42.36$ erg s^{-1} followed by 42.50 erg s^{-1} and 42.51 erg s^{-1} for SNe Ib and Ic, then 43.00 erg s^{-1} for Ic-BL category. GRB-SNe are significantly more luminous than other SN types, this is turn drives the Ic-BL subgroup to and overall higher luminosity. SNe Ic rise to maximum light quicker than He-rich SNe and their light curves are not as broad overall. Despite this, $M_{\rm Ni}$ is found to be greater for SNe Ic-BL at 0.34 M$_{\odot}$ compared with 0.16, 0.14, and 0.11 M$_{\odot}$ for SN Ic, Ib, and IIb respectively. It was found that the $g-r$ colour curves show significant scatter for all SN types.

In Chapter 3 I analysed the spectra of SE-SNe, separating the SNe according to strength of H, strength of He, and line broadness. I found that those SNe classified as type Ic naturally separated from the He-rich SNe, thus there were no SNe Ic with obvious He lines. The He-rich SNe were then ordered according to strength of the H lines, with emphasis on Hα. It was found that a continuum of line strengths could be deduced from a 2D plane that maps the equivalent width of the absorption against the ratio of emission intensity to absorption intensity. The transition region between the two occurs when the lines of the Balmer series at wavelengths shorter than Hα become too weak to observe. I then used the position on the $\langle EW \rangle$/$\langle f_{\rm em}/f_{\rm abs} \rangle$ plane to categorise

the He-rich SNe into the following groups according to H strength; IIb, IIb(I), Ib(II), Ib. The presence of H in SNe Ib(II) and Ib(I) is not proven, but the continuum of properties between IIb(I) and Ib(II) suggests that H contributes significantly to the feature at ~ 6200 Å in the latter group.

SNe Ic were categorised according to the mean number of features visible up to $t_{\rm max}$, as give by a set of lines that are common to SNe Ic. This quantified line broadness which was then related to the specific kinetic energy $E_{\rm k}/M_{\rm ej}$ for each He-poor SN group. The results show that as $\langle N \rangle$ decreases so $E_{\rm k}/M_{\rm ej}$ increases, with $E_{\rm k}/M_{\rm ej}= 1$ for Ic-6/7 SNe, $E_{\rm k}/M_{\rm ej}= 2$ for Ic-4, and $E_{\rm k}/M_{\rm ej}= 4$ for Ic-3 SNe. This is likely the result of the explosion mechanism, with $E_{\rm k}$ in Ic-3/4 SNe being enhanced by the rotational energy of a rapidly rotating neutron star or black hole.

Finally, in Chapter 4 I presented analysis on the data of 19 SNe, of which 15 were observed via my own observing proposals. Half of these SNe were observed early enough, and into the nebular phase, with a sufficient density of observations that they significantly increase the total number of well observed SE-SNe by nearly 100 percent. The SNe were analysed within the context of the bulk properties of SE-SNe. Nearly half the SNe in this sample displayed some property that was more than one standard deviation from the median of their respective distributions. I also included further analysis on ejecta mass and demonstrated that there is significant overlap between the $M_{\rm ej}$ distributions of all SN types. The SNe Ic-5/6/7 distribution has the greatest range, from 1 – 11 $\rm M_{\odot}$. The distribution appears unimodal, which suggests that SE-SNe preferentially arise from one progenitor channel. With a median $M_{\rm ej} \sim 2.5$ $\rm M_{\odot}$, which equates to a ~ 4 $\rm M_{\odot}$, the bulk of the SNe must arise from stars with $M_{\rm ZAMS} < 25$ $\rm M_{\odot}$. GRB-SNe and Ic-3/4 are found to be more massive on average. The results show that the parameter space of SE-SNe is still under-sampled, justifying further observations in an era when transient astronomy is going to be more competitive.

Thus I present several key results:

- SE-SNe are heterogeneous in their light curve properties, this makes any attempt at standardisation as per SNe Ia impossible. Despite this, there is still consider-

able overlap in the properties of SNe Ic and the He-rich SNe.

- SNe Ib and IIb can be characterised by the strength of their Hα features. This is related to envelope stripping and shows that these two groups are a continuum rather than discrete. The transition occurs when the H Balmer lines beyond Hα are too weak to have any effect on the spectra.

- Line broadness in He-poor SNe can be quantified by simply counting the number of features present before $t_{\rm max}$. This method links back to the specific kinetic energy, which is related to the explosion mechanism. With a larger sample size these subgroups and their local environments can be investigated.

- The parameter space in which SE-SNe reside is still under-sampled. A significant minority of events discovered each year are sufficiently unusual to justify intense observations an analysis.

- SN 2016coi is the best candidate for a star stripped almost entirely of its He shell at the time of explosion. Residual He, at the percent level, was found through spectroscopic modelling as part of work that I led.

- The mass distribution of SE-SNe favours low mass < 25 M$_{\odot}$ progenitors, stripped by close binary interaction, for virtually all SNe Ibc. This suggests that few massive stars explode, rather they collapse directly to black holes. Thus, SE-SNe are good candidates for NS/NS binary systems and the progenitors of SGRBs/kilonovae, while massive stars collapse to massive black holes and are sources for BH/BH binary systems.

5.0.1 Future work

I have shown that SE-SNe are diverse in their overall properties, which suggests a diverse range of progenitor stars and explosion pathways. However, there is still much debate over what kinds of stars give rise to SE-SNe. On this basis I suggest that ongoing observations are important. Firstly, this is to ensure that the parameter space in

which these SNe reside is fully sampled. Secondly, it must be ensured that the SNe are well sampled, with good multi-band photometry (near UV to NIR) and time series of spectra from shortly after explosion to the nebular phase.

I identify two key analytical tools in order to related SNe to their progenitors. The first abundance tomography, which, though modelling of the early photospheric phase spectra and identifying the composition of the ejecta, one can map the abundance distribution to models of stellar cores shortly before explosion and reveal the $M_{\rm ZAMS}$ of the progenitor star.

The second is via nebular phase spectral modelling should be used to construct mass distributions of the inner cores of the exploded stars, these again can be mapped to stellar evolution models of massive stars. Importantly, discrepancy between the photospheric and nebular results may well be indicative of asymmetries in the ejecta. As early asymmetries in SN ejecta will manifest themselves in the results obtained through analysis of photospheric phase data compared with the nebular phase, when the ejecta is optically thin.

The link with progenitor mass, metallicity, and SE-SN location in H II regions can then be re-examined with the intention of providing a solution to the question of how "bursty" star-burst regions actually are.

Finally, analysis of early data is also ideal in deriving $E_{\rm k}$ for the SN, which in addition with $M_{\rm ej}$ gives the specific kinetic energy and potential explosion pathways for the SNe when compared with the neutrino mechanism or magnetar/BH powering in explosion modelling.

Appendix A

Host-galaxy extinction

This section formed the appendix in Prentice et al. (2016) and explains the method for calculating the mean $E\left(B-V\right)_{\rm host}$ for different supernova types.

I searched the literature for core-collapse SNe with defined host-galaxy extinction in order to determine the distribution for the sample as a whole or individually. In addition to the SNe used in Table 2.1, I have also included SNe from Cano (2013), Pritchard et al. (2014), Cano et al. (2014), Richardson (2009), Richardson et al. (2006), and other individual SNe from the literature which failed the criteria described in Section 2.1. I also include all SNe II on the basis that, while the evolution of these objects may be different from that of SE-SNe, their position in the host is likely to be similar given their lifetimes (i.e., in star-forming regions). The total number used was 110.

K-S tests

I performed K-S tests on the sample on a type-by-type basis. If the K-S test revealed that the distribution was drawn from the same population by having $P > 0.05$, then the populations were combined. SNe IIP and SNe IIL were combined into a single population owing to their small numbers. The interplay between the populations means that combining similar datasets is a risky task. For example, the SN IIb versus SN Ib

K-S test returns $P = 0.055$, which is on the edge of the 5σ limit, yet SN IIb against SN Ic returns $P = 0.38$, and SN Ic against SN Ib returns $P = 0.487$; thus, populations were combined together only if the chance of the two being drawn from the same distribution was greater than 40% for all permutations of the individuals within the group. This limit is high but necessary to reduce the risk in combining datasets into a larger group that may have a low P value between some of its constituents.

The clear outlier is the distribution given by GRB-SNe, where K-S tests give $P < 0.05$ for every population. This does not imply that GRB-SN hosts are different from those of other SNe; the distribution of extinction values can be explained as a combination of distance and the luminosity function of SNe. I find that GRB-SNe, while more luminous on average than other SN types, are still limited to $L_{\rm peak} \approx 10^{43}$ erg s^{-1} in bolometric luminosity and are typically observed at redshifts much greater than other SNe. As a result, the sample is biased in two ways. First, these SNe are observed at larger distances because they are associated with GRBs; without this added high-energy component few, if any, of these SNe would be seen. Second, the limiting luminosity and distance mean that only the least-attenuated SN light will be observed, so if a GRB exploded in a dusty environment and had a corresponding SN, it would not be seen as it would be below current detection limits. Furthermore, if I consider the entire sample, the non-Gaussian nature of all the distributions may be expected but their observed shape is determined by similar constraints. The probability that a SN is detected is reduced for higher local extinctions and lower intrinsic luminosities because these lower its apparent brightness. Hence, the distribution is more likely to show SNe with low host extinction, which in turn biases the result in favour of SNe in "clean" environments.

Thus, there are find four populations:

- SNe IIP, IIL, II, IIb
- SNe Ib
- SNe Ic, Ic-BL

- GRB-SNe.

The median, upper and lower 34%, mean, and standard deviation for each population are given in Table 2.3. The discrepancy in median and mean is caused by the non-Gaussian distribution, so I use the median extinction as a typical extinction for SNe of that type and the upper and lower 34% as the 1σ boundaries. This median extinction and associated uncertainty is then applied to any SN without determined host extinction. For an individual SN such a correction could be deemed to be misleading; however, for a large dataset with several SNe utilising this method, I rely on "regression to the mean" — that is, for each SN where the extinction is underestimated, there will be a corresponding SN with extinction overestimated, and the uncertainties in this range provide a balance in terms of numbers centred on the average (the median in this case). The cumulative distributions are shown in Figure A.1.

To test the accuracy of using this method, I take the SNe from the database with known host-galaxy extinction (SNe Ic/Ic-BL/GRB-SNe = 15, SNe Ib/IIb = 22) and apply the median extinction correction when constructing the bolometric light curve. This is then compared with the case when no host extinction correction is applied and when the actual extinction is applied. The results are shown in Figure A.3 for the application of median host extinction, Figure A.2 for the actual values, and Figure A.4 for no correction. It is apparent that the character of the luminosity function changes when median $E(B-V)_{\rm host}$ is used in place of the literature value; this is to be expected around the extremes of the distribution because no SN is being corrected for a large host extinction but all are being corrected. The statistics returned in Table A.1 show that the mean and median of the luminosity functions remain similar, giving confidence in the conversion method to return bulk statistics. However, in the absence of $E(B-V)_{\rm host}$ the statistics returned are generally lower than the corrected values; again, this would be expected as they represent a lower limit. It is interesting to note that the SN Ic median values are very similar for no extinction and the known $E(B-V)_{\rm host}$, although this is not reflected in the mean value.

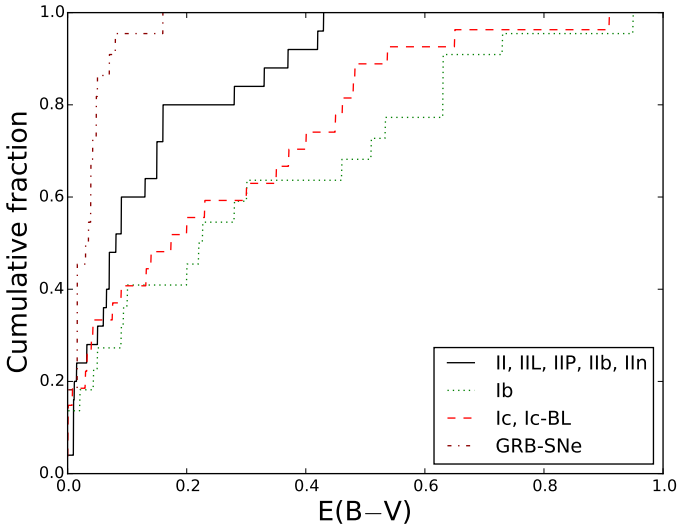

Figure A.1: Cumulative distribution of reddening values for SNe sorted by population.

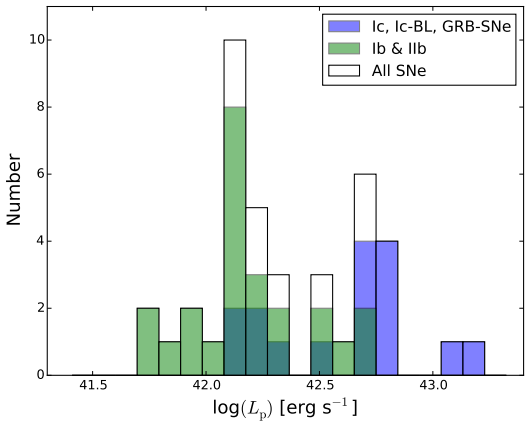

Figure A.2: *BVRI* luminosity function for SNe with their host extinction correction applied using the values given in the literature. Colours are as described in Figure 2.9.

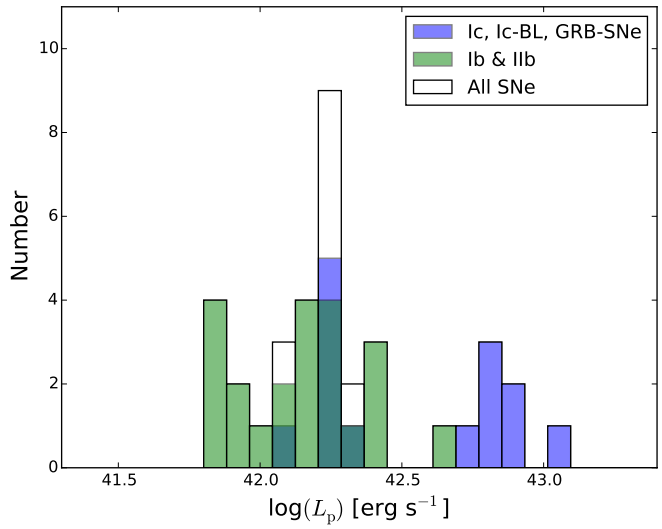

Figure A.3: *BVRI* luminosity function of the same SNe as in Figure A.2 but with a type-dependent host extinction correction applied. Colours are as described in Figure 2.9.

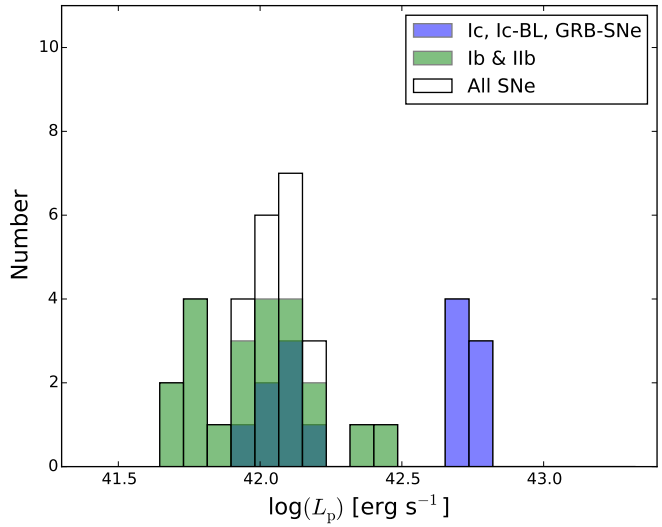

Figure A.4: *BVRI* luminosity function of the same SNe as in Figure A.2 but with no host extinction correction applied. Colours are as described in Figure 2.9.

Table A.1: Host extinction tests on peak-luminosity statistics.

Literature extinction values			
SN Type	median	mean	σ
All Ic	42.69	42.59	0.32
Ib/IIb	42.15	42.17	0.24
bulk	42.23	42.34	0.34
Median extinction values			
SN Type	median	mean	σ
All Ic	42.72	42.61	0.38
Ib/IIb	42.17	42.15	0.23
bulk	42.24	42.34	0.38
No extinction correction			
SN Type	median	mean	σ
All Ic	42.67	42.47	0.4
Ib/IIb	42.01	41.99	0.2
bulk	42.11	42.12	0.38

Appendix B

Chapter 2 tables

Table B.1: Chapter 2 *BVRI* pseudo-bolometric light curve statistics

SN	Type	$\log(L_{\rm P})$	$M_{\rm Ni}$ ($M_\odot$)	$t_{\rm P}$ (days)	$t_{-1/2}$ (days)	$t_{+1/2}$ (days)	Width (days)
1993J	IIb	$42.231\pm^{0.068}_{0.066}$	$0.087\pm^{0.015}_{0.012}$	19.148 ± 0.033	10.313 ± 0.017	12.808 ± 0.116	23.121 ± 0.118
1994I	Ic	$42.271\pm^{0.346}_{0.328}$	$0.064\pm^{0.080}_{0.034}$	12.252 ± 0.211	5.541 ± 0.137	8.522 ± 0.509	14.063 ± 0.527
1996cb	IIb	$41.871\pm^{0.123}_{0.123}$	$0.034\pm^{0.015}_{0.011}$	16.993 ± 1.650	10.737 ± 0.000	15.444 ± 0.017	26.181 ± 0.017
1998bw	GRB-SN	$42.780\pm^{0.031}_{0.023}$	$0.260\pm^{0.022}_{0.016}$	15.861 ± 0.177	9.734 ± 0.372	15.858 ± 0.779	25.593 ± 0.863
1999dn	Ib	$42.134\pm^{0.084}_{0.061}$	$0.052\pm^{0.023}_{0.015}$	13.916 ± 2.841	-	21.827 ± 3.638	-
1999ex	Ib	$42.335\pm^{0.082}_{0.082}$	$0.106\pm^{0.022}_{0.019}$	18.349 ± 0.036	9.226 ± 0.053	15.958 ± 0.606	25.183 ± 0.608
2002ap	Ic-BL	$42.217\pm^{0.010}_{0.006}$	$0.060\pm^{0.001}_{0.001}$	13.011 ± 0.000	6.466 ± 0.060	15.506 ± 0.165	21.972 ± 0.175
2003bg	IIb	$42.226\pm^{0.027}_{0.014}$	$0.076\pm^{0.012}_{0.009}$	16.624 ± 1.656	10.504 ± 0.146	28.374 ± 1.318	38.878 ± 1.326
2003jd	Ic-BL	$42.795\pm^{0.090}_{0.089}$	$0.219\pm^{0.054}_{0.042}$	12.504 ± 0.179	9.372 ± 0.505	14.067 ± 0.317	23.439 ± 0.596
2004aw	Ic	$42.448\pm^{0.030}_{0.044}$	-	-	-	21.273 ± 1.340	-
2004fe*	Ic	$42.152\pm^{0.031}_{0.030}$	$0.057\pm^{0.010}_{0.009}$	14.680 ± 1.653	9.276 ± 0.101	-	-
2004gq	Ib	$42.087\pm^{0.010}_{0.006}$	-	-	-	18.582 ± 0.465	-
2005az*	Ic	$41.981\pm^{0.013}_{0.015}$	-	-	-	27.282 ± 0.146	-
2005bf	Ib	$42.170\pm^{0.025}_{0.023}$	$0.073\pm^{0.006}_{0.005}$	18.325 ± 0.351	-	-	-
2005hg*	Ib	$42.233\pm^{0.010}_{0.013}$	-	-	-	17.943 ± 0.237	-
2005hl*	Ib	$41.993\pm^{0.008}_{0.005}$	-	-	-	21.656 ± 0.667	-
2005hm*	Ib	$41.958\pm^{-0.013}_{0.041}$	$0.048\pm^{0.002}_{0.008}$	19.927 ± 1.669	12.591 ± 0.250	14.682 ± 1.455	27.274 ± 1.476
2005kl*	Ic	$41.485\pm^{0.008}_{0.008}$	-	-	-	20.115 ± 0.027	-
2005kr*	Ic-BL	$42.759\pm^{0.072}_{0.038}$	$0.187\pm^{0.059}_{0.035}$	11.405 ± 1.669	7.207 ± 0.252	-	-
2005ks*	Ic-BL	$42.291\pm^{0.066}_{0.078}$	$0.068\pm^{0.020}_{0.017}$	12.368 ± 1.656	7.815 ± 0.142	-	-
2005kz*	Ic	$42.004\pm^{0.034}_{0.031}$	-	-	-	-	-
2005mf*	Ic	$42.121\pm^{0.033}_{0.024}$	-	-	-	17.281 ± 0.493	-
2006T*	IIb	$42.145\pm^{0.011}_{0.011}$	$0.054\pm^{0.007}_{0.007}$	14.148 ± 1.651	8.940 ± 0.051	14.433 ± 0.031	23.372 ± 0.059
2006aj	GRB-SN	$42.685\pm^{0.020}_{0.019}$	$0.138\pm^{0.007}_{0.006}$	9.587 ± 0.040	6.779 ± 0.155	-	-
2006el*	IIb	$42.041\pm^{0.024}_{0.016}$	-	-	-	15.594 ± 0.660	-
2006ep*	Ib	$41.942\pm^{0.012}_{0.013}$	$0.042\pm^{0.005}_{0.005}$	18.002 ± 1.653	11.375 ± 0.101	15.034 ± 0.013	26.409 ± 0.102
2006fe*	Ic	$42.263\pm^{0.025}_{0.026}$	$0.079\pm^{0.013}_{0.012}$	15.830 ± 1.711	10.002 ± 0.455	19.197 ± 1.431	29.199 ± 1.502
2006fo*	Ib	$42.164\pm^{0.019}_{0.019}$	-	-	-	19.017 ± 0.124	-
14475*	Ic-BL	$42.558\pm^{0.047}_{0.048}$	$0.110\pm^{0.029}_{0.024}$	10.501 ± 1.760	6.635 ± 0.613	18.037 ± 1.403	24.672 ± 1.531
2006jo*	Ib	$42.371\pm^{0.020}_{0.020}$	$0.071\pm^{0.013}_{0.011}$	10.366 ± 1.651	6.550 ± 0.067	10.081 ± 0.472	16.630 ± 0.476
2006lc*	Ib	$41.954\pm^{0.005}_{0.008}$	$0.034\pm^{0.004}_{0.004}$	13.837 ± 1.651	8.743 ± 0.050	14.036 ± 0.050	22.779 ± 0.071
2006nx*	Ic-BL	$42.847\pm^{0.051}_{0.021}$	$0.276\pm^{0.067}_{0.040}$	14.279 ± 1.698	9.022 ± 0.401	-	-
2007C	Ib	$42.588\pm^{0.085}_{0.084}$	-	-	-	12.373 ± 0.186	-
2007D*	Ic-BL	$42.121\pm^{0.085}_{0.082}$	-	-	-	-	-
2007Y	Ib	$41.750\pm^{0.064}_{0.072}$	$0.028\pm^{0.005}_{0.005}$	18.757 ± 0.350	9.284 ± 0.569	15.327 ± 0.285	24.610 ± 0.636
2007ag*	Ib	$41.884\pm^{0.015}_{0.014}$	-	-	-	20.052 ± 0.673	-
2007cl*	Ic	$42.077\pm^{0.010}_{0.010}$	-	-	-	15.616 ± 0.259	-

2007gr	Ic	$42.087\pm^{0.042}_{0.043}$	$0.045\pm^{0.005}_{0.005}$	13.146±0.229	8.530±0.025	15.270±0.081	23.800±0.085
2007kj*	Ib	$42.017\pm^{0.009}_{0.008}$	-	-	-	-	-
2007ms*	Ic	$42.319\pm^{0.008}_{0.017}$	$0.122\pm^{0.011}_{0.013}$	22.231±1.666	14.047±0.231	24.625±0.434	38.672±0.491
2007nc*	Ib	$42.065\pm^{0.064}_{0.016}$	$0.055\pm^{0.015}_{0.007}$	17.734±1.800	11.205±0.718	19.059±4.382	30.264±4.440
2007qv*	Ic	$42.514\pm^{0.023}_{0.022}$	-	-	-	-	-
2007qx*	Ic	$42.118\pm^{0.197}_{0.041}$	$0.054\pm^{0.045}_{0.013}$	15.094±2.758	9.537±2.211	-	-
2007ru	Ic-BL	$42.810\pm^{0.038}_{0.009}$	$0.194\pm^{0.018}_{0.005}$	10.242±0.047	-	14.640±0.485	-
2007sj*	Ic	$41.961\pm^{0.022}_{0.021}$	$0.036\pm^{0.006}_{0.005}$	14.542±1.658	9.188±0.164	-	-
2007uy	Ib	$42.675\pm^{0.270}_{0.260}$	$0.241\pm^{0.214}_{0.110}$	19.075±0.284	-	15.360±1.160	-
2008D	Ib	$42.125\pm^{0.252}_{0.240}$	$0.069\pm^{0.055}_{0.030}$	19.293±0.229	13.239±0.194	17.042±0.722	30.281±0.747
2008ax	IIb	$42.099\pm^{0.025}_{0.024}$	$0.065\pm^{0.004}_{0.004}$	19.283±0.127	10.144±0.085	15.279±0.318	25.423±0.329
2008bo	IIb	$41.757\pm^{0.011}_{0.011}$	-	-	-	9.240±0.010	-
2008hw	GRB-SN	$43.156\pm^{0.050}_{0.050}$	$0.496\pm^{0.064}_{0.057}$	12.307±0.100	-	-	-
2009bb	Ic	$42.685\pm^{0.123}_{0.121}$	$0.171\pm^{0.057}_{0.042}$	12.631±0.095	6.637±0.059	13.060±0.357	19.697±0.362
2009er*	Ib	$42.724\pm^{0.013}_{0.012}$	-	-	-	14.225±0.049	-
2009iz*	Ib	$42.085\pm^{0.010}_{0.010}$	$0.070\pm^{0.006}_{0.006}$	21.828±1.650	13.793±0.000	23.220±0.169	37.013±0.169
2009jf	Ib	$42.478\pm^{0.022}_{0.027}$	$0.169\pm^{0.010}_{0.011}$	21.267±0.164	11.212±0.444	19.901±0.631	31.113±0.771
2010as	IIb	$42.524\pm^{0.088}_{0.087}$	$0.117\pm^{0.027}_{0.022}$	12.442±0.122	9.661±0.024	16.541±0.415	26.202±0.415
2010bh	GRB-SN	$42.365\pm^{0.053}_{0.053}$	$0.082\pm^{0.011}_{0.010}$	12.737±0.099	3.287±0.303	9.286±0.884	12.573±0.934
2010ma	GRB-SN	$43.060\pm^{0.234}_{0.071}$	$0.346\pm^{0.444}_{0.136}$	10.331±4.338	-	12.450±0.482	-
2011bm	Ic	$42.705\pm^{0.031}_{0.037}$	$0.427\pm^{0.033}_{0.036}$	34.586±0.151	-	43.446±1.544	-
2011dh	IIb	$42.084\pm^{0.008}_{0.012}$	$0.052\pm^{0.001}_{0.001}$	15.712±0.017	9.638±0.034	14.525±0.119	24.163±0.124
2011ei	IIb	$41.969\pm^{0.089}_{0.088}$	$0.044\pm^{0.010}_{0.008}$	17.732±0.033	10.247±0.033	16.893±0.360	27.140±0.362
2011fu	IIb	$42.338\pm^{0.008}_{0.012}$	-	-	-	18.016±0.283	-
2011hs	IIb	$41.903\pm^{0.011}_{0.012}$	$0.021\pm^{0.001}_{0.001}$	8.588±0.057	7.718±0.023	11.199±0.263	18.917±0.264
2011kl[a]	GRB-SN	$43.324\pm^{0.166}_{0.157}$	-	15.169±0.071	6.889±0.142	12.712±0.355	19.601±0.382
2012ap	Ic-BL	$42.472\pm^{0.162}_{0.158}$	$0.109\pm^{0.052}_{0.035}$	13.192±0.308	8.648±1.337	15.546±0.174	24.193±1.348
2012bz	GRB-SN	$42.795\pm^{0.029}_{0.032}$	$0.240\pm^{0.026}_{0.013}$	13.491±0.224	9.838±0.066	17.110±0.177	26.947±0.189
2013cq	GRB-SN	$42.960\pm^{0.050}_{0.100}$	-	-	-	-	-
2013cu	IIb	$42.661\pm^{0.007}_{0.006}$	$0.125\pm^{0.003}_{0.002}$	9.009±0.082	6.890±0.031	12.516±0.163	19.406±0.166
2013df	IIb	$42.198\pm^{0.034}_{0.037}$	$0.091\pm^{0.008}_{0.008}$	21.793±0.103	13.897±0.101	11.727±0.310	25.624±0.326
2013dx	GRB-SN	$42.831\pm^{0.027}_{0.032}$	-	-	11.697±1.768	14.389±0.841	26.086±1.958
2013ge	Ibc	$42.132\pm^{0.019}_{0.024}$	$0.068\pm^{0.009}_{0.009}$	18.878±1.697	11.928±0.395	19.953±0.285	31.881±0.487
PTF09dh/2009dr*	Ic-BL	$42.892\pm^{0.035}_{0.03}$	-	-	-	18.546±0.247	-
PTF10gvb*	Ic-BL	$42.775\pm^{0.067}_{0.067}$	-	-	18.179±19.629	14.344±0.483	32.522±19.635
PTF10inj*	Ib	$42.438\pm^{0.157}_{0.143}$	-	-	-	36.035±0.490	-
PTF10qif*	Ib	$42.455\pm^{0.123}_{0.118}$	-	-	-	13.452±1.764	-
PTF10vgv*	Ic	$42.493\pm^{0.065}_{0.063}$	$0.094\pm^{0.029}_{0.022}$	10.347±1.687	6.538±0.354	9.969±0.000	16.507±0.354
PTF11bli*	Ibc	$42.071\pm^{0.018}_{0.018}$	$0.065\pm^{0.008}_{0.007}$	20.627±1.658	13.033±0.164	-	-
PTF11jgj*	Ic	$42.088\pm^{0.022}_{0.018}$	$0.072\pm^{0.010}_{0.009}$	22.072±2.170	13.947±1.409	-	-
PTF11klg*	Ic	$42.105\pm^{0.144}_{0.125}$	$0.057\pm^{0.030}_{0.018}$	16.393±1.678	10.358±0.303	14.530±0.039	24.887±0.306
PTF11qiq*	Ib	$42.161\pm^{0.500}_{0.010}$	-	-	-	17.000±1.000	-
PTF11rka*	Ic	$42.723\pm^{0.050}_{0.045}$	-	-	-	45.781±3.909	-
PTF12gzk	Ic	$42.708\pm^{0.031}_{0.029}$	$0.226\pm^{0.023}_{0.020}$	16.345±0.455	-	23.643±0.065	-
PTF12os*	IIb	$41.409\pm^{0.007}_{0.010}$	-	-	-	17.095±0.492	-
iPTF13bvn	Ib	$41.997\pm^{0.012}_{0.011}$	$0.043\pm^{0.001}_{0.001}$	15.953±0.098	8.990±0.024	13.582±0.098	22.572±0.101
iPTF14dby*	Ic-BL	$42.373\pm^{0.043}_{0.042}$	$0.140\pm^{0.025}_{0.022}$	22.462±1.678	14.193±0.303	20.615±0.884	34.808±0.934

* SN has not been corrected for host extinction. $L_{\rm p}$ and $M_{\rm Ni}$ values are lower limits

[a] SN 2011kl was primarily powered by a magnetar. The mass of ^{56}Ni synthesised in the explosion was negligible (Greiner et al., 2015)

Table B.2: *UBVRI*NIR pseudo-bolometric light curve statistics.

SN	Type	$\log(L_{\rm p})$	$M_{\rm Ni}$ ($M_\odot$)	$t_{\rm p}$ (days)	$t_{-1/2}$ (days)	$t_{+1/2}$ (days)	Width (days)
1998bw	GRB-SN	$42.953\pm^{0.042}_{0.026}$	$0.386\pm^{0.043}_{0.026}$	15.861±0.177	9.445±0.607	14.639±0.894	24.084±1.081
1999dn	Ib	$42.360\pm^{0.191}_{0.163}$	$0.088\pm^{0.073}_{0.038}$	13.916±2.841	-	19.790±4.210	-
2002ap	Ic-BL	$42.373\pm^{0.018}_{0.008}$	$0.086\pm^{0.004}_{0.002}$	13.011±0.000	6.076±0.130	13.629±0.362	19.705±0.384
2003dh	GRB-SN	$42.94\pm^{0.08}_{0.09}$	$0.308\pm^{0.102}_{0.083}$	12.65±1.66	-	15.845±0.590	-
2005bf	Ib	$42.385\pm^{0.033}_{0.032}$	$0.119\pm^{0.012}_{0.010}$	18.325±0.351	-	-	-
2005hg*	Ib	$42.377\pm^{0.029}_{0.027}$	-	-	12.215±0.051	19.900±0.727	32.115±0.728
2005mf*	Ic	$42.255\pm^{0.095}_{0.051}$	-	-	-	18.696±0.899	-
2006aj	GRB-SN	$42.839\pm^{0.025}_{0.017}$	$0.197\pm^{0.012}_{0.008}$	9.587±0.040	6.227±0.526	11.059±4.141	17.285±4.175
2007Y	Ib	$41.963\pm^{0.065}_{0.099}$	$0.046\pm^{0.008}_{0.010}$	18.757±0.350	7.406±0.916	11.507±0.916	18.912±1.295

2007gr	Ic	$42.258\pm^{0.061}_{0.059}$	$0.066\pm^{0.011}_{0.009}$	13.146±0.229	7.951±0.051	14.300±0.067	22.251±0.084
2007uy	Ib	$42.846\pm^{0.360}_{0.318}$	$0.358\pm^{0.474}_{0.188}$	19.075±0.284	-	12.944±1.512	-
2008D	Ib	$42.292\pm^{0.355}_{0.305}$	$0.101\pm^{0.130}_{0.051}$	19.293±0.229	13.697±0.106	16.897±0.606	30.594±0.615
2008ax	IIb	$42.284\pm^{0.037}_{0.036}$	$0.099\pm^{0.009}_{0.008}$	19.283±0.127	9.259±0.243	13.262±0.526	22.522±0.579
2009iz*	Ib	$42.200\pm^{0.028}_{0.024}$	$0.091\pm^{0.014}_{0.012}$	21.750±1.936	12.959±0.278	25.824±0.893	38.782±0.936
2009jf	Ib	$42.640\pm^{0.034}_{0.036}$	$0.246\pm^{0.022}_{0.021}$	21.267±0.164	10.633±0.652	18.821±0.285	29.453±0.711
2011bm	Ic	$42.880\pm^{0.058}_{0.049}$	$0.638\pm^{0.094}_{0.070}$	34.586±0.151	-	43.461±1.449	-
2011dh	IIb	$42.205\pm^{0.019}_{0.016}$	$0.068\pm^{0.003}_{0.003}$	15.712±0.017	9.837±0.075	13.346±0.045	23.182±0.087
2011hs	IIb	$42.027\pm^{0.017}_{0.018}$	$0.028\pm^{0.001}_{0.001}$	8.588±0.057	8.303±0.000	12.072±0.227	20.375±0.227

* SN has not been corrected for host extinction. $L_{\rm p}$ and $M_{\rm Ni}$ values are lower limits

Table B.3: Parameters derived from the fully bolometric $L_{\rm p}$ values.

SN	Type	log ($L_{\rm P}$)	$t_{\rm p}$ (days)	$M_{\rm Ni}$ ($M_\odot$)
1993J	IIb	$42.456\pm^{0.109}_{0.088}$	19.148±0.033	$0.146\pm^{0.042}_{0.027}$
1994I	Ic	$42.473\pm^{0.409}_{0.363}$	12.252±0.211	$0.102\pm^{0.164}_{0.059}$
1996cb	IIb	$42.082\pm^{0.179}_{0.163}$	16.993±1.650	$0.055\pm^{0.036}_{0.021}$
1998bw	GRB-SN	$43.061\pm^{0.080}_{0.046}$	15.861±0.177	$0.496\pm^{0.091}_{0.047}$
1999dn	Ib	$42.402\pm^{0.229}_{0.183}$	13.916±2.841	$0.097\pm^{0.097}_{0.044}$
1999ex	Ib	$42.544\pm^{0.124}_{0.105}$	18.349±0.036	$0.172\pm^{0.058}_{0.037}$
2002ap	Ic-BL	$42.415\pm^{0.055}_{0.028}$	13.011±0.000	$0.094\pm^{0.013}_{0.006}$
2003bg	IIb	$42.424\pm^{0.086}_{0.058}$	16.624±1.656	$0.119\pm^{0.040}_{0.024}$
2003dh	GRB-SN	$42.981\pm^{0.116}_{0.107}$	12.65±1.66	$0.339\pm^{0.153}_{0.102}$
2003jd	Ic-BL	$42.988\pm^{0.134}_{0.115}$	12.504±0.179	$0.341\pm^{0.128}_{0.082}$
2004aw	Ic	$42.659\pm^{0.063}_{0.056}$	-	-
2004fe*	Ic	$42.354\pm^{0.099}_{0.083}$	14.680±1.653	$0.091\pm^{0.035}_{0.023}$
2004gq	Ib	$42.388\pm^{0.046}_{0.028}$	-	-
2005az*	Ic	$42.173\pm^{0.086}_{0.070}$	-	-
2005bf	Ib	$42.426\pm^{0.071}_{0.052}$	18.325±0.351	$0.131\pm^{0.026}_{0.017}$
2005hg*	Ib	$42.418\pm^{0.067}_{0.047}$	-	-
2005hl*	Ib	$42.167\pm^{0.060}_{0.027}$	-	-
2005hm*	Ib	$42.237\pm^{0.073}_{0.093}$	19.927±1.669	$0.092\pm^{0.025}_{0.023}$
2005kl*	Ic	$41.979\pm^{0.080}_{0.064}$	-	-
2005kr*	Ic-BL	$43.006\pm^{0.117}_{0.057}$	11.405±1.669	$0.330\pm^{0.153}_{0.073}$
2005ks*	Ic-BL	$42.440\pm^{0.107}_{0.087}$	12.368±1.656	$0.096\pm^{0.040}_{0.026}$
2005kz*	Ic	$42.212\pm^{0.101}_{0.084}$	-	-
2005mf*	Ic	$42.296\pm^{0.133}_{0.071}$	-	-
2006T*	IIb	$42.322\pm^{0.054}_{0.036}$	14.148±1.651	$0.082\pm^{0.020}_{0.014}$
2006aj	GRB-SN	$42.880\pm^{0.062}_{0.038}$	9.587±0.040	$0.217\pm^{0.034}_{0.019}$
2006el*	IIb	$42.237\pm^{0.086}_{0.063}$	-	-
2006ep*	Ib	$42.142\pm^{0.075}_{0.060}$	18.002±1.653	$0.067\pm^{0.019}_{0.014}$
2006fe*	Ic	$42.533\pm^{0.094}_{0.081}$	15.830±1.711	$0.147\pm^{0.053}_{0.037}$
2006fo*	Ib	$42.372\pm^{0.099}_{0.080}$	-	-
14475*	Ic-BL	$42.753\pm^{0.108}_{0.092}$	10.501±1.760	$0.173\pm^{0.077}_{0.050}$
2006jo*	Ib	$42.542\pm^{0.086}_{0.052}$	10.366±1.651	$0.105\pm^{0.039}_{0.023}$
2006lc*	Ib	$42.130\pm^{0.044}_{0.030}$	13.837±1.651	$0.051\pm^{0.011}_{0.008}$
2006nx*	Ic-BL	$43.032\pm^{0.111}_{0.066}$	14.279±1.698	$0.422\pm^{0.181}_{0.097}$
2007C	Ib	$42.749\pm^{0.155}_{0.136}$	-	-
2007D*	Ic-BL	$42.282\pm^{0.156}_{0.135}$	-	-
2007Y	Ib	$42.005\pm^{0.103}_{0.119}$	18.757±0.350	$0.051\pm^{0.015}_{0.013}$
2007ag*	Ib	$42.085\pm^{0.078}_{0.061}$	-	-
2007cl*	Ic	$42.282\pm^{0.078}_{0.064}$	-	-
2007gr	Ic	$42.299\pm^{0.099}_{0.079}$	13.146±0.229	$0.073\pm^{0.020}_{0.013}$
2007kj*	Ib	$42.214\pm^{0.072}_{0.055}$	-	-
2007ms*	Ic	$42.556\pm^{0.052}_{0.041}$	22.231±1.666	$0.211\pm^{0.043}_{0.032}$
2007nc*	Ib	$42.260\pm^{0.125}_{0.063}$	17.734±1.800	$0.087\pm^{0.040}_{0.019}$
2007qv*	Ic	$42.783\pm^{0.062}_{0.043}$	-	-
2007qx*	Ic	$42.337\pm^{0.207}_{0.069}$	15.094±2.758	$0.090\pm^{0.078}_{0.025}$
2007ru	Ic-BL	$43.033\pm^{0.054}_{0.032}$	10.242±0.047	$0.323\pm^{0.044}_{0.024}$
2007sj*	Ic	$42.152\pm^{0.074}_{0.052}$	14.542±1.658	$0.057\pm^{0.017}_{0.011}$
2007uy	Ib	$42.887\pm^{0.398}_{0.338}$	19.075±0.284	$0.394\pm^{0.604}_{0.215}$
2008D	Ib	$42.333\pm^{0.393}_{0.325}$	19.293±0.229	$0.111\pm^{0.167}_{0.059}$

2008ax	IIb	$42.326\pm^{0.075}_{0.056}$	19.283 ± 0.127	$0.109\pm^{0.021}_{0.014}$
2008bo	IIb	$41.972\pm^{0.071}_{0.055}$	-	-
2008hw	GRB-SN	$43.337\pm^{0.095}_{0.078}$	12.307 ± 0.100	$0.751\pm^{0.190}_{0.127}$
2009bb	Ic	$42.863\pm^{0.162}_{0.143}$	12.631 ± 0.095	$0.258\pm^{0.119}_{0.073}$
2009er*	Ib	$42.916\pm^{0.089}_{0.072}$	-	-
2009iz*	Ib	$42.241\pm^{0.066}_{0.044}$	21.828 ± 1.650	$0.101\pm^{0.024}_{0.016}$
2009jf	Ib	$42.682\pm^{0.072}_{0.057}$	21.267 ± 0.164	$0.271\pm^{0.051}_{0.035}$
2010as	IIb	$42.689\pm^{0.158}_{0.139}$	12.442 ± 0.122	$0.171\pm^{0.077}_{0.048}$
2010bh	GRB-SN	$42.600\pm^{0.168}_{0.113}$	12.737 ± 0.099	$0.142\pm^{0.068}_{0.033}$
2010ma	GRB-SN	$43.244\pm^{0.272}_{0.098}$	10.331 ± 4.338	$0.529\pm^{0.789}_{0.227}$
2011bm	Ic	$42.922\pm^{0.096}_{0.069}$	34.586 ± 0.151	$0.702\pm^{0.176}_{0.106}$
2011dh	IIb	$42.246\pm^{0.057}_{0.036}$	15.712 ± 0.017	$0.075\pm^{0.011}_{0.006}$
2011ei	IIb	$42.177\pm^{0.146}_{0.129}$	17.732 ± 0.033	$0.072\pm^{0.029}_{0.018}$
2011fu	IIb	$42.538\pm^{0.045}_{0.034}$	-	-
2011hs	IIb	$42.068\pm^{0.055}_{0.038}$	8.588 ± 0.057	$0.031\pm^{0.004}_{0.003}$
2011kl[a]	GRB-SN	$43.529\pm^{0.174}_{0.148}$	15.169 ± 0.071	-
2012ap	Ic-BL	$42.676\pm^{0.203}_{0.182}$	13.192 ± 0.308	$0.174\pm^{0.109}_{0.062}$
2012bz	GRB-SN	$43.005\pm^{0.100}_{0.052}$	13.491 ± 0.224	$0.378\pm^{0.105}_{0.048}$
2013cq	GRB-SN	$43.186\pm^{0.086}_{0.117}$	13.000 ± 2.000	$0.555\pm^{0.211}_{0.184}$
2013cu	IIb	$42.843\pm^{0.067}_{0.050}$	9.009 ± 0.082	$0.191\pm^{0.033}_{0.022}$
2013df	IIb	$42.397\pm^{0.074}_{0.058}$	21.793 ± 0.103	$0.144\pm^{0.028}_{0.019}$
2013dx	GRB-SN	$42.962\pm^{0.225}_{0.077}$	12.261 ± 5.484	$0.316\pm^{0.417}_{0.139}$
2013ge	Ibc	$42.335\pm^{0.077}_{0.064}$	18.878 ± 1.697	$0.109\pm^{0.032}_{0.023}$
PTF09dh/2009dr*	Ic-BL	$43.082\pm^{0.078}_{0.059}$	-	-
PTF10inj*	Ib	$42.620\pm^{0.215}_{0.186}$	-	-
PTF10qif*	Ib	$42.636\pm^{0.182}_{0.162}$	-	-
PTF10vgv*	Ic	$42.682\pm^{0.132}_{0.115}$	10.347 ± 1.687	$0.145\pm^{0.076}_{0.047}$
PTF11bli*	Ibc	$42.266\pm^{0.081}_{0.065}$	20.627 ± 1.658	$0.101\pm^{0.030}_{0.021}$
PTF11jgj*	Ic	$42.293\pm^{0.090}_{0.072}$	22.072 ± 2.170	$0.114\pm^{0.039}_{0.026}$
PTF11klg*	Ic	$42.309\pm^{0.208}_{0.175}$	16.393 ± 1.678	$0.090\pm^{0.069}_{0.036}$
PTF11qiq*	Ib	$42.352\pm^{0.545}_{0.057}$	-	-
PTF11rka*	Ic	$42.905\pm^{0.117}_{0.097}$	-	-
PTF12gzk	Ic	$42.904\pm^{0.077}_{0.058}$	16.345 ± 0.455	$0.355\pm^{0.079}_{0.052}$
PTF12os*	IIb	$41.588\pm^{0.047}_{0.030}$	-	-
iPTF13bvn	Ib	$42.211\pm^{0.067}_{0.037}$	15.953 ± 0.098	$0.070\pm^{0.012}_{0.006}$
iPTF14dby*	Ic-BL	$42.575\pm^{0.104}_{0.087}$	22.462 ± 1.678	$0.223\pm^{0.079}_{0.053}$

* SN has not been corrected for host extinction. $L_{\rm p}$ and $M_{\rm Ni}$ values are lower limits

[a] SN 2011kl was primarily powered by a magnetar. The mass of ^{56}Ni synthesised in the explosion was negligible (Greiner et al., 2015)

Table B.4: $M_{\rm ej}^3/E_{\rm k}$ values for the sample at different opacities.

SN	Type	$\frac{M_{\rm ej}^3}{[{\rm M}_\odot]}/\frac{E_{\rm k}}{[10^{51}{\rm erg}]}$ $\kappa = 0.05$ g cm^{-2}	$\frac{M_{\rm ej}^3}{[{\rm M}_\odot]}/\frac{E_{\rm k}}{[10^{51}{\rm erg}]}$ $\kappa = 0.07$ g cm^{-2}	$\frac{M_{\rm ej}^3}{[{\rm M}_\odot]}/\frac{E_{\rm k}}{[10^{51}{\rm erg}]}$ $\kappa = 0.1$ g cm^{-2}
14475	Ic-BL	$0.567\pm^{0.487}_{0.295}$	$0.289\pm^{0.248}_{0.150}$	$0.142\pm^{0.122}_{0.074}$
1993J	IIb	$6.267\pm^{0.044}_{0.043}$	$3.198\pm^{0.022}_{0.022}$	$1.567\pm^{0.011}_{0.011}$
1994I	Ic	$1.051\pm^{0.074}_{0.071}$	$0.536\pm^{0.038}_{0.036}$	$0.263\pm^{0.019}_{0.018}$
1996cb	IIb	$3.888\pm^{1.745}_{1.304}$	$1.984\pm^{0.890}_{0.665}$	$0.972\pm^{0.436}_{0.326}$
1998bw	GRB-SN	$2.951\pm^{0.134}_{0.130}$	$1.506\pm^{0.068}_{0.066}$	$0.738\pm^{0.033}_{0.032}$
1999dn	Ib	$1.749\pm^{1.928}_{1.047}$	$0.892\pm^{0.984}_{0.534}$	$0.437\pm^{0.482}_{0.262}$
1999ex	Ib	$5.286\pm^{0.041}_{0.041}$	$2.697\pm^{0.021}_{0.021}$	$1.321\pm^{0.010}_{0.010}$
2002ap	Ic-BL	$1.336\pm^{0.000}_{0.000}$	$0.682\pm^{0.000}_{0.000}$	$0.334\pm^{0.000}_{0.000}$

2003bg	IIb	$3.561\pm^{1.646}_{1.221}$	$1.817\pm^{0.840}_{0.623}$	$0.890\pm^{0.411}_{0.305}$
2003jd	Ic-BL	$1.140\pm^{0.067}_{0.064}$	$0.582\pm^{0.034}_{0.033}$	$0.285\pm^{0.017}_{0.016}$
2004fe	Ic	$2.165\pm^{1.153}_{0.823}$	$1.105\pm^{0.588}_{0.420}$	$0.541\pm^{0.288}_{0.206}$
2005bf	Ib	$5.257\pm^{0.415}_{0.392}$	$2.682\pm^{0.212}_{0.200}$	$1.314\pm^{0.104}_{0.098}$
2005hm	Ib	$7.352\pm^{2.790}_{2.170}$	$3.751\pm^{1.423}_{1.107}$	$1.838\pm^{0.697}_{0.543}$
2005kr	Ic-BL	$0.789\pm^{0.573}_{0.370}$	$0.403\pm^{0.293}_{0.189}$	$0.197\pm^{0.143}_{0.092}$
2005ks	Ic-BL	$1.091\pm^{0.713}_{0.477}$	$0.557\pm^{0.364}_{0.243}$	$0.273\pm^{0.178}_{0.119}$
2006T	IIb	$1.868\pm^{1.037}_{0.731}$	$0.953\pm^{0.529}_{0.373}$	$0.467\pm^{0.259}_{0.183}$
2006aj	GRB-SN	$0.394\pm^{0.007}_{0.007}$	$0.201\pm^{0.003}_{0.003}$	$0.098\pm^{0.002}_{0.002}$
2006ep	Ib	$4.896\pm^{2.062}_{1.566}$	$2.498\pm^{1.052}_{0.799}$	$1.224\pm^{0.515}_{0.391}$
2006fe	Ic	$2.928\pm^{1.487}_{1.075}$	$1.494\pm^{0.759}_{0.549}$	$0.732\pm^{0.372}_{0.269}$
2006jo	Ib	$0.538\pm^{0.434}_{0.269}$	$0.275\pm^{0.221}_{0.137}$	$0.135\pm^{0.109}_{0.067}$
2006lc	Ib	$1.709\pm^{0.974}_{0.681}$	$0.872\pm^{0.497}_{0.347}$	$0.427\pm^{0.243}_{0.170}$
2006nx	Ic-BL	$1.938\pm^{1.100}_{0.770}$	$0.989\pm^{0.561}_{0.393}$	$0.485\pm^{0.275}_{0.193}$
2007Y	Ib	$5.771\pm^{0.443}_{0.419}$	$2.945\pm^{0.226}_{0.214}$	$1.443\pm^{0.111}_{0.105}$
2007gr	Ic	$1.393\pm^{0.100}_{0.094}$	$0.711\pm^{0.051}_{0.048}$	$0.348\pm^{0.025}_{0.024}$
2007ms	Ic	$11.388\pm^{3.817}_{3.049}$	$5.810\pm^{1.948}_{1.556}$	$2.847\pm^{0.954}_{0.762}$
2007nc	Ib	$4.611\pm^{2.176}_{1.606}$	$2.353\pm^{1.110}_{0.819}$	$1.153\pm^{0.544}_{0.401}$
2007qx	Ic	$2.420\pm^{2.316}_{1.341}$	$1.235\pm^{1.182}_{0.684}$	$0.605\pm^{0.579}_{0.335}$
2007ru	Ic-BL	$0.513\pm^{0.010}_{0.009}$	$0.262\pm^{0.005}_{0.005}$	$0.128\pm^{0.002}_{0.002}$
2007sj	Ic	$2.085\pm^{1.126}_{0.800}$	$1.064\pm^{0.575}_{0.408}$	$0.521\pm^{0.282}_{0.200}$
2007uy	Ib	$6.173\pm^{0.377}_{0.360}$	$3.149\pm^{0.192}_{0.184}$	$1.543\pm^{0.094}_{0.090}$
2008D	Ib	$6.460\pm^{0.312}_{0.301}$	$3.296\pm^{0.159}_{0.154}$	$1.615\pm^{0.078}_{0.075}$
2008ax	IIb	$6.447\pm^{0.172}_{0.169}$	$3.289\pm^{0.088}_{0.086}$	$1.612\pm^{0.043}_{0.042}$
2008hw	GRB-SN	$1.070\pm^{0.035}_{0.034}$	$0.546\pm^{0.018}_{0.018}$	$0.267\pm^{0.009}_{0.009}$
2009bb	Ic	$1.187\pm^{0.036}_{0.035}$	$0.606\pm^{0.018}_{0.018}$	$0.297\pm^{0.009}_{0.009}$
2009iz	Ib	$10.585\pm^{3.582}_{2.856}$	$5.401\pm^{1.828}_{1.457}$	$2.646\pm^{0.896}_{0.714}$
2009jf	Ib	$9.537\pm^{0.297}_{0.290}$	$4.866\pm^{0.151}_{0.148}$	$2.384\pm^{0.074}_{0.072}$
2010as	IIb	$1.117\pm^{0.044}_{0.043}$	$0.570\pm^{0.023}_{0.022}$	$0.279\pm^{0.011}_{0.011}$
2010bh	GRB-SN	$1.227\pm^{0.039}_{0.038}$	$0.626\pm^{0.020}_{0.019}$	$0.307\pm^{0.010}_{0.009}$
2010ma	GRB-SN	$0.531\pm^{1.628}_{0.471}$	$0.271\pm^{0.830}_{0.240}$	$0.133\pm^{0.407}_{0.118}$

2011bm	Ic	$66.714\pm^{1.170}_{1.154}$	$34.038\pm^{0.597}_{0.589}$	$16.678\pm^{0.292}_{0.289}$
2011dh	IIb	$2.842\pm^{0.012}_{0.012}$	$1.450\pm^{0.006}_{0.006}$	$0.710\pm^{0.003}_{0.003}$
2011ei	IIb	$4.609\pm^{0.034}_{0.034}$	$2.352\pm^{0.017}_{0.017}$	$1.152\pm^{0.009}_{0.008}$
2011hs	IIb	$0.254\pm^{0.007}_{0.007}$	$0.129\pm^{0.003}_{0.003}$	$0.063\pm^{0.002}_{0.002}$
2011kl	GRB-SN	$2.468\pm^{0.047}_{0.046}$	$1.259\pm^{0.024}_{0.023}$	$0.617\pm^{0.012}_{0.011}$
2012ap	Ic-BL	$1.412\pm^{0.137}_{0.127}$	$0.720\pm^{0.070}_{0.065}$	$0.353\pm^{0.034}_{0.032}$
2012bz	GRB-SN	$1.544\pm^{0.105}_{0.100}$	$0.788\pm^{0.054}_{0.051}$	$0.386\pm^{0.026}_{0.025}$
2013cq	GRB-SN	$1.332\pm^{1.029}_{0.649}$	$0.679\pm^{0.525}_{0.331}$	$0.333\pm^{0.257}_{0.162}$
2013cu	IIb	$0.307\pm^{0.011}_{0.011}$	$0.157\pm^{0.006}_{0.006}$	$0.077\pm^{0.003}_{0.003}$
2013df	IIb	$10.517\pm^{0.201}_{0.198}$	$5.366\pm^{0.103}_{0.101}$	$2.629\pm^{0.050}_{0.050}$
2013dx	GRB-SN	$1.054\pm^{3.570}_{0.955}$	$0.538\pm^{1.821}_{0.487}$	$0.263\pm^{0.892}_{0.239}$
2013ge	Ibc	$5.921\pm^{2.433}_{1.858}$	$3.021\pm^{1.241}_{0.948}$	$1.480\pm^{0.608}_{0.465}$
PTF10vgv	Ic	$0.534\pm^{0.443}_{0.272}$	$0.273\pm^{0.226}_{0.139}$	$0.134\pm^{0.111}_{0.068}$
PTF11bli	Ibc	$8.440\pm^{3.059}_{2.404}$	$4.306\pm^{1.561}_{1.226}$	$2.110\pm^{0.765}_{0.601}$
PTF11jgj	Ic	$11.066\pm^{5.037}_{3.751}$	$5.646\pm^{2.570}_{1.914}$	$2.767\pm^{1.259}_{0.938}$
PTF11klg	Ic	$3.367\pm^{1.605}_{1.181}$	$1.718\pm^{0.819}_{0.602}$	$0.842\pm^{0.401}_{0.295}$
PTF12gzk	Ic	$3.328\pm^{0.387}_{0.356}$	$1.698\pm^{0.197}_{0.181}$	$0.832\pm^{0.097}_{0.089}$
iPTF13bvn	Ib	$3.020\pm^{0.075}_{0.073}$	$1.541\pm^{0.038}_{0.037}$	$0.755\pm^{0.019}_{0.018}$
iPTF14dby	Ic-BL	$11.869\pm^{3.963}_{3.168}$	$6.056\pm^{2.022}_{1.616}$	$2.967\pm^{0.991}_{0.792}$

Appendix C

Chapter 3 tables

Table C.1: Database of SNe in Chapter 3

SN	z	Original classification	Reclassification	References
SN1993J	-0.0001	IIb	IIb	(1) (2)
SN1994I	0.0015	Ic	Ic-6(11/9)	(3) (4)
SN1996cb	0.002	IIb	IIb(I)	(3) (5)
SN1997ef	0.012	Ic-BL	Ic-4(13/45)	(3) (5) (6) (7)
SN1998bw	0.0085	GRB-SN	Ic-3(15/16)	(8)
SN1999dn	0.0093	Ib	Ib(II)	(9) (10) (5) (11)
SN1999ex	0.011	Ib	Ib(II)	(12)
SN2002ap	0.0022	Ic-BL	Ic4-9/6	(13) (14) (3) (15) (16)
SN2003bg	0.0046	IIb	IIb	(17) (18)
SN2003jd	0.019	Ic-BL	Ic-4(13/14)	(3)
SN2004aw	0.016	Ic	Ic-6(11/21)	(3) (19)
SN2004dn	0.013	Ic	Ic-6(9/15)	(3) (20)
SN2004fe	0.018	Ic	Ic-6(8/u)	(20) (3)
SN2004gq	0.0065	Ib	Ib	(3)
SN2005az	0.0085	Ic	Ic-7(11/29)	(3)
SN2005bf	0.019	Ib	Ib(II)	(21) (3)
SN2005hg	0.021	Ib	Ib	(3)
SN2006T	0.008	IIb	IIb	(3)
SN2006aj	0.033	XRF-SN	Ic-6(21/14)	(22) (23) (3)
SN2006el	0.017	IIb	IIb(I)	(3)
SN2006ep	0.015	Ib	Ib(II)	(3)
SN2006lc	0.016	Ib	Ib	(3)
SN2007Y	0.0046	Ib	Ib(II)	(24)
SN2007gr	0.0017	Ic	Ic-7(7/15)	(25) (3)
SN2007kj	0.018	Ib	Ib(II)	(3)
SN2007uy	0.0065	Ib	Ib(II)	(3)
SN2008D	0.0065	Ib	Ib(II)	(26) (27) (28)
SN2008ax	0.0019	IIb	IIb(I)	(3) (29) (30) (31)
SN2008bo	0.005	IIb	IIb	(3)
SN2009bb	0.0099	Ic-BL	Ic-6(20/13)	(32)
SN2009er	0.035	Ib	Ib	(3)
SN2009iz	0.014	Ib	Ib	(3)
SN2009jf	0.0079	Ib	Ib	(33) (3)
PTF10vgv	0.015	Ic	Ic-5(7/10)	(34)
SN2010ah	0.050	Ic-BL	Ic-3(18/17)	(35)
SN2010as	0.007	IIb	IIb(I)	(36)
SN2010bh	0.059	GRB-SN	Ic-3(32/9)	(37)
SN2011bm	0.022	Ic	Ic-7(6/43)	(38)
SN2011dh	0.002	IIb	IIb	(39) (40)
SN2011ei	0.0093	IIb	IIb	(41)
SN2011fu	0.0185	IIb	IIb	(42) (43)
SN2011hs	0.0057	IIb	IIb	(44)
PTF12gzk	0.0137	Ic	Ic-6(17/24)	(45)
SN2012ej	0.009	Ic	Ic-7(7/20)	(48)
iPTF13bvn	0.0045	Ib	Ib	(46) (47)
SN2016P	0.0146	Ic-BL	Ic-6(u/14)	(48)
SN2016coi	0.0036	Ic-BL	Ic-4(14/20)	(49)
SN2016iae	0.004	Ic	Ic-7(9/14)	(48)

References: (1) (Matheson et al., 2000a), (2) (Barbon et al., 1995), (3) (Modjaz et al., 2014), (4) (Filippenko et al., 1995), (5) (Matheson et al., 2001), (6) (Iwamoto et al., 2000), (7) (Mazzali et al., 2000), (8) (Patat et al., 2001), (9) (Deng et al., 2000), (10) (Benetti et al., 2011), (11) (Taubenberger et al., 2009), (12) (Hamuy et al., 2002), (13) (Gal-Yam et al., 2002), (14) (Chornock et al., 2013), (15) (Mazzali et al., 2002), (16) (Foley et al., 2003), (17) (Hamuy et al., 2009), (18) (Mazzali et al., 2009), (19) (Taubenberger et al., 2006), (20) (Harutyunyan et al., 2008), (21) (Folatelli et al., 2006), (22) (Pian et al., 2006), (23) (Sonbas et al., 2008), (24) (Stritzinger et al., 2009), (25) (Valenti et al., 2008), (26) (Modjaz et al., 2009), (27) (Malesani et al., 2009), (28) (Mazzali et al., 2008), (29) (Taubenberger et al., 2011), (30) (Pastorello et al., 2008), (31) (Milisavljevic et al., 2010), (32) (Pignata et al., 2011), (33) (Valenti et al., 2011), (34) (Corsi et al., 2012), (35) (Corsi et al., 2011), (36) (Folatelli et al., 2014), (37) (Bufano et al., 2012), (38) (Valenti et al., 2012), (39) (Arcavi et al., 2011), (40) (Ergon et al., 2014), (41) (Milisavljevic et al., 2013b), (42) (Morales-Garoffolo et al., 2014a), (43) (Kumar et al., 2013), (44) (Bufano et al., 2014), (45) (Ben-Ami et al., 2012), (46) (Cao et al., 2013), (47) (Srivastav et al., 2014), (48) (Prentice et al., in prep.) (49) (Prentice et al., 2018)

Appendix D

Chapter 4 tables

Table D.1: Derived $E\,(B-V)_{\rm host}$ for previously used SNe and updated parameters

SN	$E\,(B-V)_{\rm host}$ [mag]	$\log_{10}\,(L_{\rm p})$ [erg s^{-1}]	$M_{\rm Ni}$ [M$_\odot$]
2004fe	0.05±0.04	42.18±0.04	0.06±0.01
2005az	0.2±0.1	42.2±0.2	0.08±0.03
2005hg	0.3±0.2	42.4±0.4	0.18±0.05
2005kl	0.2±0.1	41.7±0.1	0.026±0.009
2005mf	0.05±0.04	42.18±0.07	0.06±0.01
2006T	0.15±0.1	42.3±0.2	0.09±0.04
2006el	0.01±0.005	42.05±0.02	0.062±0.004
2006ep	0.025±0.02	41.96±0.03	0.037±0.003
2006fe	0.1±0.05	42.36±0.09	0.08±0.02
2006fo	0.1±0.05	42.25±0.08	0.06±0.01
2006jo	0.03±0.02	42.41±0.03	0.080±0.007
2006lc	0.15±0.1	42.2±0.2	0.06±0.02
2006nx	negligible	no change	no change
2007ag	0.15±0.05	42.04±0.08	0.046±0.009
2007kj	negligible	42.017±0.009	no change
2007ms	negligible	no change	no change
2007qx	0.13±0.05	42.3±0.3	0.09±0.03
2009er	0.01±0.005	42.77±0.01	0.218±0.007
2009iz	negligible	no change	no change
PTF10vgv	0.01±0.005	42.50±0.06	0.10±0.02
PTF12os	0.29±0.08	41.9±0.1	0.04±0.01

Table D.2: New SNe included in Chapter 4

SN	Type	μ [mag]	z	$E\,(B-V)_{\rm MW}$ [mag]	$E\,(B-V)_{\rm host}$ [mag]	$\log_{10}\,(L_{\rm p})$ [erg s^{-1}]	$M_{\rm Ni}$ [M$_\odot$]	$t_{-1/2}$ [d]	$t_{+1/2}$ [d]	references
2004dn	Ic-6	32.82	0.013	0.042	0.3±0.2	41.7±0.2	0.03±0.01	10.8±0.1	16.8±0.6	(1),(2)
2008aq	IIb	32.53	0.007972	0.04	0.04±0.03	42.00±0.04	0.041±0.009	9.6±0.6	17±3	(1),(2), (3)

References: (1) (Modjaz et al., 2014), (2) (Bianco et al., 2014), (3) (Stritzinger et al., 2018a)

Table D.3: $M_{\rm ej}$ of literature SNe

SN	$t_{\rm p}$ [d]	$v_{\rm ph}$ [$\rm km\,s^{-1}$]	$M_{\rm ej}$ [$\rm M_\odot$]
PTF10vgv	11.6	9000	1.3
PTF12gzk	19.9	16000	7.0
PTF12os	17.5	5500	1.8
1993J	21	7000	3.3
1994I	10.2	9000	1.0
1996cb	16.7	7000	2.1
1997ef	15	15000	3.7
1998bw	16.1	15000	4.2
1999dn	18.0	9000	3.2
1999ex	18.0	6000	2.1
2002ap	12.6	13000	2.2
2003bg	17.5	11000	3.7
2003dh	12.6	38000	6.6
2003jd	13.7	13000	2.6
2004aw	17.0	13000	4.1
2004dn	16.5	7500	2.2
2004fe	15.1	8000	2.0
2004gq	15.3	12000	3.1
2005az	21.0	11000	5.3
2005bf	13.	5000	0.9
2005hg	17.3	7000	2.3
2005mf	15.1	9000	2.2
2006T	18.2	6000	2.2
2006aj	9.78	21000	2.2
2006el	21.	8000	3.8
2006ep	14.8	7000	1.6
2006fe	12.5	6000	1.0
2006fo	12.7	5500	0.9
2006jo	10.8	9000	1.1
2006lc	16.1	5000	1.4
2006nx	16.3	13000	3.8
2007C	9.3	9000	0.8
2007Y	15.7	5000	1.3
2007ag	15.1	8000	2.0
2007cl	14.9	9000	2.2
2007gr	14.1	7000	1.5
2007kj	12.3	6000	0.9
2007ms	20.6	8000	3.7
2007ru	12.0	19000	3.0
2007uy	16	15000	4.2
2008D	18	8000	2.9
2008aq	15.1	6000	1.5
2008ax	20.1	6000	2.6
2008bo	15.2	5000	1.2
2009bb	13.4	20000	3.9
2009er	13.2	13000	2.4
2009iz	20.4	5000	2.3
2009jf	20.4	7000	3.2
2010ah	13	18000	3.3
2010as	16.2	6000	1.7
2010bh	9.85	32000	3.4
2011bm	38	7000	11.
2011dh	20	7000	2.8
2011ei	19.4	9000	3.7
2011fu	17.0	7000	2.2
2011hs	13.1	6000	1.1
2012ap	12.5	16000	2.7
2013df	21.7	7000	3.6
2013ge	18.0	9000	3.2
iPTF13bvn	17.5	6000	2

Appendix E

Spectra

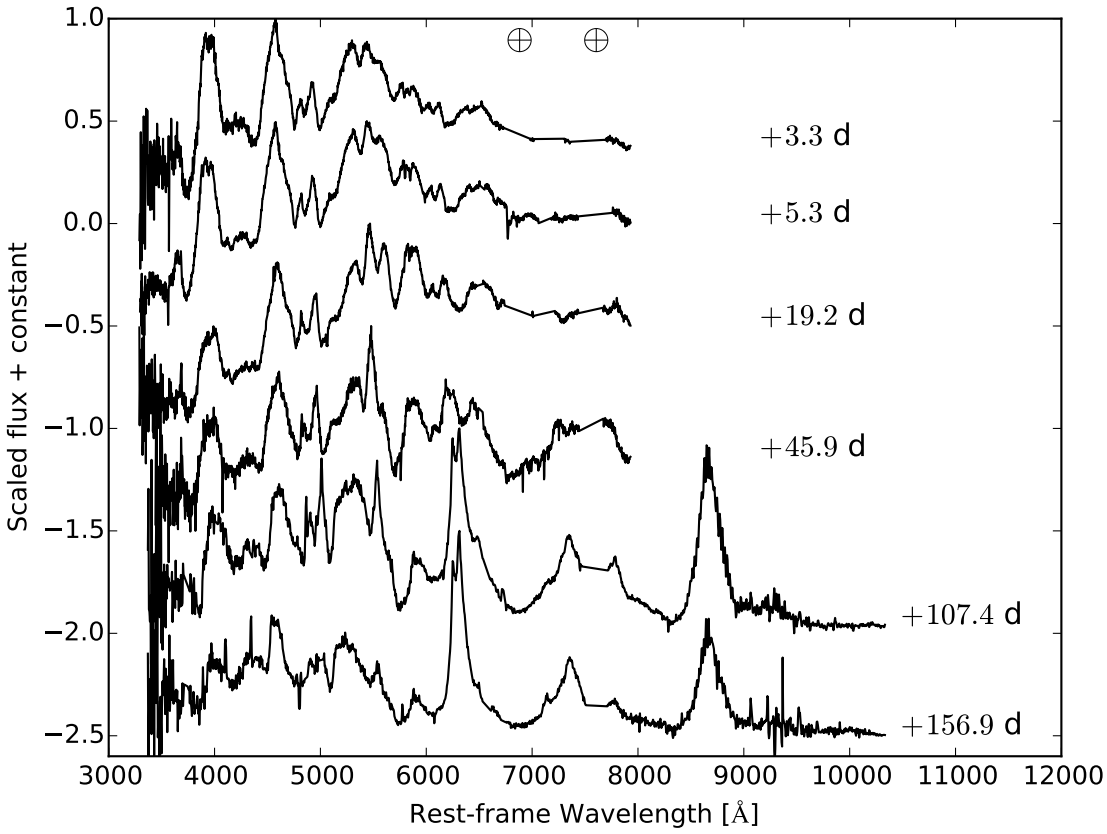

Figure E.1: The spectra of type Ic-7 SN 2012ej. Epochs are relative to $t_{\max}$. Spectra may be truncated to remove noise.

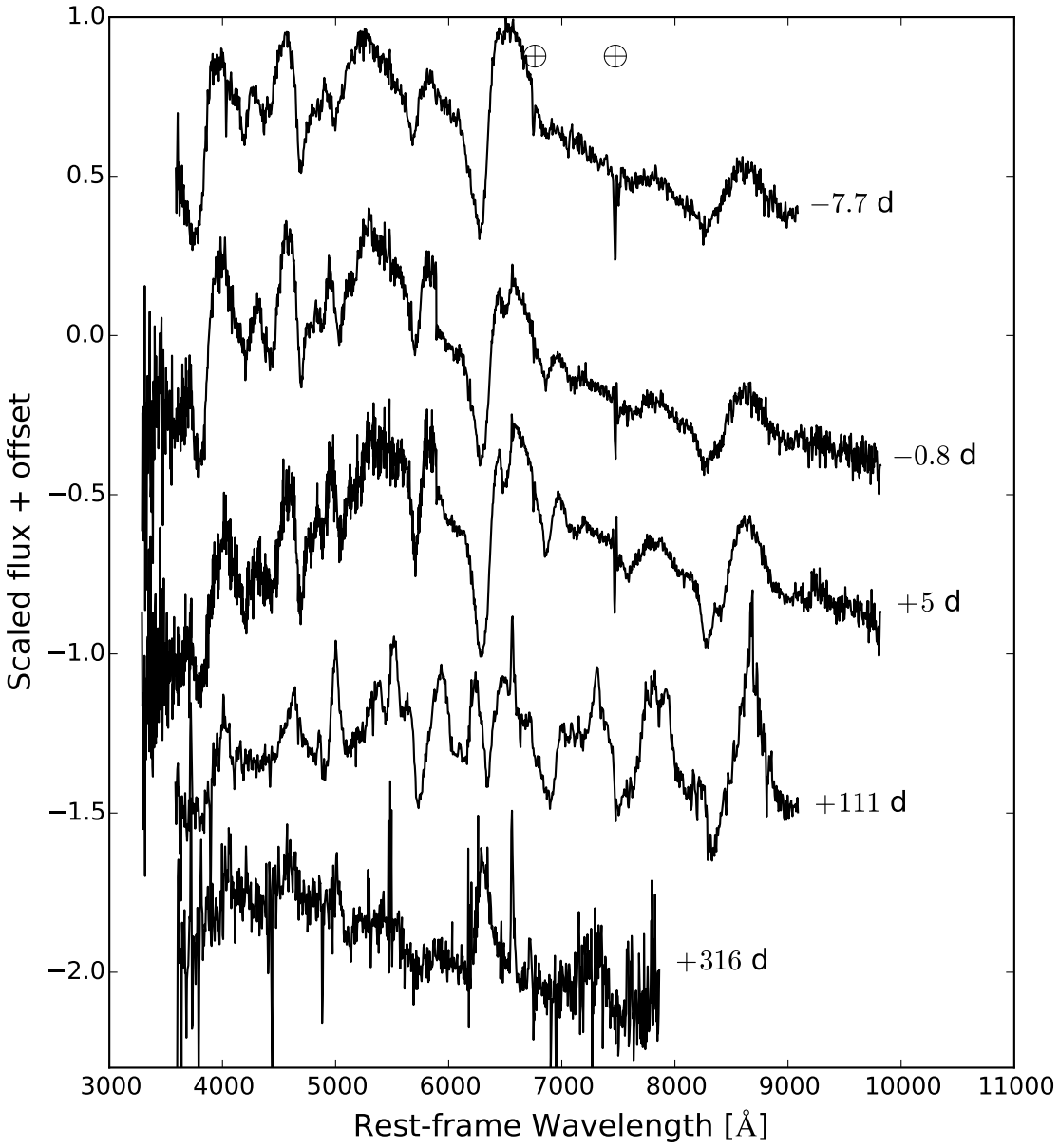

Figure E.2: The spectra of type IIb(I) SN 2013bb.

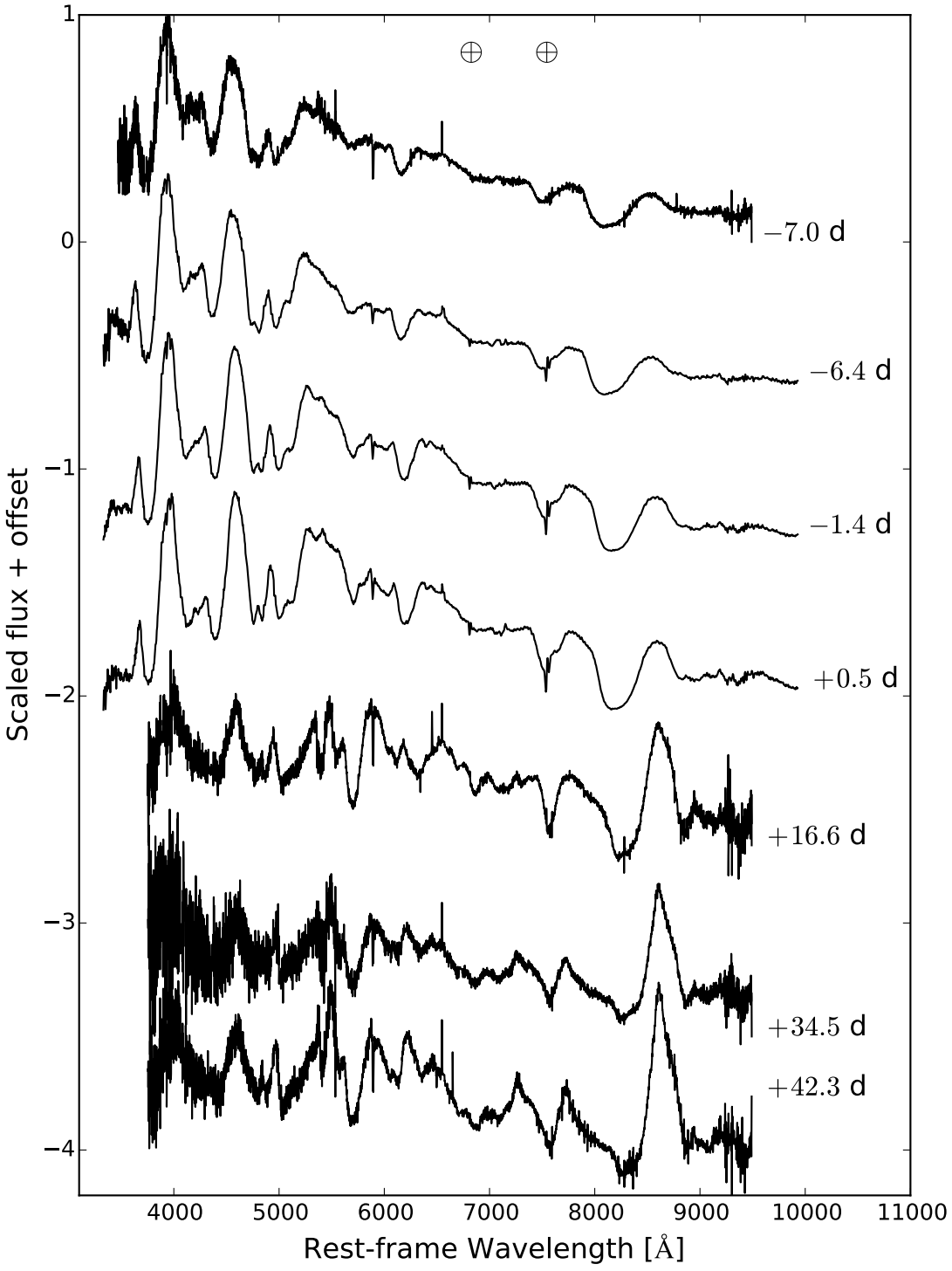

Figure E.3: The spectra of type Ic-7 SN 2014L.

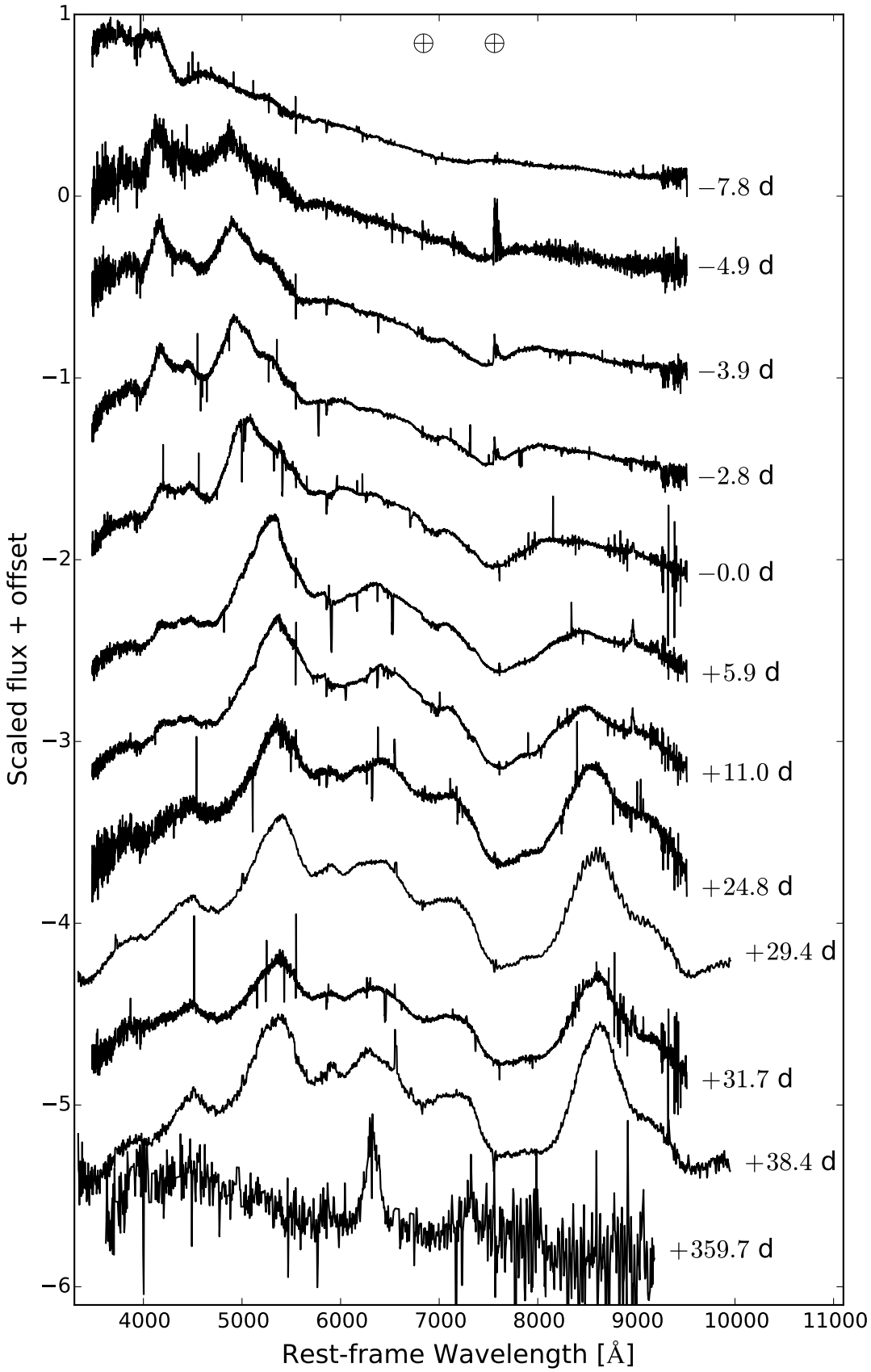

Figure E.4: The spectra of type Ic-3 SN 2014ad.

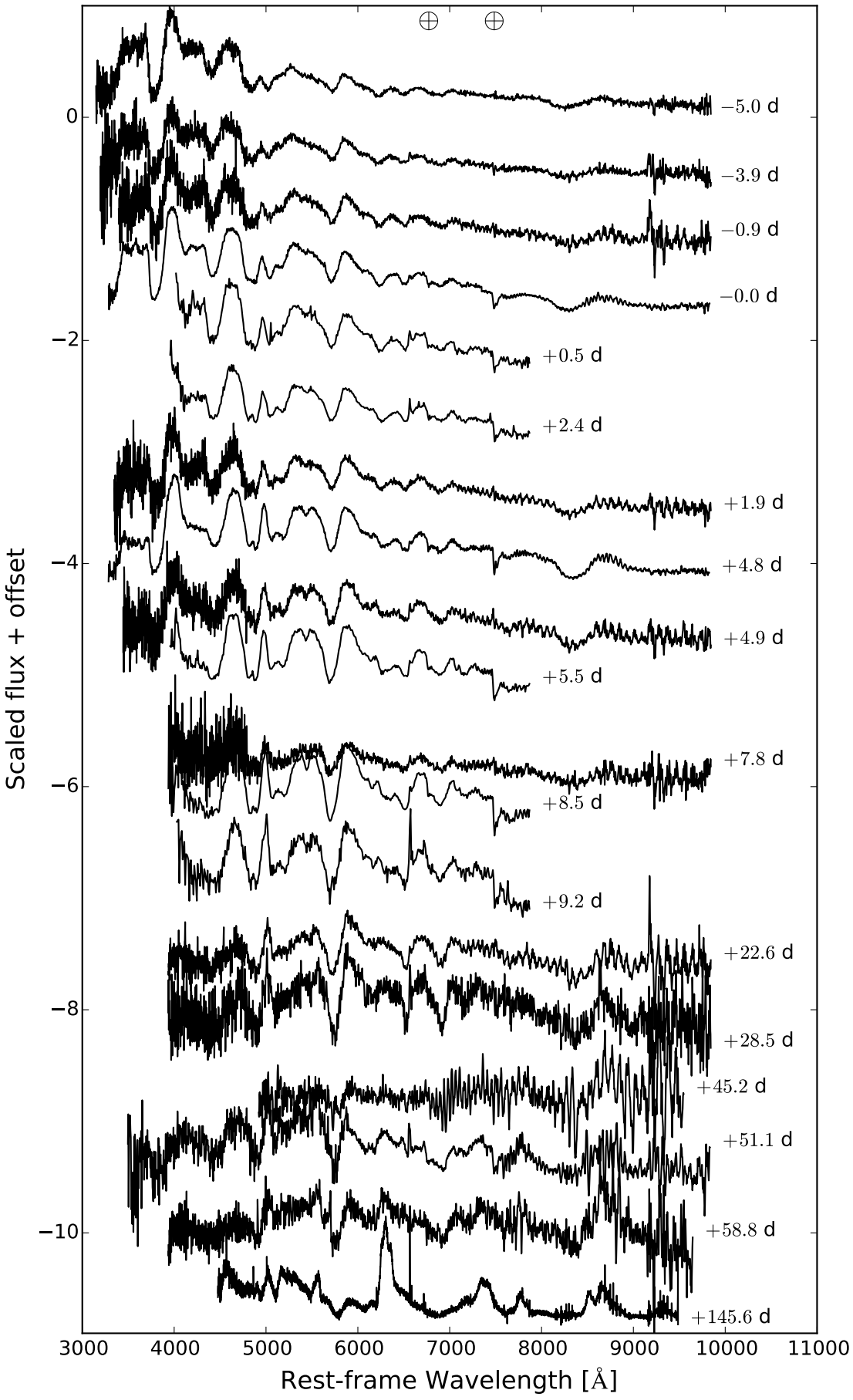

Figure E.5: The spectra of type Ib SN 2015ah.

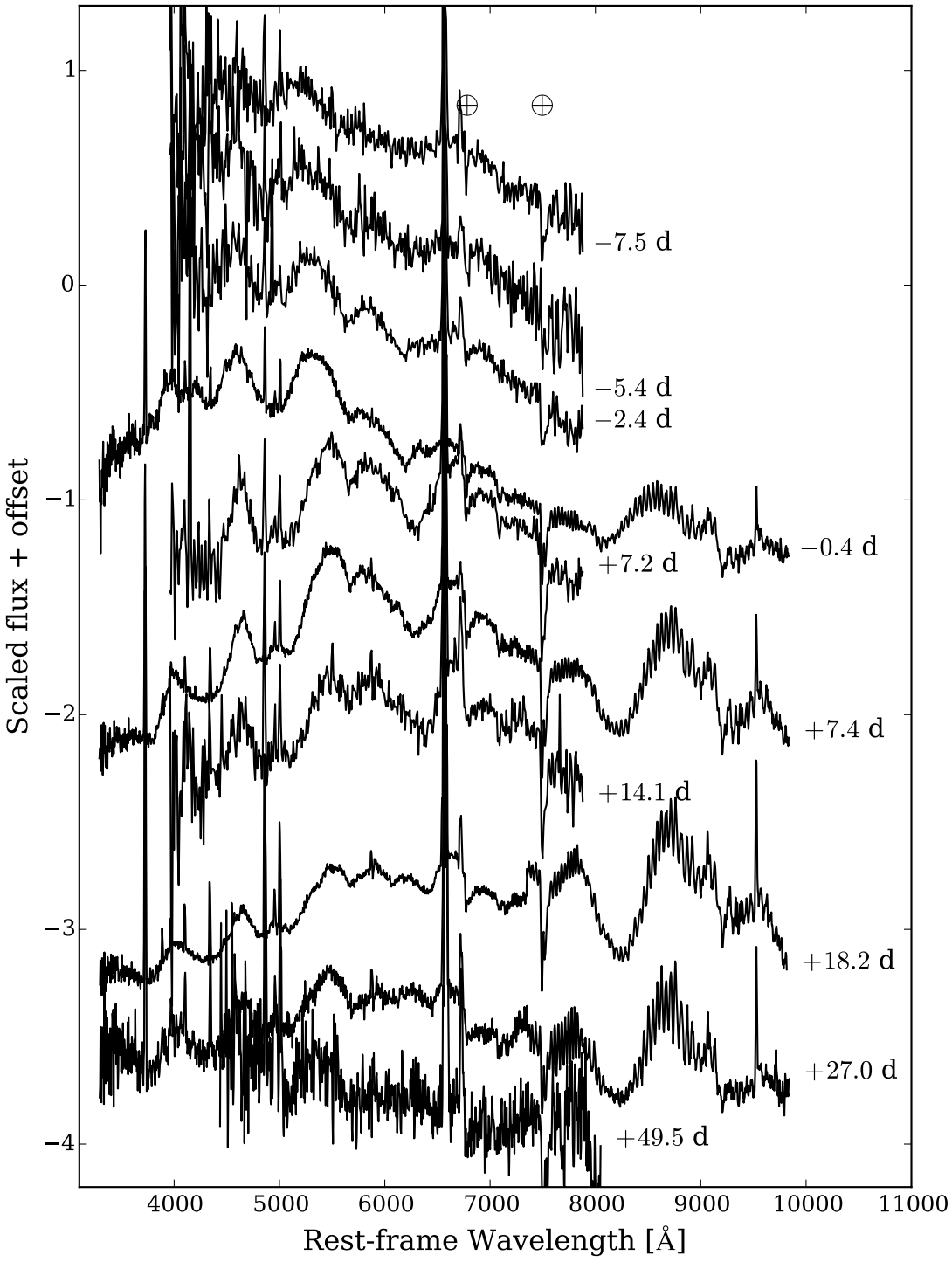

Figure E.6: The spectra of SN Ic-6 2016P.

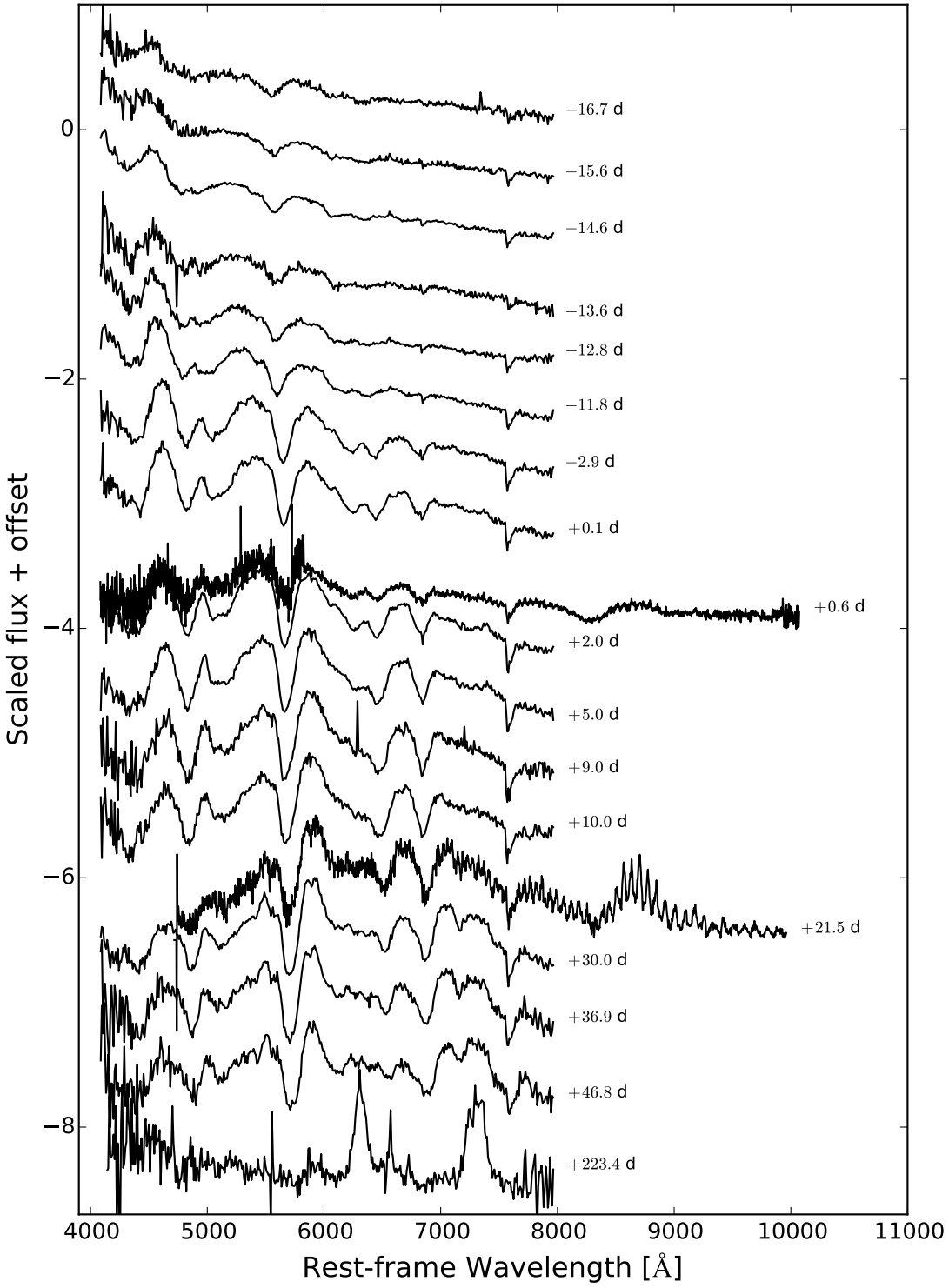

Figure E.7: The spectra of SN Ib 2016bau.

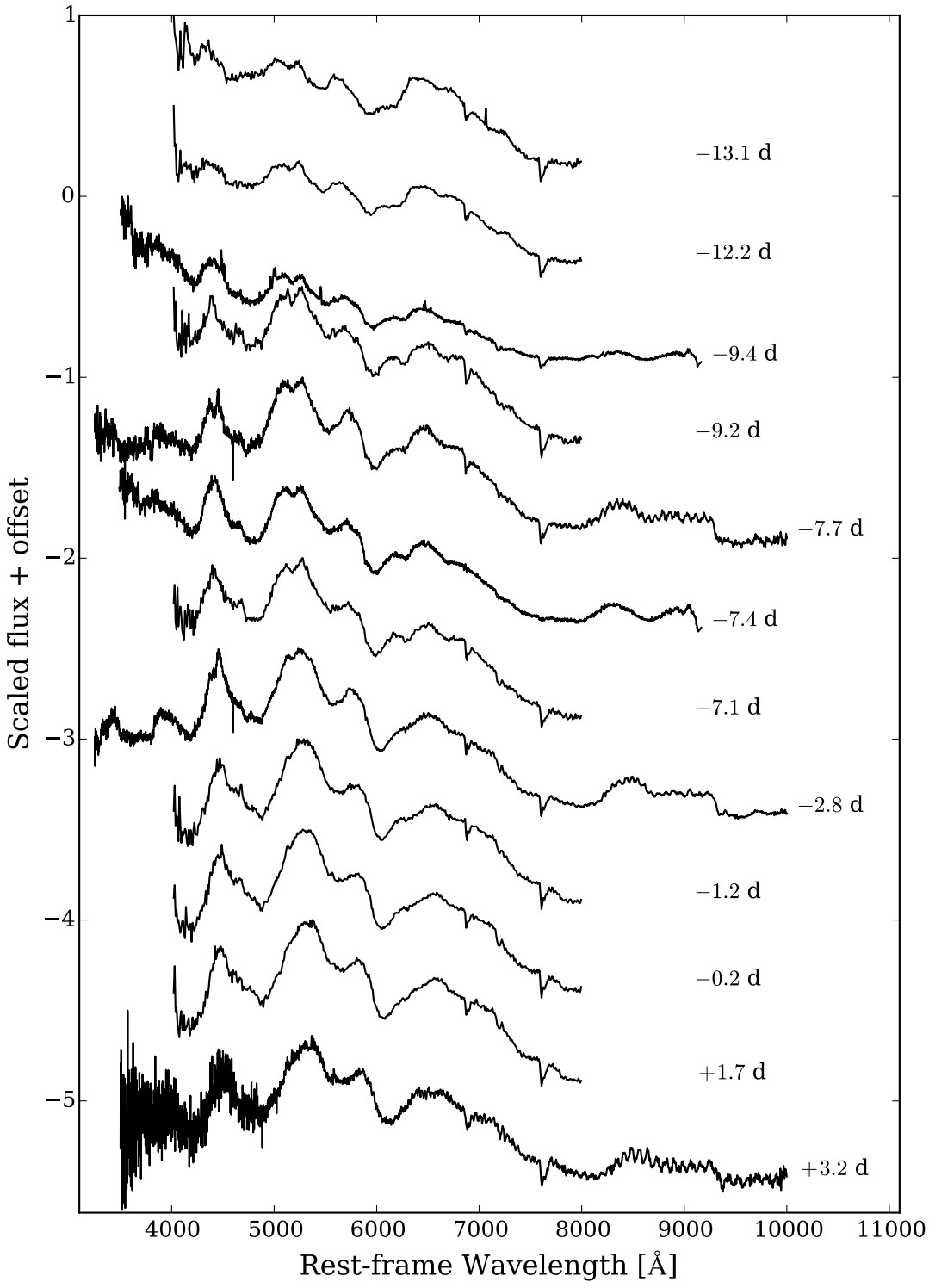

Figure E.8: The spectra of SN Ic-4 2016coi (1/5). Published in (Prentice et al., 2018).

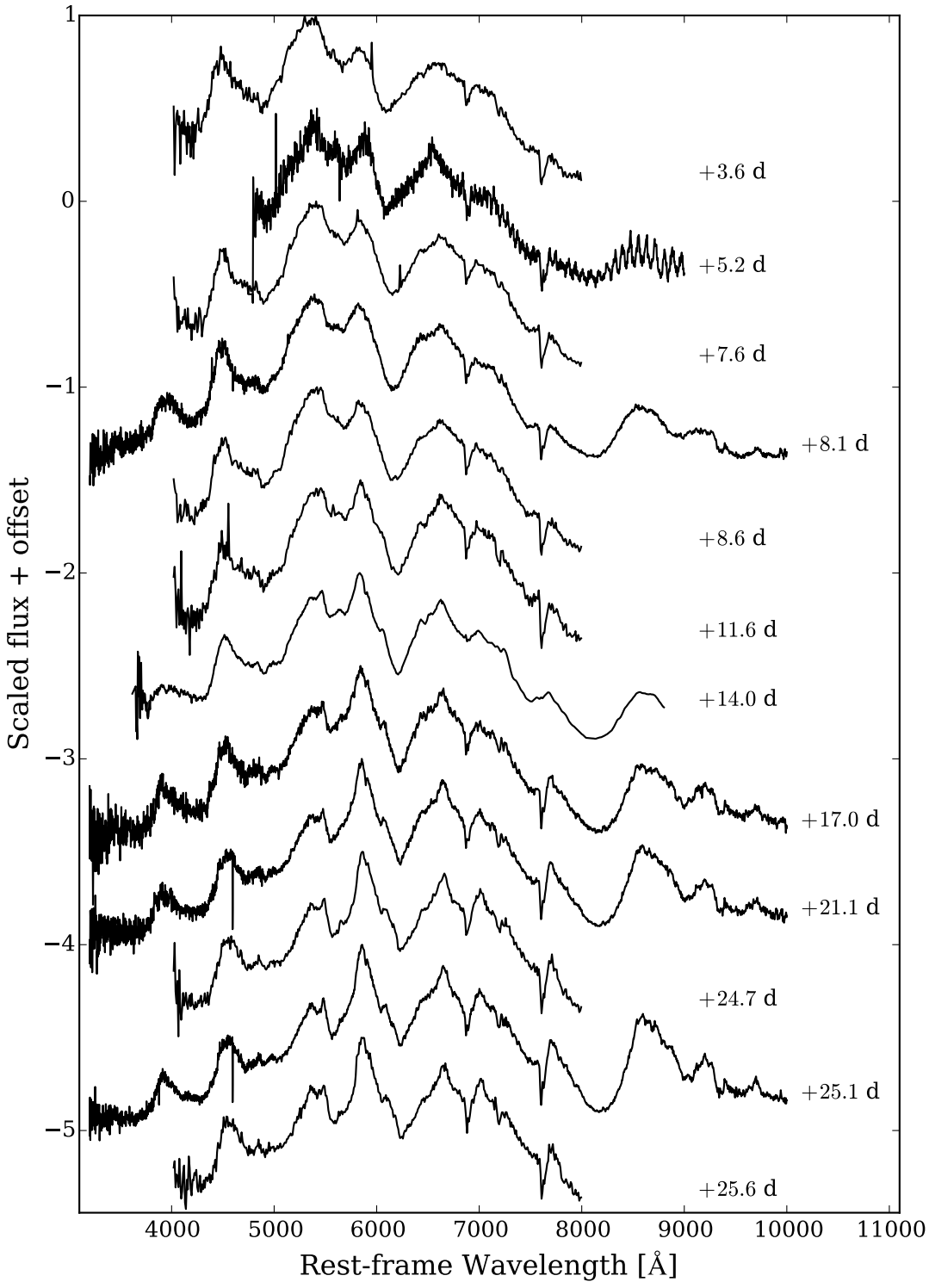

Figure E.9: The spectra of SN Ic-4 2016coi (2/5). Published in (Prentice et al., 2018).

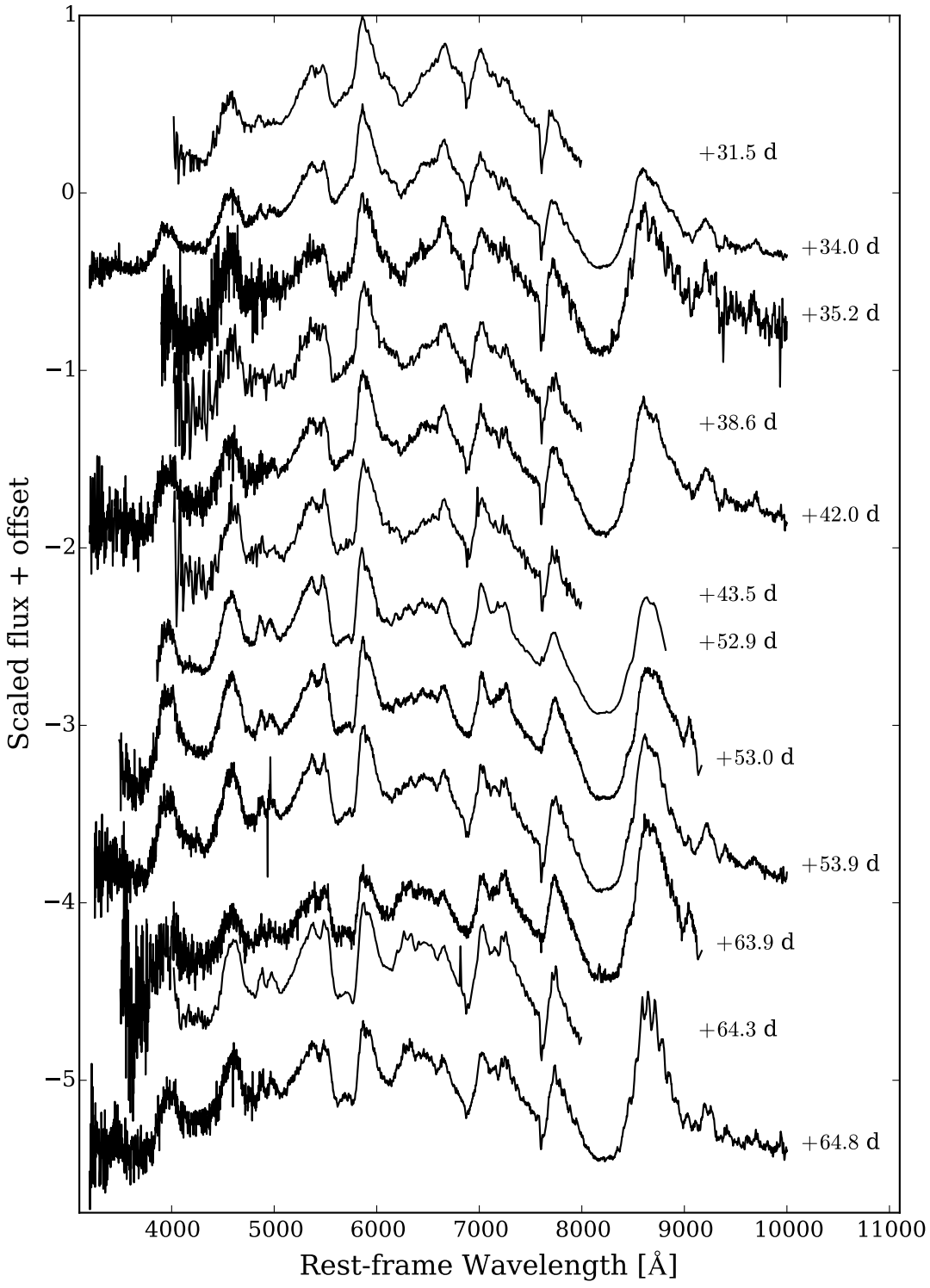

Figure E.10: The spectra of SN Ic-4 2016coi (3/5). Published in (Prentice et al., 2018).

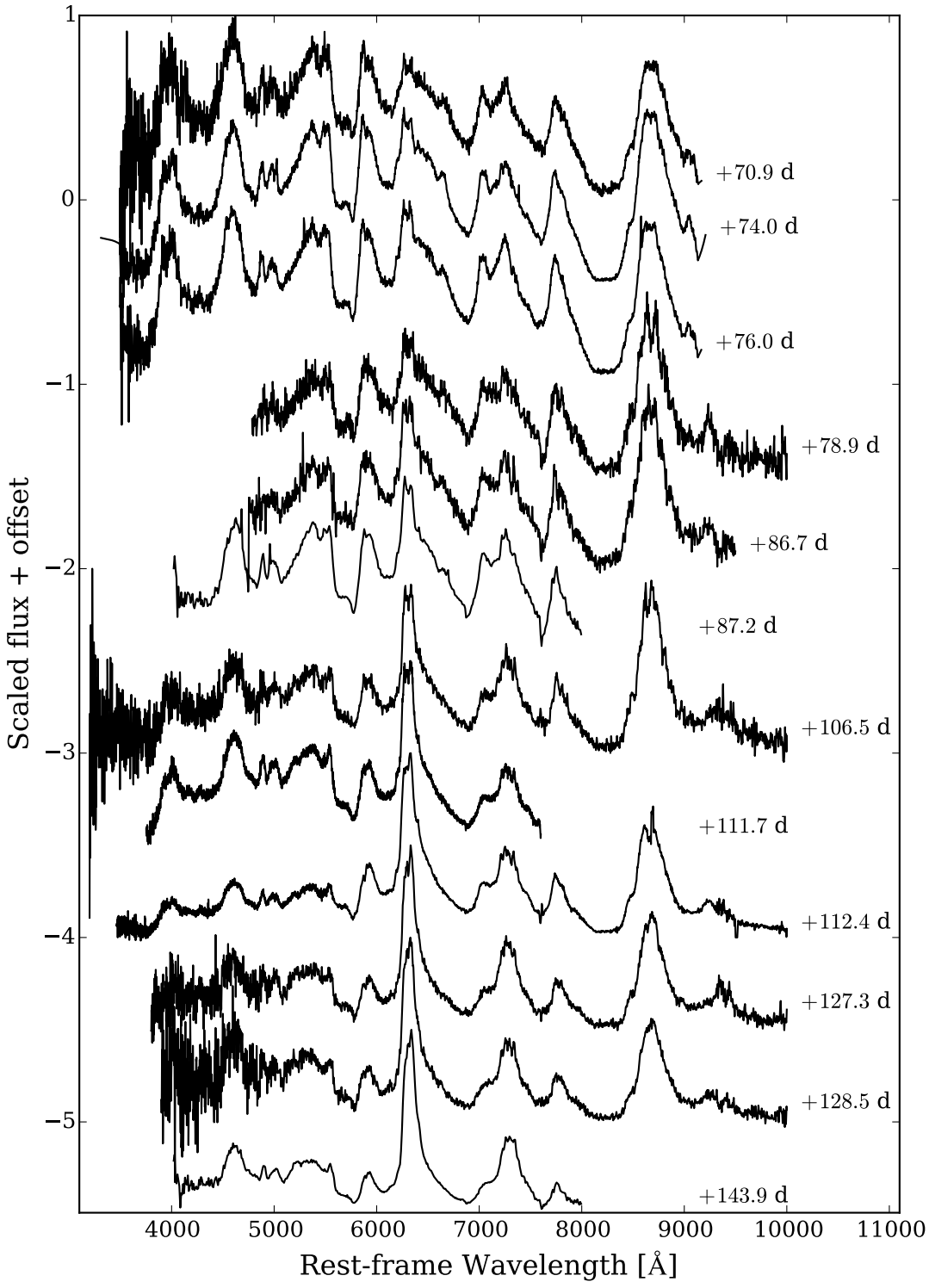

Figure E.11: The spectra of SN Ic-4 2016coi (4/5). Published in (Prentice et al., 2018).

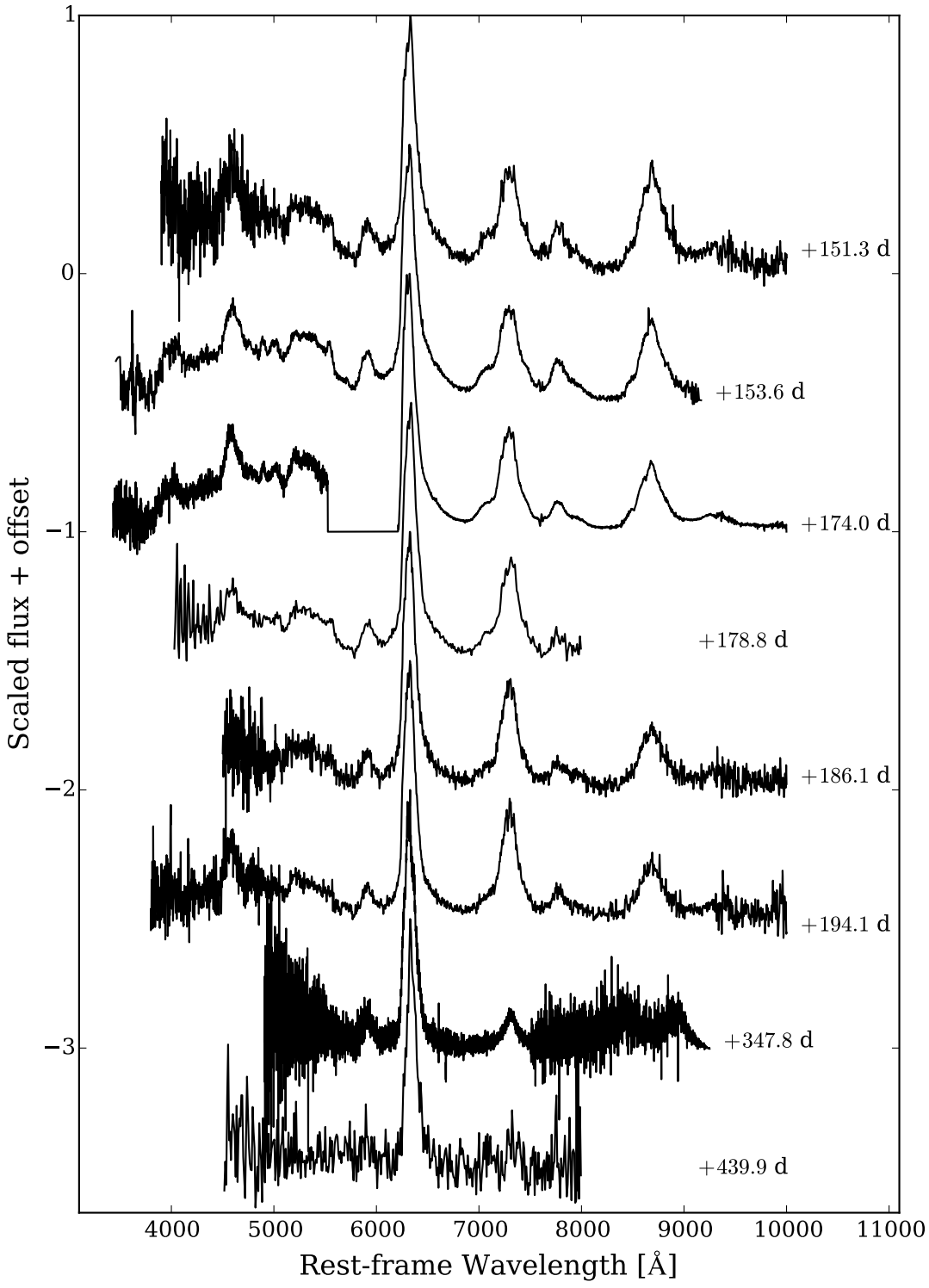

Figure E.12: The spectra of SN Ic-4 2016coi (5/5). Published in (Prentice et al., 2018).

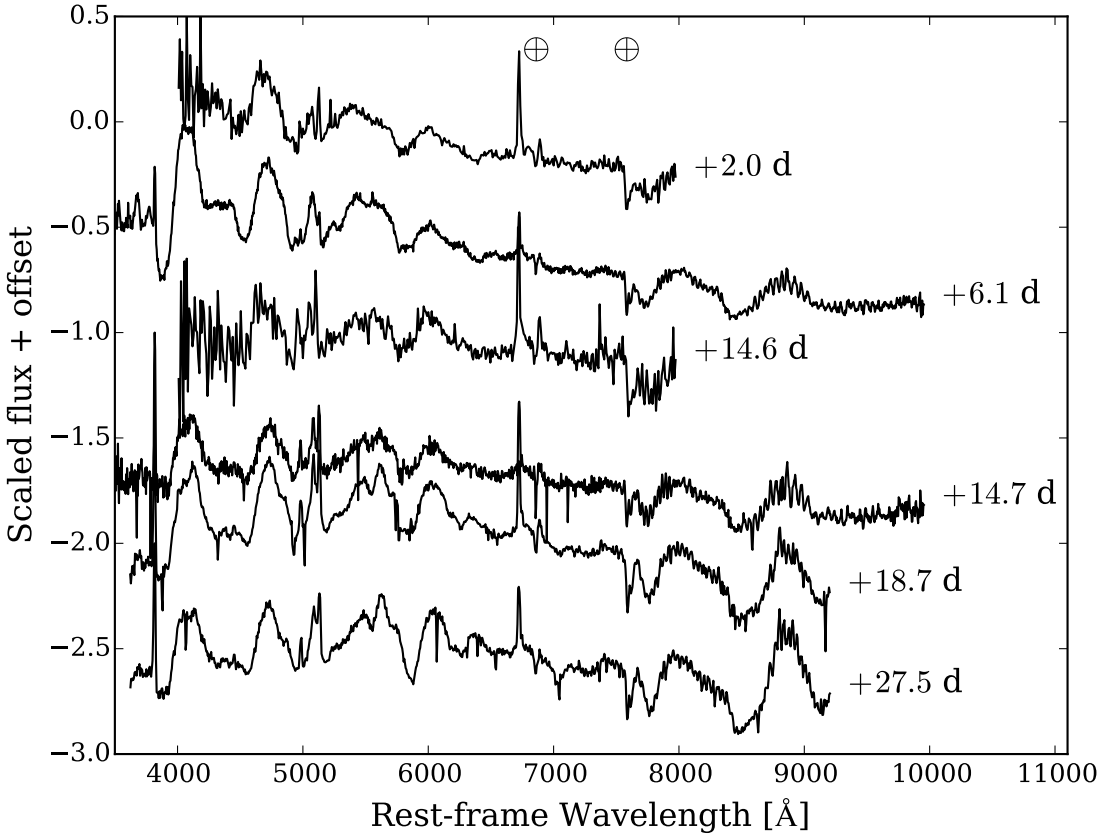

Figure E.13: The spectra of type Ib SN 2016frp.

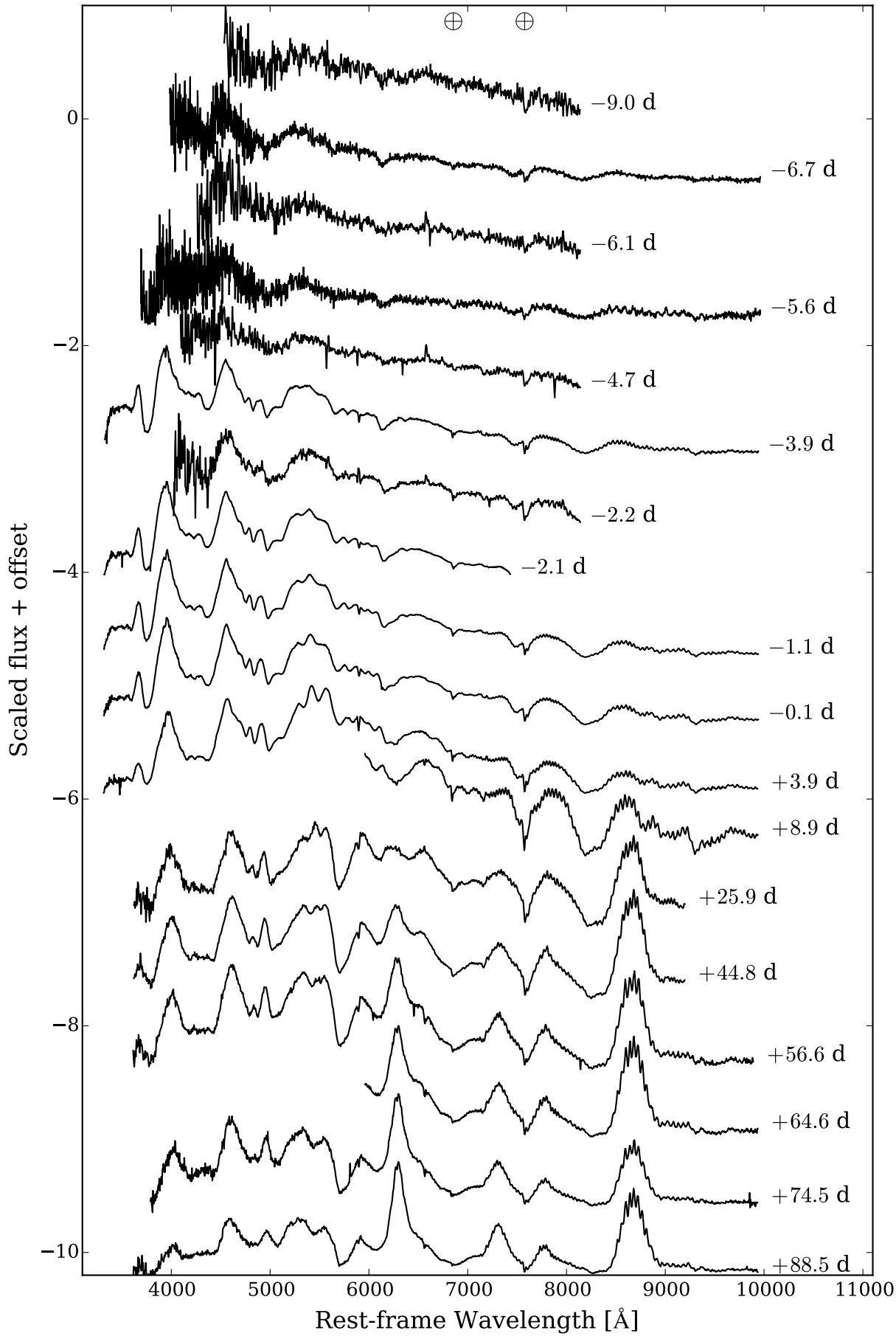

Figure E.14: The spectra of SN Ic-7 2016iae.

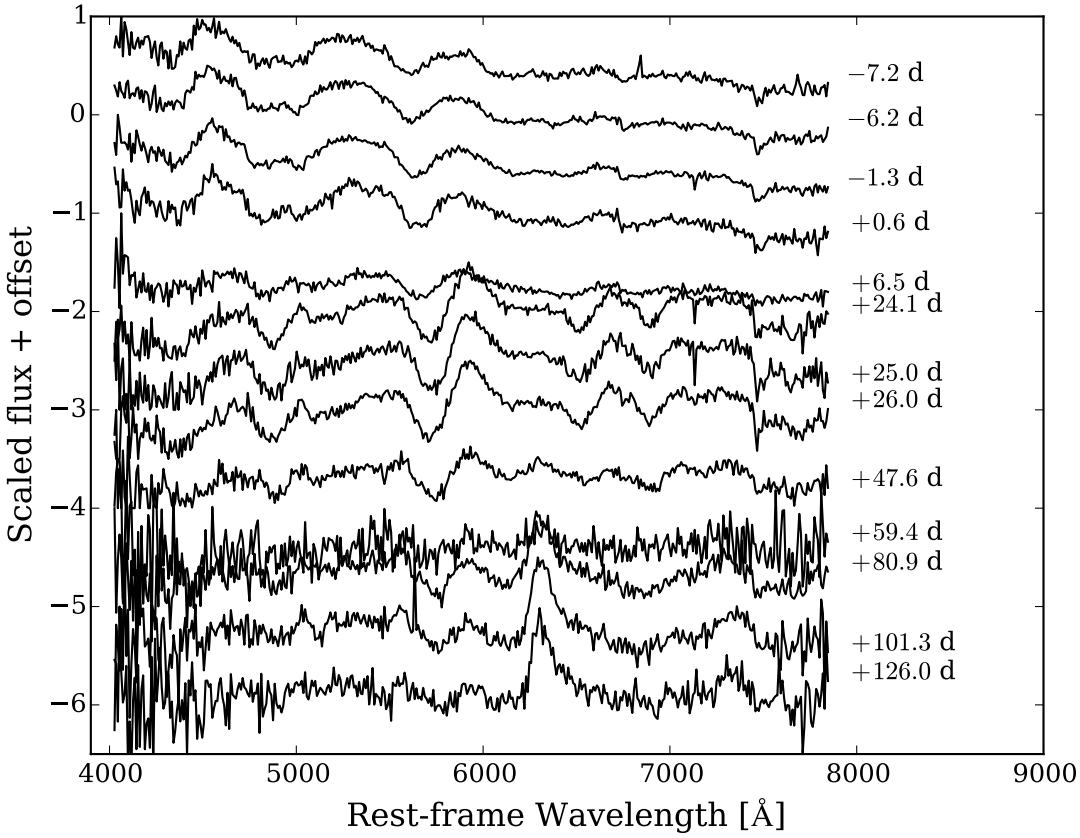

Figure E.15: The spectra of SN Ib 2016jdw.

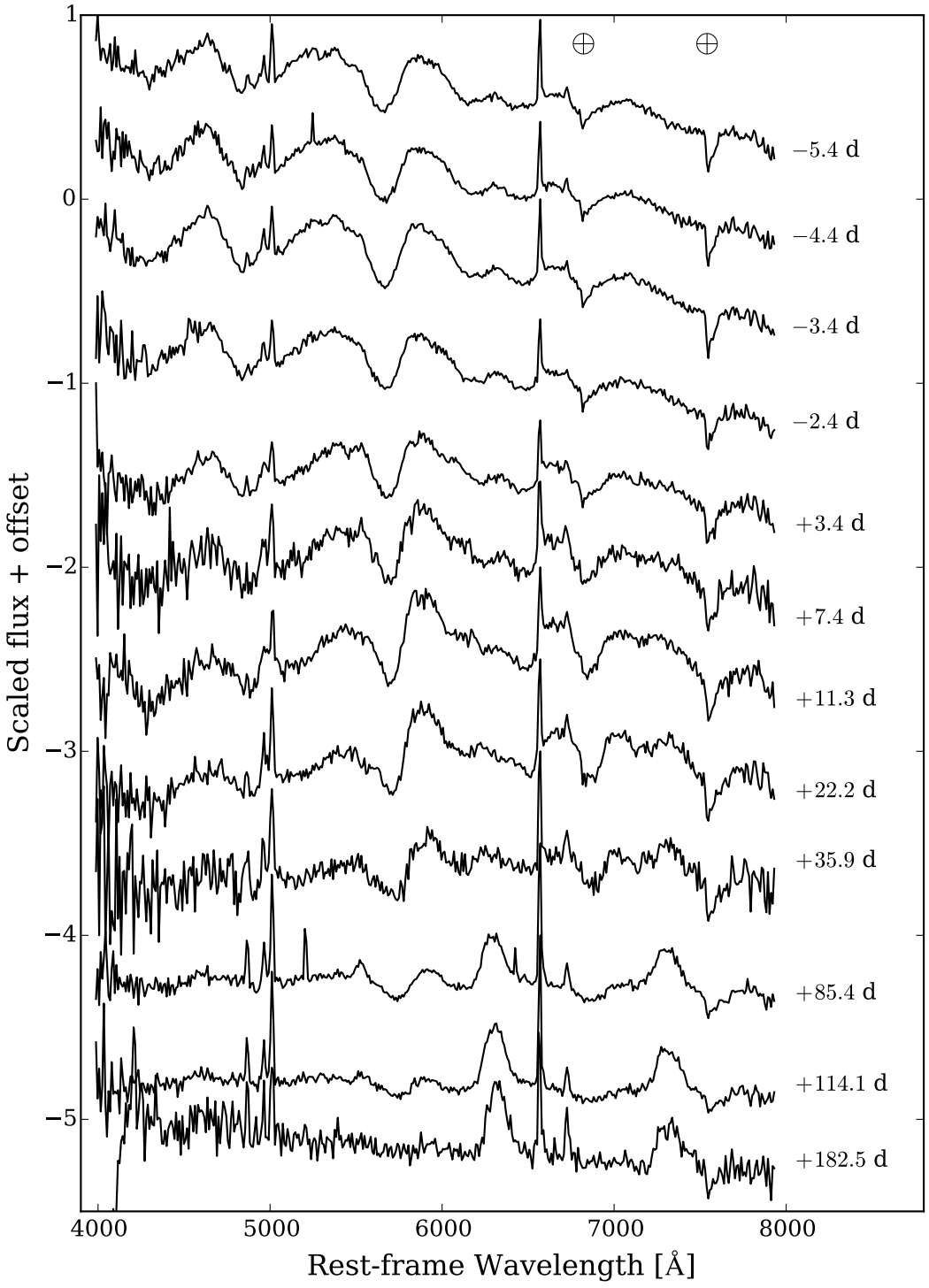

Figure E.16: The spectra of SN Ib 2017bgu.

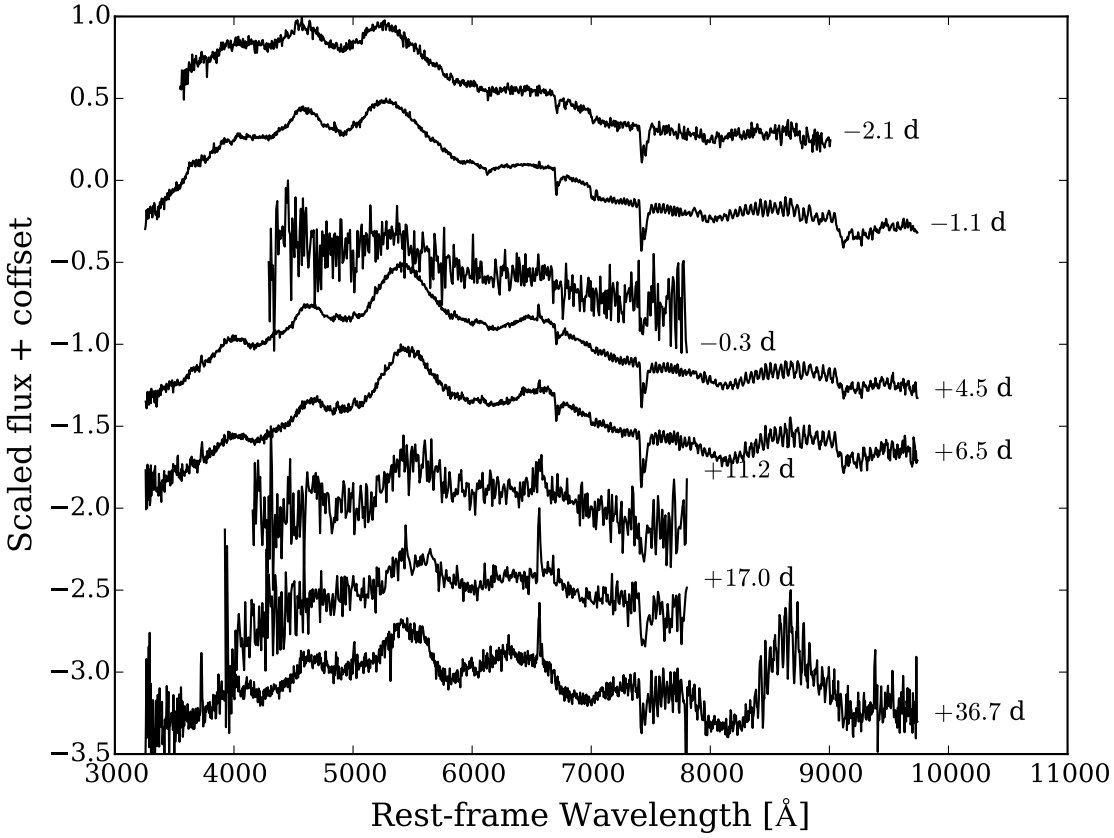

Figure E.17: The spectra of SN Ic-3 2017dcc.

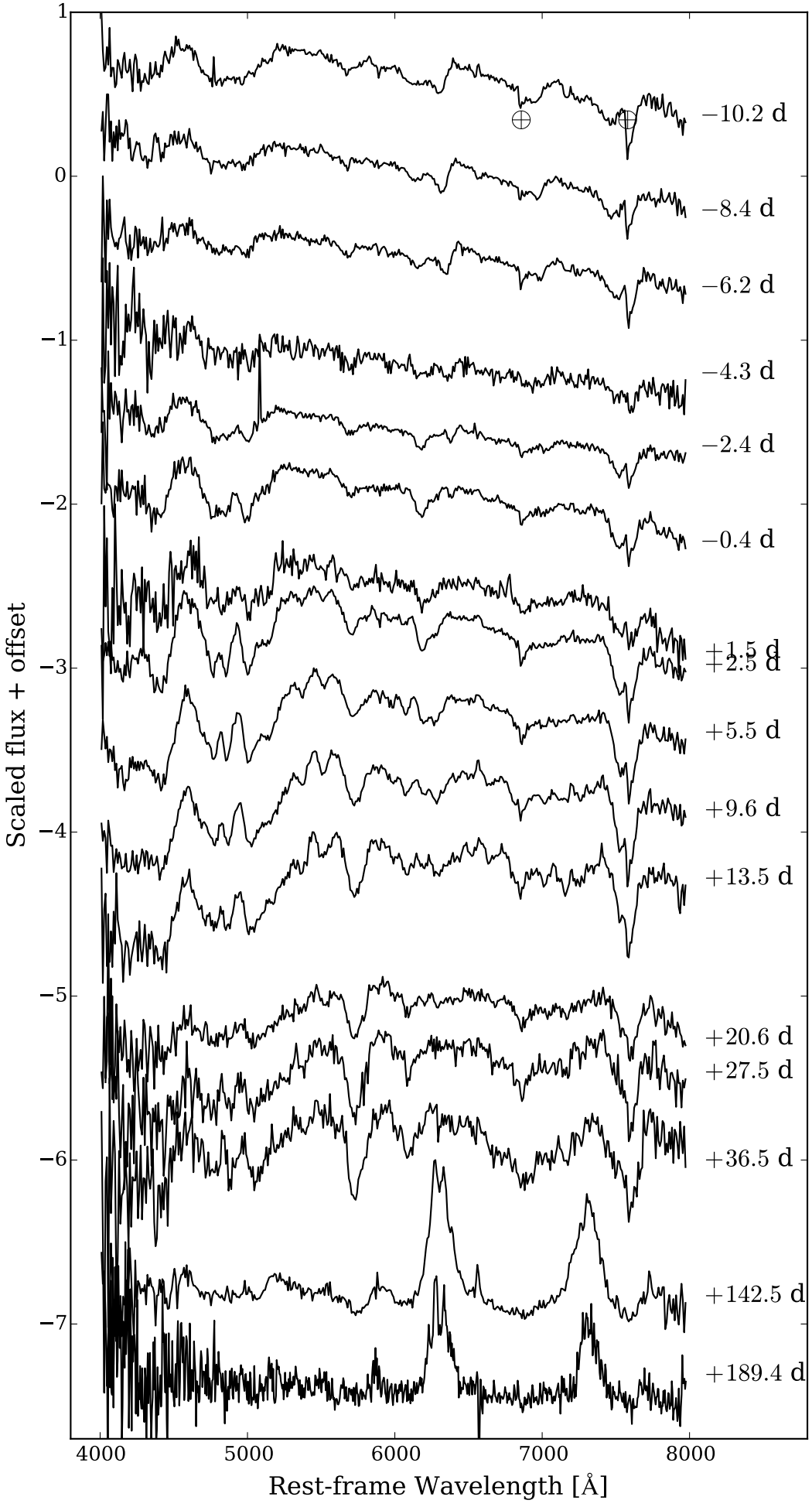

Figure E.18: The spectra of SN Ic-7 2017ein.

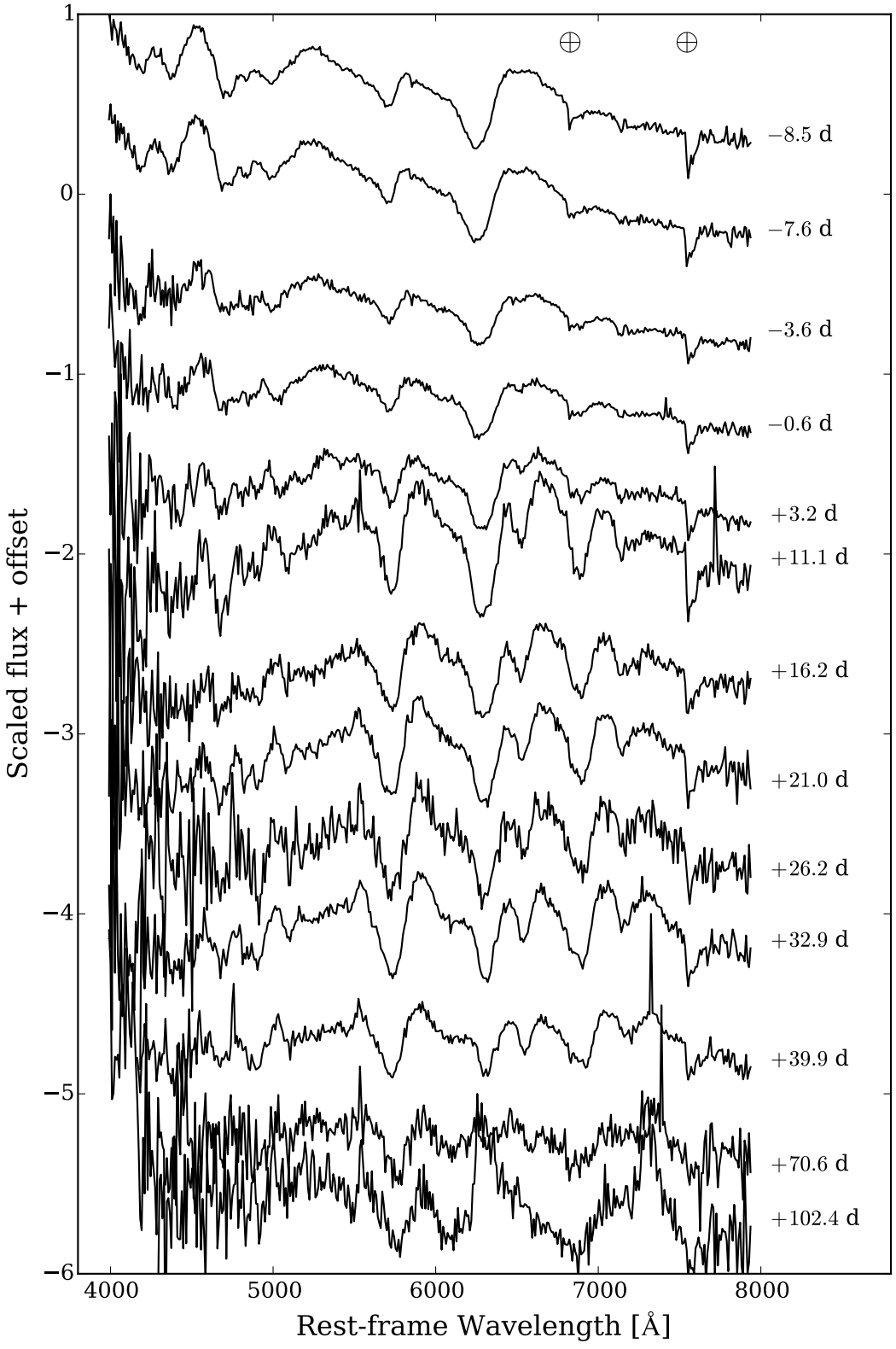

Figure E.19: The spectra of type IIb(I) SN 2017gpn.

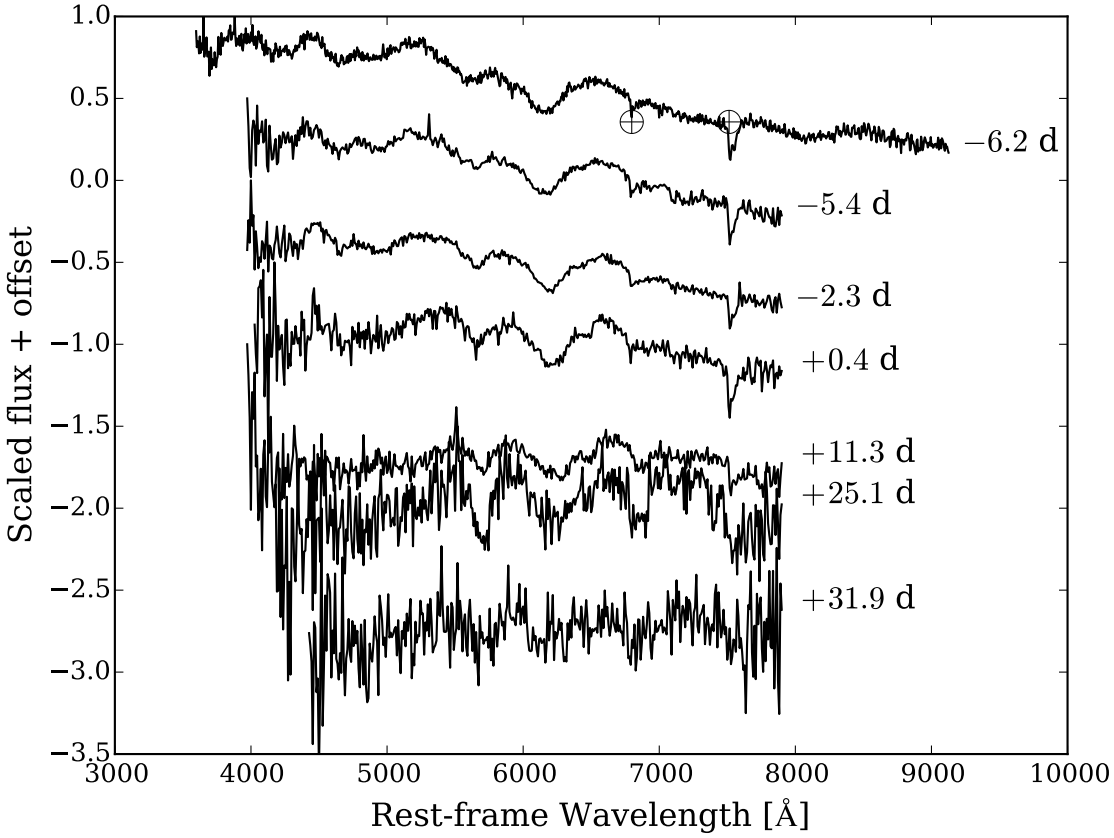

Figure E.20: The spectra of type IIb(I) SN 2017hyh.

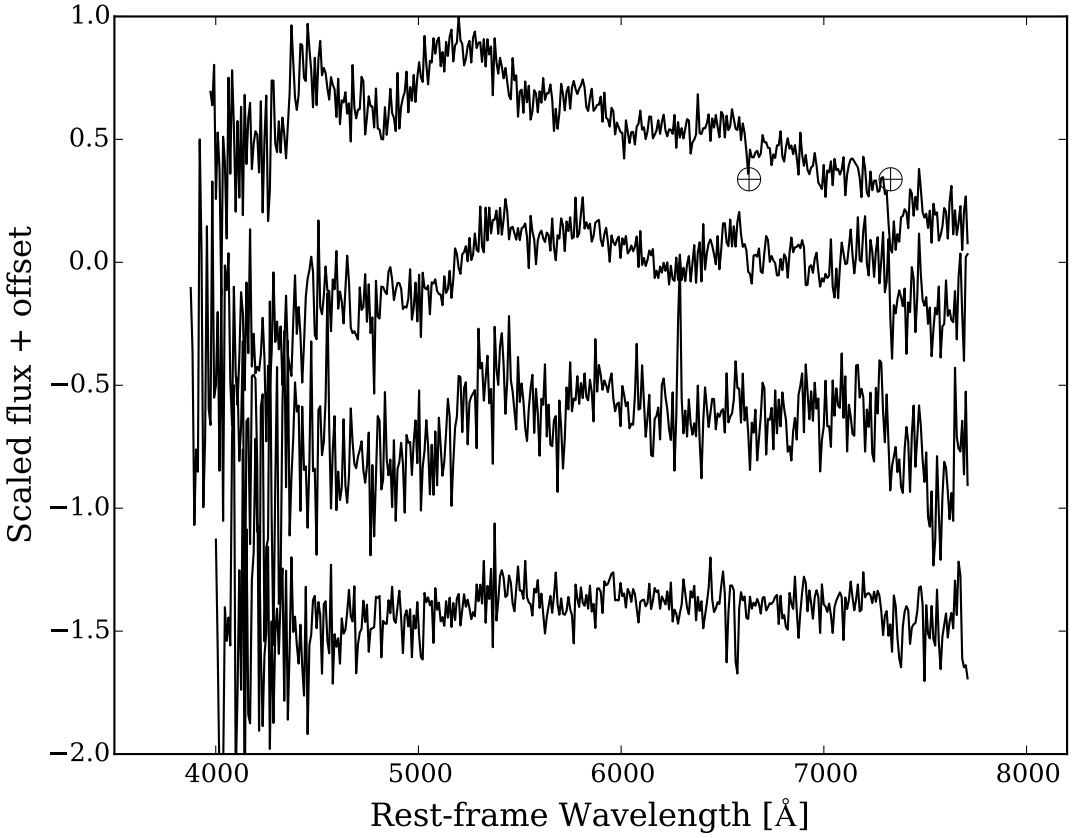

Figure E.21: The spectra of SN Ic-3 2017ifh.

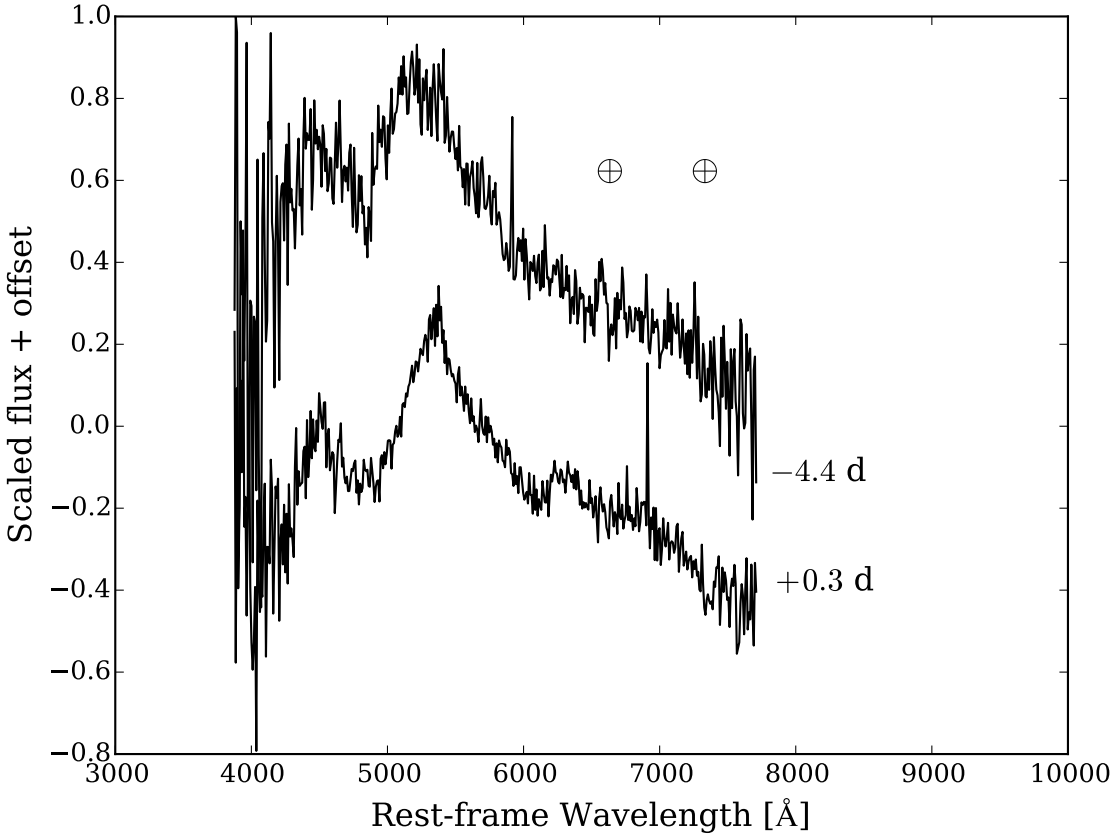

Figure E.22: The spectra of GRB-SN 2017iuk.

Bibliography

Abbott, B. P., R. Abbott, T. D. Abbott, M. R. Abernathy, F. Acernese, K. Ackley, C. Adams, T. Adams, P. Addesso, R. X. Adhikari, and et al.
2016. Observation of Gravitational Waves from a Binary Black Hole Merger. *Physical Review Letters*, 116(6):061102.

Aldering, G., R. M. Humphreys, and M. Richmond
1994. SN 1993J: The optical properties of its progenitor. *AJ*, 107:662–672.

Anderson, J. P., S. M. Habergham, P. A. James, and M. Hamuy
2012. Progenitor mass constraints for core-collapse supernovae from correlations with host galaxy star formation. *MNRAS*, 424:1372–1391.

Anupama, G. C., D. K. Sahu, J. Deng, K. Nomoto, N. Tominaga, M. Tanaka, P. A. Mazzali, and T. P. Prabhu
2005. The Peculiar Type Ib Supernova SN 2005bf: Explosion of a Massive He Star with a Thin Hydrogen Envelope? *ApJ*, 631:L125–L128.

Arcavi, I., A. Gal-Yam, M. M. Kasliwal, R. M. Quimby, E. O. Ofek, S. R. Kulkarni, P. E. Nugent, S. B. Cenko, J. S. Bloom, M. Sullivan, D. A. Howell, D. Poznanski, A. V. Filippenko, N. Law, I. Hook, J. Jönsson, S. Blake, J. Cooke, R. Dekany, G. Rahmer, D. Hale, R. Smith, J. Zolkower, V. Velur, R. Walters, J. Henning, K. Bui, D. McKenna, and J. Jacobsen
2010. Core-collapse Supernovae from the Palomar Transient Factory: Indications for a Different Population in Dwarf Galaxies. *ApJ*, 721:777–784.

Arcavi, I., A. Gal-Yam, O. Yaron, A. Sternberg, I. Rabinak, E. Waxman, M. M. Kasliwal, R. M. Quimby, E. O. Ofek, A. Horesh, S. R. Kulkarni, A. V. Filippenko, J. M. Silverman, S. B. Cenko, W. Li, J. S. Bloom, M. Sullivan, P. E. Nugent, D. Poznanski, E. Gorbikov, B. J. Fulton, D. A. Howell, D. Bersier, A. Riou, S. Lamotte-Bailey, T. Griga, J. G. Cohen, S. Hachinger, D. Polishook, D. Xu, S. Ben-Ami, I. Manulis, E. S. Walker, K. Maguire, Y.-C. Pan, T. Matheson, P. A. Mazzali, E. Pian, D. B. Fox, N. Gehrels, N. Law, P. James, J. M. Marchant, R. J. Smith, C. J. Mottram, R. M. Barnsley, M. T. Kandrashoff, and K. I. Clubb

2011. SN 2011dh: Discovery of a Type IIb Supernova from a Compact Progenitor in the Nearby Galaxy M51. *ApJ*, 742:L18.

Arcavi, I., D. A. Howell, D. Kasen, L. Bildsten, G. Hosseinzadeh, C. McCully, Z. C. Wong, S. R. Katz, A. Gal-Yam, J. Sollerman, F. Taddia, G. Leloudas, C. Fremling, P. E. Nugent, A. Horesh, K. Mooley, C. Rumsey, S. B. Cenko, M. L. Graham, D. A. Perley, E. Nakar, N. J. Shaviv, O. Bromberg, K. J. Shen, E. O. Ofek, Y. Cao, X. Wang, F. Huang, L. Rui, T. Zhang, W. Li, Z. Li, J. Zhang, S. Valenti, D. Guevel, B. Shappee, C. S. Kochanek, T. W.-S. Holoien, A. V. Filippenko, R. Fender, A. Nyholm, O. Yaron, M. M. Kasliwal, M. Sullivan, N. Blagorodnova, R. S. Walters, R. Lunnan, D. Khazov, I. Andreoni, R. R. Laher, N. Konidaris, P. Wozniak, and B. Bue

2017. Energetic eruptions leading to a peculiar hydrogen-rich explosion of a massive star. *Nature*, 551:210–213.

Arnett, W. D.

1982. Type I supernovae. I - Analytic solutions for the early part of the light curve. *ApJ*, 253:785–797.

Ashall, C., P. Mazzali, D. Bersier, S. Hachinger, M. Phillips, S. Percival, P. James, and K. Maguire

2014. Photometric and spectroscopic observations, and abundance tomography modelling of the Type Ia supernova SN 2014J located in M82. *MNRAS*, 445:4427–4437.

Ashall, C., E. Pian, P. A. Mazzali, E. Palazzi, S. J. Prentice, S. Kobayashi, A. Levan, D. Perley, F. Bufano, A. V. Filippenko, J. P. U. Fynbo, A. Melandri, P. DAvanzo, M. De Pasquale, S. Emery, A. S. Fruchter, K. Hurley, D. Malesani, P. Moller, K. Nomoto, M. Tanaka, N. Tanvir, and A. F. Valeev

2017. GRB 161219B-SN 2016jca: a powerful stellar collapse. *ArXiv e-prints*.

Asplund, M., N. Grevesse, A. J. Sauval, and P. Scott

2009. The Chemical Composition of the Sun. *ARA&A*, 47:481–522.

Balberg, S. and A. Loeb

2011. Supernova shock breakout through a wind. *MNRAS*, 414:1715–1720.

Barbon, R., S. Benetti, E. Cappellaro, F. Patat, M. Turatto, and T. Iijima

1995. SN 1993J in M 81: One year of observations at Asiago. *A&AS*, 110:513.

Barnes, J., P. C. Duffell, Y. Liu, M. Modjaz, F. B. Bianco, D. Kasen, and A. I. MacFadyen

2017. A GRB and Broad-lined Type Ic Supernova from a Single Central Engine. *ArXiv e-prints*.

Beasor, E. R. and B. Davies

2016. The evolution of red supergiants to supernova in NGC 2100. *MNRAS*, 463:1269–1283.

Ben-Ami, S., A. Gal-Yam, A. V. Filippenko, P. A. Mazzali, M. Modjaz, O. Yaron, I. Arcavi, S. B. Cenko, A. Horesh, D. A. Howell, M. L. Graham, J. C. Horst, M. Im, Y. Jeon, S. R. Kulkarni, D. C. Leonard, D. Perley, E. Pian, D. J. Sand, M. Sullivan, J. C. Becker, D. Bersier, J. S. Bloom, M. Bottom, P. J. Brown, K. I. Clubb, B. Dilday, R. C. Dixon, A. L. Fortinsky, D. B. Fox, L. A. Gonzalez, A. Harutyunyan, M. M. Kasliwal, W. Li, M. A. Malkan, I. Manulis, T. Matheson, N. A. Moskovitz, P. S. Muirhead, P. E. Nugent, E. O. Ofek, R. M. Quimby, J. W. Richards, N. R. Ross, K. J. Searcy, J. M. Silverman, N. Smith, A. Vanderburg, and E. S. Walker

2012. Discovery and Early Multi-wavelength Measurements of the Energetic Type

Ic Supernova PTF12gzk: A Massive-star Explosion in a Dwarf Host Galaxy. *ApJ*, 760:L33.

Ben-Ami, S., A. Gal-Yam, P. A. Mazzali, O. Gnat, M. Modjaz, I. Rabinak, M. Sullivan, L. Bildsten, D. Poznanski, O. Yaron, I. Arcavi, J. S. Bloom, A. Horesh, M. M. Kasliwal, S. R. Kulkarni, P. E. Nugent, E. O. Ofek, D. Perley, R. Quimby, and D. Xu
2014. SN 2010mb: Direct Evidence for a Supernova Interacting with a Large Amount of Hydrogen-free Circumstellar Material. *ApJ*, 785:37.

Benetti, S., M. Turatto, S. Valenti, A. Pastorello, E. Cappellaro, M. T. Botticella, F. Bufano, F. Ghinassi, A. Harutyunyan, C. Inserra, A. Magazzù, F. Patat, M. L. Pumo, and S. Taubenberger
2011. The Type Ib SN 1999dn: one year of photometric and spectroscopic monitoring. *MNRAS*, 411:2726–2738.

Benetti, S., L. Zampieri, A. Pastorello, E. Cappellaro, M. L. Pumo, N. Elias-Rosa, P. Ochner, G. Terreran, L. Tomasella, S. Taubenberger, M. Turatto, A. Morales-Garoffolo, A. Harutyunyan, and L. Tartaglia
2018. ASASSN-15no: The Supernova that plays hide-and-seek. *ArXiv e-prints*.

Bersten, M. C., O. G. Benvenuto, G. Folatelli, K. Nomoto, H. Kuncarayakti, S. Srivastav, G. C. Anupama, R. Quimby, and D. K. Sahu
2014. iPTF13bvn: The First Evidence of a Binary Progenitor for a Type Ib Supernova. *AJ*, 148:68.

Bersten, M. C., O. G. Benvenuto, K. Nomoto, M. Ergon, G. Folatelli, J. Sollerman, S. Benetti, M. T. Botticella, M. Fraser, R. Kotak, K. Maeda, P. Ochner, and L. Tomasella
2012. The Type IIb Supernova 2011dh from a Supergiant Progenitor. *ApJ*, 757:31.

Bessell, M. S., F. Castelli, and B. Plez
1998. Model atmospheres broad-band colors, bolometric corrections and temperature calibrations for O - M stars. *A&A*, 333:231–250.

Bethe, H. A. and J. R. Wilson

1985. Revival of a stalled supernova shock by neutrino heating. *ApJ*, 295:14–23.

Bianco, F. B., M. Modjaz, M. Hicken, A. Friedman, R. P. Kirshner, J. S. Bloom, P. Challis, G. H. Marion, W. M. Wood-Vasey, and A. Rest

2014. Multi-color Optical and Near-infrared Light Curves of 64 Stripped-envelope Core-Collapse Supernovae. *ApJS*, 213:19.

Bloom, J. S., D. A. Frail, S. R. Kulkarni, S. G. Djorgovski, J. P. Halpern, R. O. Marzke, D. R. Patton, J. B. Oke, K. D. Horne, R. Gomer, R. Goodrich, R. Campbell, G. H. Moriarty-Schieven, R. O. Redman, P. A. Feldman, E. Costa, and N. Masetti

1998. The Discovery and Broadband Follow-up of the Transient Afterglow of GRB 980703. *ApJ*, 508:L21–L24.

Branch, D., D. J. Jeffery, T. R. Young, and E. Baron

2006. Hydrogen in Type Ic Supernovae? *PASP*, 118:791–796.

Brown, T. M., N. Baliber, F. B. Bianco, M. Bowman, B. Burleson, P. Conway, M. Crellin, É. Depagne, J. De Vera, B. Dilday, D. Dragomir, M. Dubberley, J. D. Eastman, M. Elphick, M. Falarski, S. Foale, M. Ford, B. J. Fulton, J. Garza, E. L. Gomez, M. Graham, R. Greene, B. Haldeman, E. Hawkins, B. Haworth, R. Haynes, M. Hidas, A. E. Hjelstrom, D. A. Howell, J. Hygelund, T. A. Lister, R. Lobdill, J. Martinez, D. S. Mullins, M. Norbury, J. Parrent, R. Paulson, D. L. Petry, A. Pickles, V. Posner, W. E. Rosing, R. Ross, D. J. Sand, E. S. Saunders, J. Shobbrook, A. Shporer, R. A. Street, D. Thomas, Y. Tsapras, J. R. Tufts, S. Valenti, K. Vander Horst, Z. Walker, G. White, and M. Willis

2013. Las Cumbres Observatory Global Telescope Network. *PASP*, 125:1031.

Bufano, F., E. Pian, J. Sollerman, S. Benetti, G. Pignata, S. Valenti, S. Covino, P. D'Avanzo, and D. Malesani

2012. The Highly Energetic Expansion of SN 2010bh Associated with GRB 100316D. *ApJ*, 753:67.

Bufano, F., G. Pignata, M. Bersten, P. A. Mazzali, S. D. Ryder, R. Margutti, D. Milisavljevic, L. Morelli, S. Benetti, E. Cappellaro, S. Gonzalez-Gaitan, C. Romero-Cañizales, M. Stritzinger, E. S. Walker, J. P. Anderson, C. Contreras, T. de Jaeger, F. Förster, C. Gutierrez, M. Hamuy, E. Hsiao, N. Morrell, F. Olivares E., E. Paillas, S. Parker, E. Pian, T. E. Pickering, N. Sanders, C. Stockdale, M. Turatto, S. Valenti, R. A. Fesen, J. Maza, K. Nomoto, M. M. Phillips, and A. Soderberg

2014. SN 2011hs: a fast and faint Type IIb supernova from a supergiant progenitor. *MNRAS*, 439:1807–1828.

Buras, R., H.-T. Janka, M. Rampp, and K. Kifonidis

2006. Two-dimensional hydrodynamic core-collapse supernova simulations with spectral neutrino transport. II. Models for different progenitor stars. *A&A*, 457:281–308.

Cano, Z.

2013. A new method for estimating the bolometric properties of Ibc supernovae. *MNRAS*, 434:1098–1116.

Cano, Z., D. Bersier, C. Guidorzi, S. Kobayashi, A. J. Levan, N. R. Tanvir, K. Wiersema, P. D'Avanzo, A. S. Fruchter, P. Garnavich, A. Gomboc, J. Gorosabel, D. Kasen, D. Kopač, R. Margutti, P. A. Mazzali, A. Melandri, C. G. Mundell, P. E. Nugent, E. Pian, R. J. Smith, I. Steele, R. A. M. J. Wijers, and S. E. Woosley

2011. XRF 100316D/SN 2010bh and the Nature of Gamma-Ray Burst Supernovae. *ApJ*, 740:41.

Cano, Z., A. de Ugarte Postigo, A. Pozanenko, N. Butler, C. C. Thöne, C. Guidorzi, T. Krühler, J. Gorosabel, P. Jakobsson, G. Leloudas, D. Malesani, J. Hjorth, A. Melandri, C. Mundell, K. Wiersema, P. D'Avanzo, S. Schulze, A. Gomboc, A. Johansson, W. Zheng, D. A. Kann, F. Knust, K. Varela, C. W. Akerlof, J. Bloom, O. Burkhonov, E. Cooke, J. A. de Diego, G. Dhungana, C. Farina, F. V. Ferrante, H. A. Flewelling, O. D. Fox, J. Fynbo, N. Gehrels, L. Georgiev, J. J. González, J. Greiner, T. Güver, O. Hartoog, N. Hatch, M. Jelinek, R. Kehoe, S. Klose, E. Klunko, D. Kopač, A. Kutyrev, Y. Krugly, W. H. Lee, A. Levan, V. Linkov,

A. Matkin, N. Minikulov, I. Molotov, J. X. Prochaska, M. G. Richer, C. G. Román-Zúñiga, V. Rumyantsev, R. Sánchez-Ramírez, I. Steele, N. R. Tanvir, A. Volnova, A. M. Watson, D. Xu, and F. Yuan

2014. A trio of gamma-ray burst supernovae:. GRB 120729A, GRB 130215A/SN 2013ez, and GRB 130831A/SN 2013fu. *A&A*, 568:A19.

Cao, Y., M. M. Kasliwal, I. Arcavi, A. Horesh, P. Hancock, S. Valenti, S. B. Cenko, S. R. Kulkarni, A. Gal-Yam, E. Gorbikov, E. O. Ofek, D. Sand, O. Yaron, M. Graham, J. M. Silverman, J. C. Wheeler, G. H. Marion, E. S. Walker, P. Mazzali, D. A. Howell, K. L. Li, A. K. H. Kong, J. S. Bloom, P. E. Nugent, J. Surace, F. Masci, J. Carpenter, N. Degenaar, and C. R. Gelino

2013. Discovery, Progenitor and Early Evolution of a Stripped Envelope Supernova iPTF13bvn. *ApJ*, 775:L7.

Cardelli, J. A., G. C. Clayton, and J. S. Mathis

1989. The relationship between infrared, optical, and ultraviolet extinction. *ApJ*, 345:245–256.

Castor, J. I., D. C. Abbott, and R. I. Klein

1975. Radiation-driven winds in Of stars. *ApJ*, 195:157–174.

Chevalier, R. A. and C. Fransson

2006. Circumstellar Emission from Type Ib and Ic Supernovae. *ApJ*, 651:381–391.

Chevalier, R. A. and C. Fransson

2008. Shock Breakout Emission from a Type Ib/c Supernova: XRT 080109/SN 2008D. *ApJ*, 683:L135.

Chevalier, R. A. and A. M. Soderberg

2010. Type IIb Supernovae with Compact and Extended Progenitors. *ApJ*, 711:L40–L43.

Chornock, R., E. Berger, D. B. Fox, R. Lunnan, M. R. Drout, W.-f. Fong, T. Laskar, and K. C. Roth

2013. GRB 130606A as a Probe of the Intergalactic Medium and the Interstellar Medium in a Star-forming Galaxy in the First Gyr after the Big Bang. *ApJ*, 774:26.

Chornock, R., A. V. Filippenko, W. Li, G. H. Marion, R. J. Foley, M. Modjaz, M. Rafelski, G. D. Becker, W. H. de Vries, P. Garnavich, R. A. Jorgenson, D. K. Lynch, A. L. Malec, E. C. Moran, M. T. Murphy, R. J. Rudy, R. W. Russell, J. M. Silverman, T. N. Steele, A. Stockton, A. M. Wolfe, and C. E. Woodward

2011. The Transitional Stripped-envelope SN 2008ax: Spectral Evolution and Evidence for Large Asphericity. *ApJ*, 739:41.

Chugai, N. N.

1994. The oxygen mass in SN 1987A: Making use of fluctuations in the (O I) lambda lambda 6300, 6364 profile. *ApJ*, 428:L17–L19.

Chugai, N. N.

2000. Monte Carlo Simulations of Supernova Light Curves and the Hypernova SN1998bw. *Astronomy Letters*, 26:797–801.

Clocchiatti, A., N. B. Suntzeff, R. Covarrubias, and P. Candia

2011. The Ultimate Light Curve of SN 1998bw/GRB 980425. *AJ*, 141:163.

Clocchiatti, A. and J. C. Wheeler

1997. On the Light Curves of Stripped-Envelope Supernovae. *ApJ*, 491:375–380.

Colgate, S. A. and R. H. White

1966. The Hydrodynamic Behavior of Supernovae Explosions. *ApJ*, 143:626.

Corsi, A., A. Gal-Yam, S. R. Kulkarni, D. A. Frail, P. A. Mazzali, S. B. Cenko, M. M. Kasliwal, Y. Cao, A. Horesh, N. Palliyaguru, D. A. Perley, R. R. Laher, F. Taddia, G. Leloudas, K. Maguire, P. E. Nugent, J. Sollerman, and M. Sullivan

2016. Radio Observations of a Sample of Broad-line Type IC Supernovae Discovered by PTF/IPTF: A Search for Relativistic Explosions. *ApJ*, 830:42.

Corsi, A., E. O. Ofek, D. A. Frail, D. Poznanski, I. Arcavi, A. Gal-Yam, S. R. Kulkarni, K. Hurley, P. A. Mazzali, D. A. Howell, M. M. Kasliwal, Y. Green, D. Murray, M. Sullivan, D. Xu, S. Ben-ami, J. S. Bloom, S. B. Cenko, N. M. Law, P. Nugent, R. M. Quimby, V. Pal'shin, J. Cummings, V. Connaughton, K. Yamaoka, A. Rau, W. Boynton, I. Mitrofanov, and J. Goldsten

2011. PTF 10bzf (SN 2010ah): A Broad-line Ic Supernova Discovered by the Palomar Transient Factory. *ApJ*, 741:76.

Corsi, A., E. O. Ofek, A. Gal-Yam, D. A. Frail, S. R. Kulkarni, D. B. Fox, M. M. Kasliwal, M. Sullivan, A. Horesh, J. Carpenter, K. Maguire, I. Arcavi, S. B. Cenko, Y. Cao, K. Mooley, Y.-C. Pan, B. Sesar, A. Sternberg, D. Xu, D. Bersier, P. James, J. S. Bloom, and P. E. Nugent

2014. A Multi-wavelength Investigation of the Radio-loud Supernova PTF11qcj and its Circumstellar Environment. *ApJ*, 782:42.

Corsi, A., E. O. Ofek, A. Gal-Yam, D. A. Frail, D. Poznanski, P. A. Mazzali, S. R. Kulkarni, M. M. Kasliwal, I. Arcavi, and S. Ben-Ami

2012. Evidence for a Compact Wolf-Rayet Progenitor for the Type Ic Supernova PTF 10vgv. *ApJ*, 747:L5.

Crockett, R. M., J. J. Eldridge, S. J. Smartt, A. Pastorello, A. Gal-Yam, D. B. Fox, D. C. Leonard, M. M. Kasliwal, S. Mattila, J. R. Maund, A. W. Stephens, and I. J. Danziger

2008. The type IIb SN 2008ax: the nature of the progenitor. *MNRAS*, 391:L5–L9.

Crockett, R. M., S. J. Smartt, J. J. Eldridge, S. Mattila, D. R. Young, A. Pastorello, J. R. Maund, C. R. Benn, and I. Skillen

2007. A deeper search for the progenitor of the Type Ic supernova 2002ap. *MNRAS*, 381:835–850.

Crowther, P. A.

2013. On the association between core-collapse supernovae and H ii regions. *MNRAS*, 428:1927–1943.

D'Elia, V., E. Pian, A. Melandri, P. D'Avanzo, M. Della Valle, P. A. Mazzali, S. Piranomonte, G. Tagliaferri, L. A. Antonelli, F. Bufano, S. Covino, D. Fugazza, D. Malesani, P. Møller, and E. Palazzi

2015. SN 2013dx associated with GRB 130702A: a detailed photometric and spectroscopic monitoring and a study of the environment. *A&A*, 577:A116.

Deng, J., N. Tominaga, P. A. Mazzali, K. Maeda, and K. Nomoto

2005. On the Light Curve and Spectrum of SN 2003dh Separated from the Optical Afterglow of GRB 030329. *ApJ*, 624:898–905.

Deng, J. S., Y. L. Qiu, J. Y. Hu, K. Hatano, and D. Branch

2000. Spectrum Analysis of the Type IB Supernova SN 1999DN: Probable Identifications of C II and Hα. *ApJ*, 540:452–455.

Dessart, L., D. J. Hillier, R. Waldman, E. Livne, and S. Blondin

2012. Superluminous supernovae: ^{56}Ni power versus magnetar radiation. *MNRAS*, 426:L76–L80.

Dessart, L., D. John Hillier, S.-C. Yoon, R. Waldman, and E. Livne

2017. Radiative-transfer models for explosions from rotating and non-rotating single WC stars. Implications for SN 1998bw and LGRB/SNe. *A&A*, 603:A51.

Drout, M. R., D. Milisavljevic, J. Parrent, R. Margutti, A. Kamble, A. M. Soderberg, P. Challis, R. Chornock, W. Fong, and S. Frank

2015. The Double Peaked SN2013ge: a Type Ib/c SN with an Early Asymmetric Mass Ejection or an Extended Progenitor Envelope. *ArXiv e-prints*.

Drout, M. R., A. M. Soderberg, A. Gal-Yam, S. B. Cenko, D. B. Fox, D. C. Leonard, D. J. Sand, D.-S. Moon, I. Arcavi, and Y. Green

2011. The First Systematic Study of Type Ibc Supernova Multi-band Light Curves. *ApJ*, 741:97.

Eldridge, J. J., M. Fraser, S. J. Smartt, J. R. Maund, and R. M. Crockett

2013. The death of massive stars - II. Observational constraints on the progenitors of Type Ibc supernovae. *MNRAS*, 436:774–795.

Eldridge, J. J., R. G. Izzard, and C. A. Tout

2008. The effect of massive binaries on stellar populations and supernova progenitors. *MNRAS*, 384:1109–1118.

Eldridge, J. J. and J. R. Maund

2016. The disappearance of the helium-giant progenitor of the Type Ib supernova iPTF13bvn and constraints on its companion. *MNRAS*, 461:L117–L121.

Eldridge, J. J., E. R. Stanway, L. Xiao, L. A. S. McClelland, G. Taylor, M. Ng, S. M. L. Greis, and J. C. Bray

2017. Binary Population and Spectral Synthesis Version 2.1: Construction, Observational Verification, and New Results. *Publ. Astron. Soc. Australia*, 34:e058.

Elmhamdi, A., I. J. Danziger, D. Branch, B. Leibundgut, E. Baron, and R. P. Kirshner

2006. Hydrogen and helium traces in type Ib-c supernovae. *A&A*, 450:305–330.

Elmhamdi, A., I. J. Danziger, N. Chugai, A. Pastorello, M. Turatto, E. Cappellaro, G. Altavilla, S. Benetti, F. Patat, and M. Salvo

2003. Photometry and spectroscopy of the Type IIP SN 1999em from outburst to dust formation. *MNRAS*, 338:939–956.

Ensman, L. and A. Burrows

1992. Mass Loss and Type II Supernovae. In *American Astronomical Society Meeting Abstracts*, volume 24 of *Bulletin of the American Astronomical Society*, P. 1244.

Ergon, M., J. Sollerman, M. Fraser, A. Pastorello, S. Taubenberger, N. Elias-Rosa, M. Bersten, A. Jerkstrand, S. Benetti, M. T. Botticella, C. Fransson, A. Harutyunyan, R. Kotak, S. Smartt, S. Valenti, F. Bufano, E. Cappellaro, M. Fiaschi, A. Howell, E. Kankare, L. Magill, S. Mattila, J. Maund, R. Naves, P. Ochner, J. Ruiz, K. Smith, L. Tomasella, and M. Turatto

2014. Optical and near-infrared observations of SN 2011dh - The first 100 days. *A&A*, 562:A17.

Filippenko, A. V.

1997. Optical Spectra of Supernovae. *ARA&A*, 35:309–355.

Filippenko, A. V., A. J. Barth, T. Matheson, L. Armus, M. Brown, B. R. Espey, X.-M. Fan, R. W. Goodrich, L. C. Ho, V. T. Junkkarinen, D. C. Koo, M. D. Lehnert, A. R. Martel, J. M. Mazzarella, J. S. Miller, G. H. Smith, D. Tytler, and G. D. Wirth
1995. The Type IC Supernova 1994I in M51: Detection of Helium and Spectral Evolution. *ApJ*, 450:L11.

Filippenko, A. V., T. Matheson, and L. C. Ho
1993. The "Type IIb" Supernova 1993J in M81: A Close Relative of Type Ib Supernovae. *ApJ*, 415:L103.

Folatelli, G., M. C. Bersten, H. Kuncarayakti, O. G. Benvenuto, K. Maeda, and K. Nomoto
2015. The Progenitor of the Type IIb SN 2008ax Revisited. *ApJ*, 811:147.

Folatelli, G., M. C. Bersten, H. Kuncarayakti, F. Olivares Estay, J. P. Anderson, S. Holmbo, K. Maeda, N. Morrell, K. Nomoto, G. Pignata, M. Stritzinger, C. Contreras, F. Förster, M. Hamuy, M. M. Phillips, J. L. Prieto, S. Valenti, P. Afonso, K. Altenmüller, J. Elliott, J. Greiner, A. Updike, J. B. Haislip, A. P. LaCluyze, J. P. Moore, and D. E. Reichart
2014. Supernova 2010as: The Lowest-velocity Member of a Family of Flat-velocity Type IIb Supernovae. *ApJ*, 792:7.

Folatelli, G., C. Contreras, M. M. Phillips, S. E. Woosley, S. Blinnikov, N. Morrell, N. B. Suntzeff, B. L. Lee, M. Hamuy, S. González, W. Krzeminski, M. Roth, W. Li, A. V. Filippenko, R. J. Foley, W. L. Freedman, B. F. Madore, S. E. Persson, D. Murphy, S. Boissier, G. Galaz, L. González, P. J. McCarthy, A. McWilliam, and W. Pych
2006. SN 2005bf: A Possible Transition Event between Type Ib/c Supernovae and Gamma-Ray Bursts. *ApJ*, 641:1039–1050.

Foley, R. J., M. S. Papenkova, B. J. Swift, A. V. Filippenko, W. Li, P. A. Mazzali, R. Chornock, D. C. Leonard, and S. D. Van Dyk
2003. Optical Photometry and Spectroscopy of the SN 1998bw-like Type Ic Supernova 2002ap. *PASP*, 115:1220–1235.

Fox, O. D., K. Azalee Bostroem, S. D. Van Dyk, A. V. Filippenko, C. Fransson, T. Matheson, S. B. Cenko, P. Chandra, V. Dwarkadas, W. Li, A. H. Parker, and N. Smith

2014. Uncovering the Putative B-star Binary Companion of the SN 1993J Progenitor. *ApJ*, 790:17.

Fraser, M., M. Magee, R. Kotak, S. J. Smartt, K. W. Smith, J. Polshaw, A. J. Drake, T. Boles, C.-H. Lee, W. S. Burgett, K. C. Chambers, P. W. Draper, H. Flewelling, K. W. Hodapp, N. Kaiser, R.-P. Kudritzki, E. A. Magnier, P. A. Price, J. L. Tonry, R. J. Wainscoat, and C. Waters

2013. Detection of an Outburst One Year Prior to the Explosion of SN 2011ht. *ApJ*, 779:L8.

Fremling, C., J. Sollerman, F. Taddia, M. Ergon, M. Fraser, E. Karamehmetoglu, S. Valenti, A. Jerkstrand, I. Arcavi, F. Bufano, N. Elias Rosa, A. V. Filippenko, D. Fox, A. Gal-Yam, D. A. Howell, R. Kotak, P. Mazzali, D. Milisavljevic, P. E. Nugent, A. Nyholm, E. Pian, and S. Smartt

2016. PTF12os and iPTF13bvn. Two stripped-envelope supernovae from low-mass progenitors in NGC 5806. *A&A*, 593:A68.

Fremling, C., J. Sollerman, F. Taddia, M. Ergon, S. Valenti, I. Arcavi, S. Ben-Ami, Y. Cao, S. B. Cenko, A. V. Filippenko, A. Gal-Yam, and D. A. Howell

2014. The rise and fall of the Type Ib supernova iPTF13bvn. Not a massive Wolf-Rayet star. *A&A*, 565:A114.

Fukugita, M., K. Shimasaku, and T. Ichikawa

1995. Galaxy Colors in Various Photometric Band Systems. *PASP*, 107:945.

Gal-Yam, A.

2012. Luminous Supernovae. *Science*, 337:927.

Gal-Yam, A., I. Arcavi, E. O. Ofek, S. Ben-Ami, S. B. Cenko, M. M. Kasliwal, Y. Cao, O. Yaron, D. Tal, J. M. Silverman, and A. Horesh

2014. A Wolf-Rayet-like progenitor of SN 2013cu from spectral observations of a stellar wind. *Nature*, 509:471–474.

Gal-Yam, A., P. A. Mazzali, I. Manulis, and D. Bishop

2013a. Supernova Discoveries 2010–2011: Statistics and Trends. *PASP*, 125:749–752.

Gal-Yam, A., P. A. Mazzali, I. Manulis, and D. Bishop

2013b. Supernova Discoveries 2010-2011: Statistics and Trends. *PASP*, 125:749.

Gal-Yam, A., E. O. Ofek, and O. Shemmer

2002. Supernova 2002ap: the first month. *MNRAS*, 332:L73–L77.

Galama, T., P. J. Groot, J. Vanparadijs, C. Kouveliotou, C. R. Robinson, G. J. Fishman, C. A. Meegan, K. C. Sahu, M. Livio, L. Petro, F. D. Macchetto, J. Heise, J. Int Zand, R. G. Strom, J. Telting, R. G. M. Rutten, M. Pettini, N. Tanvir, and J. Bloom

1997. The Decay of Optical Emission from the gamma-Ray Burst GRB970228. *Nature*, 387:479.

Galama, T. J., P. M. Vreeswijk, J. van Paradijs, C. Kouveliotou, T. Augusteijn, H. Böhnhardt, J. P. Brewer, V. Doublier, J.-F. Gonzalez, B. Leibundgut, C. Lidman, O. R. Hainaut, F. Patat, J. Heise, J. in't Zand, K. Hurley, P. J. Groot, R. G. Strom, P. A. Mazzali, K. Iwamoto, K. Nomoto, H. Umeda, T. Nakamura, T. R. Young, T. Suzuki, T. Shigeyama, T. Koshut, M. Kippen, C. Robinson, P. de Wildt, R. A. M. J. Wijers, N. Tanvir, J. Greiner, E. Pian, E. Palazzi, F. Frontera, N. Masetti, L. Nicastro, M. Feroci, E. Costa, L. Piro, B. A. Peterson, C. Tinney, B. Boyle, R. Cannon, R. Stathakis, E. Sadler, M. C. Begam, and P. Ianna

1998. An unusual supernova in the error box of the γ-ray burst of 25 April 1998. *Nature*, 395:670–672.

Galbany, L., J. P. Anderson, S. F. Sánchez, H. Kuncarayakti, S. Pedraz, S. González-Gaitán, V. Stanishev, I. Domínguez, M. E. Moreno-Raya, W. M. Wood-Vasey, A. M.

Mourão, K. A. Ponder, C. Badenes, M. Mollá, A. R. López-Sánchez, F. F. Rosales-Ortega, J. M. Vílchez, R. García-Benito, and R. A. Marino

2018. PISCO: The Pmas/ppak Integral-field Supernova hosts COmpilation. *ArXiv e-prints*.

Galbany, L., V. Stanishev, A. M. Mourão, M. Rodrigues, H. Flores, C. J. Walcher, S. F. Sánchez, R. García-Benito, D. Mast, C. Badenes, R. M. González Delgado, C. Kehrig, M. Lyubenova, R. A. Marino, M. Mollá, S. Meidt, E. Pérez, G. van de Ven, and J. M. Vílchez

2016. Nearby supernova host galaxies from the CALIFA survey. II. Supernova environmental metallicity. *A&A*, 591:A48.

Georgy, C.

2012. Yellow supergiants as supernova progenitors: an indication of strong mass loss for red supergiants? *A&A*, 538:L8.

Georgy, C., S. Ekström, G. Meynet, P. Massey, E. M. Levesque, R. Hirschi, P. Eggenberger, and A. Maeder

2012. Grids of stellar models with rotation. II. WR populations and supernovae/GRB progenitors at Z = 0.014. *A&A*, 542:A29.

Georgy, C., G. Meynet, R. Walder, D. Folini, and A. Maeder

2009. The different progenitors of type Ib, Ic SNe, and of GRB. *A&A*, 502:611–622.

Graham, J. F. and A. S. Fruchter

2013. The Metal Aversion of Long-duration Gamma-Ray Bursts. *ApJ*, 774:119.

Graur, O., F. B. Bianco, S. Huang, M. Modjaz, I. Shivvers, A. V. Filippenko, W. Li, and J. J. Eldridge

2017a. LOSS Revisited. I. Unraveling Correlations Between Supernova Rates and Galaxy Properties, as Measured in a Reanalysis of the Lick Observatory Supernova Search. *ApJ*, 837:120.

Graur, O., F. B. Bianco, M. Modjaz, I. Shivvers, A. V. Filippenko, W. Li, and N. Smith
2017b. LOSS Revisited. II. The Relative Rates of Different Types of Supernovae Vary between Low- and High-mass Galaxies. *ApJ*, 837:121.

Greiner, J., P. A. Mazzali, D. A. Kann, T. Krühler, E. Pian, S. Prentice, F. Olivares E., A. Rossi, S. Klose, S. Taubenberger, F. Knust, P. M. J. Afonso, C. Ashall, J. Bolmer, C. Delvaux, R. Diehl, J. Elliott, R. Filgas, J. P. U. Fynbo, J. F. Graham, A. N. Guelbenzu, S. Kobayashi, G. Leloudas, S. Savaglio, P. Schady, S. Schmidl, T. Schweyer, V. Sudilovsky, M. Tanga, A. C. Updike, H. van Eerten, and K. Varela
2015. A very luminous magnetar-powered supernova associated with an ultra-long γ-ray burst. *Nature*, 523:189–192.

Groh, J. H., C. Georgy, and S. Ekström
2013. Progenitors of supernova Ibc: a single Wolf-Rayet star as the possible progenitor of the SN Ib iPTF13bvn. *A&A*, 558:L1.

Guillochon, J., J. Parrent, and R. Margutti
2016. An Open Catalog for Supernova Data. *ArXiv e-prints*.

Hachinger, S., P. A. Mazzali, S. Taubenberger, W. Hillebrandt, K. Nomoto, and D. N. Sauer
2012. How much H and He is 'hidden' in SNe Ib/c? - I. Low-mass objects. *MNRAS*, 422:70–88.

Hamuy, M., J. Deng, P. A. Mazzali, N. I. Morrell, M. M. Phillips, M. Roth, S. Gonzalez, J. Thomas-Osip, W. Krzeminski, C. Contreras, J. Maza, L. González, L. Huerta, G. Folatelli, R. Chornock, A. V. Filippenko, S. E. Persson, W. L. Freedman, K. Koviak, N. B. Suntzeff, and K. Krisciunas
2009. Supernova 2003bg: The First Type IIb Hypernova. *ApJ*, 703:1612–1623.

Hamuy, M., J. Maza, P. A. Pinto, M. M. Phillips, N. B. Suntzeff, R. D. Blum, K. A. G. Olsen, D. J. Pinfield, V. D. Ivanov, T. Augusteijn, S. Brillant, M. Chadid, J.-G. Cuby, V. Doublier, O. R. Hainaut, E. Le Floc'h, C. Lidman, M. G. Petr-Gotzens, E. Pom-

pei, and L. Vanzi

2002. Optical and Infrared Spectroscopy of SN 1999ee and SN 1999ex. *AJ*, 124:417–429.

Harutyunyan, A. H., P. Pfahler, A. Pastorello, S. Taubenberger, M. Turatto, E. Cappellaro, S. Benetti, N. Elias-Rosa, H. Navasardyan, S. Valenti, V. Stanishev, F. Patat, M. Riello, G. Pignata, and W. Hillebrandt

2008. ESC supernova spectroscopy of non-ESC targets. *A&A*, 488:383–399.

Horesh, A., S. R. Kulkarni, A. Corsi, D. A. Frail, S. B. Cenko, S. Ben-Ami, A. Gal-Yam, O. Yaron, I. Arcavi, M. M. Kasliwal, and E. O. Ofek

2013. PTF 12gzk – A Rapidly Declining, High-velocity Type Ic Radio Supernova. *ApJ*, 778:63.

Houck, J. C. and C. Fransson

1996. Analysis of the Late Optical Spectra of SN 1993J. *ApJ*, 456:811.

Hunter, D. J., S. Valenti, R. Kotak, W. P. S. Meikle, S. Taubenberger, A. Pastorello, S. Benetti, V. Stanishev, S. J. Smartt, C. Trundle, A. A. Arkharov, F. Bufano, E. Cappellaro, E. Di Carlo, M. Dolci, N. Elias-Rosa, S. Frandsen, J. U. Fynbo, U. Hopp, V. M. Larionov, P. Laursen, P. Mazzali, H. Navasardyan, C. Ries, A. Riffeser, L. Rizzi, D. Y. Tsvetkov, M. Turatto, and S. Wilke

2009. Extensive optical and near-infrared observations of the nearby, narrow-lined type Ic SN 2007gr: days 5 to 415. *A&A*, 508:371–389.

Inserra, C., S. J. Smartt, A. Jerkstrand, S. Valenti, M. Fraser, D. Wright, K. Smith, T.-W. Chen, R. Kotak, A. Pastorello, M. Nicholl, F. Bresolin, R. P. Kudritzki, S. Benetti, M. T. Botticella, W. S. Burgett, K. C. Chambers, M. Ergon, H. Flewelling, J. P. U. Fynbo, S. Geier, K. W. Hodapp, D. A. Howell, M. Huber, N. Kaiser, G. Leloudas, L. Magill, E. A. Magnier, M. G. McCrum, N. Metcalfe, P. A. Price, A. Rest, J. Sollerman, W. Sweeney, F. Taddia, S. Taubenberger, J. L. Tonry, R. J. Wainscoat, C. Waters, and D. Young

2013. Super-luminous Type Ic Supernovae: Catching a Magnetar by the Tail. *ApJ*, 770:128.

Iwamoto, K., P. A. Mazzali, K. Nomoto, H. Umeda, T. Nakamura, F. Patat, I. J. Danziger, T. R. Young, T. Suzuki, T. Shigeyama, and T. Augusteijn
1998. A hypernova model for the supernova associated with the γ-ray burst of 25 April 1998. *Nature*, 395:672–674.

Iwamoto, K., T. Nakamura, K. Nomoto, P. A. Mazzali, I. J. Danziger, P. Garnavich, R. Kirshner, S. Jha, D. Balam, and J. Thorstensen
2000. The Peculiar Type IC Supernova 1997EF: Another Hypernova. *ApJ*, 534:660–669.

Iwamoto, K., K. Nomoto, P. Höflich, H. Yamaoka, S. Kumagai, and T. Shigeyama
1994. Theoretical light curves for the type IC supernova SN 1994I. *ApJ*, 437:L115–L118.

Janka, H.-T.
2012. Explosion Mechanisms of Core-Collapse Supernovae. *Annual Review of Nuclear and Particle Science*, 62:407–451.

Janka, H.-T.
2017. Neutrino-driven Explosions. *ArXiv e-prints*.

Janka, H.-T., M.-A. Aloy, P. A. Mazzali, and E. Pian
2006. Off-Axis Properties of Short Gamma-Ray Bursts. *ApJ*, 645:1305–1314.

Janka, H.-T., K. Langanke, A. Marek, G. Martínez-Pinedo, and B. Müller
2007. Theory of core-collapse supernovae. *Phys. Rep.*, 442:38–74.

Janka, H.-T., T. Melson, and A. Summa
2016. Physics of Core-Collapse Supernovae in Three Dimensions: A Sneak Preview. *Annual Review of Nuclear and Particle Science*, 66:341–375.

Jerkstrand, A., M. Ergon, S. J. Smartt, C. Fransson, J. Sollerman, S. Taubenberger, M. Bersten, and J. Spyromilio
2015. Late-time spectral line formation in Type IIb supernovae, with application to SN 1993J, SN 2008ax, and SN 2011dh. *A&A*, 573:A12.

Jordi, K., E. K. Grebel, and K. Ammon

2006. Empirical color transformations between SDSS photometry and other photometric systems. *A&A*, 460:339–347.

Kasen, D., B. D. Metzger, and L. Bildsten

2016. Magnetar-driven Shock Breakout and Double-peaked Supernova Light Curves. *ApJ*, 821:36.

Kilpatrick, C. D., R. J. Foley, L. E. Abramson, Y.-C. Pan, C.-X. Lu, P. Williams, T. Treu, M. R. Siebert, C. D. Fassnacht, and C. E. Max

2017. On the progenitor of the Type IIb supernova 2016gkg. *MNRAS*, 465:4650–4657.

Kocevski, D., M. Modjaz, J. S. Bloom, R. Foley, D. Starr, C. H. Blake, E. E. Falco, N. R. Butler, M. Skrutskie, and A. Szentgyorgyi

2007. Multicolor Infrared Observations of SN 2006aj. I. The Supernova Associated with XRF 060218. *ApJ*, 663:1180–1186.

Kochanek, C. S.

2018. Cas A and the Crab were not stellar binaries at death. *MNRAS*, 473:1633–1643.

Krause, O., S. M. Birkmann, T. Usuda, T. Hattori, M. Goto, G. H. Rieke, and K. A. Misselt

2008. The Cassiopeia A Supernova Was of Type IIb. *Science*, 320:1195.

Kumar, B., S. B. Pandey, D. K. Sahu, J. Vinko, A. S. Moskvitin, G. C. Anupama, V. K. Bhatt, A. Ordasi, A. Nagy, V. V. Sokolov, T. N. Sokolova, V. N. Komarova, B. Kumar, S. Bose, R. Roy, and R. Sagar

2013. Light curve and spectral evolution of the Type IIb supernova 2011fu. *MNRAS*, 431:308–321.

Kuncarayakti, H., J. P. Anderson, L. Galbany, K. Maeda, M. Hamuy, G. Aldering, N. Arimoto, M. Doi, T. Morokuma, and T. Usuda

2017. Constraints on core-collapse supernova progenitors from explosion site integral field spectroscopy. *ArXiv e-prints*.

Law, N. M., S. R. Kulkarni, R. G. Dekany, E. O. Ofek, R. M. Quimby, P. E. Nugent, J. Surace, C. C. Grillmair, and J. S. Bloom

2009. The Palomar Transient Factory: System Overview, Performance, and First Results. *PASP*, 121:1395–1408.

Lazzati, D., B. J. Morsony, C. H. Blackwell, and M. C. Begelman

2012. Unifying the Zoo of Jet-driven Stellar Explosions. *ApJ*, 750:68.

Lennarz, D., D. Altmann, and C. Wiebusch

2012. A unified supernova catalogue. *A&A*, 538:A120.

Li, W., J. Leaman, R. Chornock, A. V. Filippenko, D. Poznanski, M. Ganeshalingam, X. Wang, M. Modjaz, S. Jha, R. J. Foley, and N. Smith

2011. Nearby supernova rates from the Lick Observatory Supernova Search - II. The observed luminosity functions and fractions of supernovae in a complete sample. *MNRAS*, 412:1441–1472.

Lipkin, Y. M., E. O. Ofek, A. Gal-Yam, E. M. Leibowitz, D. Poznanski, S. Kaspi, D. Polishook, S. R. Kulkarni, D. W. Fox, E. Berger, N. Mirabal, J. Halpern, M. Bureau, K. Fathi, P. A. Price, B. A. Peterson, A. Frebel, B. Schmidt, J. A. Orosz, J. B. Fitzgerald, J. S. Bloom, P. G. van Dokkum, C. D. Bailyn, M. M. Buxton, and M. Barsony

2004. The Detailed Optical Light Curve of GRB 030329. *ApJ*, 606:381–394.

Liu, Y.-Q., M. Modjaz, F. B. Bianco, and O. Graur

2016. Analyzing the Largest Spectroscopic Data Set of Stripped Supernovae to Improve Their Identifications and Constrain Their Progenitors. *ApJ*, 827:90.

Lucy, L. B.

1991. Nonthermal excitation of helium in type Ib supernovae. *ApJ*, 383:308–313.

Lyman, J. D., D. Bersier, and P. A. James

2014. Bolometric corrections for optical light curves of core-collapse supernovae. *MNRAS*, 437:3848–3862.

Lyman, J. D., D. Bersier, P. A. James, P. A. Mazzali, J. J. Eldridge, M. Fraser, and E. Pian

2016. Bolometric light curves and explosion parameters of 38 stripped-envelope core-collapse supernovae. *MNRAS*, 457:328–350.

Maeda, K., T. Hattori, D. Milisavljevic, G. Folatelli, M. R. Drout, H. Kuncarayakti, R. Margutti, A. Kamble, A. Soderberg, M. Tanaka, M. Kawabata, K. S. Kawabata, M. Yamanaka, K. Nomoto, J. H. Kim, J. D. Simon, M. M. Phillips, J. Parrent, T. Nakaoka, T. J. Moriya, A. Suzuki, K. Takaki, M. Ishigaki, I. Sakon, A. Tajitsu, and M. Iye

2015. Type IIb Supernova 2013df Entering into an Interaction Phase: A Link between the Progenitor and the Mass Loss. *ApJ*, 807:35.

Maeda, K., K. Kawabata, P. A. Mazzali, M. Tanaka, S. Valenti, K. Nomoto, T. Hattori, J. Deng, E. Pian, S. Taubenberger, M. Iye, T. Matheson, A. V. Filippenko, K. Aoki, G. Kosugi, Y. Ohyama, T. Sasaki, and T. Takata

2008. Asphericity in Supernova Explosions from Late-Time Spectroscopy. *Science*, 319:1220.

Maeda, K., M. Tanaka, K. Nomoto, N. Tominaga, K. Kawabata, P. A. Mazzali, H. Umeda, T. Suzuki, and T. Hattori

2007. The Unique Type Ib Supernova 2005bf at Nebular Phases: A Possible Birth Event of a Strongly Magnetized Neutron Star. *ApJ*, 666:1069–1082.

Malesani, D., J. P. U. Fynbo, J. Hjorth, G. Leloudas, J. Sollerman, M. D. Stritzinger, P. M. Vreeswijk, D. J. Watson, J. Gorosabel, M. J. Michałowski, C. C. Thöne, T. Augusteijn, D. Bersier, P. Jakobsson, A. O. Jaunsen, C. Ledoux, A. J. Levan, B. Milvang-Jensen, E. Rol, N. R. Tanvir, K. Wiersema, D. Xu, L. Albert, M. Bayliss, C. Gall, L. F. Grove, B. P. Koester, E. Leitet, T. Pursimo, and I. Skillen

2009. Early Spectroscopic Identification of SN 2008D. *ApJ*, 692:L84–L87.

Margutti, R., A. Kamble, D. Milisavljevic, E. Zapartas, S. E. de Mink, M. Drout, R. Chornock, G. Risaliti, B. A. Zauderer, M. Bietenholz, M. Cantiello, S. Chakraborti, L. Chomiuk, W. Fong, B. Grefenstette, C. Guidorzi, R. Kirshner, J. T. Parrent, D. Patnaude, A. M. Soderberg, N. C. Gehrels, and F. Harrison

2017. Ejection of the Massive Hydrogen-rich Envelope Timed with the Collapse of the Stripped SN 2014C. *ApJ*, 835:140.

Margutti, R., D. Milisavljevic, A. M. Soderberg, R. Chornock, B. A. Zauderer, K. Murase, C. Guidorzi, N. E. Sanders, P. Kuin, C. Fransson, E. M. Levesque, P. Chandra, E. Berger, F. B. Bianco, P. J. Brown, P. Challis, E. Chatzopoulos, C. C. Cheung, C. Choi, L. Chomiuk, N. Chugai, C. Contreras, M. R. Drout, R. Fesen, R. J. Foley, W. Fong, A. S. Friedman, C. Gall, N. Gehrels, J. Hjorth, E. Hsiao, R. Kirshner, M. Im, G. Leloudas, R. Lunnan, G. H. Marion, J. Martin, N. Morrell, K. F. Neugent, N. Omodei, M. M. Phillips, A. Rest, J. M. Silverman, J. Strader, M. D. Stritzinger, T. Szalai, N. B. Utterback, J. Vinko, J. C. Wheeler, D. Arnett, S. Campana, R. Chevalier, A. Ginsburg, A. Kamble, P. W. A. Roming, T. Pritchard, and G. Stringfellow

2014a. A Panchromatic View of the Restless SN 2009ip Reveals the Explosive Ejection of a Massive Star Envelope. *ApJ*, 780:21.

Margutti, R., D. Milisavljevic, A. M. Soderberg, C. Guidorzi, B. J. Morsony, N. Sanders, S. Chakraborti, A. Ray, A. Kamble, M. Drout, J. Parrent, A. Zauderer, and L. Chomiuk

2014b. Relativistic Supernovae have Shorter-lived Central Engines or More Extended Progenitors: The Case of SN 2012ap. *ApJ*, 797:107.

Marion, G. H., J. Vinko, R. P. Kirshner, R. J. Foley, P. Berlind, A. Bieryla, J. S. Bloom, M. L. Calkins, P. Challis, R. A. Chevalier, R. Chornock, C. Culliton, J. L. Curtis, G. A. Esquerdo, M. E. Everett, E. E. Falco, K. France, C. Fransson, A. S. Friedman, P. Garnavich, B. Leibundgut, S. Meyer, N. Smith, A. M. Soderberg, J. Sollerman, D. L. Starr, T. Szklenar, K. Takats, and J. C. Wheeler

2014. Type IIb Supernova SN 2011dh: Spectra and Photometry from the Ultraviolet to the Near-infrared. *ApJ*, 781:69.

Matheson, T., A. V. Filippenko, A. J. Barth, L. C. Ho, D. C. Leonard, M. A. Bershady, M. Davis, D. S. Finley, D. Fisher, R. A. González, S. L. Hawley, D. C. Koo, W. Li, C. J. Lonsdale, D. Schlegel, H. E. Smith, H. Spinrad, and G. D. Wirth
2000a. Optical Spectroscopy of Supernova 1993J During Its First 2500 Days. *AJ*, 120:1487–1498.

Matheson, T., A. V. Filippenko, L. C. Ho, A. J. Barth, and D. C. Leonard
2000b. Detailed Analysis of Early to Late-Time Spectra of Supernova 1993J. *AJ*, 120:1499–1515.

Matheson, T., A. V. Filippenko, W. Li, D. C. Leonard, and J. C. Shields
2001. Optical Spectroscopy of Type IB/C Supernovae. *AJ*, 121:1648–1675.

Matheson, T., P. M. Garnavich, K. Z. Stanek, D. Bersier, S. T. Holland, K. Krisciunas, N. Caldwell, P. Berlind, J. S. Bloom, M. Bolte, A. Z. Bonanos, M. J. I. Brown, W. R. Brown, M. L. Calkins, P. Challis, R. Chornock, L. Echevarria, D. J. Eisenstein, M. E. Everett, A. V. Filippenko, K. Flint, R. J. Foley, D. L. Freedman, M. Hamuy, P. Harding, N. P. Hathi, M. Hicken, C. Hoopes, C. Impey, B. T. Jannuzi, R. A. Jansen, S. Jha, J. Kaluzny, S. Kannappan, R. P. Kirshner, D. W. Latham, J. C. Lee, D. C. Leonard, W. Li, K. L. Luhman, P. Martini, H. Mathis, J. Maza, S. T. Megeath, L. R. Miller, D. Minniti, E. W. Olszewski, M. Papenkova, M. M. Phillips, B. Pindor, D. D. Sasselov, R. Schild, H. Schweiker, T. Spahr, J. Thomas-Osip, I. Thompson, D. Weisz, R. Windhorst, and D. Zaritsky
2003. Photometry and Spectroscopy of GRB 030329 and Its Associated Supernova 2003dh: The First Two Months. *ApJ*, 599:394–407.

Matzner, C. D. and C. F. McKee
1999. The Expulsion of Stellar Envelopes in Core-Collapse Supernovae. *ApJ*, 510:379–403.

Mauerhan, J. C., G. G. Williams, D. C. Leonard, P. S. Smith, A. V. Filippenko, N. Smith, J. L. Hoffman, L. Huk, K. I. Clubb, J. M. Silverman, S. B. Cenko, P. Milne,

A. Gal-Yam, and S. Ben-Ami

2015. Spectropolarimetry of SN 2011dh in M51: geometric insights on a Type IIb supernova progenitor and explosion. *MNRAS*, 453:4467–4484.

Maund, J. R.

2018. The very young resolved stellar populations around stripped-envelope supernovae. *MNRAS*.

Maund, J. R., I. Arcavi, M. Ergon, J. J. Eldridge, C. Georgy, S. B. Cenko, A. Horesh, R. G. Izzard, and R. J. Stancliffe

2015. Did the progenitor of SN 2011dh have a binary companion?*. *MNRAS*, 454:2580–2585.

Maund, J. R., M. Fraser, M. Ergon, A. Pastorello, S. J. Smartt, J. Sollerman, S. Benetti, M.-T. Botticella, F. Bufano, I. J. Danziger, R. Kotak, L. Magill, A. W. Stephens, and S. Valenti

2011. The Yellow Supergiant Progenitor of the Type II Supernova 2011dh in M51. *ApJ*, 739:L37.

Maund, J. R., S. J. Smartt, R. P. Kudritzki, P. Podsiadlowski, and G. F. Gilmore

2004. The massive binary companion star to the progenitor of supernova 1993J. *Nature*, 427:129–131.

Maurer, I., P. A. Mazzali, S. Taubenberger, and S. Hachinger

2010. Hydrogen and helium in the late phase of supernovae of Type IIb. *MNRAS*, 409:1441–1454.

Mazzali, P. A.

2000. Applications of an improved Monte Carlo code to the synthesis of early-time Supernova spectra. *A&A*, 363:705–716.

Mazzali, P. A., J. Deng, M. Hamuy, and K. Nomoto

2009. SN 2003bg: A Broad-Lined Type IIb Supernova with Hydrogen. *ApJ*, 703:1624–1634.

Mazzali, P. A., J. Deng, K. Maeda, K. Nomoto, H. Umeda, K. Hatano, K. Iwamoto, Y. Yoshii, Y. Kobayashi, T. Minezaki, M. Doi, K. Enya, H. Tomita, S. J. Smartt, K. Kinugasa, H. Kawakita, K. Ayani, T. Kawabata, H. Yamaoka, Y. L. Qiu, K. Motohara, C. L. Gerardy, R. Fesen, K. S. Kawabata, M. Iye, N. Kashikawa, G. Kosugi, Y. Ohyama, M. Takada-Hidai, G. Zhao, R. Chornock, A. V. Filippenko, S. Benetti, and M. Turatto

2002. The Type Ic Hypernova SN 2002ap. *ApJ*, 572:L61–L65.

Mazzali, P. A., J. Deng, K. Nomoto, D. N. Sauer, E. Pian, N. Tominaga, M. Tanaka, K. Maeda, and A. V. Filippenko

2006. A neutron-star-driven X-ray flash associated with supernova SN 2006aj. *Nature*, 442:1018–1020.

Mazzali, P. A., J. Deng, N. Tominaga, K. Maeda, K. Nomoto, T. Matheson, K. S. Kawabata, K. Z. Stanek, and P. M. Garnavich

2003. The Type Ic Hypernova SN 2003dh/GRB 030329. *ApJ*, 599:L95–L98.

Mazzali, P. A., K. Iwamoto, and K. Nomoto

2000. A Spectroscopic Analysis of the Energetic Type Ic Hypernova SN 1997EF. *ApJ*, 545:407–419.

Mazzali, P. A., K. S. Kawabata, K. Maeda, K. Nomoto, A. V. Filippenko, E. Ramirez-Ruiz, S. Benetti, E. Pian, J. Deng, N. Tominaga, Y. Ohyama, M. Iye, R. J. Foley, T. Matheson, L. Wang, and A. Gal-Yam

2005. An Asymmetric Energetic Type Ic Supernova Viewed Off-Axis, and a Link to Gamma Ray Bursts. *Science*, 308:1284–1287.

Mazzali, P. A. and L. B. Lucy

1993. The application of Monte Carlo methods to the synthesis of early-time supernovae spectra. *A&A*, 279:447–456.

Mazzali, P. A., I. Maurer, S. Valenti, R. Kotak, and D. Hunter

2010. The Type Ic SN 2007gr: a census of the ejecta from late-time optical-infrared spectra. *MNRAS*, 408:87–96.

Mazzali, P. A., D. N. Sauer, E. Pian, J. Deng, S. Prentice, S. Ben Ami, S. Taubenberger, and K. Nomoto

2017. Modelling the Type Ic SN 2004aw: a moderately energetic explosion of a massive C+O star without a GRB. *MNRAS*, 469:2498–2508.

Mazzali, P. A., M. Sullivan, S. Hachinger, R. S. Ellis, P. E. Nugent, D. A. Howell, A. Gal-Yam, K. Maguire, J. Cooke, R. Thomas, K. Nomoto, and E. S. Walker

2014. Hubble Space Telescope spectra of the Type Ia supernova SN 2011fe: a tail of low-density, high-velocity material with $Z < Z_{\odot}$. *MNRAS*, 439:1959–1979.

Mazzali, P. A., S. Valenti, M. Della Valle, G. Chincarini, D. N. Sauer, S. Benetti, E. Pian, T. Piran, V. D'Elia, N. Elias-Rosa, R. Margutti, F. Pasotti, L. A. Antonelli, F. Bufano, S. Campana, E. Cappellaro, S. Covino, P. D'Avanzo, F. Fiore, D. Fugazza, R. Gilmozzi, D. Hunter, K. Maguire, E. Maiorano, P. Marziani, N. Masetti, F. Mirabel, H. Navasardyan, K. Nomoto, E. Palazzi, A. Pastorello, N. Panagia, L. J. Pellizza, R. Sari, S. Smartt, G. Tagliaferri, M. Tanaka, S. Taubenberger, N. Tominaga, C. Trundle, and M. Turatto

2008. The Metamorphosis of Supernova SN 2008D/XRF 080109: A Link Between Supernovae and GRBs/Hypernovae. *Science*, 321:1185.

Mazzali, P. A., E. S. Walker, E. Pian, M. Tanaka, A. Corsi, T. Hattori, and A. Gal-Yam

2013. The very energetic, broad-lined Type Ic supernova 2010ah (PTF10bzf) in the context of GRB/SNe. *MNRAS*, 432:2463–2473.

Melandri, A., E. Pian, V. D'Elia, P. D'Avanzo, M. Della Valle, P. A. Mazzali, G. Tagliaferri, Z. Cano, A. J. Levan, P. Møoller, L. Amati, M. G. Bernardini, D. Bersier, F. Bufano, S. Campana, A. J. Castro-Tirado, S. Covino, G. Ghirlanda, K. Hurley, D. Malesani, N. Masetti, E. Palazzi, S. Piranomonte, A. Rossi, R. Salvaterra, R. L. C. Starling, M. Tanaka, N. R. Tanvir, and S. D. Vergani

2014. Diversity of gamma-ray burst energetics vs. supernova homogeneity: SN 2013cq associated with GRB 130427A. *A&A*, 567:A29.

Melandri, A., E. Pian, P. Ferrero, V. D'Elia, E. S. Walker, G. Ghirlanda, S. Covino, L. Amati, P. D'Avanzo, and P. A. Mazzali
2012. The optical SN 2012bz associated with the long GRB 120422A. *A&A*, 547:A82.

Metzger, B. D., B. Margalit, D. Kasen, and E. Quataert
2015. The diversity of transients from magnetar birth in core collapse supernovae. *MNRAS*, 454:3311–3316.

Milisavljevic, D., R. A. Fesen, C. L. Gerardy, R. P. Kirshner, and P. Challis
2010. Doublets and Double Peaks: Late-Time [O I] $\lambda\lambda$6300, 6364 Line Profiles of Stripped-Envelope, Core-Collapse Supernovae. *ApJ*, 709:1343–1355.

Milisavljevic, D., R. Margutti, A. Kamble, D. J. Patnaude, J. C. Raymond, J. J. Eldridge, W. Fong, M. Bietenholz, P. Challis, R. Chornock, M. R. Drout, C. Fransson, R. A. Fesen, J. E. Grindlay, R. P. Kirshner, R. Lunnan, J. Mackey, G. F. Miller, J. T. Parrent, N. E. Sanders, A. M. Soderberg, and B. A. Zauderer
2015a. Metamorphosis of SN 2014C: Delayed Interaction between a Hydrogen Poor Core-collapse Supernova and a Nearby Circumstellar Shell. *ApJ*, 815:120.

Milisavljevic, D., R. Margutti, J. T. Parrent, A. M. Soderberg, R. A. Fesen, P. Mazzali, K. Maeda, N. E. Sanders, S. B. Cenko, J. M. Silverman, A. V. Filippenko, A. Kamble, S. Chakraborti, M. R. Drout, R. P. Kirshner, T. E. Pickering, K. Kawabata, T. Hattori, E. Y. Hsiao, M. D. Stritzinger, G. H. Marion, J. Vinko, and J. C. Wheeler
2015b. The Broad-lined Type Ic SN 2012ap and the Nature of Relativistic Supernovae Lacking a Gamma-Ray Burst Detection. *ApJ*, 799:51.

Milisavljevic, D., R. Margutti, A. M. Soderberg, G. Pignata, L. Chomiuk, R. A. Fesen, F. Bufano, N. E. Sanders, and J. T. Parrent
2013a. Multi-wavelength Observations of Supernova 2011ei: Time-dependent Classification of Type IIb and Ib Supernovae and Implications for Their Progenitors. *ApJ*, 767:71.

Milisavljevic, D., R. Margutti, A. M. Soderberg, G. Pignata, L. Chomiuk, R. A. Fesen, F. Bufano, N. E. Sanders, J. T. Parrent, S. Parker, P. Mazzali, E. Pian, T. Pickering, D. A. H. Buckley, S. M. Crawford, A. A. S. Gulbis, C. Hettlage, E. Hooper, K. H. Nordsieck, D. O'Donoghue, T.-O. Husser, S. Potter, A. Kniazev, P. Kotze, E. Romero-Colmenero, P. Vaisanen, M. Wolf, M. F. Bietenholz, N. Bartel, C. Fransson, E. S. Walker, A. Brunthaler, S. Chakraborti, E. M. Levesque, A. MacFadyen, C. Drescher, G. Bock, P. Marples, J. P. Anderson, S. Benetti, D. Reichart, and K. Ivarsen

2013b. Multi-wavelength Observations of Supernova 2011ei: Time-dependent Classification of Type IIb and Ib Supernovae and Implications for Their Progenitors. *ApJ*, 767:71.

Mirabal, N., J. P. Halpern, D. An, J. R. Thorstensen, and D. M. Terndrup

2006. GRB 060218/SN 2006aj: A Gamma-Ray Burst and Prompt Supernova at z = 0.0335. *ApJ*, 643:L99–L102.

Modjaz, M., S. Blondin, R. P. Kirshner, T. Matheson, P. Berlind, F. B. Bianco, M. L. Calkins, P. Challis, P. Garnavich, M. Hicken, S. Jha, Y. Q. Liu, and G. H. Marion

2014. Optical Spectra of 73 Stripped-envelope Core-collapse Supernovae. *AJ*, 147:99.

Modjaz, M., R. P. Kirshner, S. Blondin, P. Challis, and T. Matheson

2008. Double-Peaked Oxygen Lines Are Not Rare in Nebular Spectra of Core-Collapse Supernovae. *ApJ*, 687:L9.

Modjaz, M., W. Li, N. Butler, R. Chornock, D. Perley, S. Blondin, J. S. Bloom, A. V. Filippenko, R. P. Kirshner, D. Kocevski, D. Poznanski, M. Hicken, R. J. Foley, G. S. Stringfellow, P. Berlind, D. Barrado y Navascues, C. H. Blake, H. Bouy, W. R. Brown, P. Challis, H. Chen, W. H. de Vries, P. Dufour, E. Falco, A. Friedman, M. Ganeshalingam, P. Garnavich, B. Holden, G. Illingworth, N. Lee, J. Liebert, G. H. Marion, S. S. Olivier, J. X. Prochaska, J. M. Silverman, N. Smith, D. Starr, T. N. Steele, A. Stockton, G. G. Williams, and W. M. Wood-Vasey

2009. From Shock Breakout to Peak and Beyond: Extensive Panchromatic Ob-

servations of the Type Ib Supernova 2008D Associated with Swift X-ray Transient 080109. *ApJ*, 702:226–248.

Modjaz, M., Y. Q. Liu, F. B. Bianco, and O. Graur

2015. The Spectral SN-GRB Connection: Systematic Spectral Comparisons between Type Ic Supernovae, and broad-lined Type Ic Supernovae with and without Gamma-Ray Bursts. *ArXiv e-prints*.

Morales-Garoffolo, A., N. Elias-Rosa, S. Benetti, S. Taubenberger, E. Cappellaro, A. Pastorello, M. Klauser, S. Valenti, S. Howerton, P. Ochner, N. Schramm, A. Siviero, L. Tartaglia, and L. Tomasella

2014a. SN 2013df, a double-peaked IIb supernova from a compact progenitor and an extended H envelope. *MNRAS*, 445:1647–1662.

Morales-Garoffolo, A., N. Elias-Rosa, S. Benetti, S. Taubenberger, E. Cappellaro, A. Pastorello, M. Klauser, S. Valenti, S. Howerton, P. Ochner, N. Schramm, A. Siviero, L. Tartaglia, and L. Tomasella

2014b. SN 2013df, a double-peaked IIb supernova from a compact progenitor and an extended H envelope. *MNRAS*, 445:1647–1662.

Moriya, T. J., T.-W. Chen, and N. Langer

2017. Properties of Magnetars Mimicking ^{56}Ni-powered Light Curves in Type IC Superluminous Supernovae. *ApJ*, 835:177.

Müller, B. and H.-T. Janka

2015. Non-radial instabilities and progenitor asphericities in core-collapse supernovae. *MNRAS*, 448:2141–2174.

Nakamura, T., P. A. Mazzali, K. Nomoto, and K. Iwamoto

2001. Light Curve and Spectral Models for the Hypernova SN 1998BW Associated with GRB 980425. *ApJ*, 550:991–999.

Nakar, E. and A. L. Piro

2014. Supernovae with Two Peaks in the Optical Light Curve and the Signature of Progenitors with Low-mass Extended Envelopes. *ApJ*, 788:193.

Nicholl, M., J. Guillochon, and E. Berger

2017. The Magnetar Model for Type I Superluminous Supernovae. I. Bayesian Analysis of the Full Multicolor Light-curve Sample with MOSFiT. *ApJ*, 850:55.

Nicholl, M., S. J. Smartt, A. Jerkstrand, C. Inserra, S. A. Sim, T.-W. Chen, S. Benetti, M. Fraser, A. Gal-Yam, E. Kankare, K. Maguire, K. Smith, M. Sullivan, S. Valenti, D. R. Young, C. Baltay, F. E. Bauer, S. Baumont, D. Bersier, M.-T. Botticella, M. Childress, M. Dennefeld, M. Della Valle, N. Elias-Rosa, U. Feindt, L. Galbany, E. Hadjiyska, L. Le Guillou, G. Leloudas, P. Mazzali, R. McKinnon, J. Polshaw, D. Rabinowitz, S. Rostami, R. Scalzo, B. P. Schmidt, S. Schulze, J. Sollerman, F. Taddia, and F. Yuan

2015. On the diversity of superluminous supernovae: ejected mass as the dominant factor. *MNRAS*, 452:3869–3893.

Nomoto, K., T. Suzuki, T. Shigeyama, S. Kumagai, H. Yamaoka, and H. Saio

1993. A type IIb model for supernova 1993J. *Nature*, 364:507–509.

Nomoto, K., H. Yamaoka, O. R. Pols, E. P. J. van den Heuvel, K. Iwamoto, S. Kumagai, and T. Shigeyama

1994. A carbon-oxygen star as progenitor of the type Ic supernova 1994I. *Nature*, 371:227–229.

O'Connor, E. and C. D. Ott

2011. Black Hole Formation in Failing Core-Collapse Supernovae. *ApJ*, 730:70.

Ofek, E. O., M. Sullivan, N. J. Shaviv, A. Steinbok, I. Arcavi, A. Gal-Yam, D. Tal, S. R. Kulkarni, P. E. Nugent, S. Ben-Ami, M. M. Kasliwal, S. B. Cenko, R. Laher, J. Surace, J. S. Bloom, A. V. Filippenko, J. M. Silverman, and O. Yaron

2014. Precursors Prior to Type IIn Supernova Explosions are Common: Precursor Rates, Properties, and Correlations. *ApJ*, 789:104.

Ohtani, Y., A. Suzuki, T. Shigeyama, and M. Tanaka

2018. X-Ray Light Curve and Spectra of Shock Breakout in a Wind. *ApJ*, 853:52.

Olausen, S. A. and V. M. Kaspi

2014. The McGill Magnetar Catalog. *ApJS*, 212:6.

Paragi, Z., G. B. Taylor, C. Kouveliotou, J. Granot, E. Ramirez-Ruiz, M. Bietenholz, A. J. van der Horst, Y. Pidopryhora, H. J. van Langevelde, M. A. Garrett, A. Szomoru, M. K. Argo, S. Bourke, and B. Paczyński

2010. A mildly relativistic radio jet from the otherwise normal type Ic supernova 2007gr. *Nature*, 463:516–518.

Parrent, J. T., D. Milisavljevic, A. M. Soderberg, and M. Parthasarathy

2016. Line Identifications of Type I Supernovae: On the Detection of Si II for These Hydrogen-poor Events. *ApJ*, 820:75.

Pastorello, A., M. M. Kasliwal, R. M. Crockett, S. Valenti, R. Arbour, K. Itagaki, S. Kaspi, A. Gal-Yam, S. J. Smartt, R. Griffith, K. Maguire, E. O. Ofek, N. Seymour, D. Stern, and W. Wiethoff

2008. The Type IIb SN 2008ax: spectral and light curve evolution. *MNRAS*, 389:955–966.

Patat, F., E. Cappellaro, J. Danziger, P. A. Mazzali, J. Sollerman, T. Augusteijn, J. Brewer, V. Doublier, J. F. Gonzalez, O. Hainaut, C. Lidman, B. Leibundgut, K. Nomoto, T. Nakamura, J. Spyromilio, L. Rizzi, M. Turatto, J. Walsh, T. J. Galama, J. van Paradijs, C. Kouveliotou, P. M. Vreeswijk, F. Frontera, N. Masetti, E. Palazzi, and E. Pian

2001. The Metamorphosis of SN 1998bw. *ApJ*, 555:900–917.

Phillips, M. M.

1993. The absolute magnitudes of Type IA supernovae. *ApJ*, 413:L105–L108.

Pian, E., P. A. Mazzali, N. Masetti, P. Ferrero, S. Klose, E. Palazzi, E. Ramirez-Ruiz, S. E. Woosley, C. Kouveliotou, J. Deng, A. V. Filippenko, R. J. Foley, J. P. U. Fynbo, D. A. Kann, W. Li, J. Hjorth, K. Nomoto, F. Patat, D. N. Sauer, J. Sollerman, P. M. Vreeswijk, E. W. Guenther, A. Levan, P. O'Brien, N. R. Tanvir, R. A. M. J. Wijers, C. Dumas, O. Hainaut, D. S. Wong, D. Baade, L. Wang, L. Amati, E. Cappellaro,

A. J. Castro-Tirado, S. Ellison, F. Frontera, A. S. Fruchter, J. Greiner, K. Kawabata, C. Ledoux, K. Maeda, P. Møller, L. Nicastro, E. Rol, and R. Starling

2006. An optical supernova associated with the X-ray flash XRF 060218. *Nature*, 442:1011–1013.

Piascik, A. S., I. A. Steele, S. D. Bates, C. J. Mottram, R. J. Smith, R. M. Barnsley, and B. Bolton

2014. SPRAT: Spectrograph for the Rapid Acquisition of Transients. In *Ground-based and Airborne Instrumentation for Astronomy V*, volume 9147 of *Proc. SPIE*, P. 91478H.

Pignata, G., M. Stritzinger, A. Soderberg, P. Mazzali, M. M. Phillips, N. Morrell, J. P. Anderson, L. Boldt, A. Campillay, C. Contreras, G. Folatelli, F. Förster, S. González, M. Hamuy, W. Krzeminski, J. Maza, M. Roth, F. Salgado, E. M. Levesque, A. Rest, J. A. Crain, A. C. Foster, J. B. Haislip, K. M. Ivarsen, A. P. LaCluyze, M. C. Nysewander, and D. E. Reichart

2011. SN 2009bb: A Peculiar Broad-lined Type Ic Supernova. *ApJ*, 728:14.

Piro, A. L.

2015. Using Double-peaked Supernova Light Curves to Study Extended Material. *ApJ*, 808:L51.

Piro, A. L. and V. S. Morozova

2014. Transparent Helium in Stripped Envelope Supernovae. *ApJ*, 792:L11.

Piro, A. L. and E. Nakar

2013. What can we Learn from the Rising Light Curves of Radioactively Powered Supernovae? *ApJ*, 769:67.

Poznanski, D., M. Ganeshalingam, J. M. Silverman, and A. V. Filippenko

2011. Low-resolution sodium D absorption is a bad proxy for extinction. *MNRAS*, 415:L81–L84.

Poznanski, D., J. X. Prochaska, and J. S. Bloom

2012. An empirical relation between sodium absorption and dust extinction. *MNRAS*, 426:1465–1474.

Prentice, S. J., C. Ashall, P. A. Mazzali, J.-J. Zhang, P. A. James, X.-F. Wang, J. Vinkó, S. Percival, L. Short, A. Piascik, F. Huang, J. Mo, L.-M. Rui, J.-G. Wang, D.-F. Xiang, Y.-X. Xin, W.-M. Yi, X.-G. Yu, Q. Zhai, T.-M. Zhang, G. Hosseinzadeh, D. A. Howell, C. McCully, S. Valenti, B. Cseh, O. Hanyecz, L. Kriskovics, A. Pál, K. Sárneczky, Á. Sódor, R. Szakáts, P. Székely, E. Varga-Verebélyi, K. Vida, M. Bradac, D. E. Reichart, D. Sand, and L. Tartaglia

2018. SN 2016coi/ASASSN-16fp: An example of residual helium in a type Ic supernova? *MNRAS*.

Prentice, S. J. and P. A. Mazzali

2017. A physically motivated classification of stripped-envelope supernovae. *MNRAS*, 469:2672–2694.

Prentice, S. J., P. A. Mazzali, E. Pian, A. Gal-Yam, S. R. Kulkarni, A. Rubin, A. Corsi, C. Fremling, J. Sollerman, O. Yaron, I. Arcavi, W. Zheng, M. M. Kasliwal, A. V. Filippenko, S. B. Cenko, Y. Cao, and P. E. Nugent

2016. The bolometric light curves and physical parameters of stripped-envelope supernovae. *MNRAS*, 458:2973–3002.

Pritchard, T. A., P. W. A. Roming, P. J. Brown, A. J. Bayless, and L. H. Frey

2014. Bolometric and UV Light Curves of Core-collapse Supernovae. *ApJ*, 787:157.

Qiu, Y., W. Li, Q. Qiao, and J. Hu

1999. The Study of a Type IIB Supernova: SN 1996CB. *AJ*, 117:736–743.

Quimby, R. M., G. Aldering, J. C. Wheeler, P. Höflich, C. W. Akerlof, and E. S. Rykoff

2007. SN 2005ap: A Most Brilliant Explosion. *ApJ*, 668:L99–L102.

Richardson, D.

2009. Absolute Magnitude Distribution and Light Curves of Gamma-Ray Burst Supernovae. *AJ*, 137:347–353.

Richardson, D., D. Branch, and E. Baron

2006. Absolute Magnitude Distributions and Light Curves of Stripped-Envelope Supernovae. *AJ*, 131:2233–2244.

Richmond, M. W., R. R. Treffers, A. V. Filippenko, Y. Paik, B. Leibundgut, E. Schulman, and C. V. Cox

1994. UBVRI photometry of SN 1993J in M81: The first 120 days. *AJ*, 107:1022–1040.

Richmond, M. W., S. D. van Dyk, W. Ho, C. Y. Peng, Y. Paik, R. R. Treffers, A. V. Filippenko, J. Bustamante-Donas, M. Moeller, C. Pawellek, H. Tartara, and M. Spence

1996. UBVRI Photometry of the Type IC SN 1994I in M51. *AJ*, 111:327.

Roberts, L. F., C. D. Ott, R. Haas, E. P. O'Connor, P. Diener, and E. Schnetter

2016. General-Relativistic Three-Dimensional Multi-group Neutrino Radiation-Hydrodynamics Simulations of Core-Collapse Supernovae. *ApJ*, 831:98.

Roy, R., B. Kumar, J. R. Maund, P. Schady, E. F. Olivares, D. Malesani, G. Leloudas, S. Nandi, N. Tanvir, D. Milisavljevic, J. Hjorth, K. Misra, B. Kumar, S. B. Pandey, R. Sagar, and H. C. Chandola

2013. SN 2007uy - metamorphosis of an aspheric Type Ib explosion. *MNRAS*, 434:2032–2050.

Ryder, S. D., S. D. Van Dyk, O. D. Fox, E. Zapartas, S. E. de Mink, N. Smith, E. Brunsden, K. Azalee Bostroem, A. V. Filippenko, I. Shivvers, and W. Zheng

2018. Ultraviolet Detection of the Binary Companion to the Type IIb SN 2001ig. *ArXiv e-prints*.

Sahu, D. K., M. Tanaka, G. C. Anupama, U. K. Gurugubelli, and K. Nomoto

2009. The Broad-Line Type Ic Supernova SN 2007ru: Adding to the Diversity of Type Ic Supernovae. *ApJ*, 697:676–683.

Sako, M., B. Bassett, A. C. Becker, P. J. Brown, H. Campbell, R. Cane, D. Cinabro, C. B. D'Andrea, K. S. Dawson, F. DeJongh, D. L. Depoy, B. Dilday, M. Doi, A. V.

Filippenko, J. A. Fischer, and R. J. Foley
2014. The Data Release of the Sloan Digital Sky Survey-II Supernova Survey. *ArXiv e-prints*.

Sana, H., S. E. de Mink, A. de Koter, N. Langer, C. J. Evans, M. Gieles, E. Gosset, R. G. Izzard, J.-B. Le Bouquin, and F. R. N. Schneider
2012. Binary Interaction Dominates the Evolution of Massive Stars. *Science*, 337:444.

Sanders, N. E., A. M. Soderberg, E. M. Levesque, R. J. Foley, R. Chornock, D. Milisavljevic, R. Margutti, E. Berger, M. R. Drout, I. Czekala, and J. A. Dittmann
2012. A Spectroscopic Study of Type Ibc Supernova Host Galaxies from Untargeted Surveys. *ApJ*, 758:132.

Sauer, D. N., P. A. Mazzali, J. Deng, S. Valenti, K. Nomoto, and A. V. Filippenko
2006. The properties of the 'standard' Type Ic supernova 1994I from spectral models. *MNRAS*, 369:1939–1948.

Schlafly, E. F. and D. P. Finkbeiner
2011. Measuring Reddening with Sloan Digital Sky Survey Stellar Spectra and Recalibrating SFD. *ApJ*, 737:103.

Schneider, F. R. N., H. Sana, C. J. Evans, J. M. Bestenlehner, N. Castro, L. Fossati, G. Gräfener, N. Langer, O. H. Ramírez-Agudelo, C. Sabín-Sanjulián, S. Simón-Díaz, F. Tramper, P. A. Crowther, A. de Koter, S. E. de Mink, P. L. Dufton, M. Garcia, M. Gieles, V. Hénault-Brunet, A. Herrero, R. G. Izzard, V. Kalari, D. J. Lennon, J. Maíz Apellániz, N. Markova, F. Najarro, P. Podsiadlowski, J. Puls, W. D. Taylor, J. T. van Loon, J. S. Vink, and C. Norman
2018. An excess of massive stars in the local 30 Doradus starburst. *ArXiv e-prints*.

Shivvers, I., M. Modjaz, W. Zheng, Y. Liu, A. V. Filippenko, J. M. Silverman, T. Matheson, A. Pastorello, O. Graur, R. J. Foley, R. Chornock, N. Smith, J. Leaman, and S. Benetti
2017. Revisiting the Lick Observatory Supernova Search Volume-limited Sample:

Updated Classifications and Revised Stripped-envelope Supernova Fractions. *PASP*, 129(5):054201.

Smartt, S. J.

2009. Progenitors of Core-Collapse Supernovae. *ARA&A*, 47:63–106.

Smith, N., Y. Götberg, and S. E. de Mink

2018. Extreme isolation of WN3/O3 stars and implications for their evolutionary origin as the elusive stripped binaries. *MNRAS*, 475:772–782.

Smith, N., W. Li, A. V. Filippenko, and R. Chornock

2011. Observed fractions of core-collapse supernova types and initial masses of their single and binary progenitor stars. *MNRAS*, 412:1522–1538.

Soderberg, A. M., E. Berger, K. L. Page, P. Schady, J. Parrent, D. Pooley, X.-Y. Wang, E. O. Ofek, A. Cucchiara, A. Rau, E. Waxman, J. D. Simon, D. C.-J. Bock, P. A. Milne, M. J. Page, J. C. Barentine, S. D. Barthelmy, A. P. Beardmore, M. F. Bietenholz, P. Brown, A. Burrows, D. N. Burrows, G. Byrngelson, S. B. Cenko, P. Chandra, J. R. Cummings, D. B. Fox, A. Gal-Yam, N. Gehrels, S. Immler, M. Kasliwal, A. K. H. Kong, H. A. Krimm, S. R. Kulkarni, T. J. Maccarone, P. Mészáros, E. Nakar, P. T. O'Brien, R. A. Overzier, M. de Pasquale, J. Racusin, N. Rea, and D. G. York

2008. An extremely luminous X-ray outburst at the birth of a supernova. *Nature*, 453:469–474.

Soderberg, A. M., A. Brunthaler, E. Nakar, R. A. Chevalier, and M. F. Bietenholz

2010. Radio and X-ray Observations of the Type Ic SN 2007gr Reveal an Ordinary, Non-relativistic Explosion. *ApJ*, 725:922–930.

Soderberg, A. M., R. Margutti, B. A. Zauderer, M. Krauss, B. Katz, L. Chomiuk, J. A. Dittmann, E. Nakar, T. Sakamoto, N. Kawai, K. Hurley, S. Barthelmy, T. Toizumi, M. Morii, R. A. Chevalier, M. Gurwell, G. Petitpas, M. Rupen, K. D. Alexander, E. M. Levesque, C. Fransson, A. Brunthaler, M. F. Bietenholz, N. Chugai, J. Grindlay, A. Copete, V. Connaughton, M. Briggs, C. Meegan, A. von Kienlin, X. Zhang,

A. Rau, S. Golenetskii, E. Mazets, and T. Cline

2012. Panchromatic Observations of SN 2011dh Point to a Compact Progenitor Star. *ApJ*, 752:78.

Soderberg, A. M., E. Nakar, E. Berger, and S. R. Kulkarni

2006. Late-Time Radio Observations of 68 Type Ibc Supernovae: Strong Constraints on Off-Axis Gamma-Ray Bursts. *ApJ*, 638:930–937.

Sonbas, E., A. S. Moskvitin, T. A. Fatkhullin, V. V. Sokolov, A. Castro-Tirado, A. de Ugarte Postigo, G. Gorosabel, S. Guzij, M. Jelinec, T. N. Sokolova, and V. N. Chernenkov

2008. Stellar-wind envelope around the massive supernova progenitor XRF/GRB 060218/SN 2006aj. *Astrophysical Bulletin*, 63:228–243.

Srivastav, S., G. C. Anupama, and D. K. Sahu

2014. Optical observations of the fast declining Type Ib supernova iPTF13bvn. *MNRAS*, 445:1932–1941.

Steele, I. A., R. J. Smith, P. C. Rees, I. P. Baker, S. D. Bates, M. F. Bode, M. K. Bowman, D. Carter, J. Etherton, M. J. Ford, S. N. Fraser, A. Gomboc, R. D. J. Lett, A. G. Mansfield, J. M. Marchant, G. A. Medrano-Cerda, C. J. Mottram, D. Raback, A. B. Scott, M. D. Tomlinson, and R. Zamanov

2004. The Liverpool Telescope: performance and first results. In *Ground-based Telescopes*, J. M. Oschmann, Jr., ed., volume 5489 of *Proc. SPIE*, Pp. 679–692.

Stevance, H. F., J. R. Maund, D. Baade, P. Höflich, S. Howerton, F. Patat, M. Rose, J. Spyromilio, J. C. Wheeler, and L. Wang

2017. The evolution of the 3D shape of the broad-lined Type Ic SN 2014ad. *MNRAS*, 469:1897–1911.

Stevance, H. F., J. R. Maund, D. Baade, P. Höflich, F. Patat, J. Spyromilio, J. C. Wheeler, A. Clocchiatti, L. Wang, Y. Yang, and P. Zelaya

2016. Spectropolarimetry of the Type IIb SN 2008aq*. *MNRAS*, 461:2019–2024.

Stritzinger, M., M. Hamuy, N. B. Suntzeff, R. C. Smith, M. M. Phillips, J. Maza, L.-G. Strolger, R. Antezana, L. González, M. Wischnjewsky, P. Candia, J. Espinoza, D. González, C. Stubbs, A. C. Becker, E. P. Rubenstein, and G. Galaz

2002. Optical Photometry of the Type Ia Supernova 1999ee and the Type Ib/c Supernova 1999ex in IC 5179. *AJ*, 124:2100–2117.

Stritzinger, M. and B. Leibundgut

2005. Lower limits on the Hubble constant from models of type Ia supernovae. *A&A*, 431:423–431.

Stritzinger, M., P. Mazzali, M. M. Phillips, S. Immler, A. Soderberg, J. Sollerman, L. Boldt, J. Braithwaite, P. Brown, C. R. Burns, C. Contreras, R. Covarrubias, G. Folatelli, W. L. Freedman, S. González, M. Hamuy, W. Krzeminski, B. F. Madore, P. Milne, N. Morrell, S. E. Persson, M. Roth, M. Smith, and N. B. Suntzeff

2009. The He-Rich Core-Collapse Supernova 2007Y: Observations from X-Ray to Radio Wavelengths. *ApJ*, 696:713–728.

Stritzinger, M. D., J. P. Anderson, C. Contreras, E. Heinrich-Josties, N. Morrell, M. M. Phillips, J. Anais, L. Boldt, L. Busta, C. R. Burns, A. Campillay, C. Corco, S. Castellon, G. Folatelli, C. González, S. Holmbo, E. Y. Hsiao, W. Krzeminski, F. Salgado, J. Serón, S. Torres-Robledo, W. L. Freedman, M. Hamuy, K. Krisciunas, B. F. Madore, S. E. Persson, M. Roth, N. B. Suntzeff, F. Taddia, W. Li, and A. V. Filippenko

2018a. The Carnegie Supernova Project I. Photometry data release of low-redshift stripped-envelope supernovae. *A&A*, 609:A134.

Stritzinger, M. D., F. Taddia, C. R. Burns, M. M. Phillips, M. Bersten, C. Contreras, G. Folatelli, S. Holmbo, E. Y. Hsiao, P. Hoeflich, G. Leloudas, N. Morrell, J. Sollerman, and N. B. Suntzeff

2018b. The Carnegie Supernova Project I. Methods to estimate host-galaxy reddening of stripped-envelope supernovae. *A&A*, 609:A135.

Sukhbold, T., T. Ertl, S. E. Woosley, J. M. Brown, and H.-T. Janka

2016. Core-collapse Supernovae from 9 to 120 Solar Masses Based on Neutrino-powered Explosions. *ApJ*, 821:38.

Summa, A., H.-T. Janka, T. Melson, and A. Marek

2018. Rotation-supported Neutrino-driven Supernova Explosions in Three Dimensions and the Critical Luminosity Condition. *ApJ*, 852:28.

Svirski, G. and E. Nakar

2014a. SN 2008D: A Wolf-Rayet Explosion Through a Thick Wind. *ApJ*, 788:L14.

Svirski, G. and E. Nakar

2014b. Spectrum and Light Curve of a Supernova Shock Breakout through a Thick Wolf-Rayet Wind. *ApJ*, 788:113.

Taddia, F., C. Fremling, J. Sollerman, A. Corsi, A. Gal-Yam, E. Karamehmetoglu, R. Lunnan, B. Bue, M. Ergon, M. Kasliwal, P. M. Vreeswijk, and P. R. Wozniak

2016. iPTF15dtg: a double-peaked Type Ic Supernova from a massive progenitor. *ArXiv e-prints*.

Taddia, F., J. Sollerman, C. Fremling, E. Karamehmetoglu, R. M. Quimby, A. Gal-Yam, O. Yaron, M. M. Kasliwal, S. R. Kulkarni, P. E. Nugent, G. Smadja, and C. Tao

2018a. PTF11mnb: First analog of supernova 2005bf. Long-rising, double-peaked supernova Ic from a massive progenitor. *A&A*, 609:A106.

Taddia, F., J. Sollerman, G. Leloudas, M. D. Stritzinger, S. Valenti, L. Galbany, R. Kessler, D. P. Schneider, and J. C. Wheeler

2015. Early-time light curves of Type Ib/c supernovae from the SDSS-II Supernova Survey. *A&A*, 574:A60.

Taddia, F., M. D. Stritzinger, M. Bersten, E. Baron, C. Burns, C. Contreras, S. Holmbo, E. Y. Hsiao, N. Morrell, M. M. Phillips, J. Sollerman, and N. B. Suntzeff

2018b. The Carnegie Supernova Project I. Analysis of stripped-envelope supernova light curves. *A&A*, 609:A136.

Takiwaki, T., K. Kotake, and Y. Suwa

2012. Three-dimensional Hydrodynamic Core-collapse Supernova Simulations for an 11.2 $M_\odot$ Star with Spectral Neutrino Transport. *ApJ*, 749:98.

Tan, J. C., C. D. Matzner, and C. F. McKee

2001. Trans-Relativistic Blast Waves in Supernovae as Gamma-Ray Burst Progenitors. *ApJ*, 551:946–972.

Tanaka, M., K. S. Kawabata, K. Maeda, T. Hattori, and K. Nomoto

2008. Optical Spectropolarimetry and Asphericity of the Type Ic SN 2007gr. *ApJ*, 689:1191–1198.

Tanaka, M., K. S. Kawabata, K. Maeda, M. Iye, T. Hattori, E. Pian, K. Nomoto, P. A. Mazzali, and N. Tominaga

2009a. Spectropolarimetry of the Unique Type Ib Supernova 2005bf: Larger Asymmetry Revealed by Later-Phase Data. *ApJ*, 699:1119–1124.

Tanaka, M., K. Maeda, P. A. Mazzali, and K. Nomoto

2007. Multidimensional Simulations for Early-Phase Spectra of Aspherical Hypernovae: SN 1998bw and Off-Axis Hypernovae. *ApJ*, 668:L19–L22.

Tanaka, M., N. Tominaga, K. Nomoto, S. Valenti, D. K. Sahu, T. Minezaki, Y. Yoshii, M. Yoshida, G. C. Anupama, S. Benetti, G. Chincarini, M. Della Valle, P. A. Mazzali, and E. Pian

2009b. Type Ib Supernova 2008D Associated With the Luminous X-Ray Transient 080109: An Energetic Explosion of a Massive Helium Star. *ApJ*, 692:1131–1142.

Tanaka, M., M. Yamanaka, K. Maeda, K. S. Kawabata, T. Hattori, T. Minezaki, S. Valenti, M. Della Valle, D. K. Sahu, G. C. Anupama, N. Tominaga, K. Nomoto, P. A. Mazzali, and E. Pian

2009c. Nebular Phase Observations of the Type Ib Supernova 2008D/X-ray Transient 080109: Side-viewed Bipolar Explosion. *ApJ*, 700:1680–1685.

Tartaglia, L., M. Fraser, D. J. Sand, S. Valenti, S. J. Smartt, C. McCully, J. P. Anderson, I. Arcavi, N. Elias-Rosa, L. Galbany, A. Gal-Yam, J. B. Haislip, G. Hosseinzadeh,

D. A. Howell, C. Inserra, S. W. Jha, E. Kankare, P. Lundqvist, K. Maguire, S. Mattila, D. Reichart, K. W. Smith, M. Smith, M. Stritzinger, M. Sullivan, F. Taddia, and L. Tomasella

2017. The Progenitor and Early Evolution of the Type IIb SN 2016gkg. *ApJ*, 836:L12.

Taubenberger, S., H. Navasardyan, J. I. Maurer, L. Zampieri, N. N. Chugai, S. Benetti, I. Agnoletto, F. Bufano, N. Elias-Rosa, M. Turatto, F. Patat, E. Cappellaro, P. A. Mazzali, T. Iijima, S. Valenti, A. Harutyunyan, R. Claudi, and M. Dolci

2011. The He-rich stripped-envelope core-collapse supernova 2008ax. *MNRAS*, 413:2140–2156.

Taubenberger, S., A. Pastorello, P. A. Mazzali, S. Valenti, G. Pignata, D. N. Sauer, A. Arbey, O. Bärnbantner, S. Benetti, A. Della Valle, J. Deng, N. Elias-Rosa, A. V. Filippenko, R. J. Foley, A. Goobar, R. Kotak, W. Li, P. Meikle, J. Mendez, F. Patat, E. Pian, C. Ries, P. Ruiz-Lapuente, M. Salvo, V. Stanishev, M. Turatto, and W. Hillebrandt

2006. SN 2004aw: confirming diversity of Type Ic supernovae. *MNRAS*, 371:1459–1477.

Taubenberger, S., S. Valenti, S. Benetti, E. Cappellaro, M. Della Valle, N. Elias-Rosa, S. Hachinger, W. Hillebrandt, K. Maeda, P. A. Mazzali, A. Pastorello, F. Patat, S. A. Sim, and M. Turatto

2009. Nebular emission-line profiles of Type Ib/c supernovae - probing the ejecta asphericity. *MNRAS*, 397:677–694.

Tominaga, N., M. Tanaka, K. Nomoto, P. A. Mazzali, J. Deng, K. Maeda, H. Umeda, M. Modjaz, M. Hicken, and P. Challis

2005. The Unique Type Ib Supernova 2005bf: A WN Star Explosion Model for Peculiar Light Curves and Spectra. *ApJ*, 633:L97–L100.

Tomita, H., J. Deng, K. Maeda, Y. Yoshii, K. Nomoto, P. A. Mazzali, T. Suzuki, Y. Kobayashi, T. Minezaki, T. Aoki, K. Enya, and M. Suganuma

2006. The Optical/Near-Infrared Light Curves of SN 2002ap for the First 1.5 Years

after Discovery. *ApJ*, 644:400–408.

Uomoto, A. and R. P. Kirshner

1986. The late-time spectrum of the Type II supernova 1980k. *ApJ*, 308:685–690.

Valenti, S., S. Benetti, E. Cappellaro, F. Patat, P. Mazzali, M. Turatto, K. Hurley, K. Maeda, and A. Gal-Yam

2008. The broad-lined Type Ic supernova 2003jd. *MNRAS*, 383:1485–1500.

Valenti, S., M. Fraser, S. Benetti, G. Pignata, J. Sollerman, C. Inserra, E. Cappellaro, A. Pastorello, S. J. Smartt, M. Ergon, M. T. Botticella, J. Brimacombe, F. Bufano, M. Crockett, I. Eder, D. Fugazza, J. B. Haislip, M. Hamuy, A. Harutyunyan, K. M. Ivarsen, E. Kankare, R. Kotak, A. P. Lacluyze, L. Magill, S. Mattila, J. Maza, P. A. Mazzali, D. E. Reichart, S. Taubenberger, M. Turatto, and L. Zampieri

2011. SN 2009jf: a slow-evolving stripped-envelope core-collapse supernova. *MNRAS*, 416:3138–3159.

Valenti, S., D. A. Howell, M. D. Stritzinger, M. L. Graham, G. Hosseinzadeh, I. Arcavi, L. Bildsten, A. Jerkstrand, C. McCully, A. Pastorello, A. L. Piro, D. Sand, S. J. Smartt, G. Terreran, C. Baltay, S. Benetti, P. Brown, A. V. Filippenko, M. Fraser, D. Rabinowitz, M. Sullivan, and F. Yuan

2016. The diversity of Type II supernova versus the similarity in their progenitors. *MNRAS*, 459:3939–3962.

Valenti, S., S. Taubenberger, A. Pastorello, L. Aramyan, M. T. Botticella, M. Fraser, S. Benetti, S. J. Smartt, E. Cappellaro, N. Elias-Rosa, M. Ergon, L. Magill, E. Magnier, R. Kotak, P. A. Price, J. Sollerman, L. Tomasella, M. Turatto, and D. E. Wright

2012. A Spectroscopically Normal Type Ic Supernova from a Very Massive Progenitor. *ApJ*, 749:L28.

Van Dyk, S. D., S. E. de Mink, and E. Zapartas

2016. Constraints on the Binary Companion to the SN Ic 1994I Progenitor. *ApJ*, 818:75.

Van Dyk, S. D., A. V. Filippenko, O. D. Fox, P. L. Kelly, D. Milisavljevic, and N. Smith
2017. A Progenitor Candidate for SN 2017ein in NGC 3938. *The Astronomer's Telegram*, 10485.

Van Dyk, S. D., W. Zheng, O. D. Fox, S. B. Cenko, K. I. Clubb, A. V. Filippenko, R. J. Foley, A. A. Miller, N. Smith, P. L. Kelly, W. H. Lee, S. Ben-Ami, and A. Gal-Yam
2014. The Type IIb Supernova 2013df and its Cool Supergiant Progenitor. *AJ*, 147:37.

Vink, J. S.
2017. Winds from stripped low-mass helium stars and Wolf-Rayet stars. *A&A*, 607:L8.

Wang, L. J., Z. Cano, S. Q. Wang, W. K. Zheng, L. D. Liu, J. S. Deng, H. Yu, Z. G. Dai, Y. H. Han, D. Xu, Y. L. Qiu, J. Y. Wei, B. Li, and L. M. Song
2017. A Monte Carlo Approach to Magnetar-powered Transients. II. Broad-lined Type Ic Supernovae Not Associated with GRBs. *ApJ*, 851:54.

Wheeler, J. C., V. Johnson, and A. Clocchiatti
2015. Analysis of late-time light curves of Type IIb, Ib and Ic supernovae. *MNRAS*, 450:1295–1307.

Whitesides, L., R. Lunnan, M. M. Kasliwal, D. A. Perley, A. Corsi, S. B. Cenko, N. Blagorodnova, Y. Cao, D. O. Cook, G. B. Doran, D. D. Frederiks, C. Fremling, K. Hurley, E. Karamehmetoglu, S. R. Kulkarni, G. Leloudas, F. Masci, P. E. Nugent, A. Ritter, A. Rubin, V. Savchenko, J. Sollerman, D. S. Svinkin, F. Taddia, P. Vreeswijk, and P. Wozniak
2017. iPTF 16asu: A Luminous, Rapidly Evolving, and High-velocity Supernova. *ApJ*, 851:107.

Woosley, S. E.
1993. Gamma-ray bursts from stellar mass accretion disks around black holes. *ApJ*, 405:273–277.

Woosley, S. E., R. G. Eastman, T. A. Weaver, and P. A. Pinto

1994. SN 1993J: A Type IIb supernova. *ApJ*, 429:300–318.

Woosley, S. E. and A. Heger

2007. Nucleosynthesis and remnants in massive stars of solar metallicity. *Phys. Rep.*, 442:269–283.

Yamanaka, M., T. Nakaoka, M. Tanaka, K. Maeda, S. Honda, H. Hanayama, T. Morokuma, M. Imai, K. Kinugasa, K. L. Murata, T. Nishimori, O. Hashimoto, H. Gima, K. Hosoya, A. Ito, M. Karita, M. Kawabata, K. Morihana, Y. Morikawa, K. Murakami, T. Nagayama, T. Ono, H. Onozato, Y. Sarugaku, M. Sato, D. Suzuki, J. Takahashi, M. Takayama, H. Yaguchi, H. Akitaya, Y. Asakura, K. S. Kawabata, D. Kuroda, D. Nogami, Y. Oasa, T. Omodaka, Y. Saito, K. Sekiguchi, N. Tominaga, M. Uemura, and M. Watanabe

2017. Broad-lined Supernova 2016coi with a Helium Envelope. *ApJ*, 837:1.

Yaron, O. and A. Gal-Yam

2012. WISeREP - An Interactive Supernova Data Repository. *PASP*, 124:668–681.

Yoon, S.-C., L. Dessart, and A. Clocchiatti

2017. Type Ib and IIb Supernova Progenitors in Interacting Binary Systems. *ApJ*, 840:10.

Zapartas, E., S. E. de Mink, S. D. Van Dyk, O. D. Fox, N. Smith, K. A. Bostroem, A. de Koter, A. V. Filippenko, R. G. Izzard, P. L. Kelly, C. J. Neijssel, M. Renzo, and S. Ryder

2017. Predicting the Presence of Companions for Stripped-envelope Supernovae: The Case of the Broad-lined Type Ic SN 2002ap. *ApJ*, 842:125.